2017

Behaviour of GFRP Reinforced and GFRP Encased Square Concrete Members under Different Loading Conditions

Jim Youssef
University of Wollongong

UNIVERSITY
OF WOLLONGONG
AUSTRALIA

School of Civil, Mining and Environmental Engineering

Behaviour of GFRP Reinforced and GFRP Encased Square Concrete Members under Different Loading Conditions

A thesis submitted in fulfilment

of the requirements for the award of the degree of

DOCTOR OF PHILOSOPHY

By

Jim YOUSSEF

2017

THESIS DECLARATION

I, Jim Youssef, hereby declare that this thesis, submitted in fulfilment of the requirements for the award of Doctor of Philosophy, in the School of Civil, Mining and Environmental Engineering, University of Wollongong, Australia, is wholly my own work unless otherwise referenced or acknowledged. The document has not been submitted for qualification at any other academic institution.

Jim Youssef

October 2017

ACKNOWLEDGMENTS

I would like express my gratitude to my supervisor, A/Professor Muhammad N.S. Hadi, for his invaluable support, patience and encouragement throughout the duration of my PhD study. His comments, constructive criticism and inspiration during the preparation of this thesis, is muchly appreciated.

I would also like to acknowledge Messrs Alan Grant, Duncan Best, Fernando Escribano, Ritchie McLean, Richard Gasser and Cameron Neilson and the other technical staff at the University of Wollongong, Australia. The technical assistance during my experimental work is muchly appreciated. Furthermore, I would like to also thank Mr. Elliot Davison and Ms. Philippa Langford for their help in the preparation stage of my experimental program.

I wish to express my sincere thanks to Dr. Thong Ming Pham for taking me under his guidance and allowing me to work with him on two preliminary studies. I am grateful for his help during my first year of PhD study. I am also grateful to Dr. Eren Uz and all my friends for their discussion and social communication during my study.

This research has been conducted with the support of the Australian Government Research Training Program Scholarship. I would like to also acknowledge the financial support of the University of Wollongong, Australia for sponsoring my PhD study.

Finally, and most importantly, I would like to deeply acknowledge my wife Sandy, parents, brother and sister for their love, continuous support and motivation during all stages of my PhD study. This thesis is dedicated to my wife and family.

LIST OF PUBLICATIONS

Journal Papers

1. Pham, T. M., Hadi, M. N.S., and **Youssef, J.** (2015). "Optimized FRP Wrapping Schemes for Circular Concrete Columns under Axial Compression." *Journal of Composites for Construction*, 19(6), 04015015-1 - 04015015-10.

2. Hadi, M.N.S., and **Youssef, J.** (2016). "Experimental Investigation of GFRP Reinforced and GFRP Encased Square Concrete Specimens under Axial and Eccentric Load, and Four-Point Bending Test." *Journal of Composites for Construction*, 20(5), 04016020-1– 04016020-16.

3. Pham, T. M., Hadi, M. N.S., and **Youssef, J.** (2017). "Effects of Fabrication Technique on Tensile Properties of Fibre Reinforced Polymer." *Journal of Testing and Evaluation*, 45(5), https://doi.org/10.1520/JTE20150525.

4. **Youssef, J.**, and Hadi, M.N.S. (2017). "Axial Load-Bending Moment Diagrams of GFRP Reinforced Columns and GFRP Encased Square Columns." *Construction and Building Materials*, 135, 550 – 564.

5. **Youssef, J.**, and Hadi, M.N.S. (2017). "Compression Behavior of Pultruded GFRP Channels." *Journal of Composites for Construction.* (Under review).

Conference Papers

1. Pham, T. M., **Youssef, J.**, and Hadi, M. N.S. (2016). "Effect of Different FRP Wrapping Arrangements on the Confinement Mechanism." *Procedia Engineering, Proceeding of Sustainable Development of Civil, Urban and Transportation Engineering*, 142, 307 – 313, Ho Chi Minh City, Vietnam.

2. **Youssef, J.**, and Hadi, M.N.S. (2016). "Experimental Investigation of GFRP Reinforced Square Concrete Columns under Axial and Eccentric Loading." *CICE 2016 – 8th International Conference on Fibre Reinforced Polymer (FRP) Composites in Civil Engineering*, 1234 – 1239, 14 – 16 December, 2016, Hong Kong, China.

ABSTRACT

The use of reinforcement with fibre reinforced polymer (FRP) composite materials have emerged as one of the alternatives to steel reinforcement for concrete structures prone to corrosion issues (ACI 440.1R–15 2015). However, the mechanical behaviour of FRP reinforcement is different from that of steel reinforcement. In general FRP bars have a higher strength-to-weight ratio, but lower modulus of elasticity as compared to steel. Furthermore, when subjected to tension, FRP bars do not experience any plastic behaviour before rupture. Also, the compressive strengths of FRP bars are relatively low compared to the tensile strengths and are subjected to significant variations. Therefore, due to the differences in properties, GFRP bars cannot simply replace steel bars (ISIS 2007).

The level of understanding of the behaviour of FRP reinforced compression members has not reached a level where design standards are available for such members. Having said this, the current ACI 440.1R – 15 (2015) design guideline recommends neglecting the compressive contribution of FRP reinforcement when used as reinforcement in columns, in compression members, or as compression reinforcement in flexural members. Most of the findings of studies investigating FRP reinforced concrete columns have been reported based on testing under concentric loading with the behaviour of such members under eccentric axial loads not sufficiently addressed in the previous studies.

In addition, FRP pultruded materials are available in a wide variety of shapes, including bars, I-sections, C-sections and other structural sections. Due to their high durability, low self-weight and reduced maintenance costs, these FRP materials are becoming a competitive option for replacing steel as structural materials especially in corrosive environments. In addition, by developing a hybrid composite member composed of the combination of conventional materials (concrete and steel) and FRP pultruded composites, the beneficial material properties of each component can be utilised to attain advanced structural performance. However, there have been no studies available in the literature on structural GFRP sections encased concrete columns.

Consequently, this study aims to investigate the axial and flexural behaviour of square concrete members reinforced with GFRP bars and embedded with pultruded GFRP structural sections under different loading conditions (concentric, 25 mm eccentric, 50 mm eccentric and flexural loadings). The main parameters investigated in this study include the magnitude of load eccentricity and type of internal reinforcement with steel reinforced, GFRP-reinforced, GFRP I-section–encased, and GFRP C-sections encased concrete specimens tested under compressive and flexural loading. A total of seventeen RC specimens were tested, of which twelve were tested as columns under compression loading and five were tested as beams under flexural loading. The concrete specimens were square in cross section with a side dimension of 210 mm and a height of 800 mm. In addition to the experimental program, an analytical model was developed to determine the axial load-bending moment interaction diagrams of the experimentally tested specimens.

Based on the experimental and the analytical analysis of this study, it can be concluded that concrete columns reinforced with GFRP bars and encased with pultruded GFRP sections can be potentially analysed using the same procedure used for conventional steel reinforced concrete columns. Furthermore, the analytical models provide reliable estimates of the maximum load and bending moment capacities of GFRP reinforced and GFRP encased concrete columns. In addition, according to a parametric study, the axial load-bending moment interaction diagrams of columns reinforced with GFRP bars do not experience balanced points unlike that of steel reinforced columns. Therefore, this study is believed to give an understanding on the behaviour of GFRP reinforced and GFRP encased concrete columns subjected to various loading conditions in comparison with conventional steel reinforced columns.

TABLE OF CONTENTS

LIST OF FIGURES

LIST OF TABLES

ABBREVIATIONS

$A_{GFRP,n}$	=	Area of the GFRP sections in the n^{th} strip – small strips method
$A_{c,strip}$	=	Gross cross sectional area of concrete in each concrete strip
A_{comp}	=	Cross-sectional area of compressive reinforcement
A_e	=	Area of effectively confined concrete core
A_f	=	Total cross-sectional area of the longitudinal GFRP bars
A_g	=	Gross sectional area of concrete
A_{st}	=	Total area of steel longitudinal reinforcement
A_{tens}	=	Cross-sectional area of longitudinal tensile reinforcement
B_y	=	Percent bending about system *y* axis (about the narrow plane)
B_z	=	Percent bending about system *z* axis (about the wide plane)
b	=	Cross-section width of concrete specimens
b_f	=	Width of pultruded GFRP sections
C	=	Compressive force of reinforcement
$C_{c,n}$	=	Force reaction in centre of each concrete strip - small strips method
C_{c1}	=	Compression force in concrete - rectangular stress block method
C_{c2}	=	Compression force in concrete using the small strips method
D	=	Depth of rectangular cross-sections or diameter of circular cross-sections
d	=	Depth from extreme fibre in compression to tensile reinforcement
d_b	=	Diameter of reinforcing FRP bar
d_{co}	=	Depth from extreme fibre in compression to compressive reinforcement
d_n	=	Depth to the neutral axis of a cross-section in bending
d_s	=	Depth of pultruded GFRP section

E_F	=	Compressive modulus of elasticity of full-size GFRP channels
E_S	=	Tensile modulus of elasticity of steel reinforcement
$E_{c,L}$	=	Longitudinal compressive modulus of elasticity of GFRP sections
E_c	=	Modulus of elasticity of concrete
E_f	=	Elastic modulus of elasticity of FRP reinforcement
E_{fc}	=	Compressive modulus of elasticity of FRP reinforcement
E_{ft}	=	Tensile modulus of elasticity of FRP reinforcement
$E_{t,L}$	=	Longitudinal tensile modulus of elasticity of GFRP sections
e	=	Load eccentricity
F^*	=	Maximum tensile force per unit width for FRP sheets
f_c	=	Compressive cylinder strength of concrete at the first day of testing
$f_{c,n}$	=	Concrete stress in the nth strip
f_c'	=	Compressive cylinder strength of concrete at age 28 days
f_{cc}'	=	Compressive strength of confined concrete
f_{co}	=	Unconfined concrete compressive strength, equal to $0.85f_c$ or $0.9f_c$
f_{co}'	=	Compressive strength of unconfined concrete
f_{comp}	=	Stress in the compressive bars or compressive flange of GFRP sections
$f_{concrete}$	=	Compressive stress of concrete corresponding to ε_c
f_{fb}	=	Design tensile strength of FRP bars at a bend
f_{fc}	=	Compressive stress in FRP reinforcement
f_{ft}	=	Tensile stress in FRP reinforcement
f_{fu}	=	Ultimate tensile strength of FRP reinforcement
f_l	=	Effective confining pressure from FRP sheets
f_l'	=	Equivalent confining pressure from the FRP sheets

f_s	=	Tensile stress in steel reinforcement
f_{sy}	=	Yield strength of the steel reinforcement
f_{tens}	=	Stress in the tensile longitudinal bars or tensile flange of GFRP sections
G	=	Shear modulus
G_f	=	Fracture energy parameters for Hashin failure criterion
K^*	=	Chord tensile stiffness per unit width for FRP sheets
k_e	=	Confinement effective coefficient of FRP sheets
k_ε	=	Strain efficiency factor of FRP sheets
M	=	Bending moment
M_{exp}	=	Experimental bending moment
$N.A$	=	Neutral axis
n	=	Number of strips in the concrete cross-section – small strips method
P	=	Load
$P_{cu,F}$	=	Ultimate load of full-size GFRP channels tested in compression
P^{max}	=	Maximum tensile force before failure for FRP sheets
P_{max}	=	First maximum load of specimens before total onset of concrete spalling
P_o	=	Axial load capacity
r_b	=	Radius of the bends of FRP reinforcement
s	=	Clear spacing between two FRP bands
T	=	Tensile force of reinforcement
t_f	=	Nominal thickness of FRP jacket
t_{flange}	=	Thickness of the flange of pultruded GFRP section
t_{web}	=	Thickness of the web of pultruded GFRP section

w	=	Width of FRP bands
w_c	=	Density of concrete
w_s	=	Width of FRP coupons tested in tension made from FRP sheets
α_2	=	Uniform stress coefficient of equivalent rectangular stress block
β_1	=	Parameter that determines the slopes in concretes stress-strain behaviour
δ_u	=	Ultimate displacement of concrete specimens
δ_y	=	Yield displacement of concrete specimens
$\varepsilon_{c,n}$	=	Unconfined concrete strain in centre of concrete strip - small strips method
ε_c	=	Compressive strain in concrete
ε_{co}	=	Unconfined concrete compressive strain corresponding to f_{co}
ε_{comp}	=	Strain in compressive longitudinal bars or compressive flange of GFRP sections
$\varepsilon_{cu,F}$	=	Rupture strain of full-size GFRP channels tested in compression
$\varepsilon_{cu,L}$	=	Longitudinal compressive rupture strain of GFRP sections
ε_f	=	Ultimate tensile strain of FRP coupons prepared from FRP sheets
ε_{fc}	=	A compressive strain in FRP reinforcement
ε_{fe}	=	Actual rupture strain of FRP sheets in the hoop direction
ε_{ft}	=	A tensile strain in FRP reinforcement
ε_{fu}	=	Tensile rupture strain of FRP reinforcement
ε_l	=	Lateral strain
ε_o	=	Strain at the peak stress of concrete in compression
ε_s	=	A strain in steel reinforcement
ε_{tens}	=	Strain in the tensile longitudinal bars or tensile flange of GFRP sections

$\varepsilon_{tu,L}$	=	Longitudinal tensile rupture strain of GFRP sections
ε_{sy}	=	Yield strain of steel reinforcement
$\sigma_{cu,F}$	=	Ultimate stress of full-size GFRP channels tested in compression
$\sigma_{cu,L}$	=	Longitudinal compressive strength of GFRP sections
$\sigma_{cu,T}$	=	Transverse compressive strength of GFRP sections
$\sigma_{tu,L}$	=	Longitudinal tensile strength of GFRP sections
$\sigma_{tu,T}$	=	Transverse tensile strength of GFRP sections
Δ	=	Axial displacement of concrete speicmens at P_{max}
ΔP	=	Difference in applied tensile force between 1000με and 3000με
$\Delta\varepsilon$	=	Difference between the two strain points, nominally 0.002
$\Delta_{u,F}$	=	Axial displacement at ultimate stress of full-size GFRP channels
γ	=	Equivalent rectangular stress block coefficient
δ	=	Lateral deflections of concrete specimens at mid-height
λ	=	Ductility of concrete specimens
τ	=	Shear strength
υ	=	Poisson's ratio

1 INTRODUCTION

1.1 General

The introduction of fibre reinforced polymer (FRP) materials in civil engineering structures is allowing engineers to optimize their structural designs in many ways that approach the limiting capabilities of these materials. The use of FRP materials as replacements to conventional materials such as steel is increasing due to their light weight, non-corrosive and high strength properties. In addition, several developments in the manufacturing processes have allowed FRP materials to become increasingly competitive and accessible. The manufacturing of FRP materials is achieved by a wide variety of techniques including pultrusion, filament winding and braiding. The common process for producing FRP bars and structural sections is the pultrusion method. The FRP materials used in civil engineering structures are categorised into three main applications: strengthening of existing structures, inclusion in concrete as reinforcement, or the use of FRP structural profiles for the primary structure or as part of a hybrid concrete system.

Existing steel reinforced concrete (RC) structures require rehabilitation or strengthening when they can no longer safely resist the loads acting on them. This is due to improper design or construction, change of the design loads or guidelines, damage caused by seismic events or environmental factors such as corrosion. One area of study that has received great attention is the use of FRP pultruded strips, sheets and shells applied externally to deteriorating bridge substructures, such as the undersides of bridge decks or support columns. The application of these FRP materials to deteriorating structures bring its flexural, shear, ductility and load-carrying capacity back to the loads or displacements for which it was designed. Most notably, the confinement effect of FRP sheets on concrete columns leads to an increase in the strength and ductility of columns (Lam and Teng 2003; Pham and Hadi 2014a). The light-weight properties of these FRP materials allows for easier handling, fewer labourers and faster rehabilitation procedures.

The use of FRP materials is not only limited to rehabilitation purposes for existing structures but they have gained widespread use as internal reinforcement for new construction of concrete members. Conventional concrete structures are typically reinforced with prestressed or non-prestressed steel bars. Initially, the steel is protected from corrosion by the alkalinity of the concrete, producing a serviceable and durable construction material. However, for many structures exposed to aggressive environments, such as parking garages, marine structures and bridges prone to moisture, temperature, de-icing salts, and chlorides diminish the concretes' alkalinity and cause the corrosion of reinforcing steel. The corrosion of steel reinforcing bars has been a serious issue to engineers worldwide as it weakens the concrete structures, resulting in a reduction in load carrying capacities and service life, leading to costly repairs and rehabilitation. The use of reinforcement with FRP composite materials have emerged as one of the alternatives to steel reinforcement for concrete structures prone to corrosion issues (ACI 440.1R-15 2015; fib 2007).

In addition, FRP structural sections can be produced in structural shapes that resemble steel shapes. In recent times, the costs associated with the maintenance and strengthening of existing structures made of conventional materials, such as steel or RC, have been increasing dramatically. Furthermore, the demand for faster and lighter construction has increased. Therefore, FRP pultruded sections low self-weight, non-corrosive nature, low maintenance requirements and high durability have allowed them to become a competitive replacement as a primary structural material in place of steel and RC. However, their use is still hindered by their buckling sensitivity (ultimate limit states), high deformability (serviceability limit states), high initial costs and the lack of consensual design codes. Having said this, the advantages of incorporating FRP pultruded sections with concrete elements are a reduction in the structures deformability, reduction in the structures self-weight, increase in the flexural stiffness and increase in the structures strength capacity while at the same time preventing the buckling phenomenon of the FRP sections (Correia et al. 2013).

In this study, the three main applications of FRP materials in construction were investigated by numerous experimental and analytical studies. Firstly, two preliminary studies were conducted on the strengthening of concrete columns using FRP sheets in terms of optimising wrapping schemes and the fabrication of FRP plates for tensile material testing. However, the main research of this study focuses on the use of FRP materials as internal reinforcement for concrete specimens in terms of bars or structural sections which are discussed herein.

1.2 Research Significance

The use of reinforcement with FRP composite materials have emerged as one of the alternatives to steel reinforcement for concrete structures prone to corrosion issues. Based on the literature, understanding the behaviour of concrete members reinforced with FRP bars has been the main objective of many researchers. In the last decade, there has been extensive research on the flexural and shear behaviour of concrete members reinforced with FRP bars (Theriault and Benmokrane 1998; Benmokrane et al. 1996). Therefore, the level of understanding of the flexural behaviour of FRP-RC beams has reached a stage where design standards and guidelines around the world have been developed for the design of these members, including ACI 440.1R-15 (ACI 2015).

However, the structural behaviour of columns reinforced with FRP bars has been examined by only a few limited studies (Mohamed et al. 2014; De Luca and Nanni 2010; Hadi et al. 2016). Consequently, the current ACI 440.1R-15 (ACI 2015) design guideline mentions to neglect the compressive contribution of FRP reinforcement when used as reinforcement in columns, in compression members, or as compression reinforcement in flexural members. On the other hand, CSA S806-2012-R2017 (CSA 2012-R2017) neglects the compressive contribution of FRP longitudinal reinforcement. Given the lack of experimental data about FRP reinforcement in compression members, this study aims to expand the understanding of the compression behaviour of concrete columns internally reinforced with glass fibre reinforced polymer (GFRP) bars.

Furthermore, most of the findings of studies investigating FRP RC columns have been reported based on testing under concentric loading (Afifi et al. 2014;Tobbi et al. 2012; De Luca et al. 2010), whereas only a few studies presented investigations of columns subjected to eccentric loading (Kawaguchi 1993; Hadi et al. 2016). In reality, columns are not subjected to perfect concentric loading but are influenced by a combination of axial compression loads and bending moments (Hadi 2006). Even for columns nominally carrying only axial compression load, bending moments always exist. These bending moments are introduced by unintentional load-eccentricities and by out-of-straightness of the constructed column (Warner et al. 2007). Consequently, this study also investigates the structural behaviour and performance of GFRP-RC columns subjected to eccentric loading.

The alternative use of FRP structural sections and tubes in concrete members presents a very interesting potential, either for rehabilitation of existing structures or for new construction due to their many advantages including low self-weight, ease of installation, low maintenance costs and corrosion resistance. However, pultruded FRP sections generally have low in-plane moduli and wall slenderness making them particularly vulnerable to local buckling (Barbero 2000; Qiao et al. 2001). Having said this, there is an interesting potential for the use of GFRP-pultruded sections in hybrid GFRP-concrete structural compression and flexural elements to make better use of the profiles (Correia et al. 2009; Kwan and Ramli 2013). However, the encasement of GFRP structural sections in concrete columns has not yet been analysed and is investigated in this study.

Finally, in the future the fabrication of GFRP pultruded sections is optimized. This means that the buckling resistance will be improved and these sections' compressive strength will be reached. Therefore, this study will also investigate the mechanical compressive properties of pultruded GFRP sections.

Based on the above-mentioned discussion, this study aims to investigate experimentally and analytically the structural behaviour and performance of both square concrete specimens reinforced with GFRP bars and specimens encased with pultruded GFRP structural sections subjected to different types of loading. A total of seventeen square concrete specimens with side dimensions of 210 mm and height of 800 mm were cast and tested. Parameters investigated include the magnitude of load eccentricity (concentric, 25 mm eccentric, 50 mm eccentric and flexural loading) and type of internal reinforcement with steel-reinforced, GFRP-reinforced, GFRP I-section-encased, and GFRP C-sections encased concrete specimens analysed. In addition to the experimental analysis, an analytical study was conducted to predict the axial load-bending moment interaction diagrams of the experimentally tested specimens. In addition, the compressive strength properties of GFRP pultruded channel sections were also investigated.

1.3 Objectives

The main objective of this study is to experimentally and analytically investigate the structural performance and behaviour of GFRP-reinforced and GFRP-encased square concrete specimens under axial and eccentric load and four-point bending test. The specific objectives of this study are:

- To review literature that relates to the thesis' aim in order to present the background information and the justification for the study carried out.

- To investigate the structural behaviour of square concrete columns reinforced longitudinally and transversely with GFRP bars subjected to different types of loading (concentric, eccentric and flexural).

- To investigate the structural behaviour of square concrete columns embedded with GFRP structural sections subjected to different types of loading (concentric, eccentric and flexural).

- To develop axial load-bending moment interaction diagrams of GFRP reinforced and GFRP encased square concrete columns using an analytical method. The load and bending moment capacities obtained experimentally are than compared to the values obtained by the analytical study.

- To investigate the compressive mechanical properties of pultruded GFRP channel sections.

- To provide further recommendations for future studies that could be undertaken at the University of Wollongong, Australia in this field of study

1.4 Outline of the Thesis

This study consists of nine chapters. Chapter 1 provides the background on the current area of research and discusses the importance and objectives of this study.

Chapter 2 explains the two preliminary studies that were conducted on the strengthening of concrete members with the use of FRP sheets. The literature and significance of each study is thoroughly explained. The first study investigated wrapping circular concrete cylinders with different FRP wrapping schemes. The cylinders were tested under axial compression and different FRP wrapping schemes included fully wrapping, partially wrapping, and non-uniformly wrapping. The second study dealt with the tensile testing of FRP sheets. Two different fabrication techniques are discussed with the tensile properties of the FRP flat coupon tests explained.

Based on a thorough literature review, Chapter 3 discusses the structural behaviour of concrete members reinforced with FRP bars with the design methodology and results of existing experimental studies summarised. The material properties of the FRP bars are examined followed by a review of the strength, ductility and failure modes of concrete columns reinforced with FRP bars. Both concentrically and eccentrically loaded columns are discussed. Furthermore, the performances of concrete beams reinforced with FRP bars are also examined.

Chapter 4 provides an overview of pultruded GFRP structural sections. The mechanical properties of these GFRP sections are first discussed followed by their typical applications in civil engineering. A review of the associated literature about hybrid composite columns and beams reinforced incorporating structural sections of most notably GFRP materials is then explained followed by a summary of the available design guidelines.

Chapter 5 presents a study on the compression mechanical properties of pultruded GFRP channels. The behaviour and failure modes of the coupons and full-size specimens tested are discussed and compared. Furthermore, a numerical model was developed using the finite element analysis program ABAQUS to simulate the compressive behaviour of the full-size specimens.

Chapter 6 introduces the main experimental program of this study. The design of the specimens, their preparation, casting, instrumentation and testing methods are explained. Also, the results and methods of the preliminary tests conducted for the constituent materials used in the specimens are discussed.

Chapter 7 analyses the results of the experimental program outlined in Chapter 6. The strength, ductility and failure modes of the experimentally tested specimens are discussed.

Chapter 8 discusses an analytical model to determine the axial load-bending moment interactions diagrams of GFRP-reinforced and GFRP-encased concrete specimens. The theoretical considerations of the constituent materials of the specimens are first examined. Furthermore, the analytical results are compared to the results obtained experimentally and a parametric study is then carried out.

Chapter 9 summarises the conclusions drawn from this study and provides recommendations for further research.

2 STRENGTHENING CONCRETE MEMBERS

2.1 Introduction

Fibre-reinforced polymer (FRP) has been commonly used to strengthen existing reinforced concrete (RC) columns in recent years. In such cases, FRP is a confining material for concrete in which the confinement effect leads to increases in the strength and ductility of columns. This chapter explains two preliminary studies that were conducted on the strengthening of concrete members with the use of FRP sheets. The first study investigated different FRP wrapping schemes for circular concrete columns under axial compression. The different FRP wrapping schemes included fully wrapping, partially wrapping, and non-uniformly wrapping concrete cylinders. The second study investigated the effects of fabrication technique on the tensile properties of FRP flat coupon tests. A total of twenty FRP flat coupons were prepared by two different techniques which were tested in tension until failure. The experimental programs and results of these two studies are discussed in this chapter.

2.2 Review of Strengthening of RC Columns

Existing steel RC structures require strengthening or rehabilitation when they can no longer safely resist the loads acting on them. This strengthening may be required due to revisions in the design loads or guidelines, damage caused by seismic events or environmental factors such as corrosion as well as improper design or construction. The confinement of structurally deficient concrete columns is a recognized method utilised to improve both the compressive behaviour (Richart et al. 1928; Mander et al. 1988) as well as the flexural response of concrete members (Chai et al. 1991).

Numerous methods have been proposed for the strengthening of existing concrete columns by means of confinement. A conventional technique includes applying steel jackets to a column by means of two half shells that are welded together with a cement grout used to fill the gap between the steel jacket and concrete column (Priestly et al. 1996). However, the exterior surface of the steel requires additional protection against corrosion and the welding and grout injection requires specialised equipment. In recent times, the use of FRP materials as replacements to conventional materials such as steel for strengthening applications of RC columns is increasing due to their non-corrosive and high strength properties as well as their light weight properties that ensure easier handling, fewer labourers and faster rehabilitation procedures (Lam and Teng 2003; Pham and Hadi 2014a).

In early experimental studies that focused on retrofitting RC columns with FRP, the columns were usually wrapped fully with FRP sheets. This wrapping scheme provides continuous confinement to the columns along their longitudinal axes. Most of the studies in the literature focus only on columns fully wrapped with FRP (Chaallal et al. 2003; Hadi et al. 2013; Pham et al. 2013; Pham and Hadi 2014a; Smith et al. 2010). In addition, columns wrapped partially with FRP have also been proven to show increases in strength and ductility, as compared to equivalent unconfined columns (Colomb et al. 2008; Maaddawy 2009; Turgay et al. 2010).

However, there is no study that makes a comparison of the confinement efficacy between partially- and fully-wrapping schemes in terms of optimization of the FRP amount. In addition, the progressive failure of those specimens has not been extensively studied. Therefore, it is necessary to investigate the confinement efficacy and failure mechanisms of columns partially wrapped versus columns fully wrapped with FRP.

2.3 Optimized FRP Wrapping Schemes for Circular Concrete Columns under Axial Compression

2.3.1 Overview

The available design guidelines for columns wrapped with FRP [ACI 440.2 R-08 (ACI 2008), fib (2001), and TR 55 (TR 2012)] are utilized to estimate the capacities of partially FRP-wrapped specimens. Among these studies, ACI-440.2R-08 (ACI 2008) and technical report TR 55 (TR 2012) do not provide information about the confinement effect of concrete columns partially wrapped with FRP. Meanwhile, fib (2001) suggests a reduction factor to take into account the effect of partially wrapping columns. Furthermore, fib (2001) adopts an assumption proposed by Mander et al. (1988) for the confinement effect of steel ties in RC columns to analyse the efficacy of FRP-partially-wrapped columns. Therefore, there has been a lack of theoretical and experimental works about partial FRP-confined concrete. For this reason, an experimental program was developed in this study to compare the confinement efficacy of FRP-partially-wrapped columns as compared to FRP-fully-wrapped columns. The same amount of FRP was wrapped onto identical concrete columns by different wrapping schemes to achieve an optimized wrapping design.

2.3.2 Confinement Mechanism

2.3.2.1 Fully-Wrapped Columns

In the literature, the term FRP-confined concrete is understood automatically as concrete wrapped fully with FRP. Figure 2.1(a) shows that when a circular concrete column is horizontally wrapped with FRP around its perimeter, the lateral pressure exerted from the FRP jackets confines the whole column. Many studies have been carried out to investigate the behaviours and estimate the capacities of columns wrapped fully with FRP (De Luca and Nanni 2010; Lam and Teng 2003; Pham and Hadi 2014b; Teng et al. 2009; Toutanji 1999; Wu and Zhou 2010). The confining pressure is assumed to be uniform in the cross section and along the axial axis of the circular columns. Among the existing studies, the model proposed by Lam and Teng (2003) is adopted in this study to calculate the compressive strength for columns wrapped fully with FRP as follows:

$$\frac{f'_{cc}}{f'_{co}} = 1 + 3.3\frac{f_l}{f'_{co}} \tag{2.1}$$

where f'_{cc} and f'_{co} are respectively the compressive strength of confined concrete and unconfined concrete, and f_l is the effective confining pressure as follows:

$$f_l = \frac{2E_f \varepsilon_{fe} t_f}{D} \tag{2.2}$$

where E_f is the elastic modulus of elasticity of FRP, t_f is the nominal thickness of FRP jacket, *D* is the diameter of the column section, and ε_{fe} is the actual rupture strain of FRP in the hoop direction. The model by Lam and Teng (2003) is chosen because it provides a reasonable accuracy with a very simple form.

2.3.2.2 Partially-Wrapped Columns

As mentioned above, concrete columns wrapped partially with FRP have been experimentally verified to increase their strength and ductility. Concrete columns partially wrapped with FRP are less efficient in nature than fully-wrapped columns as both confined and unconfined zones exist [Figure 2.1(b)]. An approach similar to the one proposed by Sheikh and Uzumeri (1980) is adopted to determine the effective confining pressure on the concrete core.

Figure 2.1(b) shows the effective confining pressure is assumed to be exerted effectively on the part of the concrete core where the confining pressure has fully developed due to the arching action. A second-degree parabola with initial slope of 45° is assumed to describe the arching effect.

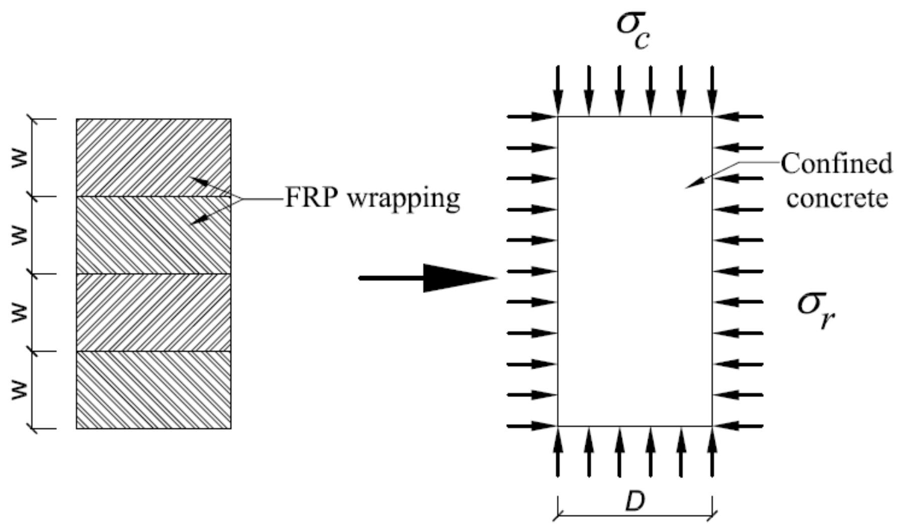

(a)

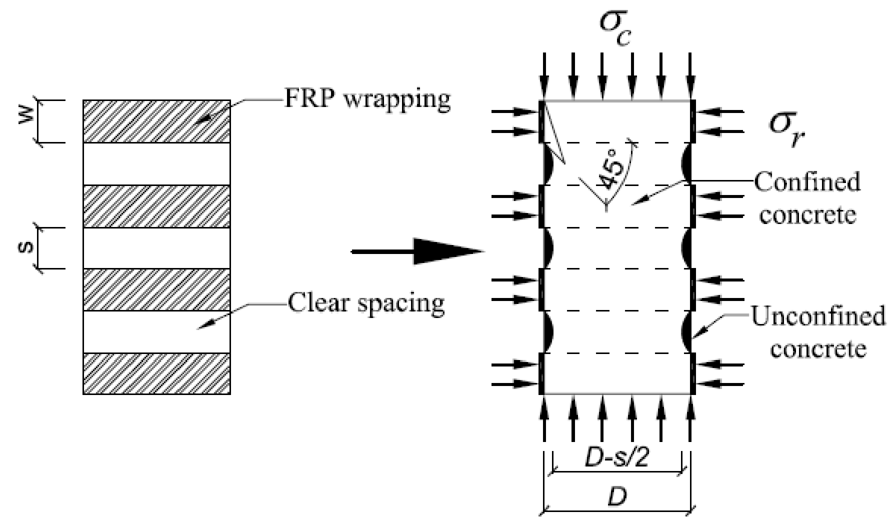

(b)

Figure 2.1. Confinement mechanism: (a) concrete columns wrapped fully with FRP; (b) concrete columns wrapped partially with FRP (Pham et al. 2015b)

In such a case, a confinement effective coefficient (k_e) is introduced to take the partial wrapping into account as follows:

$$k_e = \frac{A_e}{A_c} = \left(1 - \frac{s}{2D}\right)^2 \tag{2.3}$$

where A_e and A_c are respectively the area of effectively confined concrete core and the cross-sectional area, and s is the clear spacing between two FRP bands.

Consequently, the compressive strength of concrete columns wrapped partially with FRP could be calculated as follows:

$$\frac{f'_{cc}}{f'_{co}} = 1 + 3.3k_e \frac{f'_l}{f'_{co}} \tag{2.4}$$

where k_e is estimated based on Equation 2.3 and f'_l is the equivalent confining pressure from the FRP, assumed to be uniformly distributed along the longitudinal axis of the column. The formula to calculate the equivalent confining pressure from the FRP (f'_l) is as follows:

$$f'_l = \frac{2E_f \varepsilon_{fe} t_f}{D} \frac{w}{w+s} \tag{2.5}$$

where *w* is the width of FRP bands; and *s* is the clear spacing between FRP bands as shown in Figure 2.1(b).

2.3.3 Experimental Program

2.3.2.1 Design of Experiments

A total of 33 FRP-confined concrete cylinders were cast and tested at the High Bay Laboratory of the University of Wollongong, Australia. The dimensions of the concrete cylinder specimens were 150 mm in diameter and 300 mm in height. All the specimens were cast from the same batch of concrete. The 28-day cylinder compressive strength was 52 MPa. The test matrix for the experimental program is shown in Table 2.1.

Table 2.1. Test matrix (Pham et al. 2015b)

Group	No. of specimens	Type of FRP	Equivalent FRP layers with full wrapping	Width of each FRP band (w, mm)	Clear spacing (s, mm)	Type of Wrapping
R	3	-	-	-	-	-
GF2	3	GFRP	2	50	0	Full
GP40	3			25	25	Partial
GP31	3			25	0	Non-uniform
CF2	3	CFRP	2	75	0	Full
CP40	3			25	25	Partial
CP31	3			25	0	Non-uniform
CF3	3	CFRP	3	75	0	Full
CP60	3			25	25	Partial
CP51	3			25	0	Non-uniform
CP42	3			25	0	Non-uniform

The experimental program was composed of several groups of cylinders in order to evaluate the confinement efficacy between partially- and fully-wrapping schemes in terms of optimization of the wrapping schemes. The notation of the specimens consists of three parts: the first part states the type of confining FRP material, with G and C representing GFRP and CFRP, respectively; the second part is either a letter R, F, and P stating the name of the subgroup, namely, reference group (R), fully-wrapped group (F), and partially-wrapped group (P); the last part of the specimen notation is a number which indicates the number of FRP layers. Table 2.1 presents details of the specimens.

The partially-wrapped specimens contain FRP bands that are 25 mm in width spaced evenly along the height of the specimen. The optimized partially-wrapped specimens include two numbers in the notation, for example GP31. The first number indicates the number of 25 mm evenly spaced partial FRP layers and the second number depicts the number of FRP layers in between these evenly spaced partial layers. These specimens were designed such that they follow a non-uniform wrapping configuration but ensure the specimen is fully confined at every location. The thicker band is called a tie band and the thinner band is called a cover band. Taking Specimens of Group GP31 as an example, the tie bands have three FRP layers which are 25 mm in width, while the cover bands have one FRP layer as shown in Figure 2.2. Three identical specimens were made for each wrapping scheme.

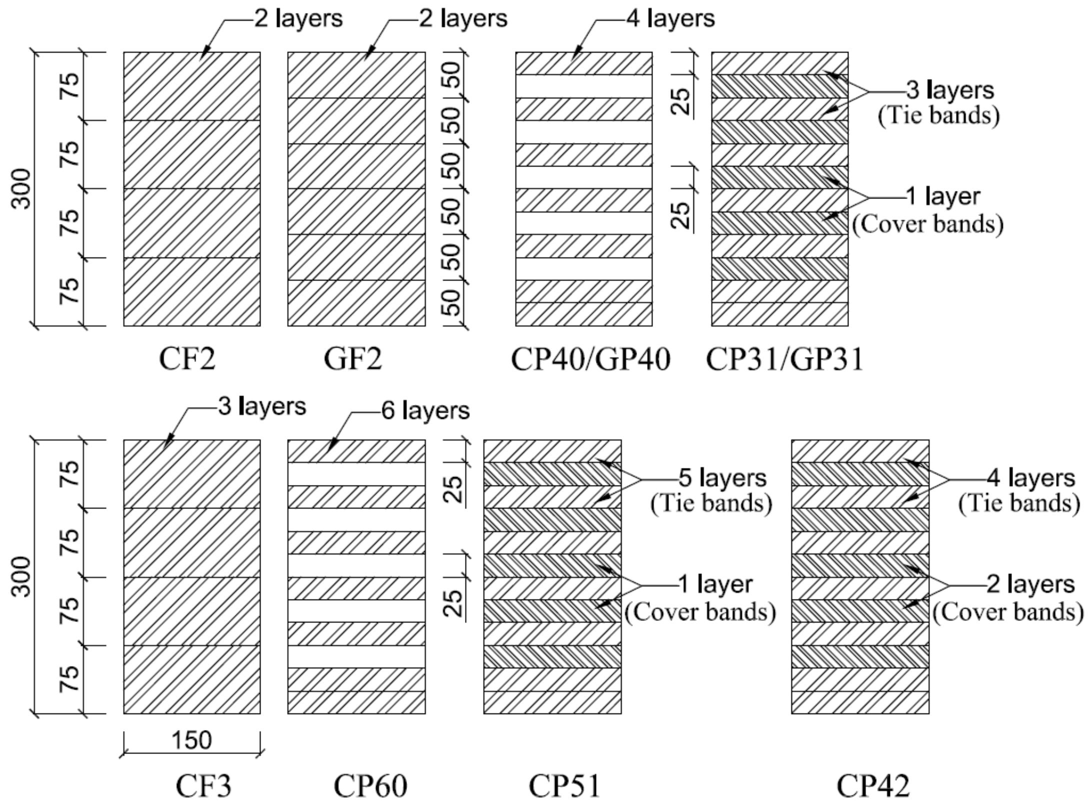

Figure 2.2. Different wrapping schemes (Pham et al. 2015b)

In order to analyze the confinement effectiveness between the different wrapping schemes, the specimens were divided into four groups (as shown in Table 2.1) such that the specimens in each group incorporate the same amount of FRP but in a different wrapping scheme, either fully, partially, or optimized non-uniformly wrapped. The specimens in the first group are reference specimens which did not include any internal or external reinforcement. The specimens in the second and third groups were confined by glass fibre reinforced polymer (GFRP) and carbon fibre reinforced polymer (CFRP), respectively, such that the fully, partially, and optimized non-uniform wrapping schemes were equivalent to two layers of full wrapping. Similarly, the wrapping schemes of the specimens in the fourth group were equivalent to three layers of full wrapping.

The specimens were wrapped after curing the concrete for 28 days after pouring. A mixture of epoxy resin and hardener at 5:1 ratio was used as the adhesive. Before the first layer of FRP was attached, the adhesive was spread onto the surface of the specimen and CFRP was attached onto the surface with the main fibres oriented in the hoop direction. After the first layer, the adhesive was spread onto the surface of the first layer of FRP and the second layer was continuously bonded. The third layer of FRP was applied in a similar manner, ensuring that 100 mm overlap was maintained. The ends of each wrapped specimen were strengthened with additional one layer of FRP strips 25 mm in width.

2.3.2.2 Instrumentation

In order to measure the hoop strains of the FRP jacket, three strain gauges with a gauge length of 5 mm were attached at the mid-height of the specimens and evenly distributed away from the overlap for the fully-wrapped specimens. In the partially-wrapped specimens, three strain gauges were bonded symmetrically on a tie band and other three were bonded on a cover band at mid-height of the specimen. Furthermore, Figure 2.3 shows a longitudinal compressometer was used to measure the axial strain of the specimens. A LVDT was mounted on the upper ring and the tip of the LVDT rested on an anvil. The readability, the accuracy, and the repeatability of the LVDT complies with the Australian Standard 1545-1976 (AS 1976).

The compression tests for all the specimens were conducted using the Denison 5,000-kN capacity testing machine. The specimens were capped with high-strength plaster to ensure full contact between the loading plate and the specimen. Calibration was carried out to ensure that the specimens were placed at the centre of the testing machine. Each specimen was first loaded to around 30% of its unconfined capacity to check the alignment. If required, the specimen was unloaded, realigned, and loaded again. The tests were conducted as deflection controlled with a rate of 0.5 mm/min.

The readings of the load, LVDT, and strain gauges were taken using a data logging system and were subsequently saved in a control computer.

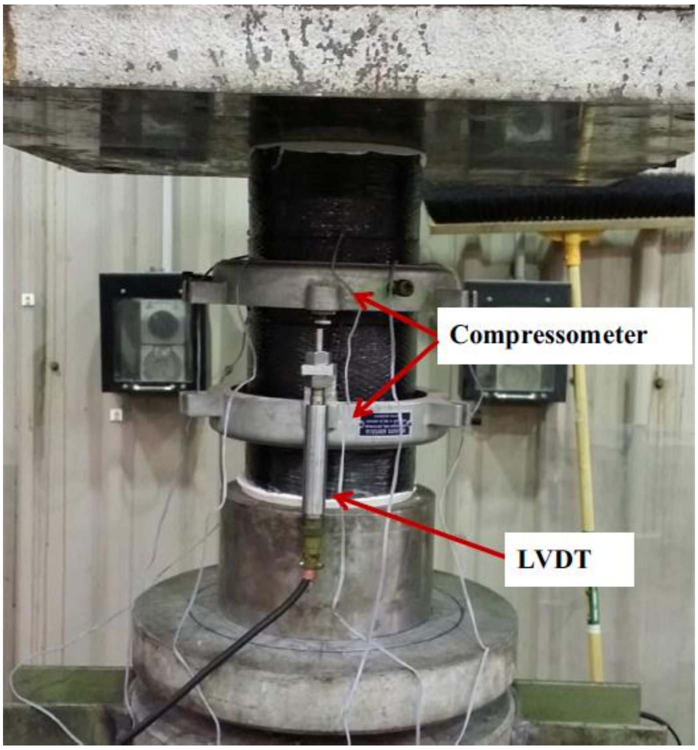

Figure 2.3. Compressometer (Pham et al. 2015b)

2.3.4 Experimental Results

2.3.4.1 Preliminary Tests

The actual compressive strength of unconfined concrete calculated from three reference specimens (R1, R2, and R3) was 54 MPa. The average axial strain of unconfined concrete at the maximum load was 0.23%. In this study two types of CFRP were used to confine the concrete, which both had a unidirectional fibre density of 340 g/m^2 and a nominal thickness of 0.45 mm, but with varying nominal widths of 75 and 25 mm. The GFRP utilized had a unidirectional fibre density of 440 g/m^2, a nominal thickness of 0.35 mm, and a nominal width of 50 mm.

Five coupons for each type of FRP were made according to ASTM D7565-10 (ASTM 2010) and tested to determine the mechanical properties. Table 2.2 shows the two types of CFRP coupons were made of three layers of FRP with a nominal thickness of

1.35 mm and both types had very similar properties. For simplicity the coupons produced from the 75 mm tape are denoted by CFRP (75) while the coupons from the 25 mm tape are referred to as CFRP (25). For GFRP, two-layered coupons containing two overlapping fibre sheets were prepared and tested. The nominal thickness of the coupons was 0.7 mm. All coupons had the dimensions 25 mm × 250 mm. The epoxy resin had 54 MPa tensile strength, 2.8 GPa tensile modulus of elasticity, and 3.4% tensile elongation (West-System 2015).

Table 2.2. Results of tensile tests on FRP flat coupons (Pham et al. 2015b)

Type of coupon specimen	Number of FRP layers	Width (mm)	Nominal thickness (mm)	Average Elastic Modulus of Elasticity (kN/mm)	Average Tensile Strength (N/mm)	Average Ultimate Strain (mm/mm)
CFRP (75)[a]	3	25	1.35	133	2171	0.0163
CFRP (25)[b]	3	25	1.35	133	2157	0.0162
GFRP	2	25	0.70	29.5	582	0.0197

[a] CFRP (75) denotes the coupons made of the FRP sheets that have 75 mm width

[b] CFRP (25) denotes the coupons made of the FRP sheets that have 25 mm width

2.3.4.2 Failure Modes

All specimens were tested until failure. The specimens wrapped fully with FRP (CF2, CF3, and GF2) failed by rupture of FRP at the mid-height. Figure 2.4(a) shows the failure surface of the fully-wrapped specimens was found to be approximately inclined at 45°. Meanwhile, Figure 2.4(b) shows the partially-wrapped specimens (Group CP40, CP60, and GP40) which showed many small cracks on the concrete surface at a stress (σ_c) equal to the unconfined concrete strength (f'_{co}). The concrete between the FRP bands, close to the outer surface of the specimen, started crushing while the concrete core was still confined by the FRP. Figure 2.4(c) shows cracks on the concrete surface developed as the applied load increased up to the maximum stress.

At the very high stress levels, the concrete between the FRP bands spalled off while the concrete under the FRP bands and the core were still confined. These specimens then failed explosively by FRP rupture at the mid-height [(Figure 2.4(d)].

The angle of the failure surface with respect to the horizon for the partially-wrapped specimens was significantly different from the fully-wrapping specimens. Figure 2.4(d) shows the failure surface took place at the spacing between FRP bands. This change of the failure surface depends on the wrapping schemes and the stiffness of the FRP bands. When the axial stress of the confined concrete was higher than the unconfined concrete strength, the 45° failure surface may have originally transpired in the concrete cores, but cracks were arrested by FRP bands under the high-stress stage. Figure 2.4(e) shows if the stiffness of the FRP bands is not strong enough (Group GP40 specimens) to prevent the development of the cracks, the failure surface takes place at approximately 45°. In contrast, Figure 2.4(d) depicts the stiffness of the FRP bands in Groups CP40 and CP60 specimens is great enough so that it changed the failure surface. It is worth mentioning that the stiffness of the FRP bands affects the tangent modulus of FRP-confined concrete. Tamužs et al. (2008) suggested that the low value of the tangent modulus causes column stability collapse directly as the unconfined concrete strength level is surpassed.

Furthermore, specimens with optimized non-uniform wrapping schemes showed a different failure mode as compared to the others. At a stress level equal to the unconfined concrete strength, the concrete was still confined by the FRP tie bands and cover bands. During the loading process, the lateral strains of the tie bands and the cover bands were almost identical, with the exception of Specimen CP40_3. The failure modes of these specimens are similar to those of the full-wrapping specimens. Figure 2.4(f) shows the non-uniform wrapped specimens failed by FRP rupture simultaneously at the two bands (tie band and cover band) at the mid-height. It is worth mentioning that intermittent confinement resulting from partial confinement (Group GP40, CP40, and CP60 specimens) makes the concrete to communicate directly with the surroundings, for instance moisture, heat, and evaporation.

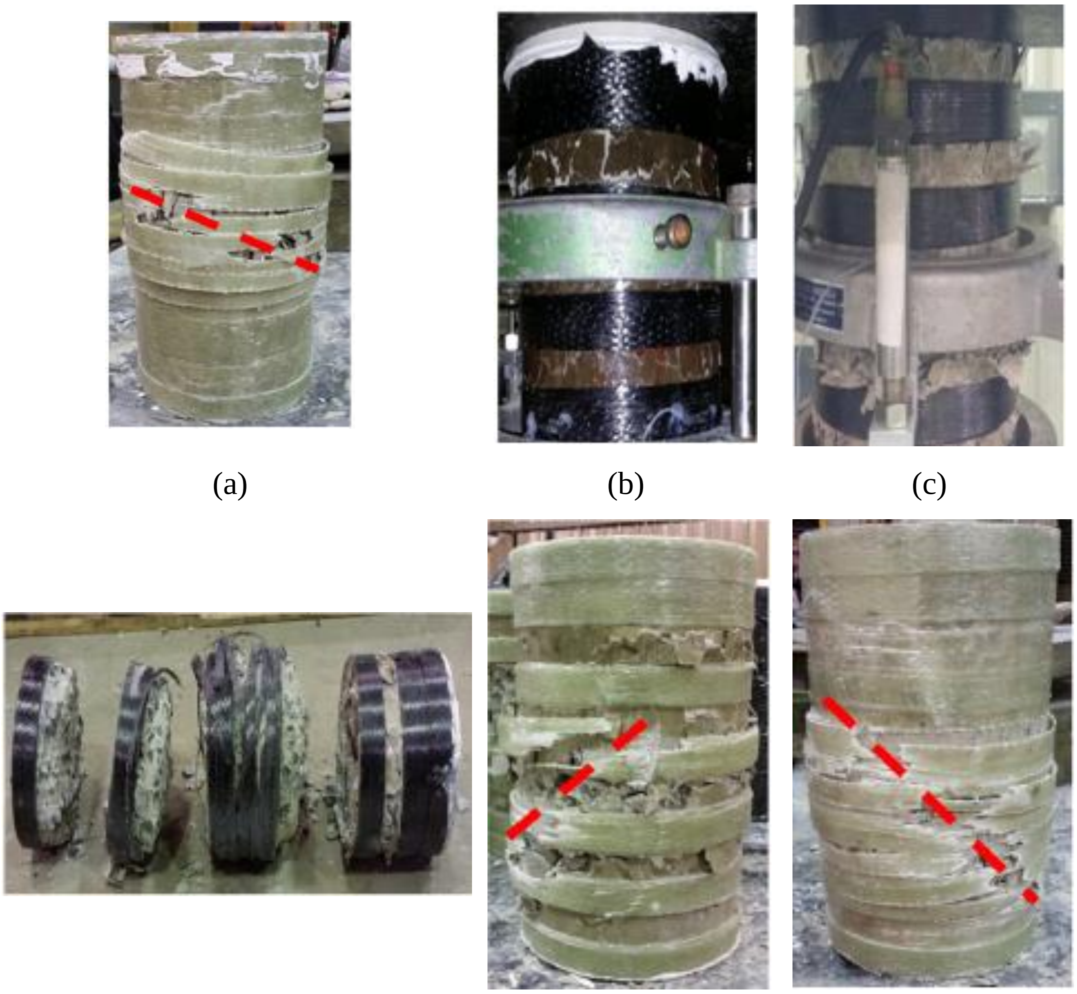

(a) (b) (c)

(d) (e) (f)

Figure 2.4. Failure modes of the tested specimens: (a) GF2; (b) CP40 (σ_c = f'_{co}); (c) CP40; (d) CP60; (e) GP40; (f) GP31 (Pham et al. 2015b)

2.3.4.3 Stress-Strain Relation

Stress-strain relations of the tested specimens were divided into two main types based on the shape of the stress-strain curves. These included specimens in the ascending branch type and descending branch type. An FRP-confined concrete column exhibits the ascending type curve as a significant improvement of the compressive strength and strain of an FRP-confined concrete column could be expected. Otherwise, FRP-confined concrete with a stress-strain curve of the descending type illustrates a concrete stress at the ultimate strain below the compressive strength of unconfined concrete. Specimens wrapped with glass fibre are designed to behave as the descending branch type while specimens wrapped with carbon fibre belong to the ascending branch type. Table 2.3 summarizes details of all tested specimens.

Figure 2.5 shows the plotting of stress-strain relations of specimens wrapped by equivalent two GFRP layers. The specimens which were wrapped with an equivalent of two layers of FRP had identical stress-strain curves at the early stages of loading and experienced slight differences at the latter stage of testing. Group GF2 and GP40 specimens had the descending branch type stress-strain curve while the stress-strain curves of Group GP31 specimens kept constant after reaching the unconfined concrete strength and then increased again to failure. Figure 2.5(a) shows the axial stress of Group GF2 specimens reached the unconfined concrete strength (54 MPa) and then kept constant until the FRP failed by rupture. The average compressive confined concrete strength and strain of Group GF2 specimens are 57 MPa and 0.97%, respectively. Although Group GP40 specimens obtained a lower maximum stress (53 MPa) as compared to that of Group GF2 specimens, they achieved a larger maximum axial strain (1.18%) than the Group GF2 specimens. The maximum axial strain of Group GP40 specimens increased by 21.31% as compared to that of Group GF2 specimens [Figure 2.5(b)]. Meanwhile, Figure 2.5(c) shows that Group GF31 specimens achieved both a higher maximum axial stress (60 MPa) and axial strain (1.02%), as compared to Group GF2 specimens.

Table 2.3. Experimental results of tested specimens (Pham et al. 2015b)

Specimen	Maximum axial stress			Maximum axial strain			Maximum lateral strain		Strain efficiency factor
	f_{cc}' (MPa)	Average (MPa)	Increase[a] (%)	ε_{cc} (%)	Average (%)	Increase[a] (%)	ε_l (%)	Average (%)	k_ε
GF2_1	57	57	-	1.30	0.97	-	1.70	1.64	0.83
GF2_2	56			0.63			1.31		
GF2_3	57			0.98			1.91		
GP40_1	55	53	-6.04	1.25	1.18	21.31	1.59	1.51	0.77
GP40_2	53			1.26			1.61		
GP40_3	51			1.02			1.34		
GP31_1	62	60	6.56	1.31	1.02	5.49	1.87	1.80	0.91
GP31_2	61			0.66			1.79		
GP31_3	59			1.10			1.74		
CF2_1	97	99	-	1.87	2.13	-	1.35	1.41	0.87
CF2_2	99			2.23			1.41		
CF2_3	101			2.28			1.47		
CP40_1	86	95	-3.62	1.58	2.08	-2.02	1.18[b]	1.30	0.80

CP40_2	95			2.05			-		
CP40_3	96			2.12			1.42		
CP31_1	97			2.23			1.52		
CP31_2	97	98	-1.56	1.97	2.12	-0.32	1.52	1.52	0.94
CP31_3	99			2.16			1.50		
CF3_1	126			2.88			1.35		
CF3_2	118	122	-	2.58	2.84	-	1.37	1.39	0.86
CF3_3	122			3.06			1.45		
CP60_1	113			3.20			1.21		
CP60_2	118	116	-4.72	3.25	3.25	14.33	1.29	1.30	0.80
CP60_3	117			3.29			1.39		
CP51_1	117			2.96			1.34		
CP51_2	121	119	-2.04	3.21	3.09	8.58	1.52	1.43	0.88
CP51_3	108			2.17			1.16[b]		
CP42_1	124			3.12			1.53		
CP42_2	128	128	5.29	3.33	3.16	11.16	1.46	1.50	0.92
CP42_3	132			3.03			1.50		

[a] Increase of a specimen compared to the fully wrapping specimens in the same group;

[b] Specimens performed premature damage

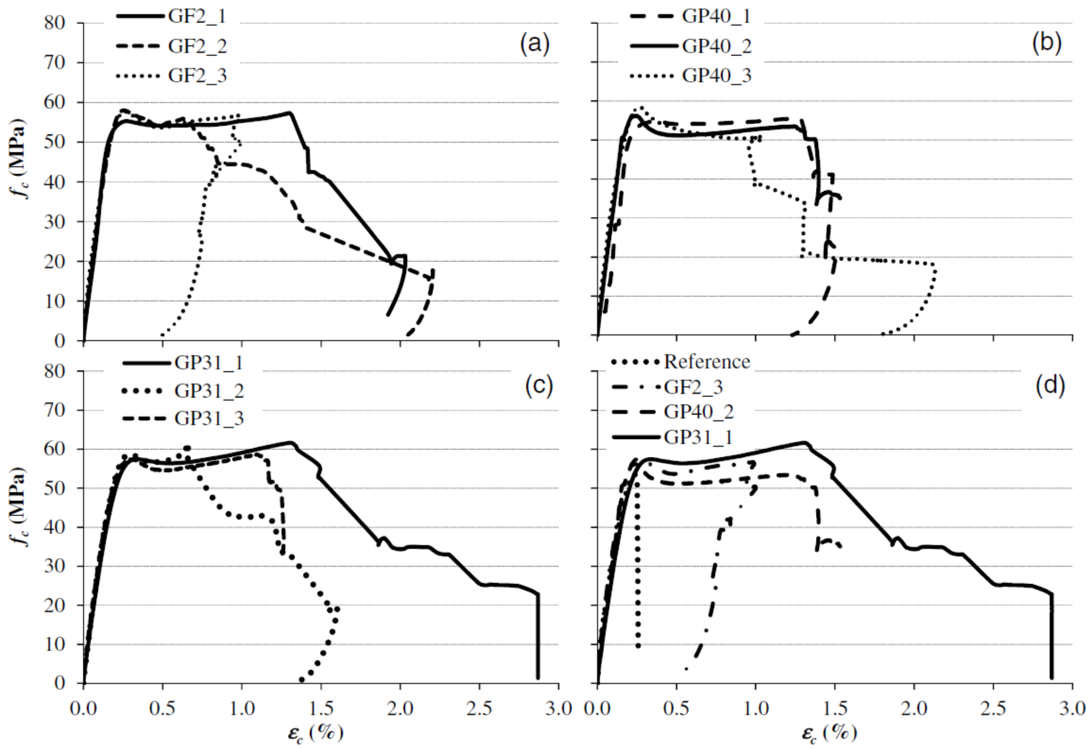

Figure 2.5. Stress-strain relation of specimens wrapped by equivalent two GFRP layers (Pham et al. 2015b)

Apart from the preceding specimens, Figure 2.6 shows the specimens that were wrapped with an equivalent of two layers of CFRP had similar stiffness during the whole loading process. The maximum axial stress of Group CF2 specimens was 99 MPa and its corresponding axial strain was 2.13%. Group CP40 specimens reached the maximum axial stress at 95 MPa and the corresponding axial strain of 2.08%. Specimen CP40_1 failed by premature rupture of FRP (ε_l = 1.18%) that resulted in very low maximum axial stress. The average maximum axial stress and axial strain of Specimen CP31 were 98 MPa and 2.12%, respectively.

Figure 2.7 shows the specimens that were wrapped with an equivalent of three layers of CFRP had similar stress-strain curves but experienced a slight difference in the axial stiffness for the whole loading process. Specimens of Group CF3 obtained an average maximum axial stress and strain at 122 MPa and 2.84%, respectively [Figure 2.7(a)]. The partially-wrapped specimens of Group CP60 again had a lower compressive strength but higher axial strain as compared to those of specimens of Group CF3. Figure 2.7(b) shows that Group CP60 specimens failed at the average compressive strength of 116 MPa and axial strain of 3.25%. The axial strain for the Group CP60 specimens increased by 14.33% in comparison with the Group CF3 specimens. As compared to Group CF3 specimens, the non-uniformly wrapped Group CP42 specimens had both higher compressive strength and axial strain.

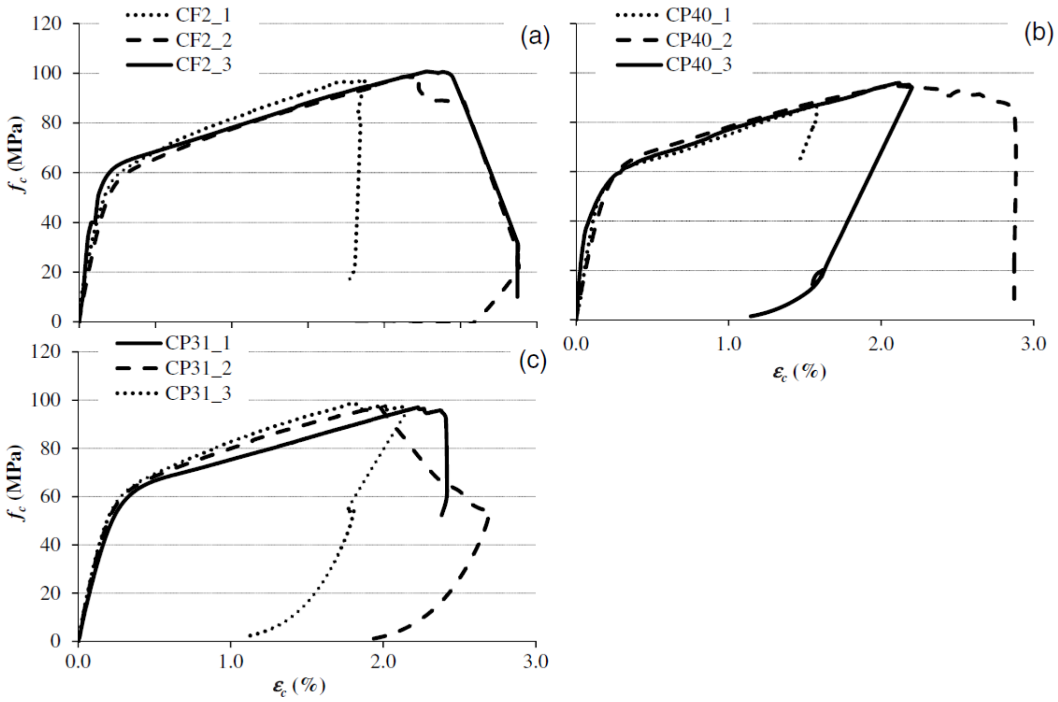

Figure 2.6. Stress-strain relation of the specimens that were wrapped with an equivalent of two layers of CFRP (Pham et al. 2015b)

Figure 2.7(c) depicts the stress-strain curves of specimens of Group CP51. Figure 2.7(d) shows that specimen of Group CP42 failed at the average compressive strength of 128 MPa and strain of 3.16%. As a result, the compressive strength and axial strain of these specimens respectively increased by 5.29 and 11.16% as compared to Group CF3 specimens. In order to compare the effectiveness of different wrapping schemes, Figure 2.7(e) plots the stress-strain curves of five specimens. Figure 2.7 shows that the partially-wrapped specimens of Group CP60 experienced a lower maximum stress and a higher maximum strain, as compared to Group CF3 specimens. On the hand, the non-uniformly wrapped Group CP42 specimens experienced both a higher maximum strain and stress in comparison with Group CF3 specimens. Figure 2.5(d) shows specimens in Group GF2 have also confirmed these findings.

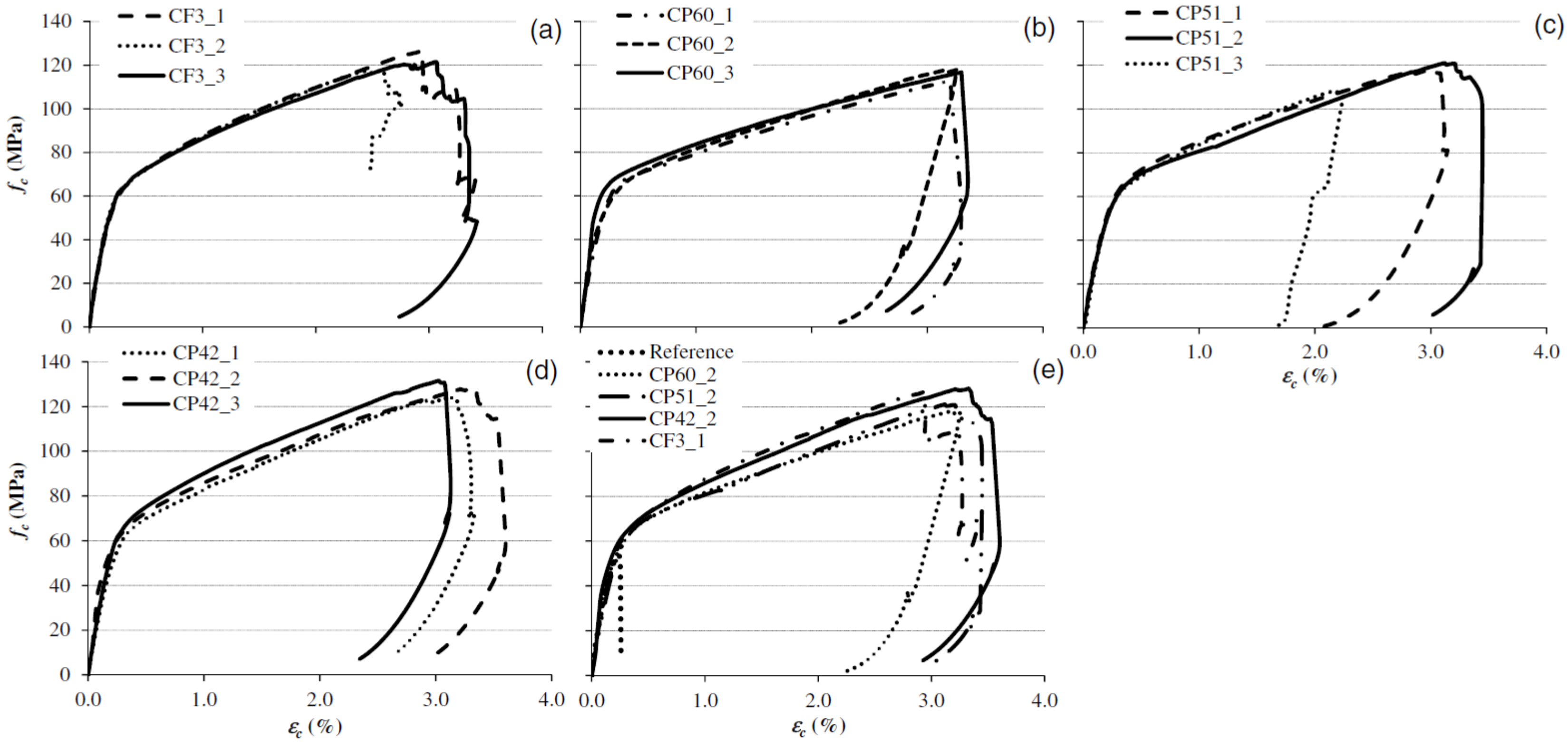

Figure 2.7. Stress-strain relation of the specimens that were wrapped with an equivalent of three layers of CFRP (Pham et al. 2015b)

2.3.5 Discussion

The lateral strain of all the specimens is obtained by taking the average of readings from three strain gauges evenly placed along the FRP at locations away from the overlap. For each specimen, Table 2.3 presents the actual rupture strain of FRP. In order to investigate the effectiveness of the fibre, the strain efficiency factor k_ε is adopted, which is the ratio of the actual rupture strain of FRP in confined specimens and the rupture strain of the FRP obtained from the tensile coupon testing. Table 2.3 shows the strain efficiency factors of fully-wrapped specimens are approximately 0.83 and 0.87 for glass fibre and carbon fibre, respectively. For glass fibre, the strain efficiency factor of partially-wrapped specimens was 0.77 and the corresponding number for non-uniformly wrapped specimens was 0.91. Meanwhile, the strain efficiency factor of specimens partially wrapped with CFRP was 0.80 and the corresponding number for non-uniformly wrapped specimens was 0.91. The experimental results have shown that the effectiveness of the fibre reduces in the partial-wrapping scheme, but increases in the non-uniformly wrapping scheme.

There is a consensus that the presence of the tri-axial stress state in FRP affects the actual rupture strain of the fibre (Chen et al. 2013). In this experimental program, it is obvious that the axial stress of the FRP jackets in the fully-wrapped specimens is higher than that of the non-uniformly wrapped specimens. The discontinuity of the jacket in the non-uniformly wrapped specimens reduces the axial stress of the FRP jacket, which could be a reason for the increase in the strain efficiency factor in these specimens. Thus, the non-uniformly wrapped specimens had a higher value of k_ε, resulting in a higher confined strength and strain. In other words, the discontinuity of the jackets of the partially-wrapped specimens did not increase the strain efficiency factor. The partially-wrapped specimens experienced a different failure mode as compared with the other wrapping schemes. This different failure mode in partially-wrapped specimens may be the reason behind the slight decrease in the strain efficiency factor for these specimens.

In addition, the lateral strain of the non-uniformly wrapped specimens at both the tie bands and cover bands of the FRP is investigated. For example, the lateral strain-axial stress of Specimen CP40_3 (Figure 2.8), illustrates that the lateral strain of FRP in a cover band is slightly higher than that of a tie band at any axial stress state. However, there was no difference in the lateral strain in other specimens.

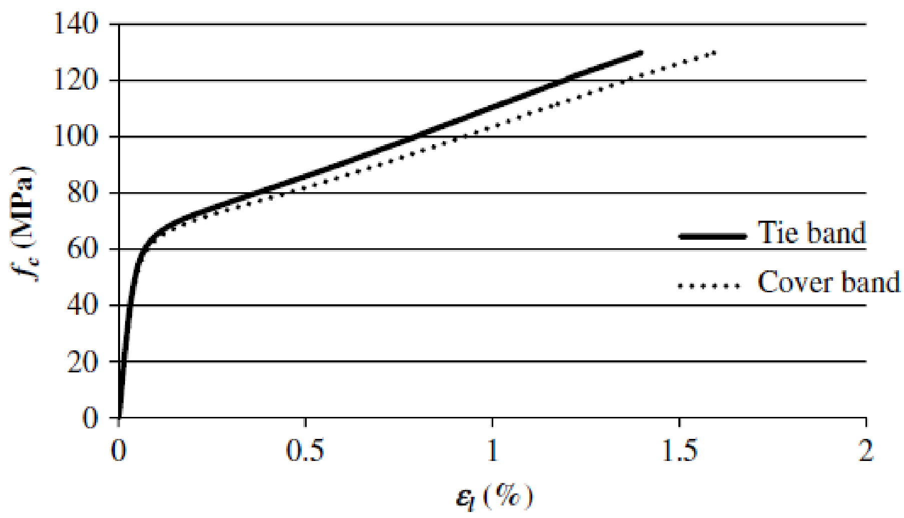

Figure 2.8. Lateral strain-axial stress relationship of Specimen CP40_3 (Pham et al. 2015b)

In summary the findings of this first preliminary study are as follows:

1. For specimens belonging to the descending branch type, the partially-wrapped specimens had a lower compressive strength but a higher strain as compared to the corresponding fully-wrapped specimens. On the other hand, the non-uniform wrapped specimens experienced both a higher compressive strength and axial strain in comparison with the fully-wrapped specimens.

2. The heavily FRP-confined specimens (CF3, CP60, CP51, and CP42), partial- and non-uniform wrapped specimens provided a higher axial strain at failure as compared to that of fully-wrapped specimens.

3. The partial-wrapping scheme changed the failure modes of the specimens. If the FRP jackets are strong enough, the angle of the failure surface significantly reduced.

4. The actual rupture strain of the FRP jackets is different for each wrapping scheme. The strain efficiency factor in the full-wrapping scheme is greater than that of the partial-wrapping scheme but is less than that of the non-uniform wrapping scheme.

2.4 Effects of Fabrication Technique on Tensile Properties of Fibre Reinforced Polymer

2.4.1 Overview

Confinement of RC columns with externally bonded FRP laminates is an effective rehabilitation technique to enhance the columns' capacity (Wu et al. 2006; Nanni and Bradford 1995; Pham and Hadi 2014a). Failure of an FRP confined concrete column is usually governed by the rupture of the FRP, and designers consequently need to know the strain and stress at which the rupture of the FRP will occur (Chen et al. 2010). It has been observed that there is a considerable variation in the experimental rupture strain of FRP. The rupture of FRP is about 58-91% of its ultimate tensile strength determined from flat coupon tests (Lam and Teng 2004). It is noted that the actual rupture strain of FRP is necessary to estimate the axial strength of FRP confined concrete (Pham and Hadi 2013; Pham and Hadi 2014c; Lam and Teng 2003). The actual rupture strain of the jackets in FRP confined concrete columns can be estimated from the ultimate tensile strength determined from flat coupon tests. The strain efficiency factor can be utilized in such cases, which can be found in the study by Lam and Teng (2003). It has also been reported that carbon fibre materials exhibit higher modulus of elasticity and tensile strength, but lower rupture strain as compared to those of glass fibres.

Furthermore, when carbon and glass fibrous materials are bonded together to achieve a hybrid composite laminate, the glass fibres delay the progress of fracture of the carbon fibres providing an increase in the elongation of the hybrid laminate (Hawileh et al. 2014). There have been a limited number of studies about the mechanical properties of FRP (Dong and Gu 2012; Gu et al. 2015; Toufigh et al. 2015). Therefore, determining the ultimate tensile strength from flat coupon tests is significantly important. It is obvious that the implementation of FRP coupons and the workmanship affect the ultimate strength of the FRP coupons (Wu and Jiang 2013). There are two common types of FRP composites: shop-manufactured FRP composite and wet lay-up FRP composite. This study focuses on the wet lay-up FRP composite materials. There have been two standards which can be utilized to conduct FRP coupon tests, which are ASTM D3039-08 (ASTM 2008) and ASTM D7565-10 (ASTM 2010). The standard ASTM D3039-08 provided helpful knowledge to determine the tensile strength of FRP coupons.

However, this standard does not mention details about the preparation of the FRP coupons. Subsequently, the standard ASTM D7565-10 was revised and details of the fabrication technique were addressed. However, some requirements in the standard ASTM D7565-10, in terms of the preparation of the coupons, result in some difficulties when conducting FRP flat coupon tests. ASTM D7565-10 recommends producing a laminated FRP with a minimum dimension of 300 mm x 300 mm, from which flat coupons are cut at the required dimensions for testing. However, the cutting fabrication technique may damage some fibres in the coupons, this in turn may lead to a reduction of the ultimate tensile strength of the FRP coupons and a degradation in the quality control. Therefore, this study introduces a new technique for the preparation FRP flat coupons for the purpose of tensile testing, which provides an alternative fabrication technique with reliable and consistent results.

2.4.2 Tensile Properties of FRP Sheets

2.4.2.1 Review of Test Standards

The contemporary standard test method for determining the tensile properties of fibre reinforced polymer matrix composites for the use in structures requiring strengthening is ASTM D7565-10 (ASTM 2010). The other constituents of externally bonded strengthening systems, such as the adhesives, primer and putty used to bond the FRP material to the substrate are excluded from the sample preparation and testing methods. This standard directly references and relies on the previous standard ASTM D3039-08 (ASTM 2008) for specimen selection and the procedure of testing. The main difference however between the two standards is the determination of the tensile properties of the FRP composite material and most notably the ultimate tensile strength.

The ASTM D3039-08 states that the ultimate tensile strength of the FRP composite is calculated as the maximum tensile load carried before failure divided by the average cross-sectional area of the specimen. This gives rise to an ultimate tensile strength in terms of ultimate tensile stress in units of MPa. On the other hand, ASTM D7565-10 expresses the ultimate tensile strength in force per unit width (N/mm) as calculated by the maximum tensile load before failure divided by the width of the specimen. In addition, for the determination of the tensile chord modulus of elasticity, ASTM D7565-10 refers to the procedure in ASTM D3039-08, but substitutes the specimen width for the specimen area. Therefore, as opposed to ASTM D3039-08, the specimen thickness is not required for the calculation of the tensile properties in ASTM D7565-10. Therefore, ASTM D7565-10 eliminates the "design thickness" which is a parameter difficult to determine accurately by the tests, but defined by each supplier of FRP system.

The standard ASTM D3039-08 does not mention information about the fabrication technique for preparing FRP coupons. This standard requires testing at least five specimens per test condition unless valid results can be gained by using fewer specimens. As a result, using the wet lay-up FRP method for the specimen fabrication is currently inconsistent among researchers worldwide. The standard ASTM D7565-10 addressed this deficiency in the previous standard (ASTM D3039) then filled in this gap, which is described in Section 8.3.1. Based on this standard, a polymer release film, typically 600 mm x 600 mm is placed on a smooth, flat horizontal surface. Resin is first applied to the release film. The first ply of dried fibre with a minimum dimension of 300 mm x 300 mm is saturated or coated with the specified amount of resin and placed on the release film. The specified number of plies are sequentially impregnated with resin and stacked onto the release film using the specified amount of resin. A second release film is then placed over the material to provide protection. In order to ensure a smooth top surface of the FRP material, a rigid flat plate should be placed on top of the top layer of release film while the resin cures. After the specified curing procedure is complete, the release films are removed from the panel. Specimens may be cut and tabbed after the curing procedure. It is worth confirming that this fabrication technique is referred to as the "Cutting Technique" in this study.

In addition, it is obvious that this wet lay-up method is essentially based and governed by the workmanship in preparing the coupons. It is very difficult to ensure the perfect alignment of fibres or bundles of fibres. This means that if the specimen is cut at a straight line, some fibres will definitely be transected and damaged. These cuts lead to an uncertainty in the number of fibres in a specimen, resulting in some specimens having a different number of fibres from other specimens. As a result, the tensile strength of these specimens may not be expected to be the same. Therefore, this study introduces a Folding Technique for specimen fabrication and compares the tensile strength of the FRP coupons obtained by the Cutting Technique and the Folding Technique. The Folding Technique is described in more details in the sections below.

2.4.2.2 Tensile Properties

In presenting the results, the ultimate tensile strength expressed as force per unit width and the tensile chord modulus of elasticity are calculated based on the following equations from ASTM D7565-10 (ASTM 2010). The thickness and width of each specimen are determined by taking the average of three measurements at different sections of the specimen, which included a reading at each end of the specimen close to the steel tabs and one reading at mid length.

$$F^* = \frac{P^{max}}{w_s} \tag{2.6}$$

where F^* is the maximum tensile force per unit width; P^{max} is the maximum tensile force before failure; and w_s is the width of the specimen

$$K^* = \frac{\Delta P/w_s}{\Delta \varepsilon} \tag{2.7}$$

where K^* is the chord tensile stiffness per unit width; ΔP is the difference in applied tensile force between the two strain points, 1000 με and 3000 με as explained in Table 3 of ASTM D3039-08; and $\Delta \varepsilon$ is the difference between the two strain points, nominally 0.002 (Table 3, ASTM D3039-08).

2.4.2.3 Bending Effects

In the standard ASTM D3039-08 (ASTM 2008), the bending effects on the tensile strength of FRP coupons are mentioned and analysed. The standard mentions that excessive bending will result in premature failure and inaccuracies in determining the modulus of elasticity. The bending may be due to poor system alignment (misaligned grips) or poor specimen preparation or specimens installed improperly in the grips. The percent bending can be evaluated using Equations 2.8, 2.9, and 2.10 as follows:

$$B_y = \frac{\varepsilon_{ave} - \varepsilon_3}{\varepsilon_{ave}} \times 100 \qquad (2.8)$$

$$B_z = \frac{\frac{2}{3}(\varepsilon_2 - \varepsilon_1)}{\varepsilon_{ave}} \times 100 \qquad (2.9)$$

$$\varepsilon_{ave} = \frac{\frac{(\varepsilon_1 + \varepsilon_2)}{2} + \varepsilon_3}{2} \qquad (2.10)$$

where B_y = percent bending about system *y* axis (about the narrow plane), detailed in ASTM D3039-08; B_z is the percent bending about system *z* axis (about the wide plane), detailed in ASTM D3039-08; ε_1, ε_2, and ε_3 are the indicated longitudinal strains displayed by Gauges 1, 2, and 3, respectively, of Figure 2.9.

It is recommended by ASTM D3039-08 that good testing practice is generally able to limit percent bending to a range of 3 to 5% at moderate strain levels (>1000 με). A system showing excessive bending for the given application should be adjusted or modified.

2.4.3 Experimental Program

2.4.3.1 Design of Experiments

A total of twenty standard FRP coupons were made and tested at the High Bay Laboratory of the University of Wollongong, Australia. In this study two different techniques of preparing coupons for tensile testing were implemented and analysed, which included the Cutting Technique outlined in the ASTM D7565-10 (ASTM 2010) test standard and a proposed Folding Technique that did not involve exposing the reinforcing fibres. These twenty coupons were divided into four groups in which each group consisted of five specimens.

The notation of the coupons consists of two parts: the first part states the technique used to prepare the coupons, with “C” and “F” representing the Cutting Technique and Folding Technique, respectively. The coupon preparation utilizing these techniques is discussed in the sections below. The second part is either a number “25” and “37.5” stating the width of the coupons. It should be noted that the 25 mm width coupons, C25 and F25, were prepared using 3 layers of CFRP, whereas the 37.5 mm width coupons were composed of 2 layers of CFRP. Aluminium tabs with a thickness of 3 mm each were bonded to the ends of the coupons in order to transfer the force from the grip of the testing machine into the coupons. The dimensions of the coupons and aluminium tabs are shown in Figure 2.9. Details of the coupons are presented in Table 2.4.

Table 2.4. Test matrix (Pham et al. 2017)

Group	No. of coupons	Width (w_s, mm)	Length (l, mm)	No. of FRP layers	Preparation Technique	Type of FRP
C25	5	25	250	3	Cutting	CFRP
F25	5	25	250	3	Folding	CFRP
C37.5	5	37.5	280	2	Cutting	CFRP
F37.5	5	37.5	280	2	Folding	CFRP

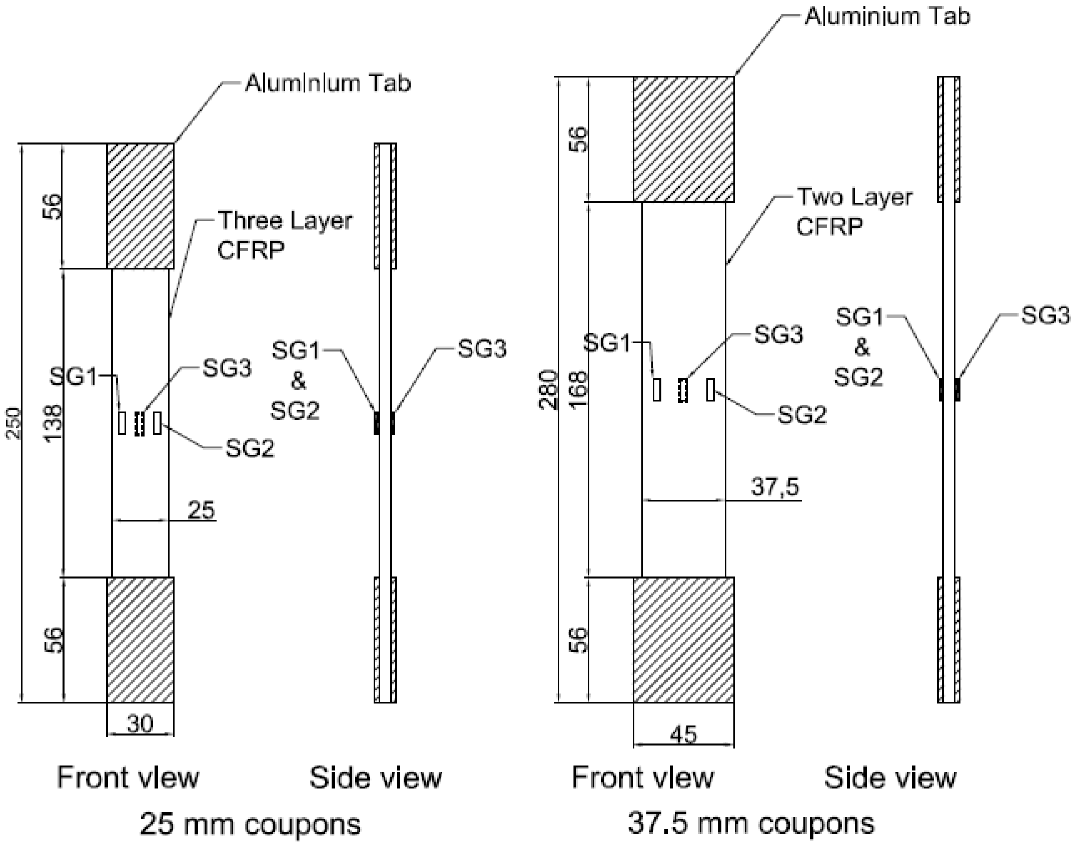

Figure 2.9. FRP flat coupons (Pham et al. 2017)

2.4.3.2 Specimen Preparation

In this study, one type of CFRP was used to prepare the coupons for tensile testing. The CFRP had a unidirectional fibre density of 340 g/m^2, a nominal width of 75 mm and a nominal thickness of 0.45 mm per sheet of fibre. The CFRP coupons were prepared following the ASTM D7565-10 (ASTM 2010) wet lay-up process, which involved the impregnation of the fibre sheets with the matching epoxy resin. The epoxy resin was prepared using a mixture of liquid epoxy resin and a hardener at a ratio of 5:1. The required number of sheets of dry fibre are consecutively saturated with resin and stacked to produce a flat rigid plate once the resin cures and hardens. In this standard, the dry fibre sheets are recommended to have a minimum dimension of 300 mm x 300 mm and the cured plate is cut into coupons or strips to meet the required dimensions. However, the carbon fibre dry sheets used in this experimental study and in other experimental studies (Hadi et al. 2013; Pham and Hao 2016; Pham et al. 2015a; Pham et al. 2015b) cannot be manufactured with minimum dimensions of 300 mm x 300 mm as recommended. It is worth mentioning that most of the studies focusing on FRP did not provide details about the specimen fabrication in terms of the preparation of the cured plate and the subsequent method of cutting it into smaller coupons. Furthermore, the cutting of the FRP plate into coupons penetrates the matrix material and in turn exposes and damages the reinforcing fibres, which may result in unexpected coupon failures and/or reduced strength.

With reference to ASTM D7565-10, the minimum width for unidirectional wet lay-up FRP specimens that have bundles (i.e. roving or tows) not wider than 3 mm when laid into the laminate, should be 25 mm. Taking this into account and considering the carbon fibre dry sheets had a nominal width of 75 mm, four groups of coupons were created having widths of 25 mm and 37.5 mm as shown in Table 2.4. The folded coupons denoted by F25 and F37.5 were prepared by evenly folding a 75 mm width dry carbon fibre sheet saturated with epoxy. To produce the Group F37.5 specimens, the epoxy saturated carbon sheet was folded once along the vertical axis to produce a 37.5 mm width two layered specimens, as shown in Figure 2.10(a). Similarly, the Group F25 specimens were prepared by folding the 75 mm wide sheet twice along the vertical axis to produce 25 mm width three layered specimens, as shown in Figure 2.10(b). In order to compare the specimens prepared by the proposed Folding Technique to specimens prepared using the Cutting Technique following the ASTM D7565-10 standard, equivalent specimens prepared by cutting a cured 75 mm wide FRP plate into widths of 25 mm and 37.5 mm were produced. These specimens are denoted by C25 and C37.5. As discussed above these hardened FRP plates were produced by stacking saturated 75 mm width fibre sheets to produce 2 layered C37.5 specimens or 3 layered C25 specimens. The dimensions of the specimens are shown in Figure 2.9.

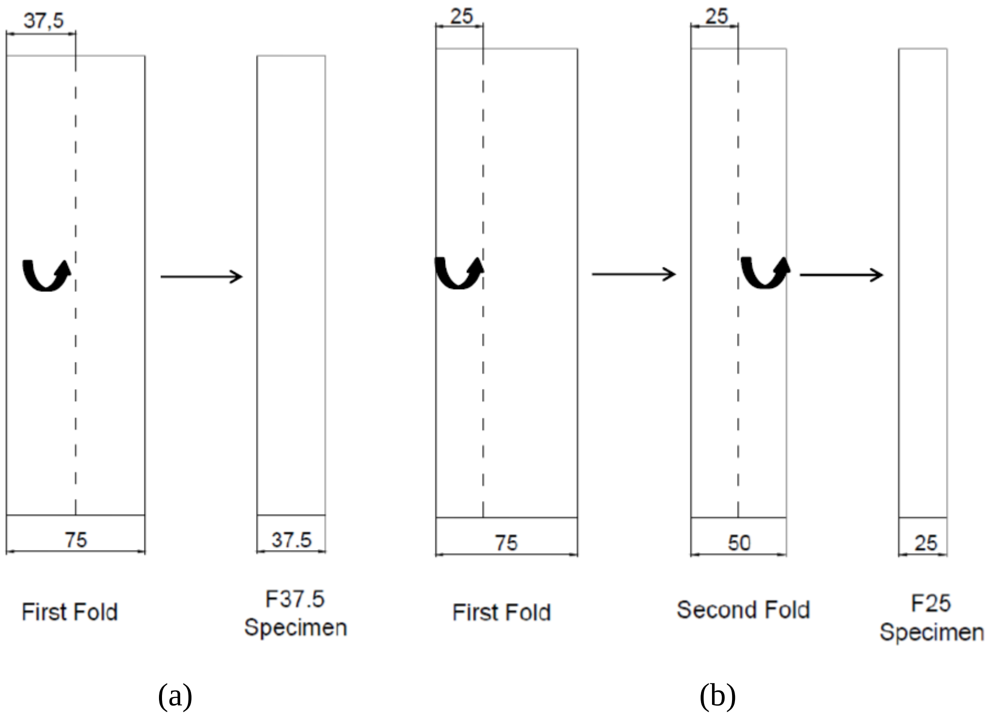

Figure 2.10. Preparation of the specimens using the Folding Technique: (a) Group F37.5 specimens; and (b) Group F25 specimens (Pham et al. 2017)

2.4.3.3 Testing Instrumentation

In order to measure the axial strains of the CFRP coupons, a total of three longitudinal strain gauges were attached. This included one strain gauge bonded to the back face of the specimen and another two at the front face at mid-length across the width of the specimen, as shown in Figure 2.9. As mentioned in the ASTM D3039-08, the amount of bending in the thickness plane (B_y) and width plane (B_z) can be measured by analysing the variations in strain between these three strain gauges as shown in Equations 2.8, 2.9, 2.10.

The tensile tests for all the coupons were conducted using a screw-driven material testing machine known as the Instron 8033. As mentioned above, aluminium tabs were bonded to the ends of the specimens in order to transfer the force from the grip of the machine into the specimen. The dimensions of these tabs are shown in Figure 2.9. The load was applied at a constant head displacement rate of 1 mm/min in order to ensure specimen failure occurs within 1 to 10 minutes as highlighted in ASTM D3039-08. The load was measured using a load cell of 500 kN capacity. The readings of the load and strain gauges were taken using a data logging system and were subsequently saved in a control computer which recorded one recording per second. In presenting the results, the strains were averaged from the readings of the three strain gauges.

2.4.4 Experimental Results

2.4.4.1 Tensile Force per Unit Width versus Strain Response

The failure modes of the tested specimens are determined as lateral or longitudinal splitting (Figure 2.11). The failure location of the tested specimens was found to be at the ends, middle or at another location. As expected, the most common failure mode was the lateral rupture of the coupons at the specimens' mid length.

The tensile forces per unit width versus the average strains of the tested specimens are shown in Figure 2.12. Initially during the early stages of loading the CFRP coupons, stress-strain responses were perfectly linear due to the elastic nature of the material. However, during the later stages of loading, the tensile force per unit width versus strain response of some of the CFRP specimens deviated slightly from the perfectly linear relationship. Some slippage occurred at close to failure for a few specimens, as shown in Figure 2.12. This behaviour at the later stages has been previously reported by others (Lam and Teng 2004; fib 2001) and is the consequence of the gradual stiffening of the CFRP due to the straightening of the fibres. As a result, the secant modulus of the CFRP at the ultimate strain is slightly different from the modulus of elasticity computed according to ASTM D3039-08. In the interpretation of the test results, the gradual stiffening and the slippage at the later stages of testing are ignored. In other words, the stress-strain relationship was modified based on the assumption that the CFRP composite is perfectly linear in nature, and the rupture strain was determined based on the linear trend.

Specimen C25_1 with lateral failure type

Specimen C37.5_3 with long splitting failure type

Figure 2.11. Failure modes of FRP coupons (Pham et al. 2017)

2.4.4.2 Tensile Properties

A total of twenty specimens or five specimens per group were tested and presented. The results of the tensile testing are shown in Tables 2.5 and 2.6. The maximum tensile force per unit width (F^*), ultimate strain (ε_f) and the chord tensile stiffness per unit width (K^*) of the Group C25 were respectively 2025 N/mm, 1.70% and 114.6 kN/mm. The corresponding values of the Group F25 were 2193 N/mm, 1.78% and 116.8 kN/mm, respectively. The tensile properties of Group F25 were found to be greater than that of Group C25. The maximum tensile force per unit width and the ultimate strain of Group F25 specimens were 8% and 5% higher than that of Group C25, respectively. Moreover, the maximum tensile force per unit width and the ultimate strain of Group F37.5 were both 5% higher than those of Group C37.5. However, the chord tensile stiffness per unit width of the two groups was similar.

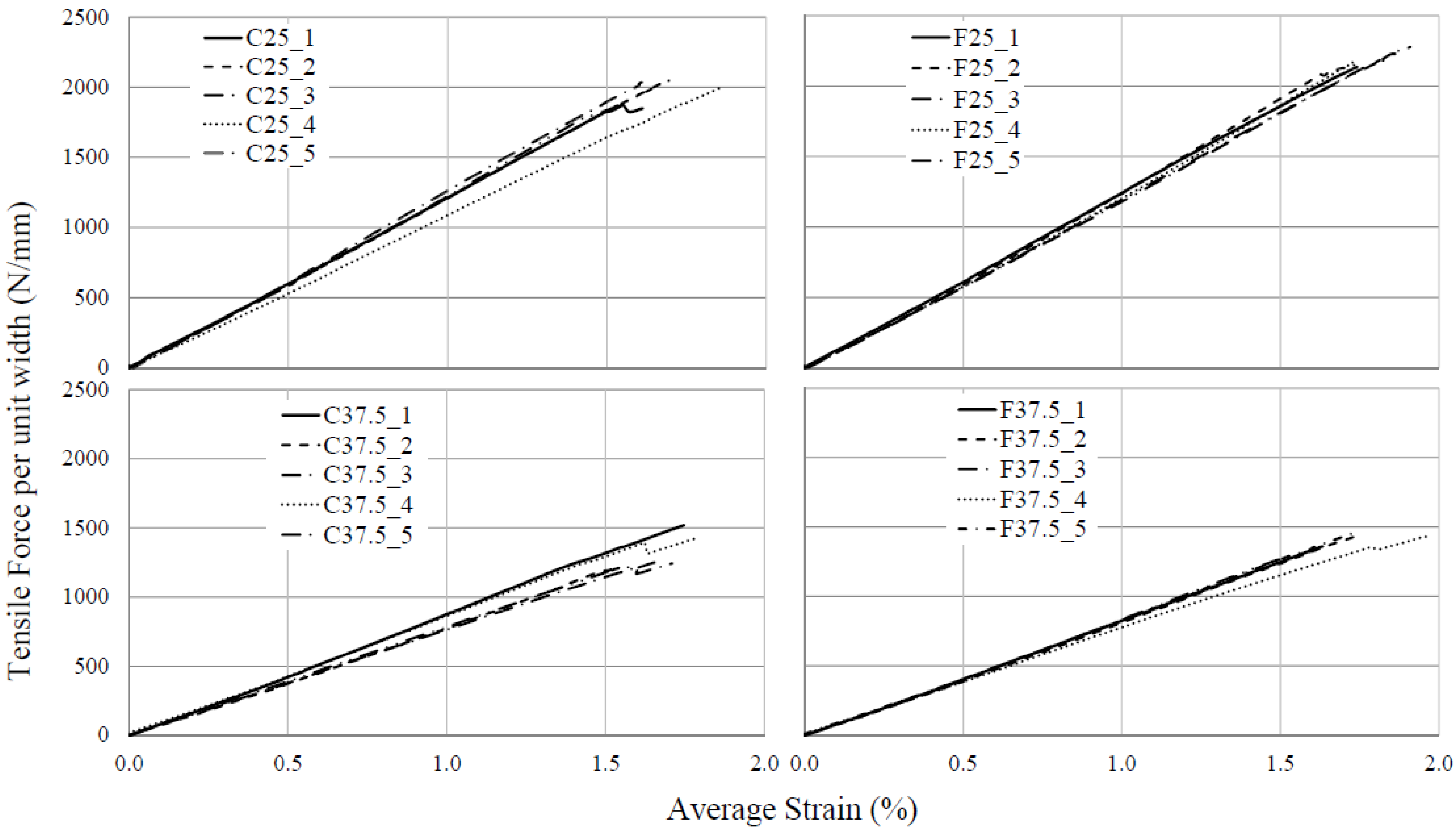

Figure 2.12. Tensile force per unit width versus average strain relationships for the specimens

Table 2.5. Tensile properties of CFRP coupon tests (width 25 mm)[Pham et al. 2017]

Sample	F^* (N/mm)	ε_{ave} (%)	B_y (%)	B_z (%)	K^* (kN/mm)	Width (mm)
C25_1	1901	1.59	OK[c]	OK	114.0	25.72
C25_2	2048	1.69	OK	OK	115.1	24.73
C25_3	1988	1.61	OK	OK	115.8	25.66
C25_4	1994	1.85	OK	X[d]	105.0	24.69
C25_5	2192	1.76	OK	OK	123.4	24.86
C25_average	**2025**	**1.70**	**-**	**-**	**114.64**	**25.13**
SD[a]	**107.3**	**0.11**	**-**	**-**	**6.55**	**0.51**
CV[b] (%)	**5.30**	**6.28**	**-**	**-**	**5.71**	**2.04**
F25_1	2136	1.74	OK	X	120.4	23.82
F25_2	2149	1.73	OK	OK	118.9	24.57
F25_3	2275	1.83	OK	X	116.7	25.09
F25_4	2179	1.73	OK	OK	114.1	23.63
F25_5	2228	1.86	OK	OK	114.0	25.20
F25_average	**2193**	**1.78**	**-**	**-**	**116.8**	**24.46**
SD	**57.80**	**0.06**	**-**	**-**	**2.85**	**0.71**
CV (%)	**2.64**	**3.46**	**-**	**-**	**2.44**	**2.92**

[a] The standard deviation; [b] The coefficient of variation; [c] OK means the percent bending less than 5%; [d] X means the percent bending greater than 5%.

F^* = maximum tensile force per unit width; B_y = percent bending about system y axis (about the narrow plane); B_z = percent bending about system z axis (about the wide plane); K^* = the chord tensile stiffness per unit width; and ε_{ave} is calculated based on Equation 2.10.

Table 2.6. Tensile properties of CFRP coupon tests (width 37.5 mm)[Pham et al. 2017]

Sample	F^* (N/mm)	ε_f (%)	B_y (%)	B_z (%)	K^* (kN/mm)	Width (mm)
C37.5_1	1520	1.75	OK[c]	OK	83.4	36.92
C37.5_2	1225	1.60	OK	OK	73.3	36.98
C37.5_3	1252	1.58	OK	OK	76.6	39.21
C37.5_4	1429	1.59	X[d]	OK	79.7	38.15
C37.5_5	1244	1.65	OK	X	75.5	37.82
C37_average	**1334**	**1.63**	**-**	**-**	**77.7**	**37.81**
SD[a]	**132.54**	**0.07**	**-**	**-**	**3.94**	**0.94**
CV[b] (%)	**9.94**	**4.26**	**-**	**-**	**5.07**	**2.49**
F37.5_1	1359	1.63	OK	OK	79.6	38.40
F37.5_2	1430	1.74	OK	OK	76.6	37.47
F37.5_3	1332	1.61	OK	OK	78.9	37.22
F37.5_4	1435	1.85	OK	OK	74.4	37.23
F37.5_5	1472	1.75	OK	OK	78.2	36.18
F37_average	**1406**	**1.72**	**-**	**-**	**77.6**	**37.30**
SD	**57.99**	**0.10**	**-**	**-**	**2.08**	**0.79**
CV	**4.13**	**5.63**	**-**	**-**	**2.69**	**2.13**

[a] The standard deviation; [b] The coefficient of variation; [c] OK means the percent bending less than 5%; [d] X means the percent bending greater than 5%.

F^* = maximum tensile force per unit width; B_y = percent bending about system y axis (about the narrow plane); B_z = percent bending about system z axis (about the wide plane); K^* = the chord tensile stiffness per unit width; and ε_{ave} is calculated based on Equation 2.10.

2.4.4.3 Bending Effects

The percent bending of the tested specimens was calculated following Equations 2.8-2.10 which were used to evaluate the bending effects. ASTM D7565-10 states that good testing practice is generally able to limit percent bending about the width plane and thickness plane as calculated by Equations 2.8 and 2.9, to a range of 3% to 5% at moderate strain levels (>1000με). Initially, specimens experienced percent bending exceeding these levels, which showed that either the alignment of the machine was unsatisfactory, specimen preparation was poor or that the specimens were installed improperly in the grips, with ultimate strengths and strains below average for the respective group. Therefore, the results of these specimens were excluded. Following a few tests, additional care was taken to improve both the preparation process of the specimens and their alignment. No slippage or excessive bending occurred for the presented specimens, although some specimens experienced percent bending of over 5%, as shown in Figures 2.13 and 2.14.

Bending stresses inadvertently arise as a result of the misalignment between the specimen axes and the applied force during the application of tensile forces ASTM E1012-14 (ASTM 2014a). Ideally, the centrelines of the top and bottom grips of the machine should be precisely aligned with one another and with the centreline of the specimen. Additionally, the specimen should be symmetric about its centreline. However, differences from the ideal situation are due to poor specimen preparation and poor system alignment. ASTM E1012-14 states that testing machines as-received from manufacturers may have deviations between the top and bottom centreline grip positions ranging from 0.03 mm to 3.18 mm or more. In addition, applied forces subjected by the machine results in further misalignment due to the machine frame deflections. It has been reported that in the worst case, the deviations in this range has resulted in a difference between extreme surface bending strains and average strains of between 50% to 100% (ASTM E1012-14). Therefore, conducting a tensile test with the percent bending between 3% to 5% is challenging.

The system alignment or bending behaviour of the specimens was analysed by plotting the percent bending about the width (B_z) and thickness plane (B_y) versus the axial average strain obtained from the three strain gauges, as shown in Figures 2.13 and

2.14, respectively. ASTM D3039-08 states that although the maximum advisable amount of system alignment is location and material dependent, good testing practice is generally able to limit percent bending to a range of 3% to 5% at moderate strain levels greater than 1000 $\mu\varepsilon$. For simplicity, the percent bending by the thickness plane and width plane will be referred to as B_y and B_z, respectively. First, the analysis of the percent bending (B_z) about the width plane versus the average strain is presented. It should be noted that for most of the specimens, B_y and B_z were very large during the early stages of loading. These large bending values may be due to the stabilization of the loading or other factors and were ignored in the analysis by plotting B_z from average strains of 0.1% (see Figure 2.13).

As can be seen from Figure 2.13 there was no common trend with the relationship of B_z versus average strain. Most of the tested specimens had the percent bending about system z axis lower than 5%. However, the percent bending at the later stage when the tested specimen almost failed fluctuated as compared to the earlier stages. It is assumed that a specimen that had the percent bending greater than 5% may cause deviation from the average values, as experienced for the initially tested specimens. However, the experimental results showed that the percent bending did not cause considerable deviation in the tensile properties of the coupon tests. For instance, Specimen F25_3 had 10% bending, which led to 4% difference in the maximum tensile force per unit width and 3% difference in the ultimate strain. Based the percent bending about the thickness plane (B_y), 90% of the specimens experienced bending B_y of less than 3%. For the remaining specimens, excluding Specimen C37_5, the percent bending was between 3% and 5% for the majority of the loading, as shown in Figure 2.14. Generally, the percent bending B_y was stable from the axial strain of about 0.5% which is different to that of the percent bending B_z.

In summary, no apparent trend was noticed in the bending versus average strain relationships. Also, the level of bending in the specimens presented in this study did not necessarily dictate the ultimate strength or strain of the specimens. Specimens with higher levels of bending did not necessarily have reduced ultimate strengths or strains compared to those specimens with lower bending values. In addition, bending about the width plane resulted in higher levels compared to bending about the thickness plane.

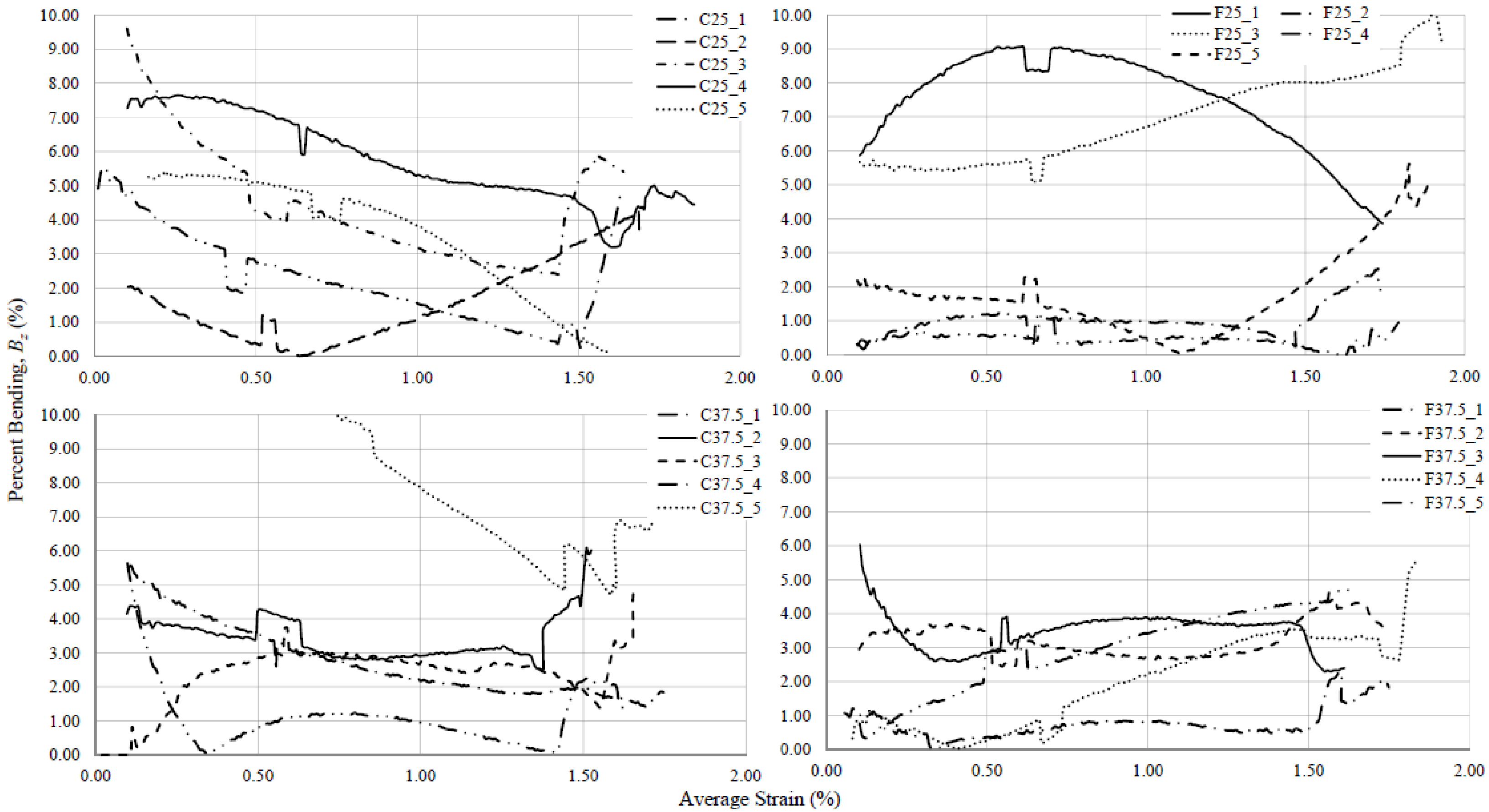

Figure 2.13. Percent bending about system *z* axis (Pham et al. 2017)

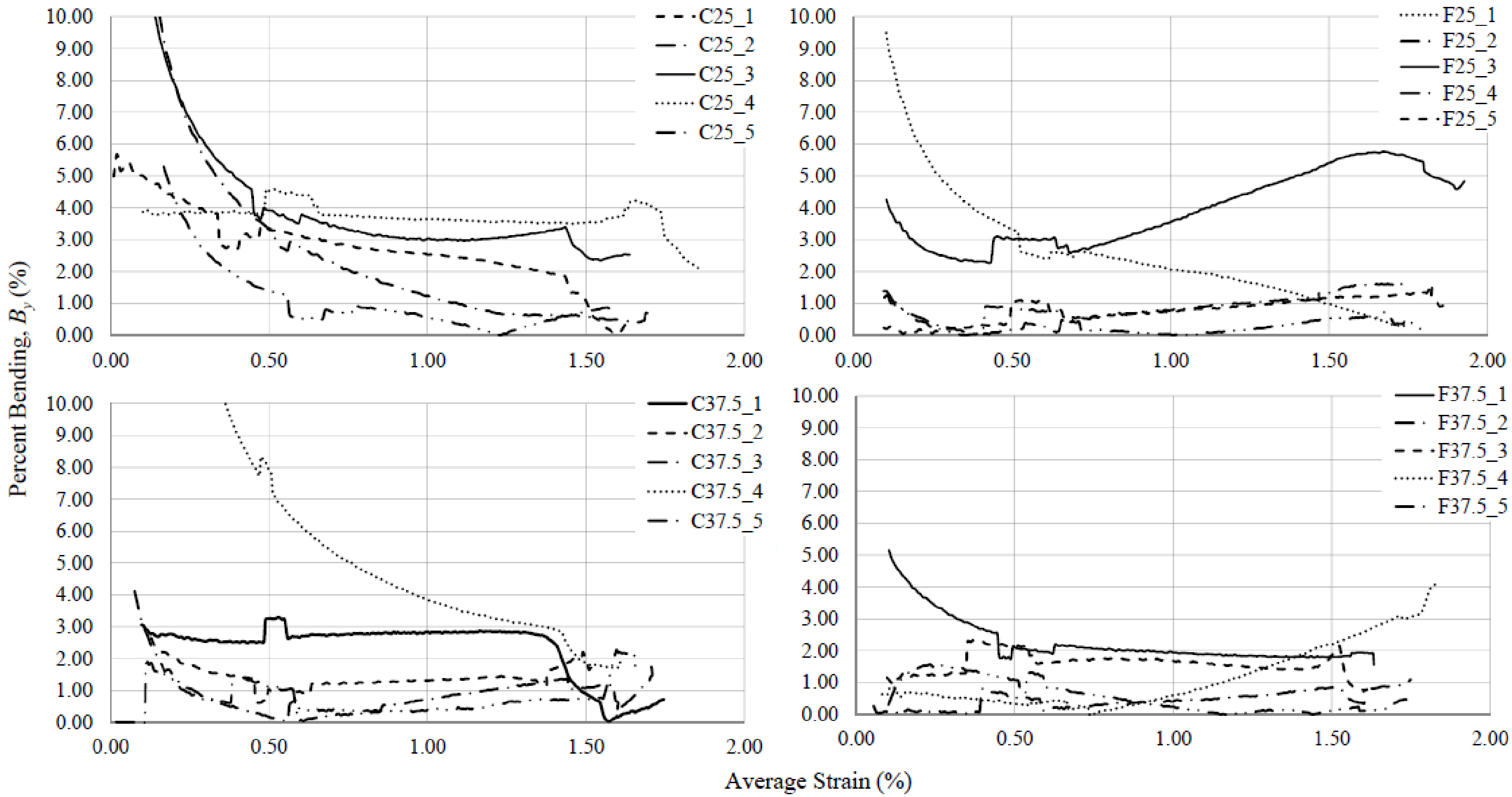

Figure 2.14. Percent bending about system *y* axis (Pham et al. 2017)

2.4.5 Discussion

2.4.5.1 Fabrication technique

ASTM D7565-10 recommends preparing FRP coupons made of dry fibre preform from an FRP laminate having a minimum dimension of 300 mm x 300 mm. The standard does not include FRPs material with widths less than 300 mm. It is noted that the standard focuses more on the thickness of the FRP sheets rather than their width. The width, in general, does not affect the tensile properties of FRP sheets, but it causes difficulties in specimen fabrication. Studies that used FRP sheets with a width less than 300 mm (Hadi et al. 2013; Pham et al. 2013) struggled to conduct the FRP coupon tests in accordance with ASTM D7565-10. Therefore, ASTM D7565-10 should consider taking this issue into account in the future revised version.

Experimental results from this study showed that FRP coupons prepared using the Folding Technique provides higher tensile properties than that of the Cutting Technique recommended by ASTM D7565-10. As mentioned above, the reduction of the tensile properties of FRP coupons made by the Cutting Technique was caused by the reduction in the number of fibre in identical coupons. This reduction resulted from the misalignment of the fibres combined with the cutting of the specimens. As shown in Figure 2.15, even though special care was taken in the cutting process to minimize the exposure of the fibres, some fibres were damaged and exposed, which may lead to the reduction of the tensile properties and premature failure.

The experimental results also confirmed that the fabrication technique did not affect the percent bending as shown in Figures 2.13 and 2.14. The percent bending of the four groups seemed to be independent of the fabrication technique. However, the fabrication technique affected the standard deviation (SD) and the coefficient of variation (CV). Most notably, the experimental results from Tables 2.5 and 2.6 showed that the Folding Technique provided less SD and CV than that of the Cutting Technique. The SD and CV of the Folding Technique were approximately half of that obtained for the Cutting Technique. For example, the values of the SD and CV in calculating the maximum tensile force per unit width of Group C25 were respectively 107.3 N/mm and 5.30% while the corresponding numbers of Group F25 were 57.8

N/mm and 2.64%. It means that the Folding Technique delivers more reliable results in comparison with the Cutting Technique.

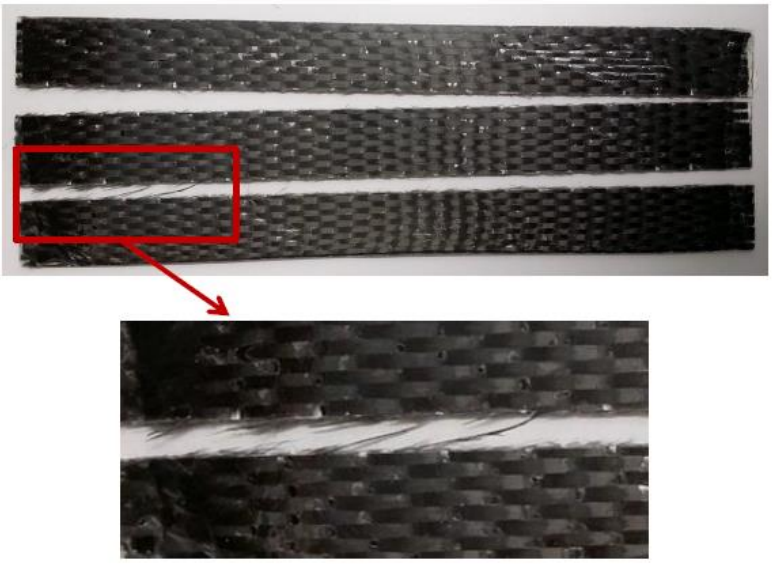

Figure 2.15. Exposure of reinforcing fibres (Pham et al. 2017)

2.4.5.2 The Width of the Coupons

ASTM D7565-10 recommends that the variation in specimen width should be no greater than ± 1%. However, the tested coupons implemented by the wet lay-up method can be affected by experience and workmanship. As a result, it is difficult to maintain the variation of the specimen width within ±1%. Experimental results from Tables 2.5 and 2.6 stated that the variation in specimen width of Groups C25, F25, C37.5 and F37.5 were 2.0%, 2.9%, 1.7% and 2.1%, respectively.

In the specimen fabrication, a metal shear machine was used to cut a large laminated FRP into small FRP coupons that had widths of 25 mm or 37.5 mm. It is assumed that one cut can yield the same number of fibres damaged. This cut yielded the same number of damaged fibres in one 25 mm coupon or 37.5 mm coupon. In order to investigate this parameter, the ratio between the number of the damaged fibres and the number of the total fibres is defined as the damage ratio. Meanwhile, the number of total fibres in the 37.5 mm coupon is greater than that of the 25 mm coupon. Therefore, the damage ratio of the 25 mm coupon is greater than that of the 37.5 mm coupon.

According to the Cutting Technique, this ratio indicates that wider coupons have smaller damage ratios as compared to smaller coupons. In such cases, the damage ratio is an indicator of the reduction in the tensile strength. For instance, the damage ratio of the 25 mm width coupons is greater than that of the 37.5 mm width coupons. Therefore, the difference in tensile strength between Groups C25 and F25 is larger than that between Group C37.5 and F37.5 (see Tables 2.5 and 2.6). For instance, the increase of the maximum tensile force per unit width of Group F25 compared to Group C25 was 8% while the corresponding number between Group F37.5 compared to Group C37.5 was only 5%.

2.4.5.3 Bending Effects

The percent bending was determined for all the specimens tested. The ASTM D3039-08 standard recommends testing one specimen to determine the system misalignment. However, other factors such as poor specimen preparation and improper placement of specimen in the grips could be a cause of bending. To check for specimen bending the standard also mentions testing at least one specimen per like sample with back to back transducers (Clause 11.6.1 of ASTM D3039-08). Therefore, considering factors other than system misalignment play a role in bending, all the specimens, rather than only one, should be tested to calculate the percent bending for the whole system and the specimen. The bending of the coupons is a function of both the testing machine and the coupon itself.

2.5 Summary

This chapter explains two preliminary studies that were conducted on the strengthening of concrete members using FRP sheets. The first study investigated the behaviour and failure modes of FRP confined concrete wrapped with different FRP schemes, including fully wrapped, partially wrapped, and non-uniformly wrapped concrete cylinders. By using the same amount of FRP, this study proposed a new wrapping scheme that provides a higher compressive strength and strain for FRP-confined concrete, in comparison with conventional fully wrapping schemes. A total of 33 specimens were cast and tested, with three of these specimens acting as reference specimens and the remaining specimens wrapped with different types of FRP (CFRP and GFRP) by different wrapping schemes. For specimens that belong to the descending branch type, the partially-wrapped specimens had a lower compressive strength but a higher axial strain as compared to the corresponding fully-wrapped specimens. In addition, the non-uniformly wrapped specimens achieved both a higher compressive strength and axial strain in comparison with the fully-wrapped specimens. Furthermore, the partially-wrapping scheme changes the failure modes of the specimens and the angle of the failure surface.

The second study investigated the effects of fabrication technique on the tensile properties of FRP flat coupon tests. A total of twenty FRP flat coupons were prepared by two different techniques which were tested in tension until failure. The first technique of preparing the FRP coupons is based on the recommendation of ASTM D7565-10, which is named the "Cutting Technique", while the second technique named the "Folding Technique" is proposed by this study. Experimental results from this study indicated that preparing FRP coupons using the Cutting Technique results in a reduction in the tensile properties as compared to coupons prepared by the proposed Folding Technique. Most notably, the tensile force per unit width obtained by the FRP flat coupons prepared using the Folding Technique was up to 8% higher than that obtained by coupons prepared using the Cutting Technique. In addition, the effect of the percent bending on the tensile properties was also studied. It was found that the percent bending about the thickness plane was greater than that of the percent bending about the width plane. Furthermore, the tensile properties of the FRP coupons were not sensitive to its percent bending.

The use of FRP materials is not only limited to strengthening purposes for existing structures but they have gained widespread use for different applications such as the internal reinforcement for new construction of concrete members. The main focus of this study is the use of FRP bars and sections for reinforcement purposes in concrete members. Consequently, the next two chapters explain the literature relating to concrete members reinforced with GFRP bars and an overview of pultruded GFRP structural sections which lead on to the main experimental program of this research.

3 CONCRETE MEMBERS REINFORCED WITH FRP BARS

3.1 Introduction

Fibre reinforced polymer (FRP) materials in civil engineering structures are allowing engineers to optimize their structural designs in many ways that approach the limiting capabilities of these materials. The use of FRP materials as replacements to conventional materials such as steel is increasing due to their light weight, non-corrosive and high strength properties. FRP materials used in civil engineering structures are categorised into three main applications: strengthening of existing structures, inclusion in concrete as reinforcement, or the use of FRP structural profiles for the primary structure or as part of a hybrid concrete members. In all these applications, FRP materials and concrete are combined in a way that the advantages of both materials are utilised efficiently, with concrete resisting compression and FRP materials providing significant tension and lateral confinement capacity.

This chapter presents a thorough review of the available studies on concrete members reinforced with FRP bars. The mechanical properties of FRP bars are first discussed followed by an overview of the available studies on concrete columns and beams reinforced with FRP bars.

3.2 Overview of the Use of FRP in Construction

The usage of FRP reinforcement can be linked back to as early as the 1940s with the use of composites after World War II. However, the use of these materials in concrete as reinforcement was not considered until the 1960s (ACI 440.1R-15 2015). Concern for the deterioration of bridges caused by corrosion and its consequences on old bridges in the United States has now been established (Boyle and Karbhari 1994). Therefore, to address the corrosion issues in bridges and other structures, FRP reinforcement started to be considered as an alternative material in place of steel (Benmokrane et al. 1996).

Up to the mid-1990s, Japan had the most applications of FRP reinforcement which resulted in design provisions for FRP adapted in the construction and design guidelines of the Japanese Society of Civil Engineering (JSCE 1997). In the 2000s, the largest user of composite reinforcement in the construction of new infrastructure in projects was China, with projects varying from underground applications to bridge decks (Ye et al. 2003). In Canada, provisions have been established by civil engineers for FRP reinforcement in the Canadian Highway Bridge Design Code, CSA-S6-2006-R2012 (CSA 2006-R2012). As a result, more than 200 bridge structures utilising FRP reinforcement have been constructed in Canada. In addition, FRP bars have been used in other structures in Canada, including parking garages, water tanks, concrete barriers and highway concrete pavements.

Therefore, based on the historical review of FRP composites, it can be seen that many applications of these materials in construction has transpired since the 1990s with design guidelines for concrete structures reinforced with FRP bars developed across the world in USA (ACI 440.1R-15 2015), Japan (JSCE 1997), Canada (CSA-S806-2012-R2017), and Europe (CNR-DT203 2006). Most notably, in 1997, the ASCE introduced the Journal of Composites for Construction. Currently, this journal is the main international archive for reporting research work and developments in the area of FRP composites in construction. In addition, extensive research studies have been performed on the use of FRP reinforcement in the construction or retrofitting of new and existing structures.

3.3 Mechanical Properties of FRP Bars

The mechanical behaviour of FRP reinforcement are different to that of steel reinforcement and is largely dependent on the fibre type, resin matrix and fibre volume ratio. In general FRP bars have a higher strength-to-weight ratio, but lower modulus of elasticity as compared to steel. There are three main types of fibres, namely, carbon (CFRP), glass (GFRP) and aramid (AFRP) fibres. The next section will discuss the tensile, compressive and shear properties of FRP bars, along with the properties of bent bars.

3.3.1 Tensile Properties

When subjected to tension, FRP bars exhibit a linear elastic behaviour up to failure. Therefore, prior to rupture, no plastic deformation is experienced by FRP bars. The tensile properties of FRP bars are dependent on the fibre volume fraction, which is the relationship between the fibre volume to the overall volume of the FRP. This is the case because the resin has a much lower strength than the fibres. The tensile property of different types of FRP bars having fibre volume fractions of 0.5 to 0.7 compared with the tensile properties of steel bars is shown in Table 3.1.

As opposed to steel, a variation in the diameter of FRP bars influences the tensile strength. Faza and GangaRao (1993) tested GFRP bars from three different manufacturers and indicated that a reduction in tensile strengths of 40% occurred as the diameter increased proportionally from 9.5 mm to 22.2 mm. The test methods available for the determination of the tensile properties of FRP bars are explained in ASTM D7205-11 (ASTM 2011).

Table 3.1. Typical properties of different types of FRP reinforcement bars in tension (ACI 440.1R -15 2015)

Property	Steel	GFRP	CFRP	AFRP
Nominal Yield Stress (MPa)	276 - 517	N/A	N/A	N/A
Tensile Strength (MPa)	483 - 1600	483 - 690	600 - 3690	1720-2540
Modulus of Elasticity (GPa)	200	35 – 51	120 – 580	41 – 125
Yield Strain (%)	0.14 - 0.25	N/A	N/A	N/A
Rupture Strain (%)	6.0 - 12.0	1.2 - 3.1	0.5 - 1.7	1.9 - 4.4

3.3.2 Compressive Properties

When loaded in compression, the behaviour of FRP bars is influenced by different modes of failure including fibre micro-buckling, transverse tensile failure, or shear failure. Therefore, for FRP composites there exists no standard axial compression test method (ACI 440.1R-15 2015). The behaviour of FRP bars in compression needs to be established to allow for the design of FRP reinforced concrete (RC) columns.

Based on the literature is has been established that the compressive strengths of FRP bars are relatively low compared to the tensile strengths and are subjected to significant variations. In early studies, the compressive strengths of GFRP, AFRP and CFRP bars were reported to be 55%, 20% and 78% of the tensile strengths, respectively (Mallick 1988; Wu 1990). In addition, compressive modulus of elasticity of 100%, 85% and 80% of the tensile modulus of elasticity for AFRP, CFRP and GFRP, respectively have been reported (Mallick 1988; Ehsani 1993).

Chaallal and Benmokrane (1993) experimentally studied the behaviour of GFRP bars tested in compression having three different diameters of 15.9 mm, 19.1 mm and 25.4 mm. The lengths of the specimens were determined using the recommended slenderness ratio of 11 as outlined by the ASTM standards. It was stated that the strength of the GFRP bars in compression was 77% of the strength in tension. Furthermore, the Poisson's ratio and modulus of elasticity in compression was similar to the respective values in tension.

Kobayashi and Fujisaki (1995) examined FRP bars tested in compression. The specimen's ends were cast in blocks of concrete. According to the results of this study, it was established that the compressive strengths of GFRP, AFRP and CFRP bars were 30 - 40%, 10% and 30 - 50% of their tensile strengths, respectively.

Deitz et al. (2003) tested in compression a total of 45 GFRP bars having a diameter of 15 mm. The ends of the specimen were restrained partially and the unbraced lengths of the specimens varied from 50 to 380 mm. It was concluded that the ultimate strength in compression is equal to about 50% of the ultimate tensile strength. The short specimens with unbraced lengths between 50 to 100 mm failed by crushing, and a wide scatter of results was seen. On the other hand, slender specimens with unbraced lengths of 210 mm to 380 mm experienced lower compressive strengths and failed by buckling of the bar as a single entity with little scatter in the results. Furthermore, based on a limited number of tests of three specimens, it was also reported that there was no difference in the modulus of elasticity in compression as compared to that in tension.

In summary, these studies indicate that the test data of compression testing of FRP bars are widely scattered and subjected to significant variations, unlike the tensile properties. Furthermore, there is a general agreement that the FRP bars' compressive strength is lower than that of the tensile strengths. In terms of GFRP bars, the variations of strengths in compression have been reported to range from 30% to 77% of the tensile strengths reported. Furthermore, the compressive modulus of elasticity of GFRP bars has been reported to be 80% to 100% of the tensile modulus of elasticity. A reason for the lower values of modulus of elasticity in compression has been reported to be due to the premature failure of the test specimens as a result of end brooming and internal fibre micro-buckling under compressive loading (ACI 440.1R-15 2015).

3.3.3 Shear Properties

As a result of the manufacturing process of FRP bars in the pultrusion process, the fibres are aligned along the longitudinal direction and there exists minimal reinforcement in the transverse direction. Therefore, the inter-laminar shear strengths of the FRP are governed by the relatively weak polymer matrix producing a weak shear resistance. To increase the shear resistance, the fibres can be orientated across the layers in an off-axis direction. In terms of FRP bars, increasing the shear resistance could be achieved by winding or braiding fibres transverse to the main fibres. This can be done during the process of pultrusion by incorporating a continuous strand mat in the roving/mat creel. Similar to the compressive properties, no standard test methods are recognized to determine the behaviour of FRP bars in shear and these properties could be obtained by the manufacturer.

3.3.4 Properties of Bent Bars

FRP bars cannot be bent after they have been cured (polymerised) and the only way to produce bends is during the manufacturing process. The tensile strengths in the bend portion of FRP bars are 40% to 50% lower compared to that of a straight bar due to stress concentrations and fibre bending (Nanni et al. 1998). For the same type of fibres, the strength of bent bars varies significantly depending on the radius of the bend, type of resin or technique of bending. The design tensile strength of FRP bars at a bend (f_{fb}) as stated in ACI 440.1R-15 (ACI 2015) can be determined as follows:

$$f_{fb} = (0.05\frac{r_b}{d_b} + 0.3)f_{fu} \leq f_{fu} \tag{3.1}$$

where r_b is the radius of the bends; d_b is the diameter of reinforcing bar; and f_{fu} is the design tensile strength of FRP.

Ehsani et al. (1995) mention that the tensile strengths of the bent regions of FRP bars depends on the ratio of the radius of the bend to the diameter of the bar (r_b / d_b), the tail length and the concrete strength. Typically, the allowable minimum bend radius for FRP bars is 3.5 to 4 times the diameter of the bar which is a higher value than that used for steel bars. According to Ehsani et al. (1995), FRP stirrups should be closed with 90-degree hooks and the minimum ratio of r_b / d_b is three. Alternatively, ACI 440.3R-12 (ACI 2012) outlines the test methods required to determine the substantial reduction in tensile strength at the bend regions of FRP bars and stirrups.

Tobbi et al. (2014) determined the ultimate strength of the bent portion of both CFRP and GFRP bars and compared them to the ultimate strengths in the straight portions (f_{fu}) of the same bar. The ratio of the strength in the bent portions to the strength in the straights ranged between 0.46 and 0.52 for the GFRP bars and 0.62 for the CFRP bars.

3.4 Concrete Columns Reinforced with FRP Bars

Concrete columns are one of the numerous structural members that could be exposed to severe environmental conditions. As explained above, when subjected to compression, FRP bars are affected by various modes of failure including buckling, shear or transverse tensile failures. In addition, many experimental studies have shown that FRP bars are substantially weaker in compression than they are in tension and are subjected to significant variations. Therefore, as a result of the lack of experimental data and the low compressive strengths of FRP bars as compared to the tensile strength, the current ACI 440.1R-15 (ACI 2015) design guideline mentions to neglect the compressive contribution of FRP reinforcement when utilised as reinforcement in compression members, in columns, or as compression reinforcement in flexural members. The acceptance of FRP by designers requires the development of design guidelines for the design of FRP bars in compression members such as columns. In this regard, experimental and analytical studies have been conducted to understand the compressive behaviour and failure modes of concrete columns internally reinforced with FRP as discussed herein.

3.4.1 Existing Studies on Concentric Loading

3.4.1.1 Longitudinal and Transverse Reinforcement

In a column there are two main types of reinforcement, which are longitudinal and transverse reinforcement. The purpose of the transverse reinforcement is to hold the longitudinal bars in position, to provide lateral support for the bars to not buckle and to develop adequate confinement to the internal core of concrete. For steel reinforcement the ACI 318-14 (ACI 2014) guideline mentions providing longitudinal bars with a reinforcement ratio of at least 1%. Considering that the mechanical properties of FRP bars are different to steel bars, it is essential to investigate the behaviour and contribution of the FRP bars in concrete columns.

Alsayed et al. (1999) studied the influence of replacing longitudinal steel bars and steel ties in concrete columns with the equivalent amount of GFRP bars and ties. A total of fifteen concrete columns of rectangular cross-section (450 mm x 250 mm x 1200 mm) were tested under concentric axial loading. The concrete columns were reinforced with six steel bars of 16 mm diameter or six GFRP bars of 15.7 mm diameter with three specimens serving as plain unreinforced concrete. The concrete columns were cast with 38.6 MPa concrete. It was concluded from this study that no matter what type of ties was used (steel or GFRP) and for the same reinforcement ratio, replacing the steel longitudinal bars with GFRP bars reduced the load carrying capacity by 13%. In addition, replacing the steel ties with GFRP ties reduced the load carrying capacity by 10%, regardless of what type of longitudinal bars was used, but had no effect on the load-displacement relationship up to about 80% of the ultimate load.

Lotfy (2010) examined the axial behaviour of square RC columns reinforced with FRP bars. All the columns had square dimensions of 250 mm x 250 mm x 1250 mm and were longitudinally reinforced with steel and three GFRP reinforcement ratios (0.72%, 1.08% and 1.45%). The transverse reinforcement for all the columns was kept the same with 6 mm steel stirrups at 120 mm spacing provided. The concrete compressive strength varied for the columns (25 MPa, 30 MPa and 35 MPa). This study concluded that the initial cracking loads, ultimate strain and ultimate load of the GFRP RC column were 1.17, 1.17, 1.18 times, respectively the corresponding values achieved for the steel RC column of similar reinforcement ratio of 0.72% and concrete strength of 25 MPa. In addition, the ductility of the concrete columns improved with the increase in the longitudinal GFRP reinforcement ratio and had a great influence on the initial cracking load, ultimate strain and ultimate load.

De Luca et al. (2010) carried out an experimental program to investigate the impact that the compressive behaviour of longitudinal GFRP bars has on the column behaviour. In addition, the importance of GFRP ties in confining the internal core of concrete and prevention of the buckling of the longitudinal reinforcement was investigated. A total of five full-scale square concrete columns (610 mm x 610 mm x 3050 mm) were tested under axial loading and were designed as stocky to ignore slenderness effects and with a nominal concrete compressive strength of 35.4 MPa. All the columns had a longitudinal reinforcement ratio of 1% but had varying tie spacing of 305 mm and 76 mm for the GFRP RC columns. The GFRP ties were made by assembling pairs of C-shaped bars. It was found that the behaviour of GFRP RC columns was comparable to steel RC columns for the longitudinal reinforcement ratio provided and no significant difference in peak capacity was observed. It was also concluded that for pure compression, the same reduction factors for conventional steel can be adopted for GFRP bars. Also, the average load carrying capacity of the GFRP longitudinal bars varied between about 2.9% and 4.5% of the peak load as compared to a value of 11.6% for the steel longitudinal bars. These results were based on assuming the GFRP bar's modulus of elasticity in tension to be similar to that in compression. Therefore, they suggested ignoring the contribution of GFRP bars when assessing the load carrying capacity of RC columns loaded axially. The Poisson's ratio of the specimens was also investigated. In relation to the shear reinforcement, it was found that the steel RC columns behaved similar to the GFRP RC counterpart. In summary, it was found that utilising smaller tie spacing did not increase the peak capacity of the columns but instead changed the failure mode and improved the ductility.

Tobbi et al. (2012) experimentally investigated the compressive performance of concrete columns reinforced longitudinally with GFRP or steel bars and transversally with GFRP ties of different configurations. The concrete compressive strength at 28 days was obtained to be 32.6 MPa. Axial compression tests on eight full-scale columns all with square dimensions of 350 mm x 350 mm x 1400 mm were carried out. The GFRP RC columns were designed with four different tie configurations and with tie spacing of 80 mm and 120 mm. From the test results, the authors realised that the contribution of the GFRP bars to the total capacity of the column was 10%, which was close to the contribution of steel bars towards the column capacity of 12%. Based on the stress-strain relationship, it was found that at the first peak load, the strain of the ties was lower than 10% of its ultimate strain. After the concrete cover spalled, the strain in the lateral reinforcement considerably increased with the specimens that were well confined reaching a second peak load. At this second peak load, the strain in the ties for the specimens well confined and lightly confined reached 55% and 70% of its ultimate tensile strain, respectively. An increase in concrete column strength of more than 20% resulted when the tie spacing was reduced from 120 mm to 80 mm.

Pantelides et al. (2013) investigated the structural behaviour of ten concrete columns of circular cross-section having diameters of 254 mm and height of 711 mm. The concrete compressive strength at the first day of testing was 36 MPa. A total of four columns were transversally reinforced with steel helixes and six of the columns were reinforced with GFRP helixes. Some of the columns were reinforced with longitudinal steel bars and others were reinforced with GFRP bars. The columns with steel longitudinal bars and GFRP helixes achieved a load capacity of 87% of the axial capacity of the column reinforced with steel bars and steel helix. Similarly, the columns reinforced with GFRP helixes and GFRP bars achieved a load capacity of 84% of the column reinforced with steel bars and steel helixes. In addition, expressions were proposed to predict the load carrying capacity of the experimentally tested columns based on the confinement stress given by the internal GFRP helixes. Also, it was shown that the expressions predicted the axial load capacity for the columns reinforced with GFRP helixes and GFRP bars as being 87% of the experimental axial column capacity.

Afifi et al. (2014) explained an experimental study on twelve circular columns having a diameter of 300 mm and height of 1500 mm tested under concentric axial loads. The compressive strength of concrete at the first day of testing was 42.9 MPa. The columns were reinforced with GFRP bars longitudinally and GFRP helixes transversally. It was found that the steel and equivalent GFRP RC columns performed in a similar fashion. However, compared with the axial capacity of the steel RC columns, the respective axial capacities of GFRP RC columns were on average 7% lower. Having said this, the longitudinal GFRP bars were able to carry an average load that was between 5% and 10% of the maximum load. It was reported that the ductility can better be enhanced by utilising small GFRP helixes at a closer spacing instead of using GFRP helixes of larger diameters at a higher spacing. Similar to Tobbi et al. (2012), the authors established that neglecting the compressive contribution of the GFRP bars when determining the axial load capacity underestimates the maximum capacity of the experimentally tested columns.

Mohamed et al. (2014) tested fourteen circular concrete columns under concentric axial loading having a height of 1500 mm and diameter of 300 mm. The compressive strength of concrete at the first day of testing was 42.9 MPa. The columns were longitudinally reinforced with steel, GFRP and CFRP bars and were provided with circular FRP helixes or hoops for confinement purposes. It was found that at the peak load, the GFRP bars had reached a value of about 15% of their ultimate tensile strain, while the steel bars had reached their yield point. In terms of the peak load, the steel bars contributed to 15% of this load, whereas the contribution of the GFRP bars was 5% to 10% while the same value for the CFRP bars was 6% to 19%. As a result of the CFRP bars low bending capacity, these bars failed before buckling. Also, it was established that circular FRP hoops were as effective in providing confinement to the concrete as compared to helixes.

Tobbi et al. (2014) experimentally investigated the compressive performance of twenty square columns (350 mm x 350 mm x 1400 mm) tested under concentric axial loading. The 28 day target concrete compressive strength was 30 MPa. The study included test variables such as the longitudinal GFRP reinforcement ratio, transverse GFRP reinforcement configuration, material type and spacing as well as the confining volumetric stiffness. It was stated that the ultimate axial strain of columns reinforced longitudinally with FRP is about 30% lower than their steel counterparts. Also, confinement efficiency of FRP transverse reinforcements that are closed which are cut from square helixes is higher than C-shape type ties. Therefore, the most important factor for the confinement efficiency in GFRP reinforced columns is the configuration of the FRP transverse reinforcement. Furthermore, the ultimate compressive axial strain for columns with longitudinal and transverse FRP bars can reach values similar to the FRP ultimate tensile strain of the bars if proper confinement is provided.

Karim et al. (2016) tested five column specimens of circular cross-section having a diameter of 205 mm and height of 800 mm subjected to concentric axial loads. The average compressive strength of the concrete at 28 days was 37 MPa. Two specimens were reinforced with GFRP bars and GFRP helixes while two specimens were reinforced with only GFRP helixes. Moreover, one specimen was wrapped with CFRP sheets for confinement purposes. The longitudinal reinforcement used was bars of 12.7 mm diameter while the transverse reinforcement was helixes of 9.5 mm diameter with the spacing being either 30 mm or 60 mm. The effects of confinement of the specimen using CFRP sheets and reducing the GFRP helixes spacing were studied. Furthermore, the axial-load against axial deformation performance of the experimentally established columns was developed by using an analytical model. This was achieved by superposing the load-deformation behaviour of the various constituents of the members. It was found that the axial load-axial deformation curves obtained experimentally and analytically agree reasonably well. In summary, the GFRP reinforced columns were able to achieve two axial peak loads, with the introduction of the longitudinal GFRP bars improving these two peak loads. Furthermore, the confinement of the specimens with CFRP sheets and the reduction in the spacing of helixes caused an improvement in the strength and ductility of the specimens.

3.4.1.2 Axial Load Capacity

When exposed to a concentric load (e = 0) a column shortens uniformly with increasing load. ACI 318-14 (ACI 2014) states that the longitudinal strains in the reinforcement and concrete are equal at all stages of loading. For a conventional steel reinforced column subjected to concentric loading, ACI 318-14 (ACI 2014) also expresses the axial load capacity as follows:

$$P_o = 0.85 f_c'(A_g - A_{st}) + f_{sy} A_{st} \tag{3.2}$$

where f_c' is the concrete compressive strength; A_g is the gross sectional area of concrete; A_{st} is the total area of steel longitudinal reinforcement; and f_{sy} is the yield strength of the longitudinal reinforcement.

In terms of FRP RC columns, the current American guide, ACI 440.1R-15 (ACI 2015) states the contribution of FRP bars should be neglected when used as reinforcement in columns. Similarly, the Canadian standard, CSA S806-2012-R2017 (CSA 2012-R2017) allows the utilisation of FRP bars as longitudinal reinforcement in axially loaded columns only, but neglects the FRP bars' compressive contribution when calculating the ultimate axial capacity, as shown in Equation 3.3.

$$P_o = \alpha_1 f_c'\left(A_g - A_f\right) \tag{3.3}$$

where $\alpha_1 = 0.85 - 0.0015 f_c' \geq 0.67$; and A_f is the total cross-sectional area of the longitudinal GFRP bars.

Based on the literature, other equations have been proposed to calculate the nominal axial capacity of GFRP RC columns. Alsayed et al. (1999) suggested a formula to determine the compressive load capacity of GFRP RC columns by reducing the ultimate tensile strength of the GFRP bars by 60% as follows:

$$P_o = 0.85 f_c'\left(A_g - A_f\right) + 0.6 f_{fu} A_f \tag{3.4}$$

where f_{fu} is the GFRP bars ultimate tensile strength.

Tobbi et al. (2012) showed that the maximum axial capacity of GFRP RC columns is underestimated using Equation 3.3 when ignoring the compressive contribution of the GFRP bars. Therefore, the GFRP bars' compressive contribution to the overall capacity of the columns was taken into account. This was done by considering the compressive contribution of the GFRP bars to be 35% of the tensile strength, which was recommended by Kobayashi and Fujisaki (1995), as shown in Equation 3.5.

$$P_o = 0.85f_c'\left(A_g - A_f\right) + 0.35f_{fu}A_f \tag{3.5}$$

On the other hand, Tobbi et al. (2014) proposed an equation to calculate nominal axial capacity where the compressive contribution of the GFRP longitudinal bars is calculated based on the elastic theory and from the material properties as shown in Equation 3.6.

$$P_o = 0.85f_c\left(A_g - A_f\right) + \varepsilon_o E_f A_f \tag{3.6}$$

where ε_o is the strain of concrete at peak stress (as defined by ACI 318-14 (ACI 2014) is equal to 0.003).

Similarly, Mohamed et al. (2014) proposed the same equation as Tobbi et al. (2014) as shown in Equation 3.6, but instead of ε_o, the strain was expressed as ε_p which was equal to strain limit at the beginning of micro-cracks in the plastic stage of concrete. The value of ε_p was expressed as 0.002. In this equation, the FRP bars gain in strength after ε_p was reached, was not taken into account, which would provide a conservative prediction. The relationship of the experimental to predicted maximum axial load utilising a strain of 0.002 were between 1.05 and 1.12 for the GFRP RC columns and between 0.99 and 1.09 for the CFRP RC columns (Mohamed et al. 2014).

3.4.1.3 Failure Mechanism

The failure mechanism of GFRP RC columns under concentric loading has been investigated by the studies mentioned above.

De Luca et al. (2010) reported that the steel RC columns behaved similar to the GFRP RC counterpart and the failure modes were strongly influenced by the spacing of the ties. The GFRP ties spaced at 76 mm did not increase the axial capacity, but greatly influenced the failure mode of the columns. This small tie spacing delayed the instability of the longitudinal bars, delayed the commencement and propagation of cracks and the crushing of internal core of concrete. However, the failure mode of the GFRP RC columns with ties spaced at 305 mm was brittle in nature with the strength instantly dropping without cracking or early warning after the peak load was reached. In summary, the failure of the steel RC column occurred as a result of the longitudinal reinforcement buckling, whereas the failure mode of the GFRP RC columns was categorised by the crushing of the internal core of concrete. This concrete core crushing occurred at higher axial strains as compared to the same values obtained in the steel RC column. After the concrete cover spalled, the paired C-shaped GFRP stirrups become only partly effective in confining the core of the concrete and a closed - loop stirrup was recommended by the researchers.

Tobbi et al. (2014) tested GFRP RC columns designed with four different tie configurations with varying tie spacings of 80 mm and 120 mm. From the experimental results, it was seen that the failure mode of the longitudinal GFRP bars was governed by the tie spacing. The smaller tie spacing resulted in the rupture of the longitudinal bars, whereas larger tie spacing caused the buckling of the bars. It was concluded that reducing the tie spacing from 120 mm to 80 mm produced an improvement in the axial load capacity of 20%. Furthermore, the ultimate axial strain of the FRP RC columns was approximately 30% lower than the value achieved for the respective columns reinforced with steel.

Pantelides et al. (2013) found that the failure mode of columns reinforced with steel bars and steel helixes were by the buckling of the longitudinal steel bars. Also, the failure mode of the columns reinforced with steel bars and GFRP helixes was due to the steel bars' buckling and the GFRP helixes rupturing in tension. On the other hand, the columns provided with GFRP bars and GFRP helixes failed by the buckling and compressive rupture of the longitudinal bars and the rupture in tension of the helixes.

Afifi et al. (2014) stated that the initial region of the stress-strain response up to the maximum peak load or onset of concrete cover spalling was similar for the steel and GFRP RC columns. At 85% to 95% of the peak loads, the onset of vertical hairline cracks appeared on the columns. The steel RC columns' maximum axial load was 8% higher than their GFRP RC columns' counterparts. The GFRP bars' average axial strain at the maximum load was 15% of the tensile ultimate strain. Furthermore, the steel bars' average axial strain at maximum load was close to the strain at yield. Also, at this maximum load, steel and GFRP stirrups confinement effect had not yet been triggered. After the concrete cover spalled, the confining restraint of the GFRP helixes was activated with the strain increasing progressively to more than 80% of its tensile ultimate strain. In summary, from observation it was determined that the failure mode of the GFRP RC columns having large helix spacings (120 mm and 145 mm) were governed by the longitudinal bars' buckling whereas the failure of the specimens with smaller to moderate helix spacings (40 mm to 80 mm) was controlled by the concrete core crushing and helixes rupturing. Interestingly, the two well-confined RC columns experienced a second peak load. The location of the rupture of the GFRP helixes was at the intersections with the longitudinal bars. After crushing of the concrete core, a single inclined shear sliding surface occurred and this resulted in the axial capacity reducing rapidly for the columns.

Mohamed et al. (2014) reported two different failure modes for the fourteen GFRP and CFRP RC columns tested. The steel and GFRP reinforced columns failure mode was ductile and was characterised by the concrete covers' gradual spalling, followed by the buckling of the longitudinal bars and followed by the rupturing of the hoops or helixes. In contrast, the failure mode of the CFRP reinforced columns was brittle and sudden in nature which was comparable to the failure of the plain concrete columns. Furthermore, it was observed that the failure mechanism of the GFRP reinforced columns designed using a small volumetric of 0.7% were dictated by the longitudinal bars' buckling due to the insufficient confinement of the GFRP helixes. However, for the GFRP RC columns which were well confined having volumetric ratios of 1.5% and 2.7%, the failure was controlled by concrete core's crushing and helixes rupturing. The large confinement developed by the GFRP helixes resulted in a higher post peak axial deformation in these specimens due to the restraint of the longitudinal bars from buckling by the helixes. Finally, the CFRP reinforced columns failed prior to the buckling of these bars as a result of the low bending capacity of the CFRP bars.

Tobbi et al. (2014) investigated GFRP RC columns that were reinforced laterally with four different GFRP reinforcement configurations. The failure modes were controlled by the configuration, shape, and diameter of the transverse reinforcement, along with the type of longitudinal bars. By observation it was seen that the failure of all the longitudinally and transversally GFRP RC columns was the result of the longitudinal bars' crushing or buckling. In summary, the columns transversally reinforced with C-shaped GFRP ties experienced a failure mode which was brittle. In these columns, the slipping of the outer C-shaped transverse ties at the splice location developed caused by the pressure of the expanding core of concrete which led to the degradation of the load until the crushing of the longitudinal GFRP bars. On the other hand, the columns with the closed ties failed progressively due to the successive crushing of the longitudinal GFRP bars before the onset of concrete core crushing. In summary, the failure modes for the columns were categorised by first the buckling or crushing of the longitudinally positioned bars and then followed by rupture of the transverse reinforcement.

3.4.2 Existing Studies on Eccentric Loading

In reality columns are not subjected to perfect concentric loading but are influenced by a combination of axial compression loads and bending moments (Hadi 2006). Even for columns nominally carrying only axial compression load, bending moments always exist. These bending moments are introduced by unintentional load-eccentricities and by out-of-straightness of the constructed column (Warner et al. 2007). Consequently, it is essential to understand the behaviour and performance of FRP RC columns subjected to eccentric loading.

3.4.2.1 Longitudinal and Transverse Reinforcement

Kawaguchi (1993) conducted an experimental study of twelve concrete specimens reinforced with AFRP bars. The cross-section of the specimens was rectangular (150 mm x 200 mm) and were reinforced with four 12 mm sand coated aramid bars. The target strength of concrete was 39.2 MPa. The specimens were tested in eccentric compression or tension. It was established that depending on their reinforcement ratio and material properties, the balance AFRP reinforcement for eccentric compression was 0.2%. Furthermore, reducing this ratio would result in the failure of the columns by the rupture of the AFRP bars. Furthermore, this study stated that the AFRP reinforced columns can be analysed using the same approach undertaken for concrete columns reinforced with steel bars.

Mirmiran (1998) and Mirmiran et al. (2001) studied slender FRP RC columns reinforced with FRP bars by assuming a deflected shape of a cosine wave of such columns. The authors recommended that in non-sway frames, the slenderness ratio for columns reinforced with FRP bars of low stiffness as compared with steel, should be reduced from 22 as reported in ACI 318-11 (ACI 2011), for columns bent in single curvature and having end moments that are equal, to 17 for concrete columns reinforced with FRP bars. Therefore, it was stated that FRP bar reinforced columns are more prone to length effect than equivalent steel reinforced columns. This is the case because FRP bars have lower modulus of elasticity as compared to steel bars. It was also suggested reducing the slenderness limits by 22% for GFRP, 5% for AFRP and 15% for CFRP bars, if the minimum reinforcement ratio is kept at 1%.

Choo et al. (2006a) developed an analytical method to study the axial load-moment curvature relationships of FRP RC columns and studied the slenderness effects of these columns by applying a numerical integration procedure. The numerical procedure was used to obtain the lateral displacements of the columns. This study reported that unlike steel reinforced columns, FRP reinforced columns' interaction diagrams do not experience balance points because of the linear elastic material properties of the FRP bars until rupture. In addition, it was reported that neglecting the FRP longitudinal bars' compressive contribution when developing the strength interaction diagrams is a conservative approach. However, compressive failure must be prevented by checking that the strain in the compressive bars does not reach the ultimate strain.

Issa et al. (2012) investigated the behaviour of steel and GFRP RC columns exposed to axial eccentric loading. A total of six columns were tested, four of which reinforced with GFRP longitudinal bars and two reinforced with steel longitudinal bars. The columns were square in cross-section (150 mm x 150 mm) and were all reinforced with steel ties of 8 mm diameter and spaced at either 80 mm or 130 mm. Two different concrete strengths were used for the GFRP RC columns (24.73 MPa or 38.35 MPa) with the steel RC columns having strength of 24.73 MPa. The eccentricity was either 25 mm or 50 mm. It was concluded that the average maximum stress was about 60% of the compressive strength of the columns with initial eccentricity of 50 mm. Furthermore, the recorded longitudinal deformations for the GFRP reinforced columns and for columns with large tie spacing were large. However, it was reported that the maximum lateral deflection and ductility of GFRP RC columns were not notably affected by the tie spacing.

Zadeh and Nanni (2013) presented a numerical analysis on short and slender GFRP reinforced columns subjected to combined flexural and axial load. By assuming that the longitudinal GFRP bars are effective only in tension, interaction diagrams were established. Therefore, an equivalent area of concrete replaced the compression GFRP bars. Furthermore, the authors suggested imposing a maximum design tensile strain limit of 1% for GFRP longitudinal bars, in order to avoid exaggerated deflections due to the high tensile rupture strains of such bars.

Xue et al. (2014) tested a total of seven concrete columns reinforced with GFRP bars under static eccentric loading. The columns had a constant square cross section of 300 mm and were longitudinally reinforced with GFRP bars and transversely reinforced with steel stirrups. The mechanical behaviour of the columns was investigated based on the primary experimental parameters of eccentricity, reinforcement ratio and nominal slenderness ratio. From the results of this study, it was found that increasing both the eccentricity and slenderness ratio of the columns, decreased the ultimate load and increased the lateral displacements under the same load.

Hadi et al. (2016) experimentally tested twelve circular concrete specimens under concentric and eccentric loading conditions. The sections had a diameter of 205 mm and were 800 mm in height. The average compressive strength of concrete at 28 days was 37 MPa. This study investigated the influence of replacing steel longitudinal and transverse reinforcement with GFRP reinforcement. The transverse reinforcement for all the specimens were helixes and the effect of changing the helixes spacing from 60 mm to 30 mm for the GFRP reinforced specimens was examined. From the test results it was concluded that for the same loading conditions, the load carrying and bending moment capacities obtained for the GFRP reinforced columns were lower than the same values determined for the steel reinforced columns. Having said this, the GFRP RC specimens achieved a slightly greater ductility as compared to the equivalent steel RC specimens. Furthermore, using the similar principles as used for typical steel reinforced members, axial load and bending moment diagrams were analytically determined for members reinforced with GFRP bars. It was realised that neglecting the compressive contribution of the GFRP bars would result in large discrepancies between the analytical and experimental results.

3.4.1.2 Failure Mechanism

The failure mechanism of GFRP RC columns under eccentric loading has been investigated by the studies mentioned in the above sections.

Kawaguchi (1993) observed that the eccentrically loaded GFRP reinforced columns' failure mode was attributed to the crushing of the concrete in the compression region with no occurrence of the rupture of the GFRP bars. Furthermore, in the compression zone the ultimate strain of concrete was reported to be between 0.004 and 0.005.

Choo et al. (2006a) analytically studied the axial load-moment curvature relationships of FRP RC columns by applying a numerical integration procedure. Based on their findings it was reported that FRP reinforced columns have a tendency to exhibit a failure point prior to the strength interaction reaching a pure bending condition, which is categorized as brittle-tension failure. In other words, the failure is a result of the tensile rupture of the FRP bars at which the ultimate strain in the outermost tensile reinforcing bar layer is reached at or before the concrete reaches its limiting ultimate strain in compression of 0.003. They reported that this failure occurs when low reinforcement ratios are considered and hence the reinforcement ratio limits outlined for steel RC columns may not be applicable to FRP RC columns. To avoid the FRP bars in the tension side failing in tension, Choo et al. (2006b) presented equations to determine the minimum FRP reinforcement ratio to prevent this phenomenon for rectangular columns subjected to pure bending.

Xue et al. (2014) tested a total of seven concrete columns reinforced with GFRP bars under static eccentric loading. It was stated that all the seven concrete columns reinforced with GFRP failed in the similar failure mechanism, which were categorized by the crushing and spalling of concrete in the compression zone at the mid-height of the columns. Furthermore, in the compression zone the longitudinal GFRP bars' buckled while in the tension zone the bars did not rupture.

Hadi et al. (2016) reported that the concentrically loaded GFRP reinforced specimens failed by GFRP helixes rupturing which was then followed by the buckling and crushing of the longitudinally placed GFRP bars and internal core of concrete. However, the failure mode of the specimens subjected to eccentric loading was in the compression side due to the concrete crushing in that area. It was realised that the horizontal cracks spacing on the tension side of the steel RC specimens was about 6.3% smaller than the same value obtained for the equivalent GFRP reinforced specimens. In addition, the cracks' spacing for the specimens having a GFRP helix of 30 mm pitch was approximately 15.6% smaller than the specimens reinforced with a GFRP helix of 60 mm pitch.

3.5 Concrete Beams Reinforced with FRP Bars

Design guidelines for flexural concrete structures reinforced with FRP bars have been developed across the world in Japan (JSCE 1997), Canada (CSA-S806-2012-R2017), USA (ACI 440.1R-15 2015) and Europe (CNR-DT203 2006). Despite the differences between steel and FRP bars, the design philosophy of FRP reinforced flexural sections is established on the same assumptions for steel reinforced sections. In reference to ACI 440.1R–15 (ACI 2015), these assumptions are as follows: (1) a perfect bond exists between the reinforcement and concrete; (2) linear strain distribution occurs over the cross-sections; (3) the maximum usable compressive strain in the concrete is 0.003; (4) the concretes' tensile strength is ignored and; (5) the tensile behaviour of the FRP reinforcement until failure is linearly elastic.

The flexural design philosophy for steel RC sections is to make sure yielding of the steel occurs before the concrete crushing to allow for a tension-controlled behaviour. This ensures good ductility and warning signs of the member's failure. However, the non-ductile behaviour of the FRP reinforcement requires a modification to this methodology. The rupture of the FRP reinforcement will result in a sudden and brittle failure (Nanni 1993b; and Theriault and Benmokrane 1998). However, this tension controlled behaviour would result in extensive cracking and large deflections due to the material properties of the FRP reinforcement which would show warning signs before failure. However, the ductility of such members would be less than the ductility of tension controlled steel RC members. Therefore, for FRP reinforced members a compression-controlled behaviour is marginally more desirable (Nanni 1993b). This will ensure the crushing of concrete occurs before the rupture of the FRP reinforcement and thus the member would experience some inelastic behaviour before failure. In summary, both the tension and compression controlled sections are acceptable in the design provided that the serviceability and strength criteria are satisfied (ACI 440.1R–15 2015).

Extensive research has been undertaken to understand the behaviour of flexural concrete members reinforced with FRP bars. These experimental studies examined the influence of the reinforcement ratios, concrete strengths and types of FRP bars on the flexural strength and performance of flexural members reinforced with FRP bars. Some of the studies are discussed herein.

3.5.1 Existing Studies of Concrete Beams Reinforced with FRP Bars

Benmokrane et al. (1996) investigated the flexural behaviour of concrete beams reinforced with FRP bars under four-point bending. The beams had a constant width and simply supported span of 200 mm and 3000 mm, respectively, but had varying depths of 300 mm and 550 mm. For each depth, the beams were reinforced GFRP bars and were compared with steel reinforced conventional beams of the same dimensions. All the beams were reinforced with the same amount of GFRP or steel bars in the tension and compression zones for comparison purposes. The results from this study indicated that the experimental ultimate moment capacity obtained for the GFRP and steel reinforced beams of 300 mm depth were similar. However, for the beams with 500 mm depth, the experimental ultimate moment capacity obtained for the GFRP reinforced beams was approximately 8% greater than those obtained for the steel reinforced beams. In addition, the failure of the specimens was governed by tension for under reinforced beams or by compression due to the concrete crushing for the over reinforced beams.

Theriault and Benmokrane (1998) tested twelve concrete beams (130 mm x 180 mm x 1800 mm) reinforced with GFRP bars subjected to four-point bending. The beams were cast with two reinforcement ratios and three different concrete strengths (normal, high and very high strengths). Each type of specimen was duplicated. It was concluded that the effect that the concrete strength and reinforcement ratio has on the crack spacing is insignificant. Also, the tested beams' stiffness remained the same regardless if the beams were tested cyclically or monotically with no loss in flexural stiffness occurring in cyclic loading. Furthermore, it was observed that as the reinforcement ratio and concrete strength increased, the beams' ultimate moment capacity also increased. On the other hand, this increase is restricted by the concrete's compressive strain at failure for the over-reinforced beams.

Kassem et al. (2011) studied the behaviour and serviceability performance of twenty four concrete beams reinforced with CFRP, GFRP and AFRP bars tested under four-point bending. The dimensions of the beams were rectangular having a width of 200 mm, depth of 300 mm and length of 3300 mm. The average compressive strength of concrete at 28 days was 40 MPa. For each type of bar, two different surface textures were investigated, which were sand coated and ribbed-deformed bars. According to the experimental results it was realised that at the service load for the GFRP RC beams, a reduction of 27% for the beams with GFRP sand-coated bars and 20% for the beams using GFRP ribbed bars was observed due to an increase of 33% in the reinforcement ratio. Moreover, in terms of the crack widths for the GFRP RC beams, the value decreased by 32% as a result of a 33% increase in the reinforcement ratio. In summary, it was realised that the sand coated bars experienced better bond as compared to the ribbed-surface bars.

El-Nemr et al. (2013) studied the influence of the concrete strength and FRP reinforcement ratio on the flexural behaviour of concrete beams. Fourteen concrete beams of 200 mm x 400 mm x 4250 mm in width, depth and length, respectively were subjected to four-point bending. The beams were cast with two types of concrete strengths, which had target strengths of 30 MPa (normal strength) and 65 MPa (high strength) and were provided with different types and ratios of GFRP reinforcement. For normal strength concrete beams the increase in reinforcement ratio from 0.36% to 1.47% and 0.55% to 1.78%, resulted in an increase of the specimens' ultimate load by 143% and 224%, respectively. In addition, for high strength concrete beams the increase in reinforcement ratio from 0.36% to 1.47% and 0.55% to 1.78%, caused an improvement of the specimens' ultimate load by 28% and 116% respectively. Therefore, for the same increase in reinforcement ratio, the ultimate load capacities of normal strength concrete beams increased approximately twice as much as the values obtained for the high strength concrete specimens. Interestingly, all the beams showed typical bilinear behaviour until failure and both the normal strength and high strength concrete specimens experienced reduced stiffness after cracking and similar behaviour until failure. For the same axial stiffness provided, the post cracking flexural stiffness of the concrete specimens with high strengths were higher than that of the specimens with the normal strengths.

Ascione et al. (2014) designed and tested six concrete beams reinforced with FRP which were tested under four-point bending. Three beams were reinforced with GFRP longitudinal bars only and the other three beams were reinforced with GFRP longitudinal bars and stirrups. It was reported that the three beams with shear reinforcement experienced three different failure mechanisms. The first beam reinforced with stirrups failed due to the failure of the stirrups in the bend corner. The second beam failed in bending due to the shear failure of the longitudinal bars and the crushing of concrete while the third beam experienced shear compression failure due to the crushing of the concrete.

Adam et al. (2015) tested ten beams reinforced with GFRP bars having rectangular cross sections (120 mm x 300 mm x 2800 mm) exposed to four-point bending. The two factors investigated were the strength of concrete and ratio of the reinforcement. It was observed that the ultimate load improved by 47% and 97% as the ratio of reinforcement increased from the balanced reinforcement ratio to a value equal to 2.7 multiplied by the balanced reinforcement ratio. Moreover, increasing the compressive strength of concrete from 25 MPa to 45MPa reduced the crack width by 52%. On the other hand, increasing the compressive strength from 25 MPa to 70 MPa resulted in the crack width decreasing by 80%. According to the failure mechanism, the GFRP reinforced beams which had reinforcement higher than the balanced reinforcement ratio failed by compression failure due to concrete crushing. On the other hand, the beams provided with a ratio lower than or approximately equal to the balanced ratio failed by the rupture of the GFRP reinforcement.

3.5.2 Ductility

The main disadvantage of RC members reinforced with FRP bars is the typical brittle and sudden failure of the material, supplemented by inadequate ductility. The limited ductility of these members under bending is a result of the FRP bars' linear elastic behaviour. As opposed to steel, FRP bars do not experience a yield point and the modulus of elasticity is relatively low. Therefore, improving the ductility capacity of FRP RC members has been the aim of many researchers.

Among many studies performed to improve the ductility of FRP RC members, four techniques have shown to have positive results. The first technique is to combine the application of FRP and steel bars. Lau and Pam (2010) demonstrated that by adding a certain amount of steel reinforcement in FRP RC beams, the ductility could be increased due to the significant inelastic deformation resulting from the steel bars yielding. Similarly, Leung and Balendran (2003) demonstrated that the post-yielding behaviour is improved since the GFRP bars become progressively important after the yielding of steel bars and it was realised that the pre-yielding load-deflection curves for both combined FRP-steel and steel reinforcement arrangements were similar.

Another technique is the use of hybrid FRP rods that combine the properties of different FRP materials in order to simulate the inelastic behaviour of steel bars. Etman (2011) indicated that using hybrid FRP bars can result in an increase in the flexural capacity and ductility of FRP RC members. However, the manufacturing process of these hybrid rods is very expensive and to date such work have resulted in limited practical developments. The third approach is to improve the concretes' performance, because the ductility of over RC members relies substantially on the engineering properties of concrete. Wang and Belarbi (2005) demonstrated that by adding discontinuous fibres into concrete, the ductility of FRP RC members are improved.

The last technique involves encasing structural sections into FRP RC concrete members in order to take advantage of the ductile behaviour of the structural sections. Li et al. (2012) proposed a new type of FRP RC encased steel composite beams consisting of a ductile structural I-section encased in FRP RC beams. The peak bending moment capacity, ductility and energy absorption of the steel encased FRP reinforced beam was 1.63, 2.38 and 2.49 times, respectively, that of the values obtained for the beam only reinforced with GFRP bars. The tested reference beam with only GFRP bars failed in a brittle manner as a result of the sudden fracture of the tensile GFRP bars, whereas the proposed beams with encased steel I-sections experienced a more ductile behaviour due to the favourable residual strength of the I-section after the crushing of concrete. From their results it was concluded that the encased reinforcement system enhanced the ductility of the FRP RC beams. Similarly, Kwan and Ramli (2013) demonstrated the improvement in ductility of a composite concrete beam consisting of an encased pultruded structural I-section.

3.6 Summary

The use of reinforcement with FRP composite materials have emerged as one of the alternatives to steel reinforcement for concrete structures prone to corrosion issues. In the last decade, there has been extensive research on the flexural and shear behaviour of concrete members reinforced with FRP bars. Therefore, the level of understanding of the flexural behaviour of FRP RC beams has reached a stage where design standards and guidelines around the world have been developed for the design of these members, including ACI 440.1R-15 (ACI 2015).

On the other hand, the level of understanding of the behaviour of FRP reinforced compression members has not reached a level where design standards are available for such members. Having said this, the current ACI 440.1R-15 (ACI 2015) design guideline mentions to neglect the compressive contribution of FRP reinforcement when used as reinforcement in columns, in compression members, or as compression reinforcement in flexural members. Given the lack of experimental data about FRP reinforcement in compression members, it is important to fully understand and investigate further the compression behaviour of concrete columns internally reinforced with GFRP bars for these members to be used in construction.

Furthermore, most of the findings of studies investigating FRP RC columns have been reported based on testing under concentric loading, whereas only a few studies presented investigations of columns subjected to eccentric loading. In reality, perfect axial concentric loading of columns does not exist because of the introduction of bending moments caused by geometric imperfections or eccentricities. Consequently, the behaviour, performance and failure modes of FRP RC columns subjected to eccentric loading must be studied further to allow engineers to have confidence in using these members in structures.

The next chapter provides an overview of pultruded GFRP structural sections. The mechanical properties of these GFRP sections are first discussed followed by their typical applications in civil engineering. A review of the associated literature about hybrid composite columns and beams reinforced incorporating GFRP materials is then explained followed by a summary of the available design guidelines for pultruded GFRP sections.

4 OVERVIEW OF PULTRUDED FRP STRUCTURAL SECTIONS

4.1 Introduction

In recent times, the cost associated with maintaining and strengthening structures made from conventional materials such as steel reinforced concrete (RC) members or steel members have been rising substantially. In addition, there has been a very big demand for faster and lighter construction. As a consequence, FRP pultruded sections are becoming a competitive option as structural materials, offering many advantages when compared with traditional materials, including lower self-weight, improved durability under aggressive environments, low maintenance costs, easier installation and the possibility of being fabricated into any cross-sectional shape.

This chapter presents a thorough review of the use of pultruded FRP structural sections in construction, their mechanical properties and available studies of hybrid structural concrete members incorporating FRP materials including FRP sections and tubes.

4.2 Overview of the use of Pultruded FRP Structural Sections in Construction

FRP composites can be manufactured using a variety of techniques. The common process to manufacture FRP structural sections is by pultrusion which is a continuous, economical and automated technique that can produce FRP structural sections of any length. In this process, raw fibres are first pulled through a bath of resin and then through a heated die. The resin impregnated fibres form a polymer matrix that hardens into the shape of the die which forms the structural section. The section is then pulled from the cured end.

Therefore, FRP pultruded sections are available in a wide variety of shapes, including equal angle, channel, I beam, square tube, round tube, and other shapes. Due to their low self-weight, high durability and reduced maintenance costs, FRP pultruded sections are becoming a competitive option for replacing steel as structural materials. Due to the pultrusion manufacturing process, pultruded FRP sections are anisotropic materials having different properties when measured in different directions. The fibres are predominately aligned in the longitudinal direction along the length of the section. Therefore, the properties in the longitudinal direction of the section are different to the properties in the transverse direction.

Gand et al. (2013) provided a thorough review of the structural and civil engineering applications, as well as current developments and research on pultruded FRP closed sections. The computer and electronics industry took the advantage of FRP profiles electromagnetic transparency to construct the first building structures using FRP profiles. This was achieved with the construction of the Electromagnetic Interference test laboratories by using FRP profiles in single-storey gable frames (Bank 2006). Around the world, engineers are continuously trying to develop solutions for the replacement and rehabilitation of infrastructure that is deteriorating.

FRP materials have become an area of substantial interest for the replacement of old timber bridges as they mimic timber performance and are as strong and durable (Van Erp et al. 2006). Most notably, in Australia, there are many bridges constructed from timber. However the hardwoods used in the building of these timber bridges are becoming less available, more expensive and are prone to deterioration over time. In recent years, pultruded FRP sections have been used to either completely replace deteriorated and damaged timber bridge components or provide a complete refurbishment of the whole bridge structure (Wagners 2014).

In 2002, the first fibre composite bridge in Australia was constructed to replace an existing timber bridge constructed in the 1940's. The composite bridge was designed to combine the high compression capacity of plain concrete with the low weight and high tensile strength of FRP. The beams for the bridge were constructed with pultruded GFRP box girders of 350 mm deep, with a 100 mm thick concrete compression flange placed on top of the girders.

The first highway bridge in Australia utilising fibre composites was Taromeo Creek Bridge which was constructed in 2005. This bridge replaced an existing timber bridge and was constructed using RC deck slab resting on pultruded FRP girders which had two spans of 10 meters and 12 meters (Wagners 2014).

In addition, walkway structures and pedestrian bridges constructed from fibre composites are also now common throughout Australia. The Bowman Parade multiuse pedestrian bridge was designed, constructed and installed by Wagners Composite Fibre Technologies (CFT). The pedestrian bridge was 3 spans with a length of 30 meters. The main deck was made up of pultruded FRP sections and the deck included glue-laminated composite sandwich panels (Wagners 2014).

The coastline of Australia is a very corrosive environment which poses serious durability issues on boardwalks, jetties and other marine structures constructed from steel and reinforced concrete. Traditionally hardwood has been used to overcome these issues but recently fibre composites have been preferred as the alternative replacement to steel in corrosive environments. In Brisbane a fibre composite whaler was constructed as part of an 800 meter long floating river walk project to replace an existing whaler constructed from steel and timber. As a result of the harsh aggressive marine environments, these existing whalers would need to be replaced each 10 to 15 years. Considering the projected design life of these whalers' is 100 years, an alternative material was required. Therefore, fibre composites were found to be the ideal replacement for the whaler. Over 100 tonnes of pultruded structural FRP sections were used in this project. Although the composite whalers cost are double the cost of steel and timber, the costs of the composite whalers during the duration of their lifetime are substantially lower (Van Erp et al. 2006).

4.3 Mechanical Properties of Pultruded FRP Structural Sections

The structural behaviour of FRP pultruded profiles is different from the behaviour experienced by conventional materials, such as steel. Unlike steel, FRP pultruded materials fail in a brittle manner and exhibit a linear elastic behaviour until failure (Keller 2001). Typical FRP pultruded sections are normally composed of glass fibres embedded in a vinyl ester or polyester polymeric matrix (GFRP). These pultruded GFRP sections generally have low wall slenderness and in-plane moduli making them particularly vulnerable to local buckling. This buckling behaviour has been analysed by many studies through experimental, analytical and numerical techniques.

Before FRP composite structures incorporating FRP structural sections are constructed and design procedures are implemented, it is essential to understand the mechanical and physical material properties of these composite materials. This section outlines the standard testing methods and related research studies to determine the mechanical properties of GFRP pultruded structural sections in tension and compression. Furthermore, the buckling behaviour of these sections in terms of the available literature is summarised.

4.3.1 Tensile Properties

The tensile properties of pultruded FRP sections are determined according to tensile tests of coupons cut out from the structural section following either the ASTM D638-14 (ASTM 2014b), ASTM D3039-08 (ASTM 2008), and ISO 527-4 (ISO 1997) test methods. The ASTM D638 (ASTM 2014b) test method utilises a flat, width-tapered specimen with a straight sided gage section. Based on the literature, the ASTM D3039 (2008) and ISO 527-4 (1997) test standards are most commonly used by researchers because they allow the use of straight-sided un-tabbed specimens instead of dog-boned or tabbed specimens. Although tabs are not compulsory, tabs are usually used in these two methods. However, the use of tabs may result in stress concentrations at those locations.

The anisotropic nature of these materials requires coupons extracted from both the longitudinal and transverse direction to determine the corresponding tensile properties in those directions. Having said this, most of the pultruded FRP structural sections are too narrow in the transverse direction to allow for the extraction of standard coupons with dimensions as specified by the test standards. Therefore, the determination of the transverse properties of FRP structural sections is not achievable following the test methods. However, a few researchers have tested non-standard coupons with short lengths to determine the transverse tensile properties.

Gosling and Saribiyik (2003) compared the tensile properties from longitudinal standard coupons following the ASTM D3039 test standard (15 mm wide by 250 mm long) and longitudinal non-standard short coupons (10 mm wide by 47.5 mm long).

These longitudinal coupons were extracted from the sides of a GFRP box section. As a result of the reduced gripping area of the short coupon compared to the ASTM D3039 coupon, the bearing stresses acting on the short coupon were eight times higher than the standard coupons which resulted in premature failure of the specimen. Therefore, it was concluded that in the longitudinal direction, the short coupon is not recommended for determining the ultimate strength but is able to determine the elastic material properties. However, in this study the tensile tests of coupons extracted in the transverse direction behaved differently. Non-standard transverse coupons of 10 mm wide and 47.5 mm long (similar to the short longitudinal coupons) were tested in tension. Due to the way the fibres are aligned, the transverse tensile strength of the GFRP is significantly lower than the longitudinal tensile strength. This meant that the axial load required to produce a tensile failure in the transverse coupon did not result in bearing stresses necessary to cause damage to the combined aluminium tabs and GFRP material nor failure of premature nature. Therefore it was concluded that in the transverse direction in the case of failure mode irregularities, the non-standard short coupon can be implemented to determine the elastic modulus of elasticity and strength values.

In addition, Sonti and Barbero (1996) and Cardoso et al. (2014a) also tested transverse GFRP coupons with short lengths of 9.5 mm × 25.4 mm × 88.9 mm and 6.4 mm × 12.7 mm × 88.9 mm, respectively. Correia et al. (2011) determined the tensile properties of pultruded I-beams by preparing coupons from both the web and flanges of the GFRP section. In addition, the compressive, inter-laminar shear and flexural properties of both the webs and flanges were determined and compared. It was observed that there were no noticeable differences in the mechanical properties of the web and flange and it is reasonable to assume the properties of both are identical.

4.3.2 Compressive Properties

The mechanical characterisation of an orthotropic material can be carried out either by experimental testing or from the basis of the classical laminate theory for composites materials (Jones 1999). In terms of experimental testing, there are three main test methods of applying a compression load into a composite specimen (Carlsson et al. 2002).

The first method is by directly loading the ends of the specimen, as indicated for example in ASTM D695-15 (ASTM 2015). This method is the simplest technique for applying a compression load into composites. However, it has been reported that direct end loading is not appropriate for composites with high strengths because the high longitudinal strength and low transverse and inter-laminar strengths of such materials result in the specimens failing prematurely by end crushing (Hodgkinson 2000). Furthermore, the property measured may not be the actual compressive strength but represents the composite bearing strength and the direct end loading of the samples is not suitable to determine the compressive strength (Barbero et al. 1999). This ASTM D695 (2015) guideline is specified for ladder rail standards and is generally utilised for pultruded composites. In addition, the ASTM D695 (2015) guideline does not require reporting the failure modes of the coupons tested, and therefore it may be possible that the data is reported as compressive strengths although premature failure modes, such as end crushing occur (ASTM D695-15 2015).

The simplicity of the ASTM D695 (2015) guidelines, ignoring the associated issues with end crushing, resulted in many researchers examining variations of this method. In summary, these altered test methods are stated as modified ASTM D695 methods. Various groups including Hercules and Boeing developed their own modified versions of ASTM D695 utilising an end-loaded straight-sided coupon with tabs. In general, many of these modified fixtures were developed to avoid the specimens splitting or crushing at the ends by placing restrictions to prevent the lateral expansion of the coupon at the ends (Häberle and Matthews 1994, Mottram 1994, Welsh and Adams 1997, and Tomblin et al. 2001).

The second method to apply a compression load into a composite material is loading the specimen by shear as explained in ASTM D3410-16 (ASTM 2016a). Both the end loading and shear loading methods require coupons having short lengths to prevent buckling.

The third method is introducing the compression load by the combination of end and shear loading as proposed in ASTM D6641-16 (ASTM 2016b). The shared load transfer in this method inherits the best features from the end loading methods (ASTM D695-15) and shear loading methods (ASTM D6641-16) which reduces the risk of slippage and end crushing of the specimen. Xie and Adam (1995) reported that the stress concentrations arising from utilising the combined loading method were lower than those achieved for either the direct end loading or shear loading method.

Hodgkinson (2000) reports on a study developed to test the same composite laminate material of the same batch but at seven different European labs which all tested the compressive properties using their own testing procedures. A total of seven composite laminate materials were tested at each lab. It was shown that in terms of the compressive strength the values were widely scattered with the range of results encompassing a factor of two for almost all of the systems. Furthermore, the test results had a high dependency on the laboratory carrying out the test with some labs generally producing higher values as compared to others for the same range of materials tested. Therefore, the results are dependent on the individual local testing practice (Hodgkinson 2000). This means that a universal standard should be developed rather than different test methods as explained in the literature, to determine the compressive properties of composites. Furthermore, the high dispersion requires more than five specimens per batch to be tested as required by many of the standards, including ASTM D695 (2015).

When comparing the test methods available to determine the compression properties of composite materials, each method should be analysed by its capability of producing failure in compression without developing stress concentrations at the loading ends and load eccentricities, while the global buckling of the specimen is prevented at the same time. Therefore, to achieve all these criteria means that is very difficult to determine the true compressive strength of these materials. Therefore, the true compressive strength is practically of insignificant interest as it is rarely attained in practical applications (Welsh and Adams 1997). Furthermore, there exists no general model that can predict the failure of composites in compression from the properties of the constituents. This is the case because it is difficult to experimentally determine the compressive strength for a given composite system and the mechanisms for activating its compression failure (Hodgkinson 2000).

Therefore, historically the field of mechanical testing of composite materials has not strictly followed a unified set of testing standards. Over the years, well over 17 coupon compression test methods have been developed for composites (Lackey et al. 2007). However, to date, no universally accepted test method has been adopted. In addition to the many test methods proposed for determining the compressive properties of polymeric composites, some research studies have investigated specialised compression test methods and made comparisons of the existing compression test methods for pultruded composites, as discussed herein.

Barbero et al. (1999) determined experimentally the compressive strengths of pultruded structural sections and compared the values obtained by coupon testing utilising a modified ASTM D695 (2015) fixture without the use of tabs. A simple formula was also proposed to determine the compressive strength of full-size structural sections based on the number of rovings in the cross-section.

Saha et al. (2000) tested pultruded composite sheet materials in compression using a short-block compression test fixture to restrict the lateral expansion of the specimens at the ends and prevent splitting or crushing at those locations. It was reported that based on back-to-back strain readings, the bending resulting from non-uniform load introductions were minimized successfully using this test method. Furthermore, uniform strains across the widths of the specimens were noticed during the testing.

Similarly, Mottram (1994) determined the compressive strengths of pultruded E-glass FRP flat sheet material utilising a non-standard test procedure designed to prevent the end crushing of the specimens ends by confining the specimens at these locations. In this study it was reported that due to the large variations in the compression strength of pultruded composites, the ASTM D695 (2015) recommendation of five coupons per batch tested to obtain average compressive properties is too low and more coupons need to be tested.

Guades et al. (2014) investigated the mechanical properties of pultruded FRP tubes. In terms of the compression properties, tests on coupons and full-size specimens were undertaken and the results were validated using finite element analysis. It was found that the compression properties determined by the coupon testing were relatively higher than the results from full-size testing.

Lackey et al. (2007) compared three compression test methods for the determination of the compressive properties of typical commercial pultruded materials such as sheet piling, ladder rail and all unidirectional products. The three test methods were ASTM D695, ASTM D6641 and SACMA SRM-1R-94 (SACMA 1994). The latter test method is a modified ASTM D695 method. It should be noted the two ASTM methods used in this study have now been updated to ASTM D695 (2015) and ASTM D6641 (2016). It was reported that it was more difficult to obtain valid compression test data for unidirectional composites as compared to mat/roving composites. Furthermore, the SACMA SRM-1R-94 (SACMA 1994) and ASTM D6641 achieved very similar results for the sheet piling and ladder rail. However, the results obtained by the ASTM D695 method were more variable than the other two methods. It was also found that the average compressive strength data was significantly lower for the tested ladder rail material as compared to the other test methods. Other studies and reports have stated that the compressive properties data obtained by the ASTM D695 test method is lower than those obtained by other methods (Gedney et al. 1987; Adams and Welsh 1997). It was seen that the achieving a valid failure mode for the stronger unidirectional composites was difficult for the SACMA SRM-1R-94 and ASTM D695 test methods. However, the ASTM D6641 method was capable of ensuring a valid compression failure instead of crushing at the ends as seen for most of the unidirectional samples.

In a continuation of the above study, Lackey et al. (2010) summarised that for both the pultruded composite materials, the measured compressive strength and modulus of elasticity properties obtained by the ASTM D6641 were higher than those obtained by the ASTM D695 test method. Furthermore, the standard deviation for the compressive property measurements was lower for the data from the ASTM D6641 method. Finally, based on the comparison of results and failure modes of pultruded composites using the two methods, and the relative simplicity of the ASTM D6641 method, general agreement was reached that the ASTM D6641 is an appropriate test method to utilize for the first pre-standard for the load and resistance factor design (LRFD) of pultruded FRP structures (ASCE 2010). Therefore, this test method was adopted in this pre-standard document.

4.4 Buckling Behaviour of Pultruded GFRP Structural Sections

Pultruded GFRP structural members are used as a direct replacement and can be produced in structural profiles that resemble cold-rolled steel sections. However, the walls of these composite members are thin and the stiffness of the walls are relatively low as compared to that of steel members. Therefore, the failure of these composite sections is governed by buckling when used as stand-alone compression members, such as columns (Qiao et al. 2001; Barbero 2000). The buckling behaviour has been researched extensively using analytical, theoretical and experimental methods with both local and global buckling studied.

Tomblin and Barbero (1994) experimentally studied the local buckling of short and intermediate GFRP wide flanged columns and compared the experimental results with analytical predictions. In a different study, Barbero and Tomblin (1994) experimentally studied the global buckling mode of wide-flange GFRP pultruded columns and an equation was proposed to take into account the interaction between the local and global buckling.

There have been different numerical and analytical formulations suggested in the literature to determine the local critical buckling load of pultruded GFRP profiles. The analysis of the local buckling behaviour of pultruded GFRP profiles are mainly performed by modelling the flanges and webs as individual orthotropic plates. Kollár (2002a) developed explicit expressions for the determination of the buckling load of axially loaded orthotropic plates of rectangular cross-section in which one of the unloaded edges is rotationally restrained while the other is free. On the other hand, the same author in Kollár (2002b) developed a simple explicit (closed-form) expression to predict the buckling load of orthotropic plates which are axially loaded and have both edges restrained rotationally. These expressions were based on previously identified expressions of the buckling loads of built in plates and simply supported plates from previous studies.

Kollár (2003) presented a summary of the buckling loads of long orthotropic plates with different edge conditions and loading from the available open literature at the time. In this study explicit expressions for the prediction of the local buckling loads of various structural sections (C, Z, I, L and box) subjected to axial loading and bending were presented. These expressions were based on a general method comparable to that presented in Qiao et al. (2001) for the analysis of the local buckling of thin-walled sections. Furthermore, numerical examples were presented to compare the local buckling loads derived to analytical and experimental values with good agreement with the three methods.

Turvey and Zhang (2006) carried out a numerical and experimental study in the aim of predicting the buckling, post-buckling and initial failure loads of GFRP wide flange short columns. From the experimental observation it was realised that the dominant failure modes were located at the web-flange junctions due to longitudinal cracking or at the longitudinal centreline of the web.

Correia et al. (2013) investigated the buckling behaviour and strength of hybrid pultruded short sections. Two series of I-sections having a length of 660 mm were tested under concentric compression. The two profile types were a bare GFRP profile and a GFRP profile that was strengthened with CFRP sheets placed on the flanges of the section. According to the experimental and numerical study, it was realised that the introduction of the CFRP sheets to the profile increased the critical buckling load, ultimate load and axial stiffness of 14%, 13-14%, and 30%, respectively, as compared to same values obtained for the bare profile.

Nunes et al. (2013) experimentally and numerically investigated the structural behaviour of GFRP pultruded columns of I-section profile tested with small eccentric loadings about its strong or major axis. The columns were 1500 mm in length and had cross-section dimensions of 120 mm in height, 60 mm width and 6 mm thickness. The ratio of the applied eccentricities to height was 0, 0.15 and 0.30. The results for the non-braced and braced columns subjected to uniform compression highlighted the significance of providing lateral bracing methods for GFRP members in compression. Furthermore, the small eccentricities that occur as a result of construction errors and geometrically imperfections are critical when analysing the compressive behaviour of these sections.

Creative-Pultrusions (2017) developed a comprehensive manual for the practical design of FRP pultruded columns. An extensive load test program consisting of more than 300 structural pultruded FRP columns of I, wide flange, round, square and angle sections was conducted at The University of Texas. The pultruded sections were Pultex products. The axial compression tests were conducted on short, intermediate and long columns with lengths ranging from 304.8 mm to 6096 mm. The columns were tested with end conditions of pinned-pinned to ensure an effective length coefficient of one. The ultimate load corresponding to local, global or bearing failure was determined from the relationship of the axial load versus the lateral displacements. The test results concluded that for a given area, the square (box) pultruded columns have the highest ultimate load capacities in comparison to the other section shapes. For these square columns, the dividing line between short and slender columns was a slenderness ratio value of 35. The short columns typically failed in a local buckling mode or bearing deformation whereas the failure mode of the slender columns was by global buckling. The design manual also developed ultimate load design equations for pultruded FRP columns with end conditions other than that provided in the experimental program.

4.5 FRP-Concrete Hybrid Members

Several developments in the last few years have allowed FRP materials to become increasingly competitive and accessible which include the improvements in manufacturing processes. The manufacturing of FRP materials is accomplished by a wide range of methods including pultrusion, filament winding and braiding. As a result, new types of FRP-concrete composite members have been introduced and investigated. By developing a hybrid composite member composed of the combination of conventional materials (concrete and steel) and FRP composites, the beneficial material properties of each component can be utilised to attain advanced structural performance. This section discusses the different types of FRP-concrete hybrid columns and beams proposed in the literature.

4.5.1 FRP-Concrete Hybrid Columns

The majority of studies and applications of FRP-concrete hybrid columns are focussed on external confinement by FRP tubes. In various studies these hybrid columns are also embedded with steel structural sections to increase the load carrying capacity and ductility. However, embedding GFRP pultruded structural sections in FRP-concrete hybrid columns has not yet been studied. Some available studies involving hybrid columns incorporating FRP, steel and concrete materials are presented below.

As outlined in a review by Ozbakkaloglu et al. (2013a), the application of FRP composites as a confining material for concrete has been widely studied and applied in practise in the strengthening of current concrete columns using FRP wrapping. In addition FRP composites can be used for constructing novel composite columns of high-performance by utilising concrete-filled FRP tubes, which are known as CFFT's (Mirmiran et al. 1998; Ozbakkaloglu 2013b). Many of these experimental studies have concluded that these CFFTs are ideal replacements to conventional steel confinement reinforcement as they fulfil multiple functions of stay-in-place formwork, confinement strengthening and a shell to protect the member from corrosion, chemical attacks and weathering. In addition, the lateral confinement given by the FRP tubes substantially increases both the ductility and compressive strength of concrete (Lam and Teng 2003). FRP tubes are usually manufactured by a technique known as filament wounding although some researchers have fabricated FRP tubes by a manual wet-lay-up process (Ozbakkaloglu 2013b).

The majority of the studies in the literature concerned with CFFTs are for circular cross-sections. However, for aesthetic and additional reasons, hybrid CFFTs of square cross-sections might be required. Having said this, the square tubes provide less confinement than circular tubes because stress concentrations occur at the edges, confinement is reduced on the flat edges and due to the confining pressure around the square sections being non-uniform (Lam and Teng 2003). One of the main solutions present in the literature to increase the confinement effectiveness of square tubes includes rounding the corners to reduce the stress concentrations (Ozbakkaloglu 2013c). In another study, Hadi et al. (2012) proposed a novel technique for strengthening square RC columns by a circularising technique and then wrapping with FRP sheets.

Wang et al. (2004) presented a new type of composite column by encasing structural steel I-sections in CFFT'S with the aim of increasing the ductility and load carrying capacity of the hybrid columns. Similarly, Karimi et al. (2011a) developed an experimental program to test structural steel encased CFFT composite columns to investigate their compressive behaviour under axial loading. The composite column utilised a GFRP tube that surrounded a steel I-section. A total of four composite columns were tested with two types of GFRP tubes, while three steel I-section column specimens were tested for comparison purposes. Based on the results of this study it was realised that the compressive strength of the concrete in the composite sections increased by 40-80%. In addition, the axial failure strains of the composite specimens were about two times more than that experienced by the steel columns.

The studies discussed above mainly focused on the use of circular CFFT columns embedded with structural steel for the purpose of new construction. In a different study, Karimi et al. (2011b) proposed a method to strengthen existing steel columns by the use of FRP. In this study a total of seven rectangular composite columns were constructed by wrapping epoxy saturated GFRP and CFRP sheets around an existing steel I-section column with fibres oriented in the hoop direction. The resulting voids between the steel and FRP jacket were filled with concrete. The main purpose of the FRP jacket was to confine the concrete core and prevent the flanges of the steel column from outward lateral buckling. The results showed that the compressive strength of the confined core of the columns with three layers of CFRP sheets increased by a factor of 2.4. The composite columns failed initially by the rupture of the FRP jacket followed by the crushing of the concrete. As the FRP jacket was removed it was observed that the steel flanges and webs experienced local buckling.

Following on from this study, Karimi et al. (2012a) tested the same rectangular columns proposed by Karimi et al. (2011b) to analyse the slenderness effects of the FRP strengthened composite columns as compared to the bare steel columns. In total, nine columns were tested, six of which were composite columns without corner strengthening technique and three bare steel columns. The heights of the sections ranged between 500 mm and 3000 mm. It was realised from the results that compared to the bare steel columns, the composite columns’ compressive strength, energy dissipation capacity and axial elastic stiffness are improved by a ratio of up to 5.2, 14.0 and 2.5, respectively. In addition, a capacity curve was established to determine the compressive strengths of the composite columns by varying the slenderness ratios.

Teng et al. (2004) presented a novel kind of hybrid composite column which is known as FRP concrete-steel double-skin tubular columns (DSTCs). This composite column comprises an outer FRP tube and an inner steel tube, with the space between them filled with concrete leaving a void in the middle of the column. This hybrid column utilises the advantages of concrete, steel and FRP. The fibres of the FRP tube are mainly oriented in the hoop direction to provide confinement for the concrete for improved ductility. The advantages of this hybrid composite column as documented by Teng et al. (2007) are the structural form of these columns allows for easier construction, the FRP tube increases the ductility of the confined concrete, construction loads can be supported through the use of the inner steel tube as opposed to CFFT's, and the existence of the inner steel tube allows for the simplicity of the connection to beams in buildings. In addition, no protection from corrosion is required because the steel tube is protected by both the concrete and FRP tube and there is no need for fire protection.

Wong et al. (2008) developed an experimental study to analyse the structural performance of FRP-concrete-steel DSTCs and compare the performances of DSTCS with that of CFFT specimens and hollow CFFT specimens. It was concluded from this study that the concrete in the DSTCs is confined effectively by the steel and FRP tubes. The surrounding concrete delays or suppresses the local buckling of the inner tube, providing a very ductile behaviour. It was also realised that the load versus axial shortening relationship of concrete in DSTCs is comparable to that of CFFTs. Furthermore, the inner steel tube prevents the concrete near the inner void from spalling inwards whereas in the hollow CFFTs there was no protection for this concrete spalling.

In another study, Yu et al. (2010) studied the behaviour of concrete-filled DTSCs when subjected to eccentric compression loading. It was concluded that the shape of the interaction curves produced for DSTCs is similar to that of conventional RC columns.

Wang et al. (2016) experimentally investigated the performance of concrete columns reinforced with FRP tubes. A total of sixteen specimens split into four groups were tested under compressive loading with varying eccentricities and under flexural loading. It was concluded that the introduction of the reinforcing FRP tube substantially improves the load carrying capacity and ductility of the hybrid specimens. In addition, the improved performance of these hybrid specimens as compared to conventional steel RC columns were shown through analytical and experimental load-bending moment interaction diagrams.

4.5.2 FRP-Concrete Hybrid Flexural Members

As summarised above, a substantial amount of research studies have been performed on the theory of combining the advantages of concrete, steel and FRP to develop a composite column to achieve a structural member of high performance. Furthermore, most of the studies and applications of FRP-concrete hybrid columns are focussed on external confinement by FRP tubes. There exist no studies investigating the encasing of GFRP pultruded structural sections in FRP-concrete hybrid columns. However an extensive amount of studies have investigated the use of GFRP pultruded sections in hybrid GFRP-concrete flexural members as discussed herein.

The first experimental studies of GFRP-concrete hybrid members were developed for strengthening purposes. Saadatmanesh and Ehsani (1991) bonded GFRP plates to the tension face of existing RC beams and indicated the increase in flexural strength achieved by this technique. When comparing steel plates, the utilisation of GFRP plates in this solution offers many advantages including the lightness, higher durability, ease of application and resistant to corrosion.

Deskovic et al. (1995) proposed a novel GFRP-concrete flexural member with the aim of mitigating the limitations of the constituent structural materials used separately and simplifying the construction process. This novel member consists of a concrete slab that is laid on the top of a GFRP rectangular box section that was fabricated by filament wounding. The upper flange of the GFRP box section serves the purpose of a stay-in-place formwork for the slab of concrete, which behaves as the compression flange of the member. In addition, to increase the flexural stiffness of the GFRP box section, a CFRP laminate was bonded onto the tension or lower surface of flange of the section. Considering the GFRP material has a higher failure strain as compared to CFRP, the CFRP would fail before the GFRP flange in tension serving the role of a sensor that indicates an imminent collapse. Based on the experiment, the most common failure mode was due to the de-bonding between the concrete slab and GFRP box section. Irrespective of this unfavourable premature failure mode, the specimen's flexural response depicted good ductility as a result of the CFRP laminate tension failure.

Fam and Rizkalla (2002) investigated the flexural behaviour of GFRP filament wound, GFRP pultruded and steel hollow and concrete filled tubes which were subjected to four-point bending. The main difference between the pultruded and filament wound tubes was the orientation of the fibres. The fibres in the pultruded tube were orientated in the axial direction whereas in the filament wound tube the fibres were oriented in both directions. The effects of different laminate structures of filament wounded tubes of similar size were also investigated. Based on the results of the experiment it was concluded that both the stiffness and strength increased by filling the hollow tubes with concrete. Compared to the hollow tubes, the strength gain for GFRP pultruded, GFRP filament wound and steel tubes by filling the tubes with concrete were 250%, 212% and 50%, respectively. It was realised that for the same thickness, concrete filled GFRP pultruded tubes displayed greater stiffness as compared to the concrete-filled filament wound tubes of the same thickness. However, the concrete filled GFRP pultruded tubes' failure mechanism was premature and was marked by the horizontal shear by splitting of the tube as a result of the insufficient amount of fibres in the hoop direction. On the other hand, the filament wound tubes failed in flexure by the rupture of the fibres.

Yu et al. (2006) implemented the composite system developed by Teng et al. (2004) to study the flexural behaviour of hybrid FRP-concrete–steel double-skin tubular beams (DSTBs), which comprised an FRP outer tube and steel inner tube with concrete filled between the two. In a similar study, Idris and Ozbakkaloglu (2014) studied the behaviour of seven FRP-concrete-steel DSTB specimens in flexure and one CFFT with an encased steel I-section as simply supported beams tested under four-point bending. Based on the experimental results it was determined that the shape of the FRP tube had only a minor influence on the flexural behaviour of the DSTB's, with the load-deflection response experiencing similar trends.

In recent years, stay-in-place formwork utilising pultruded FRP materials has been explored as a method that is not required to be removed once concrete has hardened (Cheng and Karbhari 2006). This new type of FRP formwork is lightweight and can be transported, maneuverered and easily installed without the help of substantial machines. Since FRP is strong in tension, the need for steel reinforcement is not required resulting in a non-corrosive members. In addition, the advantage of this FRP concrete hybrid member is the material properties of each member are utilised efficiently as the concrete resists compression and the FRP primarily resists the tension. In addition, the hybrid elements cross-section redundancy would also provide a type of pseudo ductility behaviour which is a great advantage considering the brittle and fragile failure modes of simple GFRP sections (Correia et al. 2007).

Correia et al. (2009) proposed a hybrid GFRP-concrete beam that consisted of a layer of concrete on the top flange of a pultruded GFRP I-section. Two shear connection schemes were adopted to connect the concrete compression layer to the flanges of the I-beam. They were a layer of epoxy adhesive and stainless bolts. When compared with simple GFRP I-sections, the proposed GFRP-concrete hybrid beam shows a significant increase in strength and stiffness, with an improved utilisation of the sections properties. It was found that regardless of the shear connections, the proposed hybrid beam can be used in slabs or beams for new construction or rehabilitation of existing structures. In terms of strength, the use of bolts as shear connection provided higher ultimate loads, while the epoxy adhesive connection attained a higher stiffness.

Honickman (2008) tested concrete slabs and girders constructed using flat pultruded GFRP plates and trapezoidal pultruded GFRP sheet pile section, respectively, as structural stay-in-place formwork. A total of three arrangements were studied for the girders, which were completely filled sheet piles, one with voided concrete fill and one with a concrete flange on the top of the girder. Based on the results, it was concluded that conventional steel-RC sections of similar size and strength have significantly higher stiffness as compared to FRP concrete members. On the other hand, steel-RC sections of equivalent stiffness have significantly lower strengths as compared to the FRP-concrete members. A total of four mechanical and adhesive bond mechanisms were examined to achieve the composite action with the concrete and

GFRP pultruded element. It was realised that prior to failure no slip was observed even though the failure was governed by de-bonding.

El-Hacha and Chen (2012) summarised an experimental program testing hybrid beams consisting a layer of ultra-high performance concrete (UHPC) on the top of a pultruded GFRP hollow box sections beams and a sheet of CFRP or steel FRP on the bottom of the beam. The concrete and sheets were used for strengthening purposes. These beams were subjected to static four-point bending. According to the results, it was found that compared to a control beam composed of only a GFRP hollow box section, the hybrid beams experienced a higher stiffness and flexural strength.

Kwan and Ramli (2013) presented a research study of encasing a pultruded FRP I-beam completely in a concrete beam for reinforcing reasons. The aim of this study was to enhance the ductility and reduce the bond slip issues of FRP RC structures. Four types of encased beams all reinforced with a pultruded I-sections were tested under four-point bending. The encased beams included a plain FRP I-beam, FRP I-beam with studs, FRP I-beam with steel shear reinforcement and studs and a FRP I-beam with studs and synthetic barchip fibre. Steel shear studs were screwed to the flange of the GFRP encased I-beam to prevent slippage between the concrete flange and the FRP I-beam. It was concluded from this study that the addition of studs is essential to prevent bond slip between the concrete matrix and FRP. In addition, the studs increased the ultimate load by approximately 13.8% and reduced the crack spacing. The addition of shear reinforcement and studs also increased the ultimate load by a further 34.5% as compared to the FRP encased beam. It was found that adding barchip fibres improved the first cracking load by 25.4% and adding stirrups increased the ultimate load carrying capacity by another 18.2%. However, the ductility of the composite beams reduced with the addition of stirrups or barchip fibres and was not recommended considering the main objective of the proposed design. Although the novel encased column is intended to increase the ductility of FRP reinforced beams, there was no direct experimental comparison with these beams and beams reinforced with either steel or FRP bars. Therefore, a direct comparison between conventionally reinforced beams and the proposed encased beam could not be drawn.

Muttashar et al. (2016) tested a hybrid beam composed of square pultruded GFRP sections (125 mm x 125 mm x 6.5 mm thickness) which were filled with concrete having compressive strengths of 10 MPa, 37 MPa and 43.5 MPa. A total of six GFRP filled beams and three hollow GFRP beams were tested under four-point bending. Based on the results, it was shown that the GFRP filled beams' capacity improved by 100% to 141% as compared to the hollow GFRP beams. On the other hand, the concrete infills compressive strength did not significantly influence the flexural behaviour of the beams. Furthermore, increasing the compressive strength of concrete from 10 MPa to 43.5 MPa improved the ultimate moment by just 17% but experienced similar flexural stiffness. Therefore, it was concluded that a concrete with low strength is a practical solution as a filler material for the pultruded GFRP sections.

4.5.3 Bond Mechanism between Concrete and FRP Structural Sections

In order for loads to be transferred in hybrid members, enough bond strength between the constituent components of the structure is required (Majdi et al. 2014). The majority of studies related to the bond mechanism of concrete to FRP are associated with FRP bars and FRP strips (Lu et al. 2006; Vilanova et al. 2015). Traditionally, for FRP strips applied to the surface of concrete, epoxy resins are used as the bonding agent. Furthermore, the manufacturers of FRP bars provide a sand-coated surface finish to improve the bond performance between the bars and surrounding concrete. Considering that the pultruded FRP sections have a considerably larger surface area, the previously proposed bond slip theories for FRP bars and FRP strips are not appropriate for FRP pultruded sections (Yuan and Hadi 2016). A few studies have been developed to investigate the bond mechanism between concrete and pultruded FRP structural sections.

Dieter et al. (2002) investigated hybrid concrete-FRP stay in place structural open formwork and FRP grid reinforcement for the application of bridge decks. A concrete slab was laid over a pultruded FRP sheet that was stiffened by hollow FRP box profiles which served the purpose of the tensile reinforcement. In addition, for the regions of negative bending moments, pultruded FRP elements were formed into a bi-directional grid to provide the upper reinforcement in the longitudinal and transverse directions.

To achieve an adequate shear bond mechanism between the concrete and FRP materials, the surfaces of the FRP form were roughened with a mix of epoxy and gravel before the placement of the concrete. However, because of the formworks' complex geometry, only the horizontal surfaces were applied this bonding mechanism. It was observed that the flexural cracking configuration in the concrete at the un-bonded parts of the system was substantially more noticeable compared to the concrete over the bonded regions. Therefore, in the areas where the bond mechanism was not applied, severe slippage transpired between the concrete overlay and the form.

Bank et al. (2007) conducted a feasibility study for the application of a commercially available pultruded FRP planks to be used as a stay-in-place formwork and the tensile reinforcement for a concrete structural components. The bond mechanism used between the concrete and smooth surface of the FRP planks was the combination of epoxy and two types of aggregate (sand and gravel). Based on the results of concrete beams tested, it was realised that sufficient bond occurred between the concrete and FRP plank because the ultimate capacity of the steel reinforced control specimen was lower than that achieved by the aggregate coated FRP plank concrete beams and well-distributed flexural cracks were evident for the hybrid beams. The use of the FRP plank without the surface treatment as a tensile reinforcement resulted in substantial slip between the FRP plank and concrete, as well as significantly less capacity and no distributed cracking. Furthermore, using finer sand coating resulted in a higher initial cracking moment as compared to using a gravel coating. Finally, it was shown that the equations in ACI 440.1R-06 (superseded by ACI 2015) guideline were able to develop good predictions of the flexural capacity of the proposed systems but the shear strengths are more accurately predicted using the ACI 318-05 (superseded by ACI 318-14 2014) guideline.

As mentioned above Kwan and Ramli (2013) presented a research study of encasing a pultruded FRP I-beam completely in a concrete beam for reinforcing reasons. To reduce the bond slip and slippage issues between the concrete flange and FRP I-beam in the proposed hybrid member, steel shear studs were screwed to the flange of the GFRP encased I-beam. It was seen that bond slipping occurred in the specimen encased with a plain FRP I-beam without shear studs, which were followed by fracture of the FRP resulting in a severe drop in the load carrying capacity. It was concluded from this study that the addition of studs is essential to prevent bond slip between the concrete matrix and FRP. Most notably, the addition of studs increased the ultimate load by approximately 13.8% and reduced the crack spacing as compared to the plain FRP I-beam encased specimen. Lastly, the beam with studs experienced the highest ductile behaviour of all the four types of tested beams.

Yuan and Hadi (2016) investigated the bond behaviour between GFRP I-sections and concrete by conducting experimental push-out tests. A total of four specimens in the arrangement of a rectangular concrete column having a GFRP I-section encased in the middle were tested. The two parameters considered in this study were the placement of stirrups and bond length. Based on the results, it was found that GFRP I-sections with longer bond lengths achieved higher bond strength. Furthermore, the placement of stirrups reduces the development of concrete cracks but did not necessary improve the specimens ultimate bond strength. Finally, a preliminary constitutive model was proposed for the bond stress-slip relationship of the experimentally tested specimens. It was found that relatively close agreement was established between the experimental and theoretical results.

4.6 Review of Design Guidelines

In summary, based on the literature it can be seen that the use of FRP pultruded sections in the construction industry have huge potential in either the retrofit of existing structures or for the construction of new ones. In addition, large scale pultrusion of FRP has further reduced the manufacturing costs, making these sections a competitive substitute to conventional materials. However, presently there exists some disadvantages that are hindering the widespread use of FRP pultruded sections in civil engineering structures which include: (i) the cost of production are high, (ii) the adverse behaviour when exposed to fire (Correia et al. 2010) and, most importantly, (iii) the lack of specific 'official' design standards and guidelines, implies the design of these structures remains a challenge.

The application of pultruded sections in the construction of infrastructure projects has allowed authorities and industries to document the behaviours of these structures and formulate several design and construction guidelines/recommendations for using FRP pultruded sections. These are often incomplete and/or are over conservative. There have been significant efforts internationally in the development of standards and guidelines for the design of FRP structural members (Cardoso et al. 2014b). These standard provisions include

- Eurocomp Design Code (Clarke 1996) which offers in general design recommendations for the use of polymer composites, but does not include address specifically pultruded elements.
- CNR-DT 205-2007 (CNR-DT205 2007) is the first design guideline for structures made of pultruded sections but is still rather incomplete.
- The most recent Pre-Standard (ASCE 2010) which is named the "Pre-Standard for load and resistance factor design (LRFD) of pultruded fibre reinforced polymer (FRP) structures". This standard was submitted to the American Composites Manufacturers Association (ACMA).

The latter is a Pre-Standard for which ASCE was the project manager for the development of this standard. At present, this Pre-Standard document is following the standards development process by ANSI and ASCE to implement it into an official ASCE Standard. The LFRD standard will establish material properties for pultruded FRP composites that will allow designers to use these products with confidence.

However, there exist many important gaps in the understanding and knowledge of the behaviour of pultruded structural members. Before design guidelines and recommendations can be developed for the design and use of pultruded FRP sections, it is essential to understand the structural behaviour of these sections by carrying out extensive research work. Aravinthan and Manalo (2012) reported that to overcome these design issues, the strength calculations of structures constructed from FRP pultruded sections needs to be analysed with standard theory as well as finite element techniques backed up by fatigue and strength.

In addition, load tables and design equations for pultruded FRP tubular compression members have been developed by manufacturers and are accessible to offer design engineers with a guideline for designing FRP pultruded columns. Creative-Pultrusions

(2017) developed a comprehensive manual for the practical design of FRP pultruded columns. In addition, this design manual provided load tables for pultruded flexural members and connections including beam deflections, stress calculations for channels, lateral-torsional buckling and other design considerations. However, the guideline does not offer an indication of any numerical or analytical models to validate the experimental results.

4.7 Summary

In summary, FRP pultruded profiles low self-weight, noncorrosive nature, low maintenance requirements and high durability have allowed them to become a competitive replacement as a primary structural material in place of steel and reinforced concrete. However, their application is still hindered by their sensitivity to buckling, high deformability, and the lack of design codes. Having said this, there is an interesting potential for the use of FRP-pultruded sections in hybrid FRP-concrete structural elements, either for new constructions or for the rehabilitation of existing structures, as reported by many researchers. Some of the advantages of these hybrid FRP-concrete structural members include a reduction in the structures' deformability, increase in the flexural stiffness, increase in the structures' strength capacity, prevent the buckling phenomena and make better use of the FRP section. However, there have been no studies available on structural FRP sections embedded in concrete columns. Furthermore, concrete beams embedded with different shapes and configurations of pultruded FRP sections have not been investigated.

Therefore, according to the literature, various research studies have been developed to determine the material characterisation, design and analysis of pultruded FRP structural sections tested in compression. However, many of these studies are performed on double-symmetrical cross-sections (I-sections and square tubes) and the main emphasis being the local buckling phenomenon. Furthermore, the fabrication of FRP pultruded sections will be optimized in the future with further advancements in technology. This would imply that the buckling resistance will be improved and these sections' compressive strength will be reached. Having said this there are no design guidelines and analysis available for FRP channel sections. Therefore, it is important to study the mechanical compressive properties of pultruded FRP channels.

Consequently, the next chapter presents a study on the compression mechanical properties of pultruded GFRP channels. The mechanical compression properties were obtained by two methods. The first method involved testing coupons extracted from the channels with a simple fixture developed to prevent the premature failures associated with end crushing. In the second method full-size specimens having free lengths of 100 mm and 200 mm were subjected to axial compression. The behaviour and failure modes of the coupons and full-size specimens are discussed and compared. Furthermore, a numerical model was developed using the finite element analysis program ABAQUS to simulate the compressive behaviour of the full-size specimens. A failure criterion was investigated to determine the location of failure initiation of the full-size specimens.

In addition, Chapter 6 discusses the main experimental program of this thesis which investigates the viability of encasing pultruded GFRP sections (I-section and C-sections) in concrete columns and beams and explains the testing of these members under compressive and flexural loading.

5 COMPRESSION BEHAVIOUR OF PULTRUDED GFRP CHANNELS

5.1 Introduction

Based on the literature in Chapter 4, several studies have been conducted to develop material characterization, analysis and design of FRP structural shapes subjected to axial compression. However, most of these studies were conducted on double-symmetrical cross-sections, such as wide flange I-sections and square tubes with the main focus being the local and global buckling phenomenon. Furthermore, there are no design guidelines and investigations available for FRP channel sections. Therefore, in order to study the compressive behaviour of FRP pultruded channels an experimental program was designed and conducted and is explained in this Chapter. The mechanical properties of the GFRP channels were first determined in compression, tension and shear. The compression behaviour of the channels was then investigated by testing full-size specimens. Furthermore, a numerical model was developed using the finite element analysis program ABAQUS to simulate the compressive behaviour of the full-size specimens. In addition, a failure criterion was investigated to determine the location of failure initiation and a comparison with the experimental results was established.

5.2 Experimental Program

The experimental program consisted of two stages. The first stage involved determining the mechanical material properties of coupons extracted from the GFRP channels. The strength and stiffness properties of these coupons were determined by means of compression, tension and shear tests. The compressive material properties were determined by tests on coupons extracted from the channels. These coupons were tested by two methods. The first method involved direct end loading of the coupons while in the second method a simple fixture was developed to prevent the premature failures associated with end crushing. The second stage involved testing full-size GFRP channels under uniform axial compression. The lengths of the full-size compression testing were chosen to ensure failure was by pure compression of crushing rather than by local buckling. A comparison of the compression properties obtained by the coupon and full-size channels are discussed. Also, the experimental results and failure modes of the coupon testing and full-size testing were reported and compared. It should be noted that due to time constraints and other factors all the testing took place over a duration of about one year. Furthermore, a numerical model was developed to simulate the compressive behaviour of the full-size channels to validate the experimental results.

5.2.1 Materials Properties and Test Methods

The GFRP pultruded channels were supplied by GRP Australia (GRP 2008) who purchased the sections from a manufacturer in China. These pultruded GFRP sections are orthotropic materials with the properties varying in each direction. The fibres are laid mainly in the longitudinal direction, which makes these sections stronger in the longitudinal direction as compared with the transverse direction. The nominal cross sectional dimensions of the channels were a flange and web thickness of 9.5 mm, flange width of 42 mm and depth of 152 mm. A total of five channels with lengths of 760 mm were used to extract the coupons for testing in compression, tension, shear and the specimens used for the full-size testing. The supplier in Australia mentioned that these channels were from the same batch.

Considering the dimensions of the sections provided by the manufacturer are nominal values, the real values were determined so that they could be used in the interpretation of the experimental results and in the numerical modelling. The thicknesses of the walls and external dimensions were measured using a digital calliper at both ends of each of the six full-size channel specimens tested. The average dimensions including the sample standard deviations are summarised in Table 5.1, with the notations defined in Figure 5.1. The average thickness of the flange and web were 9.22 mm and 9.28 mm, respectively. The average width of the flange, depth and cross-sectional area of the section were 41.24 mm, 152.45 mm and 1958 mm^2. As can be seen, no significant variations between the measured and nominal dimensions were observed with the variation of the measured wall thickness varying by 0.22 mm and 0.28 mm for the web and flange, respectively.

The following sections describe the test methods for the compression, tensile and shear testing of coupons extracted from the channels and the compression testing of the full-size specimens.

Table 5.1. Dimensions of the pultruded GFRP sections used in this study (Nominal dimensions of 152 x 42 x 9.5 mm)

Measured Dimensions	**Average ± Standard Deviation**
Flange thickness, t_{flange} (mm)	9.22 ± 0.06
Web thickness, t_{web} (mm)	9.28 ± 0.04
Flange width, b_f (mm)	41.24 ± 0.16
Depth, d_s (mm)	152.45 ± 0.14
Corner radius, R (mm)	10
Cross section area, A (mm^2)	1958[a]

[a] The area was calculated using AutoCAD with the average values of the measured dimensions utilised.

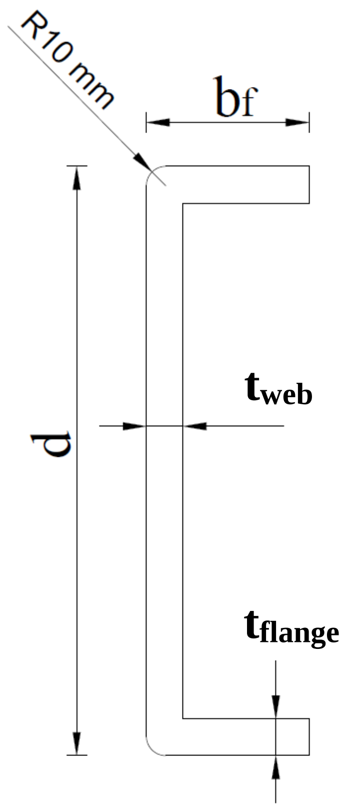

Figure 5.1. Notations for the dimensions of the GFRP sections

5.2.1.1 Compressive Properties - Longitudinal Direction

As mentioned in the literature in Chapter 4, the compression testing of pultruded composites has been widely investigated. The compressive properties of pultruded materials and in general composites have been reported to be very difficult to measure, most notably when using the end loading method. Hodgkinson (2000) reported that the compression testing of high strength composites is difficult due to the high longitudinal strength and low transverse strength of the material (Hodgkinson 2000). This difficulty is also due to the strong tendency of the material toward premature failure due to geometric instability, local end crushing, or local end brooming. Furthermore, the property measured may not be the actual compressive strength but represent the composite bearing strength and the direct end loading of the samples is not possible to determine the compressive strength (Barbero et al. 1999).

In this section, the compressive properties were first determined by direct end loading of coupons and then by using a simple fixture to prevent the premature failures associated with end crushing. The results and failure modes of both methods are investigated. Although the first pre-standard for the design of pultruded structures (ASCE 2010) has adopted the ASTM D6641-2014 (currently superseded by ASTM D6641 2016b) test standard for determining the compressive properties of pultruded materials, in this study the end loading method adopting the ASTM D695-15 (ASTM 2015) was utilized considering the test fixture needed for ASTM D6641-16 (ASTM 2016b) was not readily available at the time of this study.

The ASTM D695 (2015) test standard mentions the coupon dimensions required for strength measurements and for modulus of elasticity measurements. Considering these guidelines and the dimensions of the coupons extracted from the pultruded section are dictated by the thickness of the section, the nominal coupon dimensions used for strength measurements were 25.4 mm long and 12.7 mm wide. In addition, the nominal coupon dimensions used for modulus of elasticity measurements were 37.6 mm long and 12.7 mm wide based on the limits on the slenderness ratio.

The compressive properties of channels were determined for both the longitudinal and transverse directions. The coupons were extracted either longitudinally or transversely from the web of the channels using a wet saw machine. It is assumed that the compressive properties in the web and flange are the same. To compensate for levelling errors, the top and bottom ends of the coupons were levelled with a mill and the coupons were placed on a spherical seat. The test standard requires a special testing device to ensure the loading is axial and applied through surfaces that are flat and parallel to each other in a plane normal to the vertical loading axis. However, this device is not always available and hard to manufacture and the coupons were directly end-loaded using the screw-driven testing machine known as the 500 kN Instron 8033 machine under a displacement controlled loading rate of 1.3 mm/min. The test set-up for the compression testing of the coupons is shown in Figure 5.2.

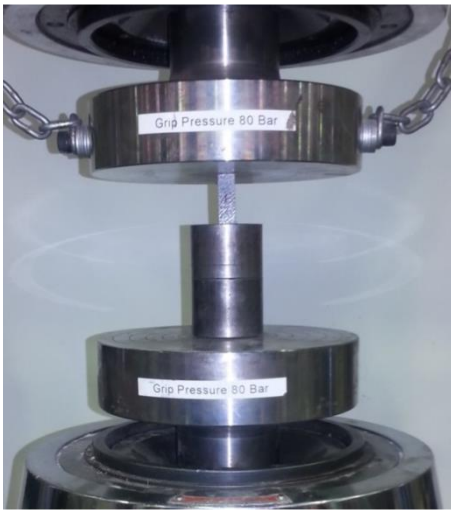

Figure 5.2. Compression testing setup for coupons

A total of ten coupons of length 25.4 mm and a total of twenty five coupons of length 37.6 mm were tested. All these coupons were not extracted from the channels nor tested on the same day. The lengths of the coupons ranged from 25.34 mm to 25.56 mm and 36.38 mm to 38.00 mm for the respective nominal lengths tested, while the widths ranged from 11.80 mm to 13.27 mm and thickness from 9.19 mm to 9.33 mm. The variation in the coupon dimensions was due to both the cutting and pultrusion process. Out of the 25 coupons having a nominal length of 37.6 mm, 15 coupons were instrumented with one strain gauge of 5 mm gauge length at mid-length while the 25.4 mm long coupons were not instrumented with strain gauges due to the small coupon length.

The longitudinal compressive strengths (in MPa) for the 25.4 mm coupons in ascending order are 183, 210, 211, 213, 224, 230, 240, 243, 246 and 252. The longitudinal compressive strengths (units in MPa) in ascending order for the 37.6 mm long coupons are: 199, 208, 212, 216, 222, 226, 230, 235, 239, 246, 251, 251, 252, 270, 275, 281, 285, 297, 338, 345, 352, 358, 377, 416, and 428. The moduli in compression (units in MPa) in ascending order for the 37.6 mm long coupons are: 21.7, 22.6, 22.9, 23.8, 24.0, 24.0, 24.1, 26.2, 26.3, 27.6, 28.1, 29.7, 30.1, 30.4, and 31.2. The average modulus of elasticity in compression was 26.2 MPa. The behaviour of the coupons tested in compression was linear elastic until failure. For a few of the coupons, the stress versus strain curve deviated slightly from the linear trend just before the onset of failure. This slight deviation may be the result of small bending deformations.

The typical failure modes of the coupons are shown in Figure 5.3. All the coupons having a nominal free length of 25.4 mm and the majority of the coupons of 37.6 mm length failed prematurely due to end crushing or end brooming. Therefore, the average compressive strength of the coupons could not be calculated based on all these data points because the majority of these coupons failed prematurely. The failure type that ensures a valid test result is marked by the longitudinal splitting or delamination of the layers of the coupon.

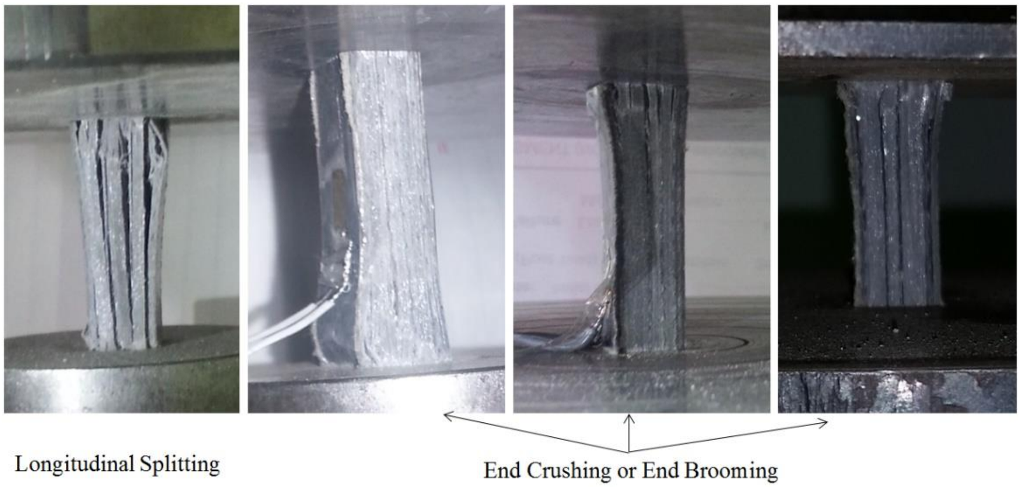

Figure 5.3. Failure mode of longitudinal coupons tested in compression by direct end-loading

In terms of the 37.6 mm long coupons, it was realised that the coupons that failed predominately by longitudinal splitting achieved considerably higher compressive strengths compared to the coupons that failed by crushing and/or end brooming. Most notably, it is interesting to note that the first five coupons tested which failed by longitudinally splitting had an average compressive strength of 386 MPa, whereas the next five coupons which failed by end crushing had an average strength of only 220 MPa. As mentioned above, the coupons for testing were extracted from five channels having lengths of 760 mm. It should also be noted that these two groups of five coupons were extracted from two different channel sections and were tested on two different days. A few of the coupons experienced a combination of these failure modes, with end crushing and longitudinal splitting at one edge of the coupon resulting in outward bulging of one face of the coupons, as shown in Figure 5.3. Predominately, these coupons with a combination of the failure modes achieved higher compressive strengths than those that failed by end crushing but lower than those that failed by longitudinal splitting.

Along with premature failure issues, possible reasons for the dispersion in results may also be the result of different issues such as poor quality control at the manufacturing level arising from poor wet out or large mat fold, the intrinsic nature of the test setup or as reported by Mottram (1994) due to the non-uniform spacing of the roving bundles throughout the cross section and because coupons were extracted from different locations and sections of the channels.

Another factor for premature failures and high dispersion in the results may be geometric instabilities due to bending or global buckling. Having said this, the test method ASTM D695 (2015) does not discuss the use of strain gauges or the determination of the bending or global buckling effects. However, the bending and global buckling was investigated by instrumenting the last coupon with a nominal length of 37.6 mm tested with back-to-back strain gauges. The test method, ASTM D 6641 (2016) provides a formula to determine the percent bending as shown in Equation 5.1 which was used in this study. The percent bending of the coupon with back-to-back strain gauges was determined to be approximately 10% during the duration of testing with the modulus of elasticity in compression varying from 26.2 MPa on one face of the coupon to 21.3 MPa on the other face. This value would imply that bending or buckling issues may have been evident and could further explain the high dispersion in the modulus of elasticity in compression. Bending and buckling of coupons tested by direct end loading should be investigated further.

$$Percent\ bending = \frac{\varepsilon_1 - \varepsilon_2}{\varepsilon_1 + \varepsilon_2} \times 100 \tag{5.1}$$

where ε_1 and ε_2 are the strain from Gauge 1 and 2, respectively.

Many test fixtures have been developed to prevent the premature failure of composite coupons at the ends from crushing or brooming, by introducing restrictions to the lateral expansion at the ends of the coupon and to reduce the effect of specimen end conditions (Mottram 1994; Häberle and Matthews 1994; Barbero et al. 1999; Saha et al. 2000; Hodgkinson 2000; ASTM D6641-2016). However, many of these test fixtures are not readily available and are very difficult to manufacture.

Therefore, in this study a simple fixture was developed to serve the purpose of confining the top and bottom ends of the coupon. The fixture was a set of two aluminium loading plates attached to both ends of the coupon. The loading plates were square in dimension having a side width of 50 mm and thickness of 25 mm. An inner square void having side dimension of 30 mm and depth 10 mm was machined in the middle of the plates. The ends of each coupon were placed in the voids of the loading plates and capped with high strength plaster at a length of 10 mm for both the top and bottom end as shown in Figure 5.4. The testing machine and loading rate were the same as that used for the unconfined coupons.

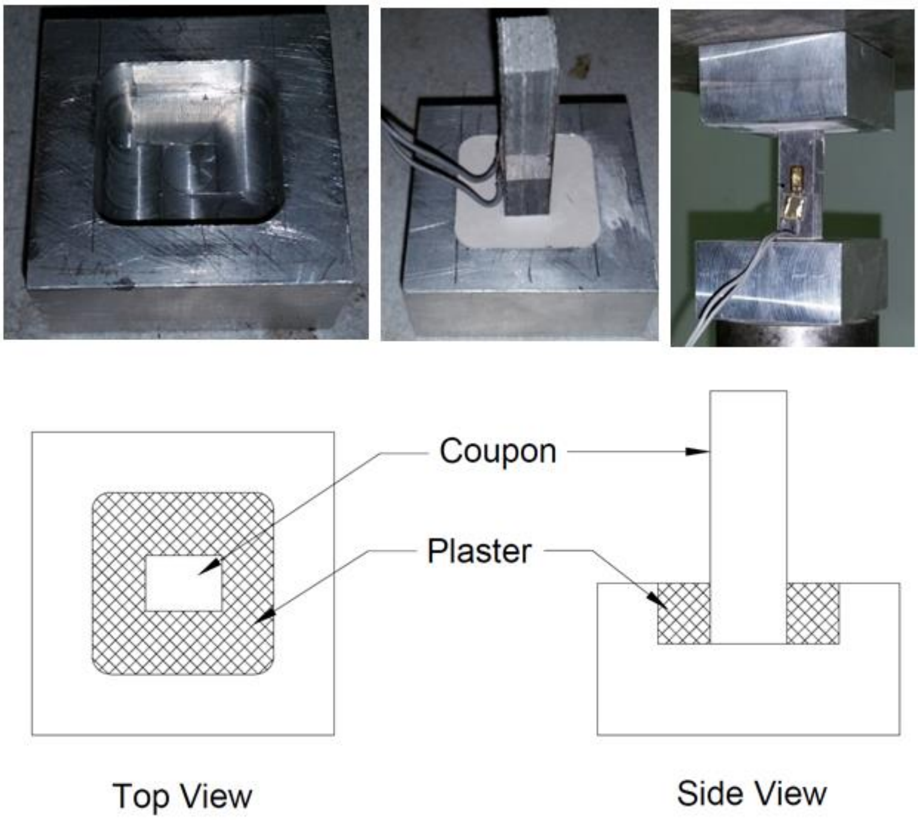

Figure 5.4. Compression testing set-up for coupons confined at the ends

Therefore, to maintain the coupon nominal free length of 25.4 mm and 37.6 mm as done for the unconfined coupons, the coupons were cut to a nominal length of 45.4 and 57.6 mm, respectively, with the top 10 mm and bottom 10 mm ends confined. The loading plates along with the ends of the coupons were machined to ensure all the surfaces were parallel. The coupon was also placed on a spherical seat as done for the unconfined coupons. A total of six coupons having nominal free lengths of 25.4 mm (C25-1 - C25-6) and six coupons having nominal free lengths of 37.6 mm (C37-1 - C37-6) were tested. All the confined coupons along with all the 25.4 mm long coupons and a few 37.6 mm long coupons directly end loaded were extracted from the same 760 mm long channel section. The C25 coupons were not instrumented with strain gauges while Coupons C37-1 and C37-2 were instrumented with one strain gauge and the rest of the C37 coupons were instrumented with back-to-back strain gauges at the coupon mid-length to monitor the bending or buckling effects. Again similar to the unconfined coupons, slight variations in the coupon dimensions from the nominal values were evident due to both the cutting and pultrusion process.

The results of these six coupons for each of the nominal free lengths tested are shown in Table 5.2. In terms of the coupons confined by high strength plaster, no failures associated with end crushing or brooming occurred. The failure was seen to occur in the instrumented region away from the ends of the coupon. The failure of all the coupons were similar which were marked by predominately the longitudinal splitting along the coupon height as shown in Figure 5.5, which is the preferred failure mechanism. These failures were instantaneous, followed soon afterwards by sideway buckling or outwards bulging of either one or two of the sides of the coupon where the coupon thicknesses had been reduced by the splitting, as shown in Figure 5.5.

The average strength of the confined coupons with a nominal length of 37.6 mm was higher than that of the confined coupons with nominal length of 25.4 mm. However, as explained above many factors can govern the variation in the compression properties including the lower sample size. Having said this, the failure mechanism for the confined coupons was satisfactory with no end crushing occurring. For the purposes of this study, the test data for the confined coupons for the two different nominal lengths were combined to obtain a global value for the average compressive strength and standard deviation for the GFRP channels. This global value is used to compare the compressive strength of the full-size channels and in the numerical analysis for the material properties. The global average compressive strength and standard deviation for the confined coupons were 303 MPa and 23 MPa, respectively, with a coefficient of variation of 7.6% obtained, as shown in Table 5.2. The global average modulus of elasticity and rupture strain were simply obtained from the C37 coupons tested with the values obtained by the unconfined coupons ignored.

Table 5.2. Results of the longitudinal coupons tested in compression with both ends confined

Coupon	Compressive Strength $\sigma_{cu,L}$ (MPa)	Modulus of Elasticity in Compression $E_{c,L}$ (GPa)	Compressive Rupture Strain $\varepsilon_{cu,L}$ (%)	Percent bending Eq. (5.1)[b]
Confined coupons with nominal free lengths of 25.4 mm				
C25-1	322.9	-	-	-
C25-2	293.4	-	-	-
C25-3	306.9	-	-	-
C25-4	267.8	-	-	-
C25-5	278.0	-	-	-
C25-6	265.8	-	-	-
Average	289.1	-	-	-
Standard Deviation	22.8	-	-	-
COV (%)	7.9	-	-	-
Confined coupons with nominal free lengths of 37.6 mm				
C37-1	303.7	23.3	1.30	-
C37-2	311.7	25.5	1.22	-
C37-3	316.9	24.9	1.29	9.8
C37-4	302.8	25.1	1.23	11.8
C37-5	333.8	24.8	1.36	7.6
C37-6	331.9	24.6	1.35	1.2
Average	316.8	24.7	1.29	-
Standard Deviation	13.5	0.7	0.06	-
COV (%)	4.3	3.0	4.42	-
GLOBAL VALUES				
Global Average[a]	303.0	24.7	1.29	-
Global SD[a]	23.0	0.7	0.06	-
Global COV (%)	7.6	3.0	4.42	-

Note: Missing values are for the specimens not instrumented with strain gauges.

[a] Taken as the average of all the confined coupons with both nominal free lengths of 25.4 and 37.6 mm.

[b] Taken as the average value for bending between the stress range of 75 and 300 MPa.

Coupon C37-2 Coupon C37-3 Coupon C25-3

Figure 5.5. Failure mode of longitudinal coupons tested in compression with the ends confined

The percent bending of the 37.6 mm long confined coupons with back-to-back strain gauges was determined by Equation 5.1 as explained above. The average percent bending for Coupons C37 was determined as the average of the values between the stress of 75 and 300 MPa. As shown in Table 5.2, the percent bending varied from 1.2 to 11.8%. It can be seen that the coupon that experienced the lowest percent bending did not necessarily achieve the highest compressive strength. The variation in the two gauges' readings resulted in a substantial variation in the modulus of elasticity obtained by the two gauges. For example, for Coupon C37-3, the moduli obtained by Gauges 1 and 2 were 22.5 MPa and 27.3 MPa, respectively. In interpreting the results for each coupon, the modulus of elasticity was taken as the average value obtained by the two gauges.

In addition to bending, buckling effects may have played a role in the test, which may have resulted in premature failures. However, regardless of the bending effects and potential buckling issues there was a lower dispersion in compressive strength for the coupons confined by high strength plaster as compared to the coupons tested by end loading and the failure mechanism was satisfactory for the confined coupons. However, the lower sample size may be a governing factor with this.

In summary, testing the pultruded composites by end loading has been seen to be difficult due to the premature failures associated with end crushing. Confining the ends of the coupon form lateral expansion prevented the end crushing. Having said this, it can be seen that some of the coupons that were loaded by direct end-loading with a nominal length of 37.6 mm and failed by longitudinal splitting achieved a higher compressive strength as compared to all the confined coupons tested for both nominal lengths. This would suggest that for a low sample size, obtaining the actual compressive strength is very difficult to achieve. Furthermore, the confined coupons may not have achieved the true compressive strength. Having said this, for the purposes of this study and due to the material and resources available, the compression properties of the confined coupons tested by end-loading are deemed to be satisfactory and conservative.

The supplier mentioned that all five 760 mm long channel sections used to extract the coupons from were from the same batch. The variation in properties may have been due to the non-uniform placement of the fibres or other factors arising in the manufacturing process. Whether or not they were from the same batch could not be guaranteed from the author perspective but regardless other researchers have drawn similar conclusions that were explained above. Furthermore, milling the ends of the coupons may have resulted in areas of weakness at the ends resulting in variations in failure modes and strengths. However, capping the ends will reduce the issues arising from this.

5.2.1.2 Compressive Properties – Transverse Direction

The compressive properties of channels were also determined for the transverse directions. A total of seven coupons having a nominal free length of 25.4 mm and nine coupons having a nominal free length of 37.6 mm were extracted from the webs of the channels in the transverse direction and tested by direct end-loading using the same testing machine and loading rate as the longitudinal coupons. Five of the transverse coupons having free lengths of 37.6 mm were instrumented with one strain gauge of 5 mm gauge length at the mid-length.

The ultimate transverse compressive strengths (units in MPa) in ascending order for the 25.4 mm long coupons are 50.5, 52.3, 56.9, 58.1, 58.9, 59.7 and 60.4. The transverse compressive strengths (units in MPa) for the 37.6 mm long coupons are 53.0, 53.6, 60.1, 94.2, 95.1, 96.5, 96.8, 105.8, and 111.0. It should be noted that two of the coupons instrumented with strain gauges experienced a non-linear stress-strain relationship (coupons with strength 53.0 MPa and 53.6 MPa), which resulted in compressive strengths substantially lower than that of the other coupons. This phenomenon may be the result of the placement of the rovings of fibres. In the transverse direction the fibres are arranged in a non-linear arrangement, as opposed to the linear arrangement for the longitudinal coupons, as seen in Figure 5.6(a). As a result, buckling of the internal fibres may have resulted in premature failures, as shown in Figure 5.6(b).

The compressive modulus of elasticity of the coupons was obtained for the three coupons which exhibited a linear behaviour. For one of these coupons with the lower compressive strength (60.1 MPa) and modulus of elasticity, the stress-strain curve deviated from the linear trend at the latter stages of loading. These coupons achieved a modulus of elasticity value of 5640, 6850 and 9740 MPa, with an average value of 7410 MPa obtained. Furthermore, the average rupture strain was 1.14% with a coefficient of variation of 17.9% obtained. In addition, some of the coupons failed prematurely due to end crushing. For the coupons that failed at a higher compressive strength, the typical failure mode by direct end-loading was by splitting of the coupons diagonally as shown in Figure 5.6(c). The coupons with the lower compressive strengths failed by either end crushing or by what seemed to be the buckling of the fibres.

A total of three transverse coupons having a free length of 25.4 mm were tested by capping the top and bottom ends of the 45.4 mm long coupons similar to what was performed for the longitudinal coupons. The compressive strengths of the three coupons tested were 59.2, 60.8 and 62.6 MPa. Similar to the unconfined coupons, the nonlinear arrangement of the fibres in the transverse direction resulted in all these coupons failing by what seemed prematurely due to the buckling of the fibres as shown in Figure 5.6(d).

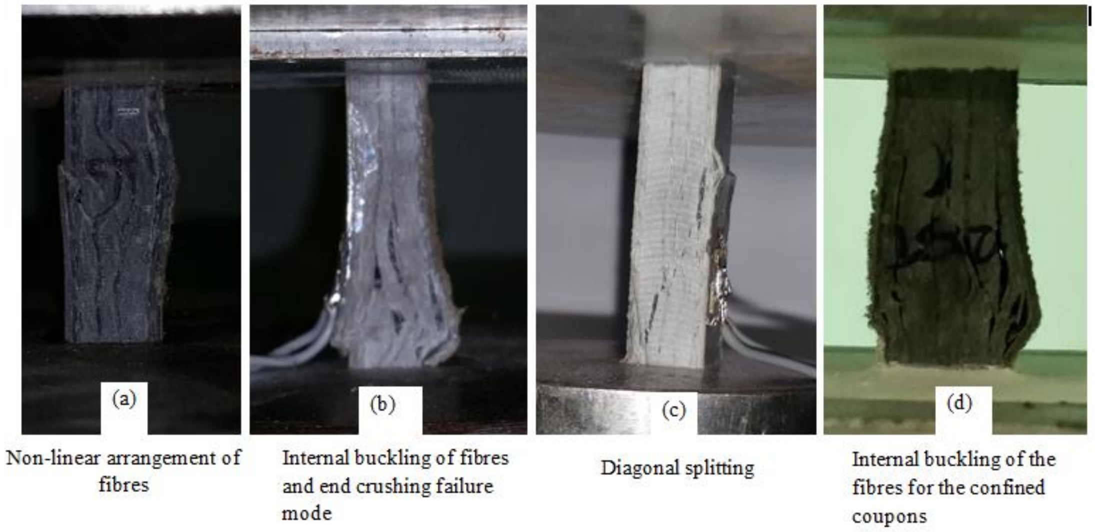

Figure 5.6. Failure mode of the transverse coupons tested in compression

For the analysis in the sections below, the average transverse strength for the confined coupons were utilised even though some of the unconfined coupons achieved a higher transverse strength as compared to the confined coupons and the failure mode of the confined coupons is not preferred. The average transverse compressive strength for the confined coupons was 60.9 MPa. Furthermore, the average modulus of elasticity and rupture strain in the transverse direction were taken from the three instrumented uncapped coupons that did not exhibit non-linear behaviour. As expected, the transverse compressive properties were substantially lower than that of the longitudinal properties. Most notably, in terms of the capped coupons loaded by direct end loading having a free length of 25.4 mm, the average transverse compressive strength and modulus of elasticity were both approximately 20.1% that of the same average values obtained longitudinally. This value seems low and would imply that the transverse compressive strength is lower than what it should be. This shows the difficulty in accurately obtaining the transverse compressive strengths of pultruded GFRP sections and further research is required.

5.2.1.3 Tensile Properties

The longitudinal tensile properties of the GFRP pultruded sections were determined based on the test method ISO 527-4 (ISO 1997). Seven coupon samples (T1-T7) from the web of the C-section were extracted in the longitudinal direction using a wet saw machine. The tensile testing was performed using the 500 kN Instron 8033 machine using a loading rate of 2 mm/min. The sections were too narrow in the transverse direction to enable the extraction of standard coupons with dimensions as specified by the test standards. Therefore, the transverse tensile properties of the pultruded structural sections could not be determined.

Six of the coupons were bonded with strain gauges with a gauge length of 12.7 mm positioned at the mid-length in the longitudinal direction. Only the first coupon (T1) was instrumented with two back-to-back strain gauges while the rest of the coupons were instrumented with one strain gauge. Furthermore, the last coupon (T7) was instrumented with one strain gauge in the longitudinal direction and another in the transverse direction at mid–length to measure the materials' Poisson's ratio. The strain gauges for Coupon T7 had a gauge length of 5 mm.

The dimensions of the coupons and positioning of the strain gauges are shown in Figure 5.7(a). Tabs were provided at the ends of the coupons to prevent the crushing of the coupon at the gripping location. The tabs used were the same material under test, having dimensions of 75 mm length and 28 mm wide to ensure a distance between end tabs of 150 mm. The adhesive used to bond the GFRP tabs to the same GFRP material coupon was a mixture of epoxy resin and hardener at 5:1 ratio. The experimental set-up of the tensile testing is shown in Figure 5.7(b).

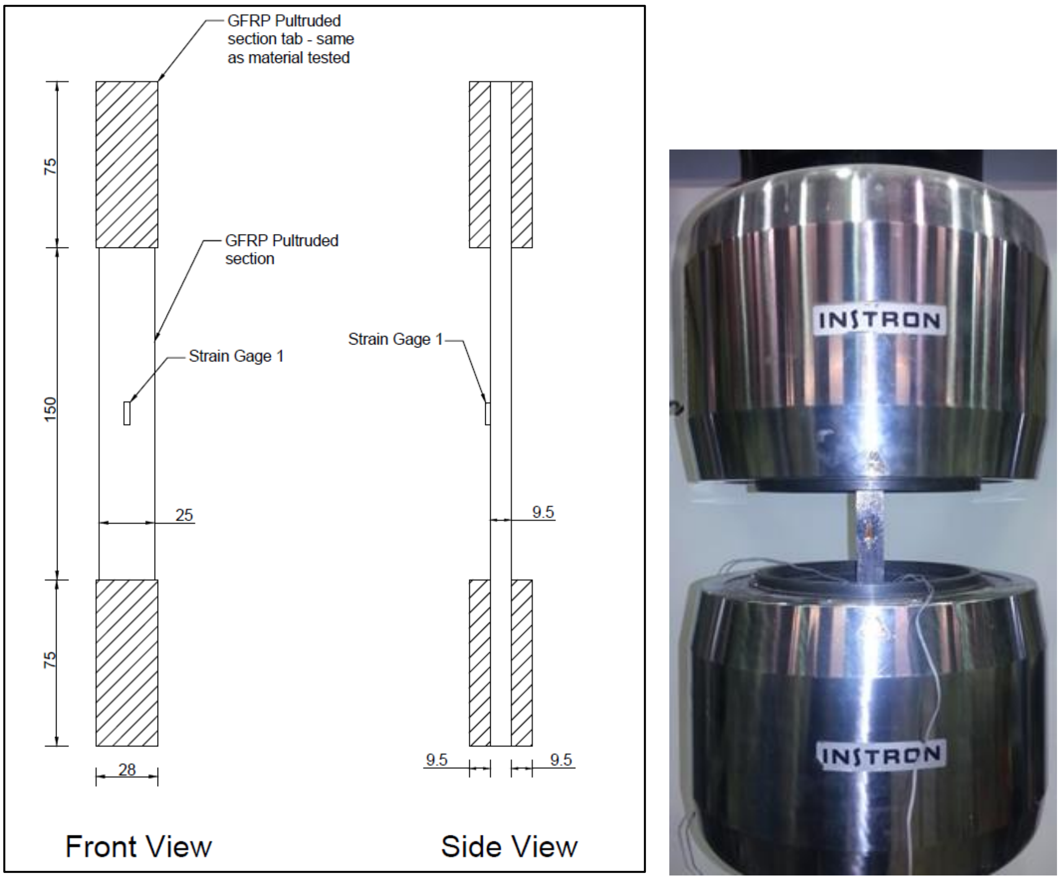

(a) (b)

Figure 5.7. Tensile testing of coupons: (a) Dimensions of coupons; and (b) Experimental set-up

The results of the tensile testing of the coupons in the longitudinal direction are shown in Table 5.3. The stress versus strain relationships obtained by the strain gauge data and the typical failure mode of the tensile tested coupons are shown in Figures 5.8 and 5.9, respectively. It can be seen that the coupons tested in tension behaved in a linear manner until failure. The failure was sudden and brittle in nature. All of the coupons experienced tensile failure by the gradual splitting and rupture of the glass fibres at a region close to the gauge length. Having said this, along with considerable delamination due to longitudinal splitting, the surface of the coupons experienced horizontal cracks which were not throughout the thickness but seemed to occur on the top surface of the coupon. The horizontal cracks for some of the coupons occurred at a location close to the tab location while others occurred centrally, as shown in Figure 5.9.

Table 5.3. Results of the coupons tested in tension

Coupon	Tensile Strength $\sigma_{tu,L}$ (MPa)	Modulus of Elasticity in Tension $E_{t,L}$ (GPa)	Tensile Rupture Strain $\varepsilon_{tu,L}$ (%)
T1	359	27.9	1.29
T2	345	28.6	1.21
T3	300	24.1	1.28
T4	296	-	-
T5	290	27.8	1.08
T6	324	21.8	1.48
T7	350	24.6	1.42
Average	323	25.8	1.29
Standard Deviation	28.45	2.7	0.15
COV (%)	8.80	10.5	11.25

Note: Missing values represent strain gauge malfunction and no result could be obtained.

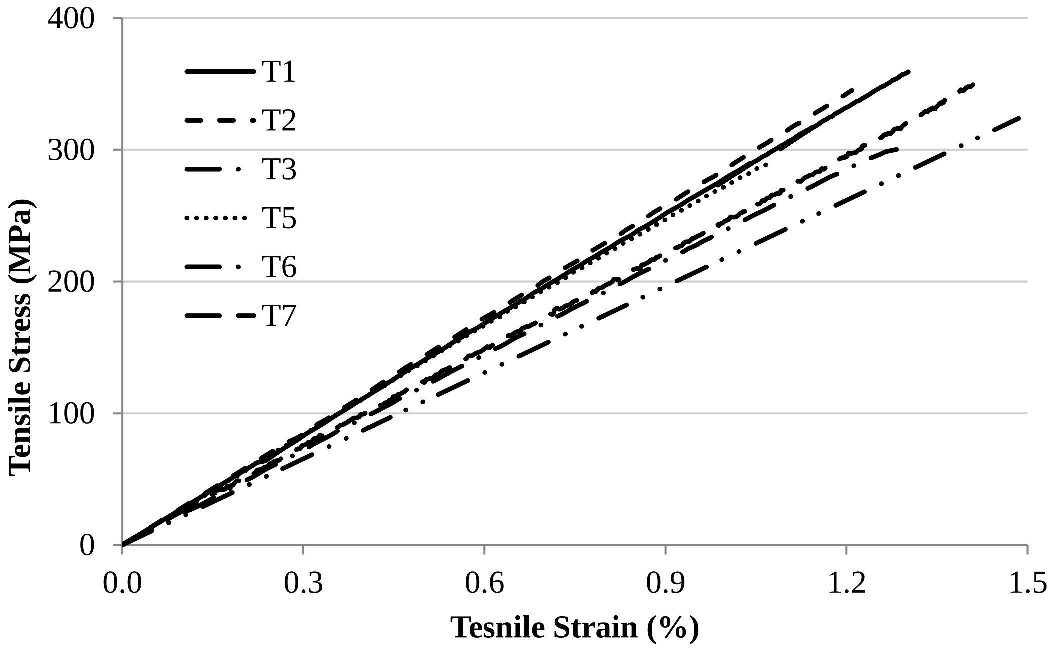

Figure 5.8. Stress-strain relationship of the coupons tested in tension

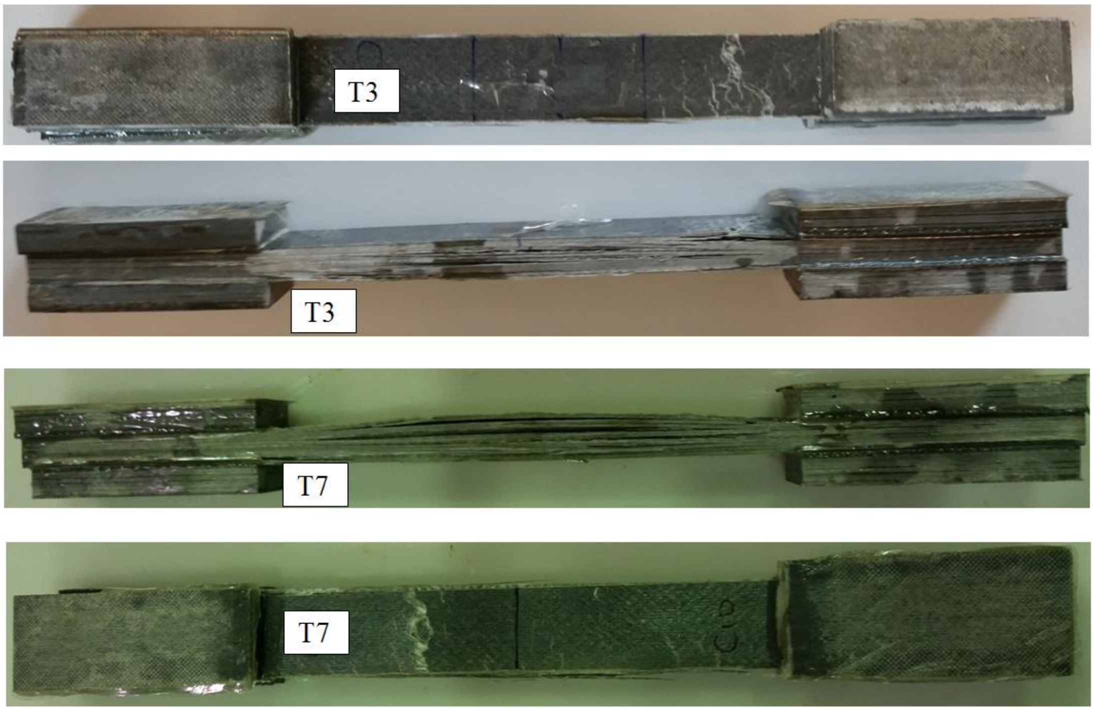

Figure 5.9. Failure mode of coupons tested in tension

The modulus of elasticity in tension was determined as the slope of the stress-strain relationship, with values ranging from 21.8 GPa to 28.6 GPa, with a coefficient of variation of 10.5% obtained. The tensile strengths ranged from 290 MPa to 359 MPa, with an average tensile strength of 323 MPa and coefficient of variation of 8.80% obtained. Furthermore, the average rupture strain in tension was 1.29%. Unfortunately, the strain gauges attached to the coupon instrumented to determine the Poisson's ratio failed and the value could not be established. Therefore, the Poisson's ratio was assumed to be equal to 0.30.

5.2.1.4 In-Plane Shear Properties

The in-plane shear properties were determined based on the 10° off-axis tensile test as outlined in Hodgkinson (2000). One coupon sample from the web of the C-section was extracted at a direction of 10° from the longitudinal plane having dimensions similar to that outlined in ISO 527-4 (ISO 1997). Similar to the tensile testing, this coupon was tested using the 500 kN Instron 8033 testing machine at a loading rate of 2 mm/min with tabs of the same material tested placed at the gripping location.

Therefore, the dimension of the coupon was 250 mm long and 25 mm wide with the tabs at each end being 50 mm long and 28 mm wide producing a test span of 150 mm.

The determination of the shear strength of the coupons was in accordance with formulas provided by Hodgkinson (2000). The failure mode of the coupon testing is shown in Figure 5.10. Typically the shear failure mechanism is along a diagonal line. However, it can be seen that the failure mode seemed to be along a horizontal line. Nevertheless, the average in-plane shear strength based on the testing ($\tau_{u,LT}$) was determined to be 32.5 MPa. The in-plane shear modulus (G_{LT}) could not be obtained accurately. Therefore, a shear modulus value of 3700 MPa was assumed for the GFRP channels. This value is similar to values obtained in the literature for pultruded sections. It should be noted herein that the in-plane shear properties will be denoted as the longitudinal shear properties.

Figure 5.10. Failure mode of coupons tested in 10° off-axis tension

5.2.2 Full-size Compression Testing

To study the structural behaviour of GFRP channels a total of six full-size specimens were tested under uniform axial compression. The lengths of the tested specimens were kept small to prevent the local buckling phenomenon and to ensure specimens failed by pure compression or crushing failure. Therefore two groups of specimens having nominal free lengths of 160 mm and 260 mm were tested. For each length, three replicate specimens were tested making the total number of specimens six. To ensure that the rotations at the ends of the specimens were fully restrained and no warping or bearing failures (end crushing or end brooming) occurred, both ends at a 30 mm length were confined. This was achieved by capping the ends of the specimens with high strength plaster at the top and bottom at a length of 30 mm, similar to what was done for the confined coupons tested in compression. Thus, the nominal free lengths of the two groups of specimens was 100 mm and 200 mm. Herein, the notation of the specimens will be denoted by their free length with the first part representing the free length and the second part representing the specimen number. For example, Specimen 100-2 is the second of the Group 100 specimens tested of the replicate specimens having a free length of 100 mm. The full-size specimens were cut using a wet saw machine. The ends of the specimens were machined to ensure that the loading surfaces were parallel.

The test set up for the compression testing of the full-size channels is shown in Figure 5.11. All of the specimens were tested with the Denison 5000 kN compression testing machine until failure. The loading system comprised a set of high strength steel loading heads which were attached to both ends of the specimens. As mentioned above the capping of the ends of the specimen in the loading heads at a 30 mm length was achieved using high strength plaster as shown in Figure 5.11(a). In addition, to measure the axial displacement of the columns, two linear variable differential transformers (LVDTs) were directly connected to the testing machine at opposite ends [Figure 5.11(b) and 5.11(c)]. It should be noted that considering the short lengths of the specimens, both of the specimens' loading heads were placed on high strength steel plates in order for the LVDT's to take accurate readings. Figure 5.11(b) and Figure 5.11(c) show the typical set-up for Group 100 and 200 specimens, respectively. Furthermore, each specimen was instrumented with four strain gauges of 5 mm gauge length, positioned at mid-height on the webs and the flanges of the specimen [Figure 5.11(d)]. The channels were tested under displacement control with a loading rate of 1.3 mm/min until failure. The loading rate was the same rate as used for the coupons tested in compression as explained above.

(a)

(b)

(c)

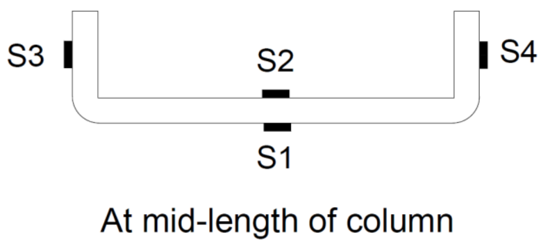

(d)

Figure 5.11. Compression testing set-up for full-size specimens: (a) Loading heads and plaster capping at ends; (b) Test set-up for Group 100 Specimens; (c) Test set-up for Group 200 Specimens; and (d) Strain gauge positioning

The results of the full-size compression testing of the channels are shown Table 5.4. The axial load versus axial deformation of the channels is shown in Figure 5.12. In addition, the stress versus strain of the channels is shown in Figure 5.13. The strain of the specimens was taken as the average of the readings from the attached strain gauges on the web and flanges of the specimen. Similarly, the modulus of elasticity in compression was taken as the average of the initial slope of the stress versus strain relationships.

Table 5.4. Experimental results of the full-size compression testing of the channels

Specimen	$P_{cu,F}$ (kN)	$\sigma_{cu,F}$ (MPa)	$\Delta_{u,F}$ (mm)	E_F (GPa)	$\varepsilon_{cu,F}$(%)
Group 100 Specimens					
100-1	585.1	296.9	2.16	29.7	1.00
100-2	690.7	352.6	2.28	29.3	1.20
100-3[a]	-	-	-	26.4	-
Average	637.9	324.8	2.22	28.5	1.10
Standard Deviation	74.7	39.4	0.09	1.8	0.14
Group 200 Specimens					
200-1	538.7	274.7	2.86	28.1	0.98
200-2	550.0	280.0	3.00	29.2	0.96
200-3[a]	-	-	-	27.6	-
Average	544.3	277.4	2.93	28.3	0.97
Standard Deviation	8.0	3.8	0.10	0.8	0.01

Note: The notation $P_{cu,F}$ is the ultimate load, $\sigma_{cu,F}$ is the ultimate stress, $\Delta_{u,F}$ is the axial displacement at ultimate stress, E_F is the modulus of elasticity in compression and $\varepsilon_{cu,F}$ is the rupture strain at ultimate stress.

[a] The compressive strength and rupture strain results of Specimens 100-3 and 200-3 were omitted due to premature failure. However, the modulus of elasticity in compression of these specimens was used to determine the average modulus of elasticity for all the three specimens per group.

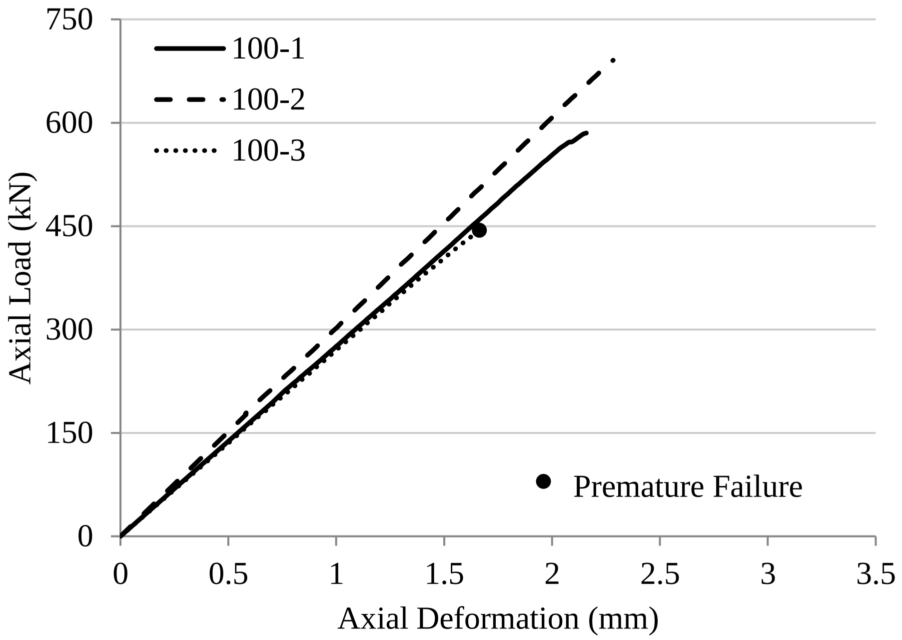

(a)

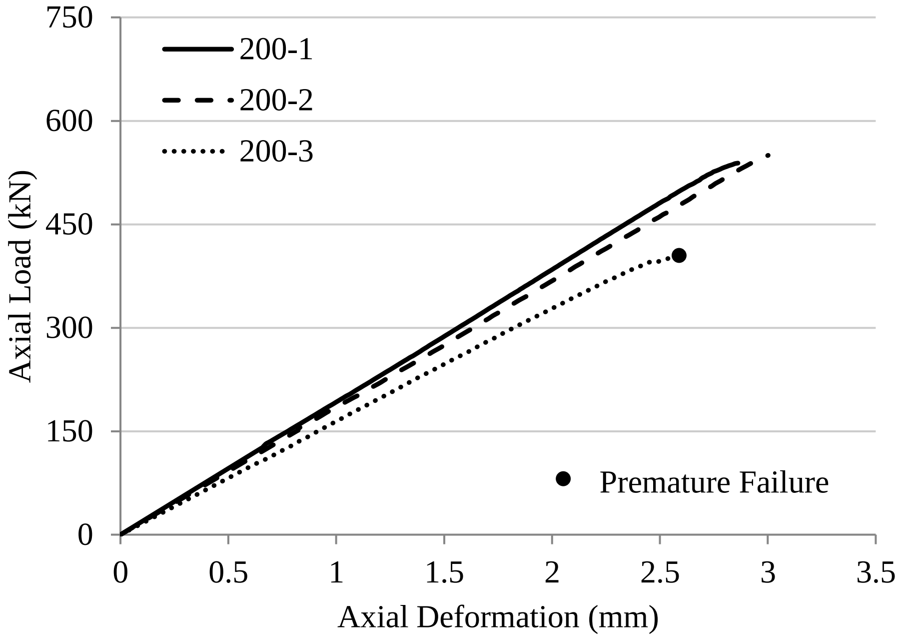

(b)

Figure 5.12. Axial load versus axial deformation relationship of the full-size specimens: (a) Group 100 Specimens; and (b) Group 200 Specimens

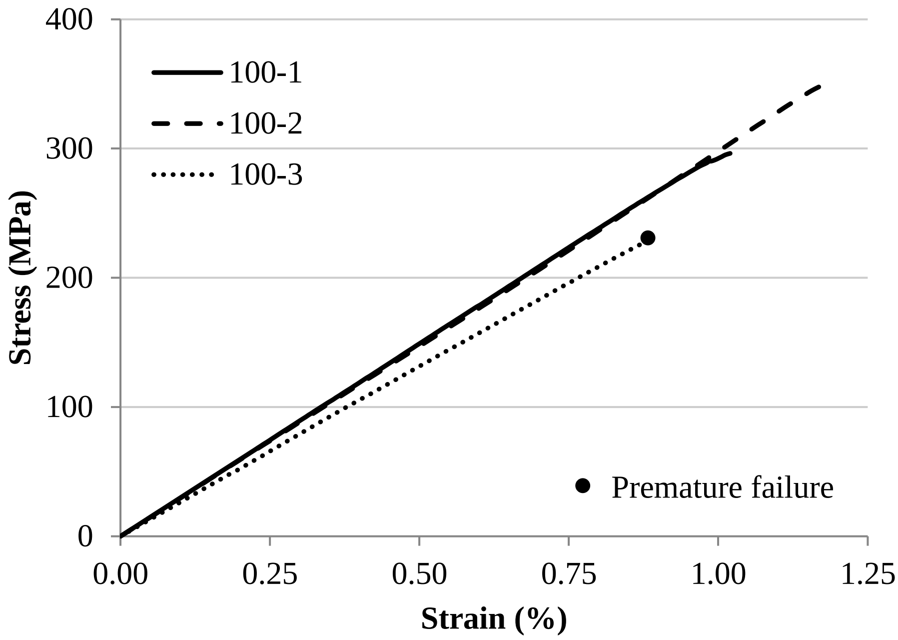

(a)

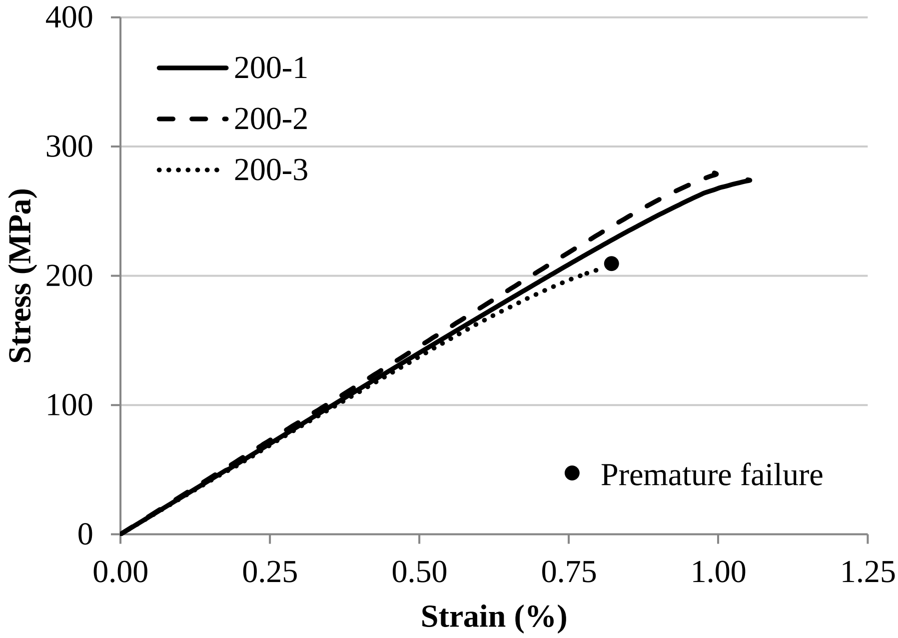

(b)

Figure 5.13. Stress versus strain relationship of the full-size specimens: (a) Group 100 Specimens; and (b) Group 200 Specimens

It can be seen from Figure 5.13 that the full-size channels experienced linear elastic behaviour up until failure. It should be noted that during the latter stages of loading at close to failure, the stress versus strain response of the full-size specimens deviated slightly from the perfectly linear relationship. This may be due to small bending deformations due to possibly the non-symmetrical arrangement of the fibre reinforcement and/or slight buckling of the flanges and webs of the sections. This can be seen from the stress versus strain response of Specimen 200-2 as shown in Figure 5.14. However, in interpreting the results, the deviation from the linear trend for each strain gauge was ignored and the rupture strain was extrapolated similar to the method used for the coupons.

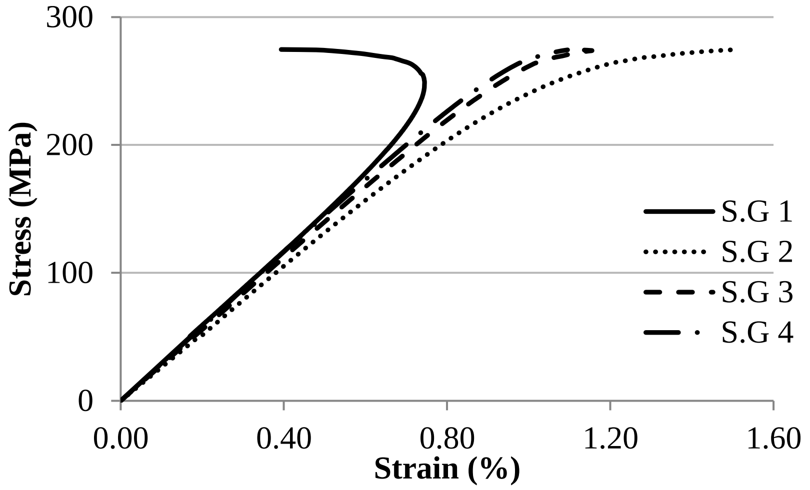

Figure 5.14. Stress-strain response of the strain gauges bonded to Specimen 200-2

For each group of specimens, the last specimen tested (100-3 and 200-3) appeared to fail prematurely. Therefore, the results of these specimens in terms of the compressive strength and rupture strain were omitted when determining the average compressive properties herein. However, the modulus of elasticity in compression for these specimens was included to determine the average modulus of elasticity for the three specimens per group tested, as shown in Table 5.4. Both Specimens 200-1 and 200-2 experienced similar results with an average compressive strength and rupture strain of 277.4 MPa and 0.97%, respectively. However, in comparison to the other two specimens, Specimen 200-3 failed prematurely at a considerably lower rupture strain of 0.75% with a compressive strength of 207.1 MPa. In terms of the specimens with free lengths of 100 mm, Specimen 100-2 achieved the highest strength of 352.6 MPa, which was 18.8% higher than the value obtained for Specimen 100-1. However, Specimen 100-3 appeared to have failed prematurely due to irregularities in manufacturing, which is explained below, with the rupture strain (0.87%) and modulus of elasticity (26.4 GPa) lower than that of the other two specimens. Most notably, the rupture strains of Specimens 100-1 and 100-2 were 1.00% and 1.20%, respectively with the average value of the modulus of elasticity in compression for Specimens 100-1 and 100-2 obtained to be 29.7 GPa and 29.3 GPa, respectively.

Removing the compressive strength and rupture strain results of Specimens 100-3 and 200-3, it can be seen that the average strength and rupture strain of the Group 100 specimens were 17.1% and 13.4% higher than that of the respective average values obtained for Group 200 specimens. On the other hand, at failure the Group 100 specimens displaced axially less than that of Group 200 Specimens, while the modulus of elasticity in compression for both groups of three specimens was relatively similar. Therefore, the smaller the free length the higher the strength obtained. This may stem from the fact that although the Group 200 Specimens were short, local buckling instabilities may have still occurred. This can be evident by the lateral displacements of the Group 200 specimens at the mid-length [Figure 5.15(a)] with no lateral displacements obvious for the Group 100 specimens.

The failure of all the channels was sudden and brittle in nature with no warning signs evident. At failure, both specimens failed with a loud noise, although the 100 mm free length specimens were much louder than that of the 200 mm specimens. The failure mechanism of Specimens 200-1 and 200-2 is shown in Figure 5.15 with both the specimens failing in a similar manner. The front of the web of these channels bowed outwards and the glass fibres at the corner radius severely ruptured resulting in the slight separation of the web and flanges as shown in Figure 5.15(a). The rupture of the fibres at the corner radius occurred along the flange of the channel up until the end of the flange with fibres extruding out at that end location [Figure 5.15(b)]. Interestingly, the back of the webs experienced diagonal cracks appearing to originate from the location of the failure of the flanges and moving inwards towards the centre of the mid-length of the specimen [Figure 5.15(c) and 15(d)]. On the other hand, the failure of Specimen 200-3 was not at mid-length but closer to the top end of the specimen

[(Figure 5.15(e)]. The flange of this specimen severely ruptured with cracks also evident on one side of the web. This unexpected failure may be due to either eccentricity in testing, weakness or stress concentrations in the channels at the failure location or due to the unpredictable nature of the compression behaviour of the material.

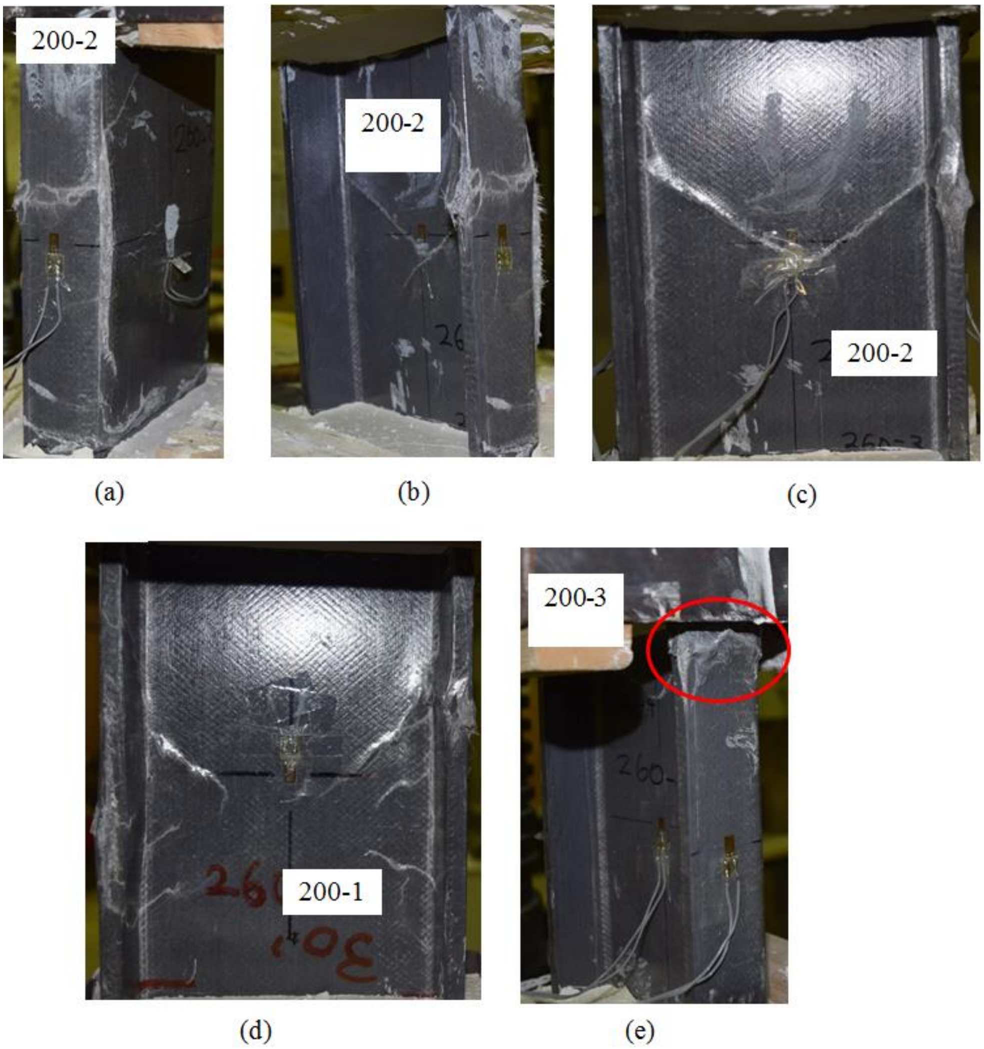

Figure 5.15. Failure mechanism of the 200 mm free length full-size specimens

Unlike the failure mechanism of the Group 200 specimens, Specimens in Group 100 did not fail in the instrumented region but failed close to the ends of the specimens near the plaster support location, as shown in Figure 5.16. This may be due to the relatively short lengths of these specimens. Having said this, the Group 100 specimens achieved a higher ultimate stress as compared to the Group 200 specimens. Specimen

100-1 failed at the location close to the bottom end near the plaster supports. The failure was marked by outward bulging at the front face of the web with horizontal cracks also visible [Figure 5.16(a)]. Similarly, the front face of the web for Specimen 100-2 experienced outwards bulging [Figure 5.16(b)]. When the plaster was removed, cracking was evident in the web of the confined bottom zone. In addition, this specimen experienced the same diagonal cracking as experienced for Group 200 specimens with one edge of the flange severely ruptured [Figure 5.16(c)]. Prior to testing Specimen 100-3, one of the flanges seemed to have defects or irregularities which may have been from the manufacturing process. As a result, upon testing the failure of this specimen occurred due to the glass rupture at this location [Figure 5.16(d)]. It is believed that premature failure due to this area of weakness is the result of the lower than expected ultimate stress.

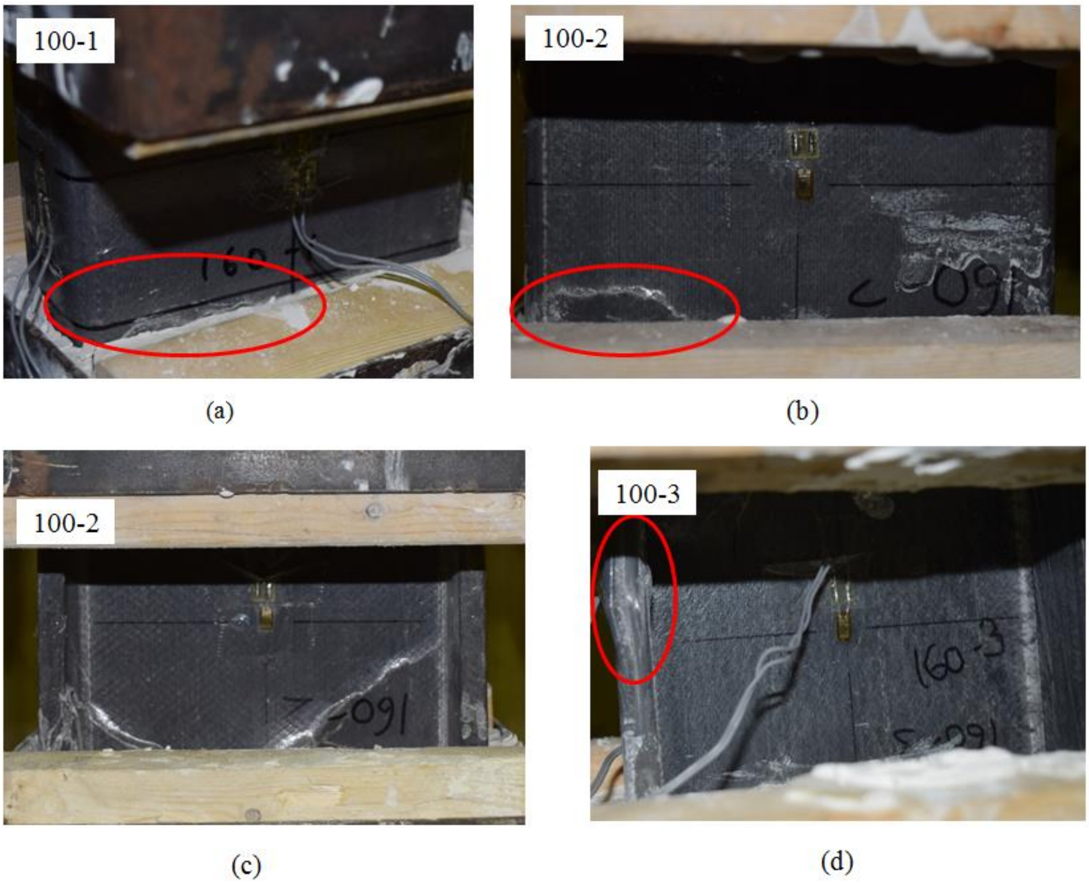

Figure 5.16. Failure mechanism of the 100 mm free length full-size specimens

Considering the brittle and sudden failure of the specimens it is impossible to determine the location of the failure initiation for both groups of specimens. It is assumed that the failure of the Group 200 specimens initiated at the intersection of the web and flanges and then propagated instantly to middle of the web at mid-length. On the other hand, for Group 100 specimens it is assumed that failure was initiated close to the ends. It is possible that for Specimen 100-2 failure may have been initiated close to the end of the specimen and propagated into the gauge length.

5.2.3 Comparison of Coupon and Full-Size Testing in Compression

Table 5.5 summarises the average values of the compression properties obtained for the coupon and full-size specimens. It should be noted that the results of the coupons are for the longitudinal coupons tested with confined top and bottom ends rather than the coupons tested by direct end loading as explained above (Global value in Table 5.2).

As can be seen from Table 5.5, the average compressive strength obtained by the coupons was 303.0 MPa. Therefore, the average compressive strength obtained by the Group 100 full-size specimens was 7.2% higher than the same value obtained by the coupons. On the other hand, the average compressive strength for the Group 200 specimens was 8.4% lower than the value obtained by the coupons. A variation of 7.6% for the compressive strengths was obtained for the coupon testing while a variation of 12.1% and 1.4% was obtained for Group 100 and Group 200 specimens, respectively, taking into account only two specimens were analysed per full-size group. The reason for this could be due to the sample size of the coupons as compared to only two specimens analysed for the full-size testing per like group.

Table 5.5. Summary of compression properties of coupon and full-size specimens

Specimen	Compressive Strength (MPa)	Modulus of Elasticity in Compression (GPa)	Rupture Strain (%)
Coupon[a]	303.0 ± 23.0	24.7 ± 0.7	1.29 ± 0.06
Full-size (Group 100)[b]	324.8 ± 39.4	28.5 ± 1.9	1.10 ± 0.14
Full-size (Group 200)[b]	277.4 ± 3.8	28.3 ± 0.8	0.97 ± 0.01

[a] Results are only for the coupons tested with the ends confined with the compressive properties for both 25 mm (C25) and 37.6 mm (C37.6) confined coupons combined to obtain the average properties, i.e. Global values in Table 5.2.

[b] The compressive strength and rupture strain results of Specimens 100-3 and 200-3 were omitted due to premature failure. However, the modulus of elasticity in compression of these specimens was used to determine the average modulus of elasticity for all the three specimens per group.

Therefore, to provide a conclusive summary of the comparison of the coupon and full-size specimens a larger sample size for the latter specimens is required. In fact, Guades et al. (2014) found from tests on coupons and full-size specimens from pultruded FRP tubes that the compression properties determined by the coupon testing were relatively higher than the results from full-size testing. This was not achieved in this study and it could imply as mentioned above that the compression testing by direct end loading by capping or uncapping coupons produces a smaller value than the actual value due to many factors.

It is interesting to note that the average modulus of elasticity in compression obtained from the two groups of three full-size specimens was similar but higher than the value obtained by the coupons tested. For example, the average compressive modulus of elasticity of Group 100 full-size specimens was 15.4% higher compared to the value obtained by the coupon testing. This may stem from the fact that the coupons instrumented with back-to-back strain gauges achieved different values for the modulus of elasticity for the back and front face of the coupon as explained above and an average of the two was taken to obtain a result.

5.3 Numerical Modelling

To validate the experimental results of the full-size compression testing of the GFRP channels, a numerical model was developed using the finite element modelling software ABAQUS (2013). First the finite element model is explained with the meshing, loading and boundary conditions described. The failure criteria of composite materials are then discussed after which the numerical results are presented and compared with the experimental results.

5.3.1 Numerical Model

The cross-section dimensions of the GFRP channels were taken as the measured dimensions as shown in Table 5.1 with the thickness taken as 9.25 mm, which is the average of the web and flange thickness. The channels were meshed using eight-node doubly curved thick shell elements with reduced integration (S8R). The shell elements were modelled with five section points (SPs) (integration points) through the thickness of the shell. The SP1 represents the bottommost section point, SP3 is the middle section point and SP5 denotes the topmost section point of the selected ply. The GFRP pultruded channels were modelled as composite, laminar and elastic materials. The channels were modelled as composite with a ply count of one. A mesh convergence study was performed with the meshing of the webs and flanges performed at an approximate global size of 1.0, 1.5, 2.0 and 3.0. Slightly varying ultimate stress and strain values were obtained for the four types of meshes analysed. However, meshing of the sections at an approximate global size of 2.0 was deemed to be satisfactory and was utilised. The meshing of the channels and the coordinate system referred to below is shown in Figure 5.17, with the z direction representing the longitudinal direction.

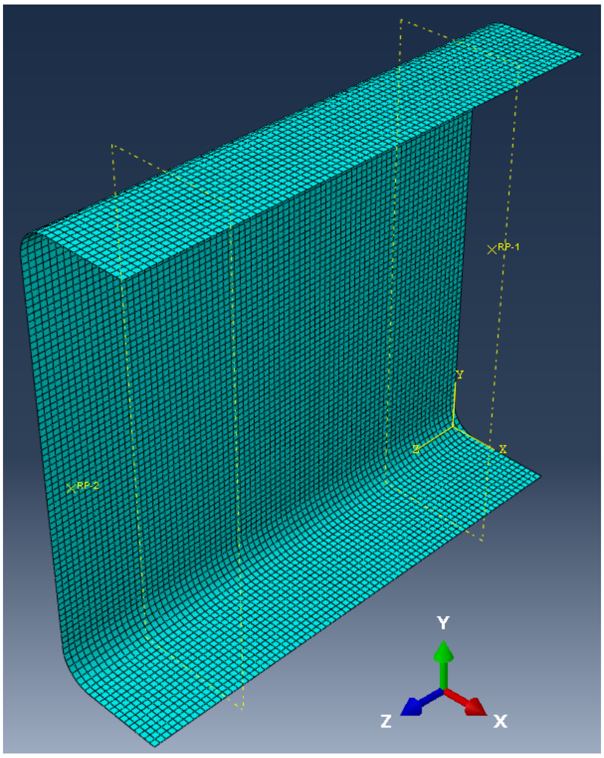

Figure 5.17. Numerical model for compression testing of Group 200 specimens

The elastic and ultimate strength properties inputted into the numerical model are shown in Table 5.6 and 5.7, respectively. These were the average values obtained from the individual coupons tested in tension, compression (confined top and bottom ends) and shear. However, since it was readily impossible to determine all the properties required for the input data in the numerical data due to the dimension requirements of specimens, assumptions were made as follows. The transverse tensile strength was estimated from the assumption that the ratio of the longitudinal tensile to compressive strength was equal to the same ratio in the transverse direction. The longitudinal shear strength ($\tau_{u,LT}$) determined by testing was assumed to be equal the transverse shear strength. Furthermore, the materials longitudinal shear modulus value (G_{12}=G_{LT}) was assumed based on similar results in the literature. In addition, it was assumed that G_{13} is equal to G_{12}. The G_{23} parameter has been set as the resin shear modulus in other studies calculated using the rule of mixtures (Nunes et al. 2016). Considering the resin properties are not known, G_{23} is assumed to equal half of G_{12}. These assumptions are shown on the bottom of the respective tables.

Table 5.6. Elastic properties of the GFRP pultruded sections inputted in the numerical model

Property	Notation from testing	Value (MPa)
E_1	$E_{c,L}$	24700
E_2	$E_{c,T}$	7410[a]
v_{12}	v	0.30[b]
G_{12}	G_{LT}	3700[c]
G_{13}	G_{LT}	3700[c]
G_{23}	$G_{LT}/2$	1850[c]

Notes: The sub notations c denote the property in tension and compression, respectively, while *L* and *T* represent the longitudinal and transverse properties, respectively. The shear modulus is denoted by *G* and ν is the Poisson's ratio.
[a] Based on the results of three coupons tested by direct end loading as explained in "Compressive Properties – Transverse Direction".
[b] No units. The materials Poisson's ratio was assumed.
[c] The materials longitudinal shear modulus value ($G_{12} = G_{LT}$) was assumed based on similar results in the literature. Furthermore, it was assumed that G_{13} is equal to G_{12}. The G_{23} has been set as the resin shear modulus in other studies calculated using the rule of mixtures (Nunes et al. 2016). Considering the resin properties are not known, G_{23} is assumed to equal half of G_{12}.

Table 5.7. Ultimate strength properties of the GFRP pultruded sections inputted in the numerical model

Property	Notation from testing	Value (MPa)
Tensile Strength (*L*)	$\sigma_{tu,L}$	323
Compressive Strength (*L*)	$\sigma_{cu,L}$	303[a]
Tensile Strength (*T*)	$\sigma_{tu,T}$	65[b]
Compressive Strength (*T*)	$\sigma_{cu,T}$	61[c]
Shear Strength (*L*)	$\tau_{u,LT}$	32.5
Shear Strength (*T*)	-	32.5[d]

Notes: The sub notations *L* and *T* represent the longitudinal and transverse properties, respectively.
[a] Average values for the confined coupons having nominal free lengths of 25.4 mm and 37.6 mm. Global value in Table 5.2.
[b] The transverse tensile strength was estimated from the assumption that the ratio of the longitudinal tensile to compressive strength was equal to the same ratio in the transverse direction.
[c] Average values for the confined transverse coupons having a nominal free length of 25.4 mm.
[d] The longitudinal shear strength ($\tau_{u,LT}$) determined by testing was assumed to be equal the transverse shear strength.

It is important to model the boundary conditions to simulate the appropriate end supports and loading. Therefore, one end was fully fixed while the other end (loading end) of the channels was allowed to displace in the longitudinal direction (along the *z*-axis) with all other rotations and displacements in the *x*, *y* and *z* directions constrained. It should be noted that a rigid body constraint was applied to the nodes of both the ends of the specimen and tied in with reference points. The boundary conditions were applied to these reference points. Furthermore, to simulate the confinement effect of the plaster on the top and bottom 30 mm ends of the channels, all the rotations in the *x, y* and *z* directions as well as the displacements in the *x* and *y* directions were constrained to zero for the nodes in this location. The nodes in this confined region were allowed to displace in the *z* direction. Two different lengths were modelled, which were a total length of 160 mm and 260 mm, with 30 mm confinement at the top and bottom of these channels producing a free length of 100 mm and 200 mm, respectively. Based on the meshing explained above, the total number of nodes for the Group 100 and 200 models were 25329 and 41029 nodes, respectively.

A static analysis was performed to obtain the axial stress (*S11*) versus strain (*E11*) response at the node at the mid-height of the specimen using the Unique Nodal output option. The loading was applied such that the maximum displacement in the longitudinal direction on the loading end was set to 5 mm. The failure criteria used to simulate the failure stresses and strains are explained below.

5.3.2 Failure Criteria

It is important to select a suitable failure criterion in any numerical analysis to determine the initiation and propagation of failure in pultruded GFRP sections. There have been several criteria that have been adopted in numerical analyses for pultruded GFRP sections which include the Maximum Stress, Tsai-Hill, Tsai-Wu and the Hashin criterion (Turvey and Zhang 2006 and Nunes et al. 2016). The simplest criterion among them is the Maximum Stress criteria (Jones 1999). This criterion assumes that no interaction in stress occurs and that for a given composite, failure will transpire once either the longitudinal, transverse or shear strengths are reached. On the other hand, the Tsai-Hill and Tsai-Wu criteria examine the interaction between the materials' longitudinal, transverse and shear stresses (Jones 1999 and Tsai and Wu 1971). In both these methods a failure index is computed for each node in the numerical model and once this value is greater than zero in a given node, it implies that the node has failed (Correia et al. 2013). However, in the above mentioned criteria the analysis continues without considering the loss of stiffness of the failed nodes and progressive failure is not taken into account. Therefore, these criteria do not simulate the progressive failure of the composite but only allow for the prediction of failure initiation (Correia et al. 2013).

The Hashin criterion also allows the identification of the failure initiation and models the materials' progressive failure (Hashin 1980; Barbero et al. 2013 and Nunes et al. 2016). In summary, this criterion includes four different and independent failure indexes with the tensile failure modes distinguished from the compressive failure modes. According to the Hashin criterion, a given point is safe if all the failure indexes are less than one. The four failure modes are fibre tension, fibre compression, matrix tension and matrix compression. In this method, ABAQUS requires fracture energy parameters (G_f) to determine the four failure mode indexes. According to Nunes et al. (2016) the determination of the fracture energies of FRP composites is not yet standardized. Therefore, the fracture energy for each failure mode was defined as the area under the stress vs. strain curves obtained from the coupon testing (Nunes et al. 2016).

In this study, the Hashin failure criterion was utilised to determine the numerical failure load of the specimens. The approach to determine the fracture energies of FRP composites discussed by Nunes et al. (2016) was used in this study with the values shown in Table 5.8 calculated based on the coupon testing with the results of the confined coupons (Global values in Table 5.2) used for compression properties. As mentioned above, it is readily impossible to determine the transverse properties due to dimension limitations. Therefore, the fracture energy of the transverse tensile failure mode was calculated by assuming the ratio of the longitudinal tensile to compressive fracture energy was equal to the same ratio in the transverse direction. In addition, a value of 1.0×10^{-5} was used for all the materials' viscosity coefficients while the stress limit was set to zero. In addition, considering the material damage will not be governed by the fibre tension condition, the α parameter in the Hashin damage criterion was kept to the default value of zero (Nunes et al. 2016).

Furthermore, a second method was implemented to determine the numerical failure stress. This was done by analysing the axial stress-strain curve extracted from the numerical models and obtaining the numerical failure stress as the stress corresponding to the average rupture strain obtained experimentally for the full-size specimens.

Table 5.8. Fracture energy corresponding to each failure mode

Failure Mode	Fracture Energy	Value (N/mm)
Longitudinal Tension	$G_{t,L}$	2.08
Longitudinal Compression	$G_{c,L}$	1.95
Transverse Tension	$G_{t,T}$	0.37[a]
Transverse Compression	$G_{c,T}$	0.35

[a] The fracture energy of the transverse tensile failure mode was calculated by assuming the ratio of the longitudinal tensile to compressive fracture energy was equal to the same ratio in the transverse direction.

5.3.3 Numerical Results

The summary of the experimental and numerical failure stresses and strains is shown in Table 5.9. It should be noted that the stress and strain values extracted were for both SP1 and SP5 located on either the inner and outer surface of the shell, respectively. Both the ultimate stresses and strains for both these points are shown in Table 5.9. The values in the brackets are for Section Point SP1 of the shell. The other value is for SP5 which is the higher value and determined to be the critical stress and strain. The difference in values is for the SP5 outputs. As can be seen, the ultimate stress and strain for SP1 and SP5 for the Group 100 specimens were very similar. However, for the Group 200 specimens, the ultimate stress and strain values for SP1 were lower than those obtained for SP5, which could imply the occurrence of some minor bending or buckling.

Table 5.9. Comparison between the experimental and numerical failure stresses and strains

Specimens	Source	Average Compressive Strength σ (MPa)[a]	Difference (%)	Average Rupture Strain ε (%)[a]	Difference (%)
Group 100	Experimental	325	-	1.10	-
	Numerical (Hashin)	226 (223)	-30.5	0.91 (0.89)	-17.3[a]
	Numerical (Exp. strain)	275	-15.4	1.10[b]	-
Group 200	Experimental	277	-	0.97	-
	Numerical (Hashin)	227 (205)	-18.1	0.92 (0.83)	-5.2[a]
	Numerical (Exp. strain)	240	-13.4	0.97[b]	-

[a] The values in the brackets are for Section Point SP1 of the shell. The other value is for SP5 which is the higher value and determined to be the critical stress and strain. The difference in values is for the SP5 outputs.
[b] Assumed equal to the same value as obtained experimentally to determine the numerical compressive strength

For both specimens, the higher value obtained from the section points was assumed to be the failure stress and strain, which was for SP5. In addition, the comparison of the longitudinal stress-strain curve obtained from the numerical analysis using the Hashin failure criterion and the experimental curve of the two groups of specimens are shown in Figure 5.18. The numerical curve was plotted using the SP5 outputs. It can be seen that the slope of the stress-strain curve for the experimentally tested specimens was higher than that obtained by the numerical model. Also, the numerical analyses provided conservative results of the ultimate stresses and strains. Before the results are compared the location of the initiation of failure is discussed.

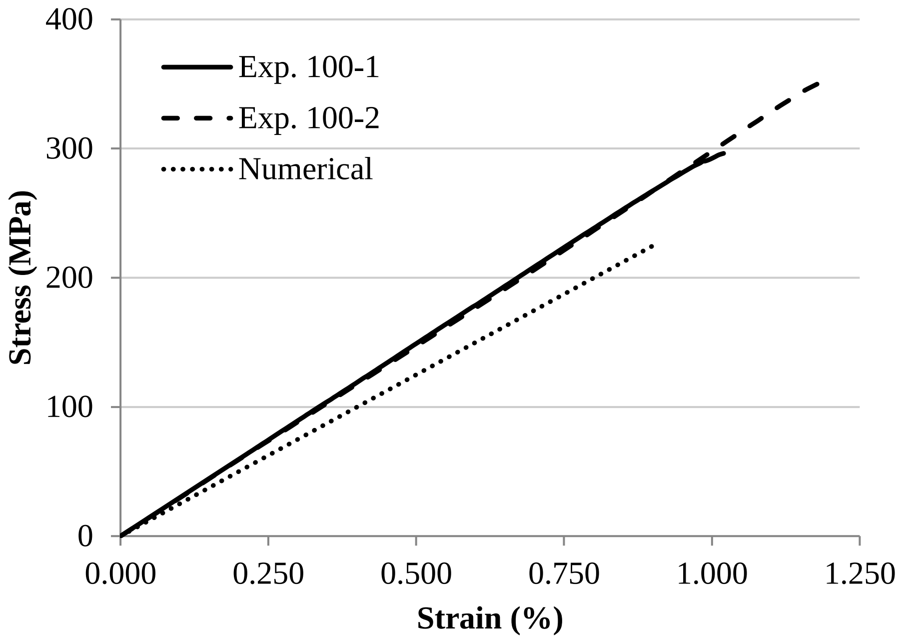

(a)

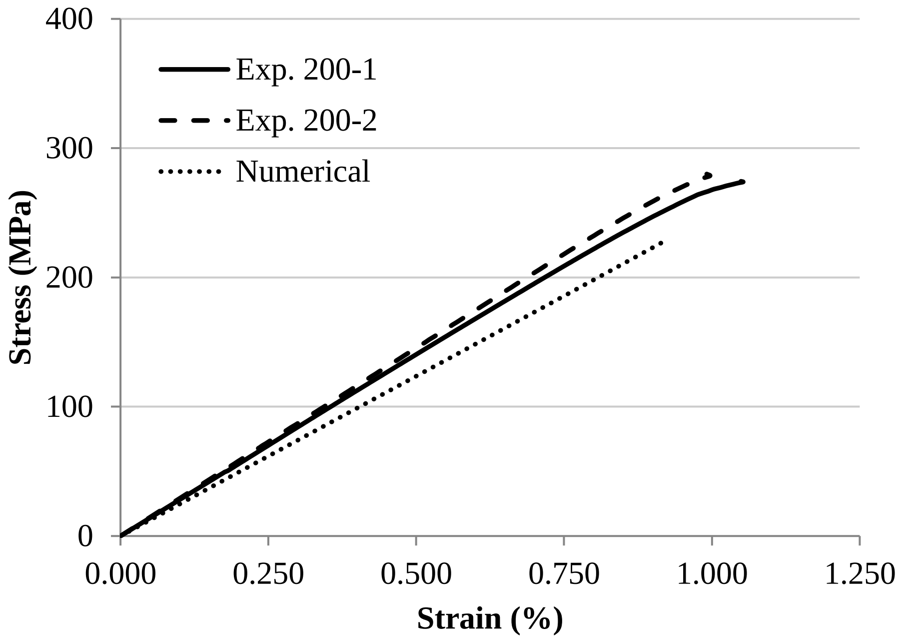

(b)

Figure 5.18. Numerical and Experimental stress versus strain relationship of the full-size specimens: (a) Group 100 Specimens; and (b) Group 200 Specimens

In determining the nodes that triggered the initiation of failure, the ABAQUS software allows the visualization of the Hashin failure indexes pattern for the whole structure. Using this tool, the critical zones where failure is initiated (i.e. index greater than 1) was investigated. For both Group 100 and 200 specimens, the failure location was similar. The nodes in which failure was first initiated were located at the corner radius at the ends of the channels just above the plaster support on all four sides, as shown in Figure 5.19. The colour patterns are symmetrical with a node in the four circular shapes at each of the four corner radii denoting this first failure location. The failure index that first reached the critical value of one was the fibre compressive failure mode, denoted as HSNFCCRT in Abaqus (Figure 5.19). It should be noted that the fibre tensile failure index (HSNFTCRT) was zero throughout the channel length for all stages of loading.

Experimentally, specimens in Group 100 failed close to the ends of the specimens near the plaster support location (Figure 5.16), which is similar to the location predicted in the numerical analysis. On the other hand, for the experimentally tested Group 200 specimens the failure was seen to originate in the instrumented region of the specimen (Figure 5.15). It should also be noted that the experimentally tested Group 200 specimens experienced some lateral displacements which may imply local buckling occurred. This may be the reason the experimental failure location was different to the numerical predictions.

As shown in Table 5.9, the numerical model provided a conservative estimate of the failure stresses and strains of both groups of specimens for both the failure criteria. Most notably, the numerical model implementing the Hashin criterion underestimated the failure stress and strain of the Group 100 specimens by 30.5% and 17.3%, respectively, as compared to the experimental values. On the other hand, the numerical model predicted the failure stress and strain more accurately for the Group 200 specimens, with an underestimation of 18.1% in strength and 5.2% in strain as compared to the experimental values. The conservative results may stem from the fact that it is difficult to obtain the true longitudinal and compressive strengths of pultruded GFRP materials as explained above and these compressive strengths inputted in the model were lower than they should have been.

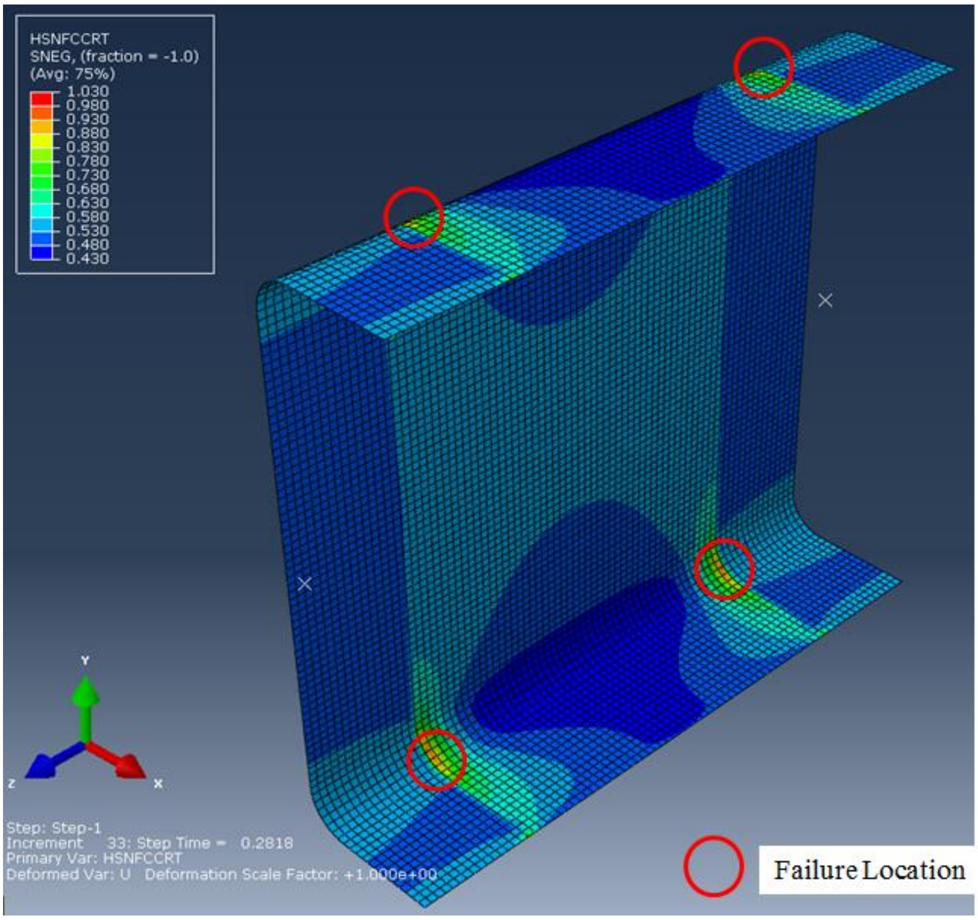

Figure 5.19. Nodes where failure initiation occurred for Group 100 specimens

It should be noted that the numerical failure stress and strain for the two groups of specimens were similar. Furthermore, the numerical stress-strain relationship of both Group 100 and 200 specimens followed the same trend. Having said this, the most accurate approximation of the failure stress was achieved by adopting the failure strain of the specimens obtained from experimental testing and using it in the numerical stress-strain relationship. Using this approach, the difference in the failure stress determined numerically compared to experimentally was 15.4% for the Group 100 specimens and 13.4% for the Group 200 specimens.

5.4 Summary

This chapter explained a study on the compression mechanical properties of pultruded GFRP channels. The mechanical compression properties were obtained by two methods. The first method involved testing coupons extracted from the channels, while in the second method full-size specimens having free lengths of 100 mm and 200 mm were subjected to axial compression. The behaviour and failure modes of the coupons and full-size specimens are discussed and compared. It can be concluded that the compressive properties obtained from the coupon testing by direct end loading showed high variation and could not be obtained accurately due to premature failures associated with end crushing and geometric instabilities. Therefore, a simple fixture was developed to confine the ends of the coupons and prevent the premature failures with more consistent results obtained. In addition, the GFRP channels behaved in a linear elastic manner up until failure. Furthermore, the tensile and shear properties of the channels were investigated. A numerical model was developed using the finite element analysis program ABAQUS to simulate the compressive behaviour of the full-size specimens. A failure criterion was investigated to determine the location of failure initiation. The numerical results showed conservative predictions of the failure stresses and strains as compared to the values obtained experimentally.

The next Chapter discusses the main experimental program of this thesis which investigates the viability of encasing pultruded GFRP sections (I-section and C-sections) in concrete columns and beams and explains the testing of these members under compressive and flexural loading.

6 EXPERIMENTAL PROGRAM

6.1 Introduction

In order to study the axial and flexural behaviour of square concrete members reinforced with GFRP bars and embedded with pultruded GFRP structural sections under different loading conditions, an experimental program was designed and conducted. The main parameters investigated in this study include the magnitude of load eccentricity and type of internal reinforcement with steel reinforced, GFRP-reinforced, GFRP I-section–encased, and GFRP C-sections encased concrete specimens tested under compressive and flexural loading. A total of seventeen RC specimens were tested, of which twelve were tested as columns under compression loading and five were tested as beams under flexural loading. The concrete specimens were square in cross section with a side dimension of 210 mm and a height of 800 mm. The experimental program was carried out at the High Bay Laboratory of the School of Civil, Mining and Environmental Engineering at the University of Wollongong, Australia. This chapter describes the details of the experimental program in terms of the specimen design methodology, specimen preparation, instrumentation and testing procedure. Furthermore, the preliminary testing results of the constituent materials used in the construction of the concrete specimens are explained.

6.2 Design of Specimens

The test matrix was organized to investigate the influence of reinforcement type (steel bars, GFRP bars and encased pultruded GFRP structural sections) and magnitude of load eccentricity on the compressive and flexural behaviour of square concrete specimens. Table 6.1 shows the test matrix. In this study the specimens were classified into four groups: reference steel reinforced (RS), reference GFRP reinforced (RF), GFRP I-section encased (I) and GFRP C-sections encased (C). Each group consisted of four specimens; one specimen was tested concentrically, one tested under 25 mm eccentricity, one tested under 50 mm eccentricity and the last specimen was tested as a beam under four-point bending test. Each specimen had a square cross section with a side dimension of 210 mm and a height of 800 mm. A spare beam specimen was constructed for Group RF.

The notation of the specimens consists of two parts: the first part is either a letter "RS", "RF", "I" and "C" stating the name of the group, and the second part is either "0", "25", "50" or "B" which indicates the eccentricity under which the specimens are subjected to with the letter "B" denoting a beam tested under flexural loading. For example, Specimen RS-50 is a concrete column reinforced with steel and tested with the load applied at an eccentricity of 50 mm.

The reinforcement details of the reference specimens in Groups RS and RF are shown in Figure 6.1(a) and Figure 6.1(b), respectively. The reinforcement details of the GFRP encased specimens are shown in Figure 6.2. The specimens of the first group (Group RS) were considered as a reference group designed with longitudinal and transverse steel reinforcement in accordance with AS3600-2009 (AS 2009). The concrete standard specifies a minimum longitudinal reinforcement ratio of 1%. For this study the internal longitudinal steel reinforcement ratio was designed as the lowest ratio required by the standard. Therefore, the specimens were designed with four N12 (12 mm deformed bars with 500 MPa nominal tensile strength) as longitudinal reinforcement with a reinforcement seel ratio of 1.03%. The shear reinforcement provided was R10 stirrups (10 mm diameter plain bars with 250 MPa nominal tensile strength) spaced at 50 mm centre to centre.

Specimens of the second group (Group RF) were designed to have similar longitudinal and transverse reinforcement ratios as the specimens in the reference steel group (RS) but instead of steel, these specimens were reinforced with GFRP bars. These specimens were designed in accordance with ACI 440.1R-15 (ACI 2015). The spacing of the shear reinforcement for the two reference specimens was dictated by the design of the GFRP reinforced specimens. The amount of stirrups was chosen to ensure that the beam specimen reinforced with GFRP bars would fail in flexure rather than in shear and a consistent reinforcement arrangement was used for all the reference specimens. The expected failure was uncertain and as a result a spare beam for Group RF was fabricated in case shear wrapping was needed to prevent unwanted shear failure for the beam specimen. The nominal diameter of the longitudinal GFRP reinforcement and transverse reinforcement was 12.7 and 9.5 mm, respectively. The geometry of the stirrups used in the reference specimens is shown in Figure 6.3.

Specimens of the third group (Group I) were designed with an encased pultruded GFRP I-section, as shown in Figure 6.2(a). The encased I - section had a nominal height of 152 mm, nominal flange width of 152 mm and nominal thickness of 9.5 mm. The GFRP I-section was completely encased in the concrete specimens for reinforcing purposes. Similarly, specimens of the fourth group (Group C) were designed with encased GFRP C-sections. The C-sections had a nominal height of 152 mm, nominal flange width of 42 mm and a nominal thickness of 9.5 mm, as shown in Figure 6.2(b). Two GFRP C-sections were positioned side by side in a box arrangement to serve as encased longitudinal reinforcement and to confine the internal concrete core.

The GFRP reinforcement ratio of the Specimens in Group I and C were similar, with a value of approximately 9.3% and 8.9% for Group I and C specimens, respectively. Therefore, a direct comparison of the influence of the shape of encased structural GFRP section on the structural behaviour could be analysed from these two groups of specimens. In the design for shear it was assumed that the I-section and C-section would provide some shear resistance in the beam specimens as opposed to the negligible shear resistance of the longitudinal bars in the reference beam specimens. Therefore, specimens in Group I and Group C were provided with steel R10 stirrups (10 mm diameter plain bars) at an increased centre to centre spacing of 100 mm, as compared to the reference specimens.

The main purpose of the stirrups was to: increase the shear capacity of the specimen; confine the concrete core between the web of the I-section and extremities of the specimen; position the C-sections in place as a box arrangement; and to prevent the GFRP sections from outward lateral buckling. It should be noted that the stirrups for these specimens and that of the reference steel specimens were of the same batch but varied with the radius of the bend.

The concrete cover at the top and bottom of the specimens was maintained at 20 mm, while the side covers for all the groups of specimens varied slightly depending on the tolerances in the internal reinforcement cages, as shown in Figure 6.1 and Figure 6.2. For example, the side cover for Groups RS and RF were 17.5 mm while the side covers for Groups I and C were 16 mm.

To ensure the failure mode occurred in the instrumented region of the column specimens (at mid-height) and to prevent premature failure, the ends of each specimen were strengthened and confined with two layers of CFRP sheets in the circumferential direction. However, wrapping CFRP sheets around the sharp edges of square specimens has been reported to result in stress concentration and premature failure at these locations (Ozbakkaloglu 2013c). Therefore, the top and bottom of the specimens at a length of 100 mm were rounded to provide a curved round finish to wrap the CFRP sheets.

A corner radius of 20 mm was applied at these locations. In addition, for each eccentrically loaded column specimen, two layers of CFRP wrap were applied longitudinally on the tension zone in combination with the two layers wrapped circumferentially to ensure no premature tensile failure occurred at these regions. These longitudinal sheets were 100 mm in length.

Furthermore, the five beam specimens were rounded at a radius of 20 mm throughout the length of the specimen. This was done as a precaution if the beam specimens were required to be wrapped by CFRP in the shear zones, at the outer thirds of the beam to ensure failure occurs due to bending rather than shear.

Table 6.1. Experimental test matrix (Hadi and Youssef 2016)

Group	Test Specimen	Longitudinal Reinforcement				Transverse Reinforcement			Encased Sections		Test Eccentricity (mm)
		Material	Number of bars	Diameter (mm)	Reinforcement Ratio (%)	Material	Diameter (mm)	Spacing (mm)	Material	Type	
RS	RS-0	Steel	4	12	1.03	Steel	10	50	-	-	0
	RS-25										25
	RS-50										50
	RS-B										Bending
RF	RF-0	GFRP	4	12.7	1.15	GFRP	9.5	50	-	-	0
	RF-25										25
	RF-50										50
	RF-B[a]										Bending
I	I-0	-	-	-	-	Steel	10	100	GFRP	I - section	0
	I-25										25
	I-50										50
	I-B										Bending
C	C-0	-	-	-	-	Steel	10	100	GFRP	C - sections	0
	C-25										25
	C-50										50
	C-B										Bending

[a] Two specimens were fabricated with one serving as a spare

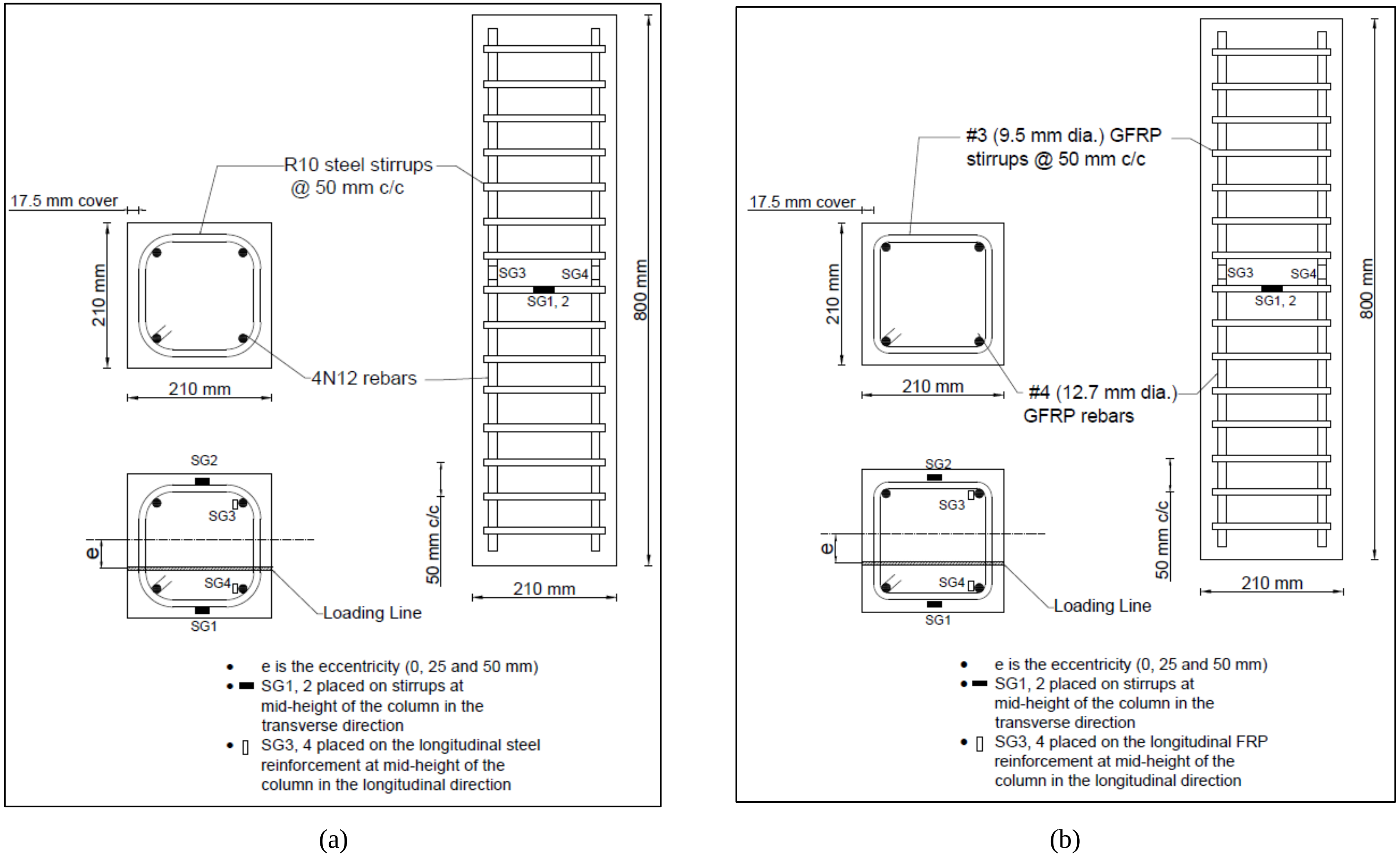

Figure 6.1. Reinforcement details, dimensions and strain gauge setup for the reference specimens: (a) Group RS specimens; and (b) Group RF specimens (Hadi and Youssef 2016)

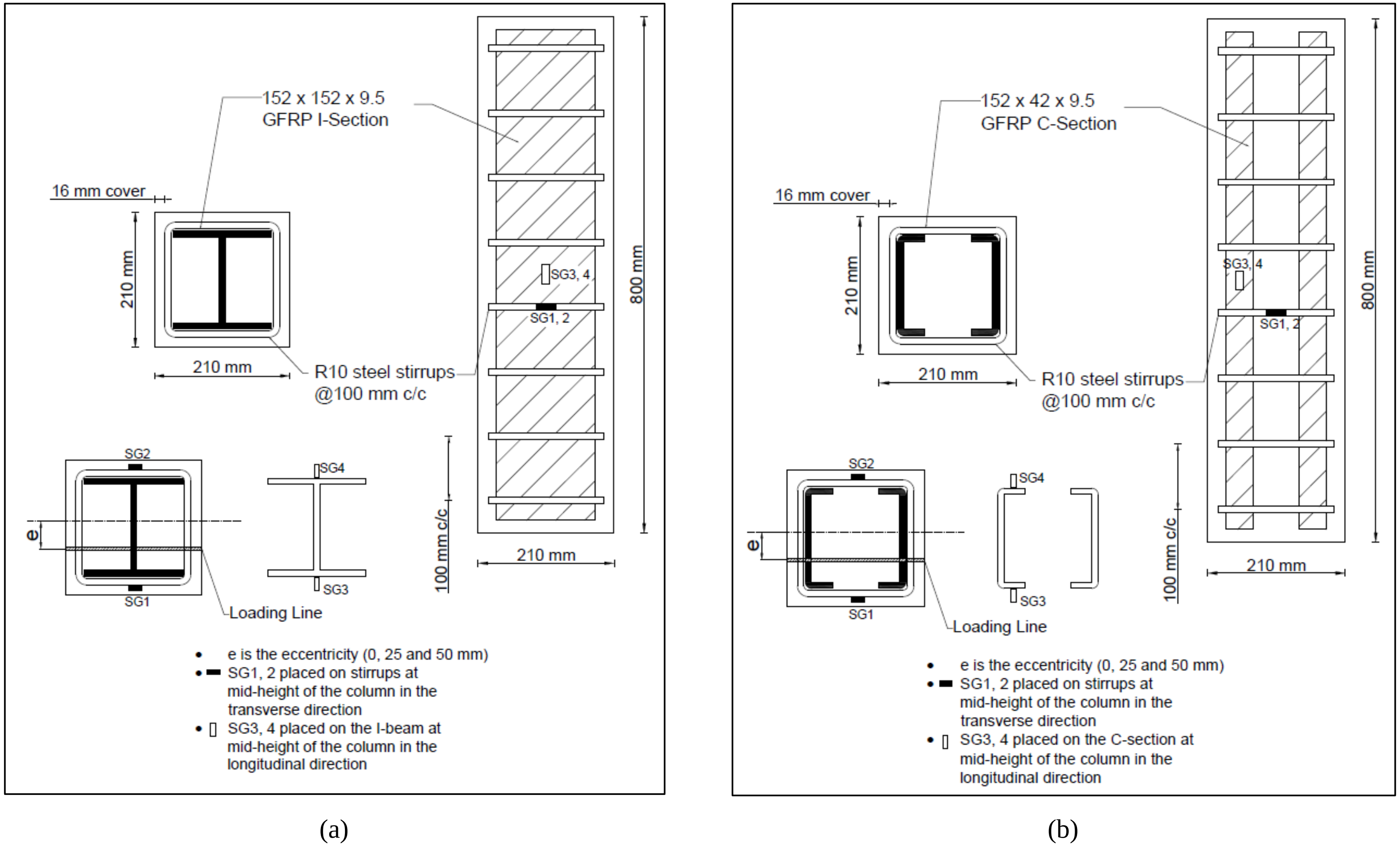

Figure 6.2. Reinforcement details, dimensions and strain gauge setup for the GFRP encased specimens: (a) Group I specimens; and (b) Group C specimens (Hadi and Youssef 2016)

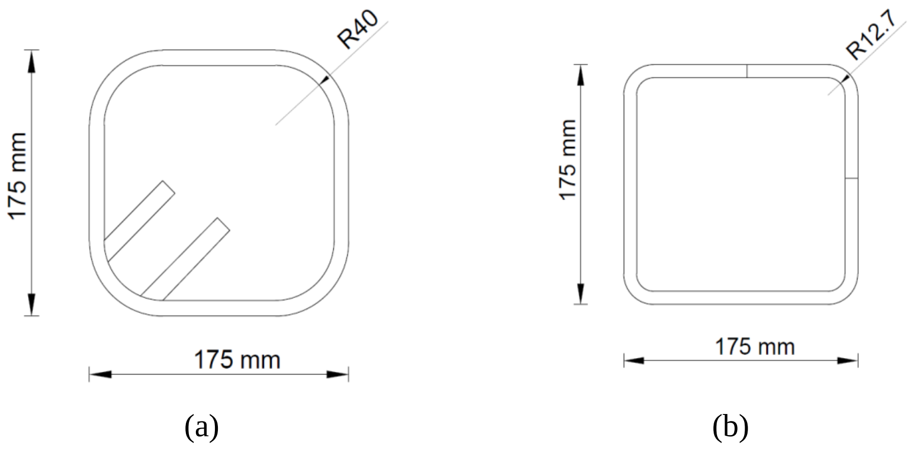

Figure 6.3. Geometry of stirrups (a) Steel stirrups in Group RS Specimens; (b) GFRP stirrups in Group RF Specimens (Hadi and Youssef 2016)

6.3 Specimen Preparation

6.3.1 Formwork

The formwork used for moulding the concrete column and beam specimens was made from 17 mm thick plywood (form-ply). The surface of the plywood was bonded with a resin paper to protect the wood and provide a very smooth finish once the concrete was cured and the form-ply was removed. The edges of the plywood were sealed with an acrylic based paint to maintain the durability and moisture resistance. The formwork fabricated was an integrated set up rather than one formwork per specimen as shown in Figure 6.4. The advantages of an integrated formwork are less material was required, the size of formwork was reduced and the specimen casting process was quicker. Before pouring of the concrete, the formwork was vertically fixed to a base and tied together laterally with timber, in order to prevent any movement while pouring and vibrating the concrete.

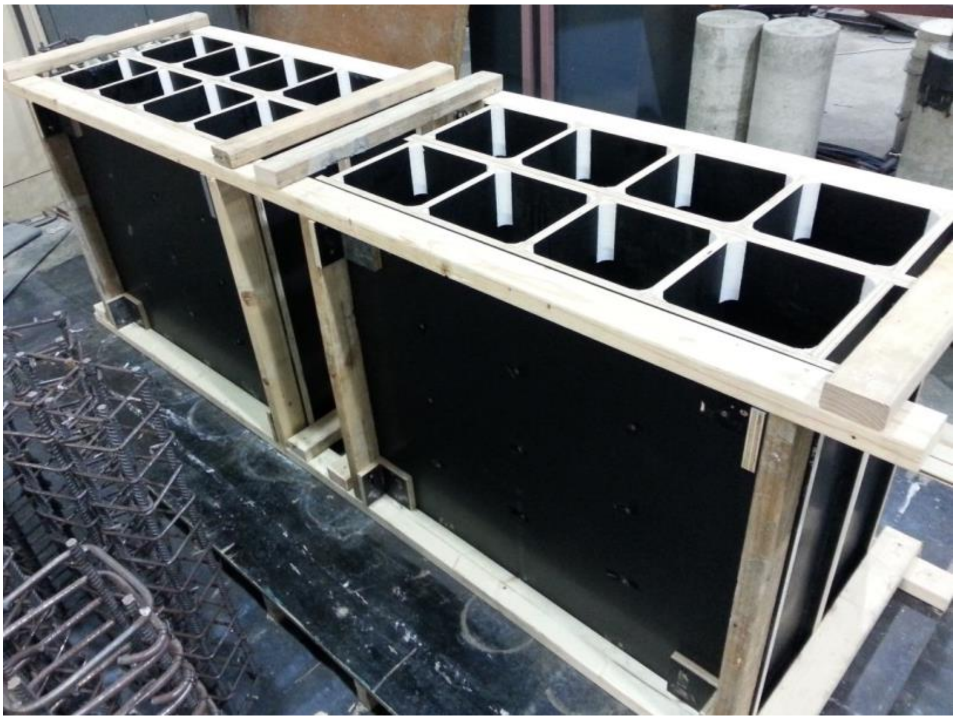

Figure 6.4. The constructed formwork

6.3.2 Reinforcement Cages

The completed reinforcement cages for the four groups of specimens are shown in Figure 6.5. The GFRP square stirrups used in the Group RF specimens were manufactured by Pultrall (2012). GFRP bars cannot be bent after they have been cured (polymerized) and the only way to produce bends was during the manufacturing process.

The radius of the bends of the square GFRP stirrups is 12.7 mm. The steel stirrups used in the Group RS specimens were fabricated having similar dimensions to that of the GFRP stirrups but varied in the radius of the bends, as shown in Figure 6.3.

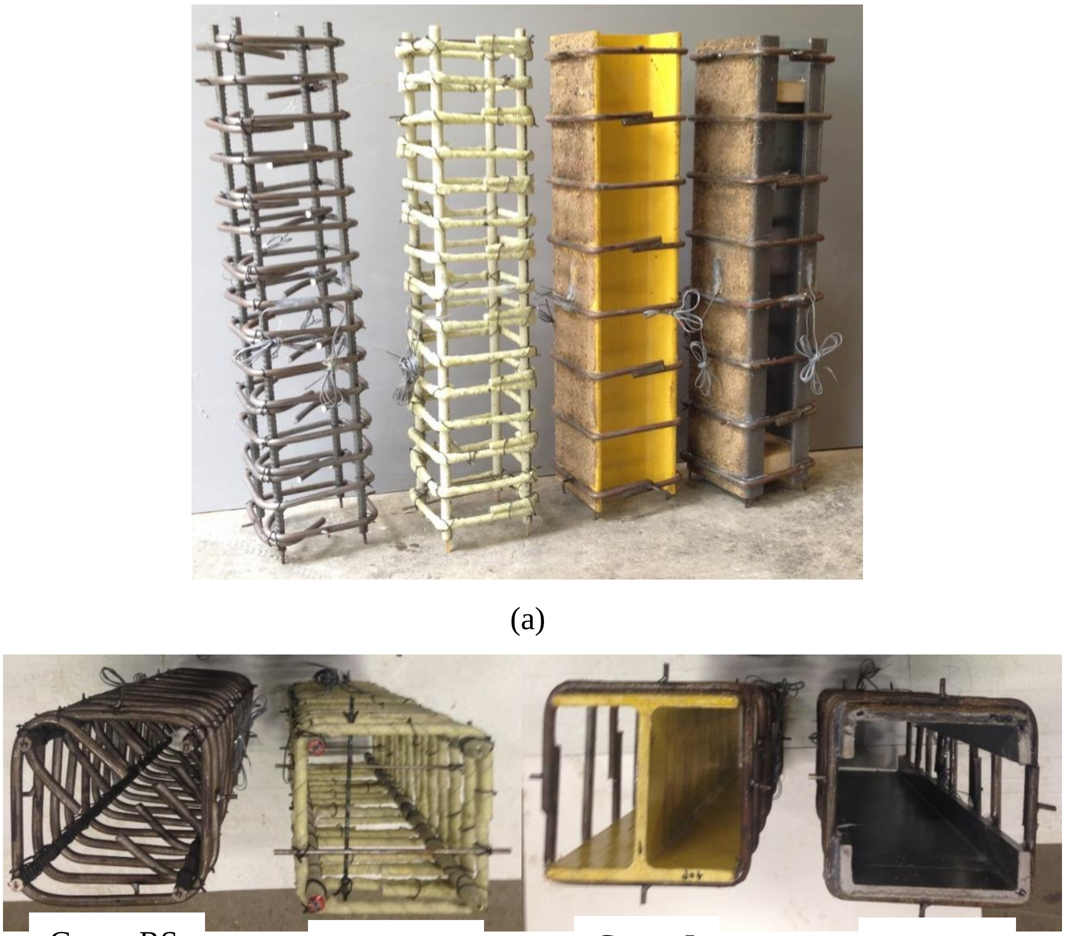

(a)

Group RS Group RF Group I Group C

(b)

Figure 6.5. Completed reinforcement cages: (a) Side-view; (b) Cross-sections

The radius of the bends of the steel stirrups was 40 mm. The difference in corner bend radius of stirrups between the two reference specimens meant that the centre to centre spacing of the longitudinal bars was slightly greater for the Group RF specimens as compared to the Group RS specimens. On the other hand, the steel stirrups for Group I and Group C specimens were fabricated in the lab with a corner bend radius of 6.5 mm, to ensure the stirrups fit over the GFRP sections and maintain the required cover. Furthermore, it can be seen from Figures 6.3 and 6.5 that the hooks of the steel stirrups were long and were kept at that length as it was assumed they would not affect the behaviour of the columns.

For the Group I and C specimens, steel stirrups were bonded onto the GFRP sections with silicone at 100 mm centre to centre spacing. Due to the symmetry of the GFRP sections, hooks could not be made for the steel stirrups. Instead the overlap regions, which were approximately 80 mm long were continuously stitch welded together to ensure the stirrups would provide adequate confinement to the internal concrete core and GFRP sections. The welded overlap regions were positioned to be parallel to the web of the I-section.

The encased section of the Group C specimens consisted of two C sections forming a box section as shown in Figure 6.2(b). To form this profile, a square wooden piece of the required dimension was temporarily glued with silicone onto two C-sections positioned side by side, at both the top and bottom. Once the GFRP C-sections were ready to be placed into the formwork, the wood pieces holding the two sections in place were removed with the steel stirrups holding the GFRP sections in place.

To ensure that the concrete and GFRP sections had adequate bond and no bond-slip occurred, a layer of sand was coated onto the smooth sides of the GFRP I-sections and box C-sections. It was assumed that by coating the largest outside surface area of the sections, an adequate bond would occur between the sections and concrete. Therefore, only the outside faces of both the flanges of the I-section and the long dimension of the C-sections were sand coated along the full height as shown in Figure 6.6. This was done by first applying a thin layer of epoxy resin on the GFRP sections and then placing coarse sand on the resin.

Figure 6.6. Sand coating of the GFRP structural encased sections (Hadi and Youssef 2016)

6.3.3 Strain Gauge Setup

To measure the strains in the internal reinforcement and imbedded sections, strain gauges were bonded to these sections prior to pouring of the concrete. The data obtained from the strain measurement were used for the observation of the stress-strain relationship of the steel and GFRP reinforcements. Strain gauges were attached on steel bars, GFRP bars and GFRP pultruded sections at the mid-height of the specimens on the outside of the longitudinal, transverse and encased reinforcement. The positioning of the strain gauges on the reinforcement is shown in Figure 6.1 and Figure 6.2. Three types of strain gauges supplied from Bestech (2014) were used in this study. Type PFL strain gauge with 10 mm gauge length was used for the steel longitudinal reinforcement, Type FLA, 5 mm strain gauge was used for the steel transverse reinforcement, and Type BFLA strain gauge with 5 mm gauge length was used for all the longitudinal, transverse and encased GFRP reinforcement. The strain gauges were attached on the steel and GFRP reinforcement after the reinforcement cages were constructed. They were then covered with sealant to protect them from the environment.

For simplicity, the placement of the strain gauges for the reference specimens (Groups RS and RF) tested under concentric, eccentric and flexural loading were all the same. For each specimen with longitudinal reinforcement, two couples of strain gauges were bonded to the longitudinal reinforcement at mid-height. However, one strain gauge was placed on the compression side and the other on the tension side for the eccentrically loaded and flexural specimens, as shown in Figure 6.1. In addition, two couple strain gauges were bonded onto the shear reinforcement on opposite sides of the square stirrups to measure the strain in the hoop directions. It should be noted that no strains were measured in the shear zone of the beam specimens.

For the GFRP encased specimens, the eccentric loading is about the major axis which dictated the positioning of the strain gauges on the pultruded GFRP sections. For the Group I specimens, two strain gauges were bonded on the outside flange of the I-section at mid-height in the longitudinal direction, one on the tension side and one on the compression side of the eccentrically and flexurally loaded specimens. Similarly, for the Group C specimens, two strain gauges were placed on opposite sides with one on the tension side and one on the compression side. Only one GFRP C-section per specimen was instrumented with strain gauges which were located on the two flanges at mid-height, as shown in Figure 6.2(b). Two couple strain gauges were also placed on the stirrups in the hoop direction similar to that of the reference specimens.

For the concentrically loaded specimens, the strain results from the two attached strain gauges on the longitudinal reinforcement were used to obtain an average result. Similarly, an average value for the readings on the stirrups was obtained for the concentrically loaded specimens from the two attached gauges.

6.3.4 CFRP Confinement

As mentioned above, for the purpose of avoiding premature failure, the ends of each column specimen were strengthened and confined with two layers of CFRP sheets in the hoop direction. To avoid stress concentrations from the sharp edges of the specimens, rounded styro-foam (polystyrene) sets of 20 mm radius and 100 mm in length were glued to the internal edges of the formwork with silicone at the top and bottom ends to provide a curved round finish to wrap the CFRP sheets, as shown in Figure 6.7. A wrapped column specimen is shown in Figure 6.8. The connection between this corner radius and the sharp edges of the column specimen created a point of stress concentration with the implications on the behaviour as discussed in Chapter 7. In addition, the five beam specimens were provided with 20 mm radius foam sets throughout the length as a precaution if they were required to be wrapped in the shear zones to increase the shear capacity.

After casting, a wet mesh was placed over all the specimens and was watered daily and covered with plastic sheets to maintain the moisture in the concrete and allow for adequate curing. After 28 days of this curing process, the specimens were removed from the formwork and were wrapped with CFRP as explained above. The adhesive used to bond the CFRP to the concrete was a mixture of epoxy resin and hardener at 5:1 ratio.

Figure 6.7. Rounding the edges of the specimens with styrofoam sets

Figure 6.8. Confinement of the ends of the specimens with CFRP sheets

6.4 Material Testing

The materials used in this study were concrete, steel bars, GFRP bars, pultruded GFRP structural sections and CFRP sheets. The results of the material testing are discussed below.

6.4.1 Concrete

Three types of concrete tests were undertaken on the concrete in this study to determine the compressive strength, tensile strength and flexural strength (or modulus of rupture) of the concrete. The tests include compressive strength test, indirect tensile strength test and modulus of rupture test. The test method used for making and curing the compression and indirect tensile test specimens was AS 1012.8.1-2014 (AS 2014a). In addition, the flexure test specimens were prepared by following the test method AS 1012.8.2-2014 (AS 2014b).

The concrete compressive strength was carried out and determined in accordance with AS 1012.9-2014 (AS 2014c). Normal strength concrete having a 28-day compressive strength of 32 MPa was aimed for casting the concrete specimens. A total of twelve cylinders having a diameter of 100 mm and height of 200 mm were tested to obtain the 7, 28, 56, day concrete compression strength. In addition, three cylinders of the same diameter were tested to obtain the concrete strength at the first day of testing the main specimens while five cylinders were tested to obtain the concrete strength at the last day of testing.

The first day after the casting, the concrete cylinders were placed in a water tank for curing. For each day of testing, between three and five concrete cylinders were tested and an average was obtained. Before testing the concrete cylinders, the ends were capped with high strength plaster to ensure full contact between the loading plate and specimen to prevent premature cracking.

The compression testing was conducted on a 180 tonne Avery machine with the load applied at a pacing rate of 17.5% until failure. This is equivalent to the (20±2MPa) compressive strength per minute rate specified by the standard (AS 1012.9-2014). The results of the compression testing are shown in Table 6.2. The average 28-day concrete compressive strength of 29.3 MPa was obtained. In addition, the concrete compression strength at the first day and last day of specimen testing was determined to be 31.00 MPa and 35.30 MPa, respectively.

Table 6.2. Concrete compressive strength test results

Age (days)	Sample no.	Diameter (mm)	Height (mm)	Maximum Load, P (kN)	Compressive strength (MPa)	Average Compressive Strength (MPa)
7	1	100	200	147.5	18.81	18.49
	2	102	200	140.0	17.24	
	3	102	200	157.5	19.41	
28	1	100	201	230.5	29.44	29.26
	2	100	200	229	29.11	
	3	100	201	223	28.36	
	4	102	203	243.5	30.07	
	5	100	203	230.5	29.31	
40 (1st Day of testing)	1	102	204	253	31.24	30.99
	2	100	201	239	30.51	
	3	102	202	253	31.23	
56	1	102	202	241.5	29.81	31.93
	2	102	202	261.5	32.17	
	3	102	201	271	33.40	
	4	100	201	254	32.35	
69 (Last Day of Testing)	1	100	200	285	36.04	35.30
	2	101	201	294	36.34	
	3	100	200	278	35.57	
	4	102	202	274.5	33.85	
	5	102	200	282	34.68	

The tensile strength of the concrete was determined by conducting an indirect tensile strength test (known as the Brazil or splitting test) following the Australian Standard AS 1012.10-2000-R2014 (AS 2000-R2014). A total of five cylinders having a diameter of 150 mm and height of 300 mm were tested at 28 days after casting in the 180 tonne Avery compression machine The average 28-day concrete tensile strength of 2.50 MPa was obtained.

The flexural strength (modulus of rupture) of the concrete was determined in accordance with AS 1012.11-2000-R2014 (AS 2000-R2014). A total of three beams having a square cross section of 100 x 100 mm and length of 500 mm were tested. The beam specimen was placed in a flexure testing apparatus after 28 days after casting and tested under four-point bending in the testing machine until failure occurred within the middle third of the specimens. The average modulus of rupture obtained after 28 days after casting was 4.43 MPa.

6.4.2 Steel bars

Deformed steel N12 bars were used as longitudinal reinforcement in Group RS specimens and plane steel R10 bars were fabricated into square stirrups to serve as transverse reinforcement in Group RS, I and C specimens. Five samples of each diameter were tested in accordance with AS 1391- 2007 (AS 2007) using the 500 kN Instron 8033 machine to determine the tensile properties of the reinforcing steel bars and stirrups. It should be noted that the AS1391-2007 standard was reconfirmed in 2017 as AS1391-2007(R2017).

The total length of the samples was 500 mm while the free length between the machine grips was 340 mm (80 mm grip length provided). An extensometer with a gauge length of 101.6 mm was placed at the mid-height of the specimen to determine the strains of the steel sample, as shown in Figure 6.9. The results of the testing are shown in Table 6.3.

Table 6.3. Tensile properties of the Steel Bars

Bar	Reinforcement	Diameter (mm)	Average tensile yield strength f_{sy} (MPa)	Average tensile yield strain ε_{sy} (%)	Average tensile modulus of elasticity, E_S (GPa)[a]
R10	Transverse	10	326[b]	0.370[b]	191.7
N12	Longitudinal	12	540	0.324	199.8

[a] Calculated as the slope of the elastic linear region of the stress-strain relationship.

[b] Determined by the 0.2% Offset Method

The stress vs strain relationship of one N12 bar and one R10 bar is shown in Figure 6.10. The N12 steel bar experienced strain hardening behaviour with the yield stress easily identified. However, the yield stress of the R10 bar was not easily recognized and was determined using the 0.2% offset method. This offset method is used for materials without a distinct yield load and involves constructing a line parallel to the initial straight portion of the stress-strain curve, but offset by 0.2% from the origin. The intersection of this parallel line with the original stress-strain curve is known as the 0.2% offset yield stress.

Figure 6.9. Tensile testing of steel reinforcement

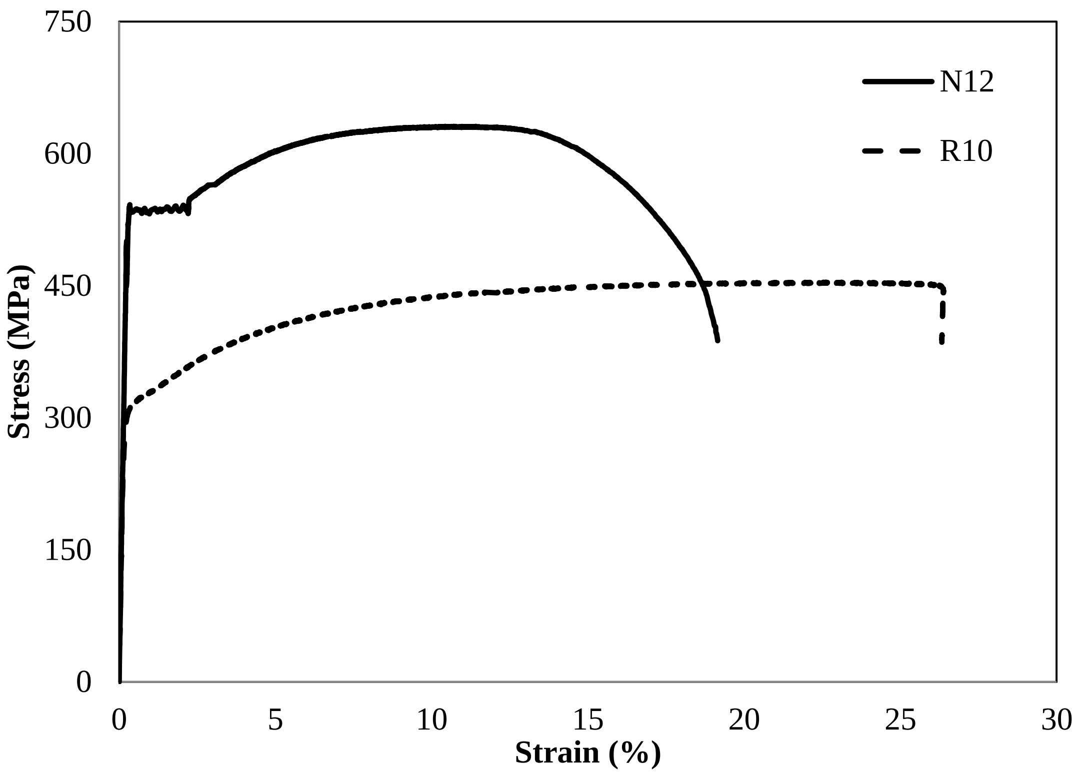

Figure 6.10. Stress – Strain relationship for the steel bars

6.4.3 GFRP bars

Sand coated GFRP bars and GFRP stirrups were used to reinforce the Group RF specimens. The No. 4 (#4) GFRP bars of 12.7 mm nominal diameter were used as longitudinal reinforcement and No. 3 (#3) GFRP bars of 9.5 mm nominal diameter were used as square stirrups for the transverse reinforcement. The GFRP reinforcement was supplied with a sand-coated surface to improve the bond performance between the bars and surrounding concrete. Five samples of the No.4 and four samples of the No.3 bars were tested in accordance with ASTM D7205-11 (ASTM 2011) to determine the tensile properties of the GFRP bars.

The nominal diameter of the GFRP bars does not take into account the layers of sand surrounding it. Therefore, the equivalent diameter and subsequently cross sectional area of the bars including the sand coating was determined by Immersion testing as outlined in ASTM D7205-11 (ASTM 2011). A total of five representative specimens of 200 mm long were cut from each type of bar. The equivalent cross-sectional areas were simply determined as the change in volume of the specimens in the dry and fully immersed states divided by the original length of the specimen. The average results of the cross-section measurements plus the standard deviations are shown in Table 6.4. It can be seen that the nominal diameter is 72.5% and 81.4% of the diameter determined by Immersion testing for the 9.5 mm and 12.7 mm nominal diameter GFRP bars, respectively. However, in this study it is assumed that the sand coating will not contribute to any load carrying capacity. Therefore, the tensile properties were calculated based on the bars standard cross-sectional area determined by the nominal diameter.

Table 6.4. Cross-sectional area measurements of GFRP bars (Hadi and Youssef 2016)

Bar	Nominal diameter (mm)	Standard Cross-sectional Area (mm^2)	Cross-sectional Area by Immersion Testing (mm^2)	Equivalent diameter by Immersion Testing (mm)
#3 (9.5)	9.5	70.9	134.9 ± 8.2	13.1 ± 0.4
#4 (12.7)	12.7	126.7	190.7 ± 9.6	15.6 ± 0.4

In the preparation for tensile testing, steel tubes were provided at the ends of the bars as a load transferring medium and to prevent the bar from slipping. The steel tube was filled with expansive cement known as Bristar 100 as recommended by the test standard, to facilitate the gripping of the GFRP bars. Upon curing, the expansive cement grout exerts a uniform pressure on the bar and allows a small degree of stable and progressive slip as the tensile loading increases (ASTM D7205-11 2011). In reference to the guidelines provided in ASTM D7205-11 (ASTM 2011), the free length (L) for the 9.5 mm and 12.7 mm bars was 400 mm and 500 mm, respectively, while the anchor length (L_a) for both bars was maintained at 380 mm, as shown in Figure 6.11(a). An extensometer was set-up at mid-height of the specimens to determine the longitudinal strain, as shown in Figure 6.11(b). The results of the tensile testing of the GFRP bars are shown in Table 6.5. The stress-strain relationships of the GFRP bars were linear elastic until failure. The failure of the GFRP bars was by the gradual splitting and delamination of the fibres as shown in Figure 6.11(c).

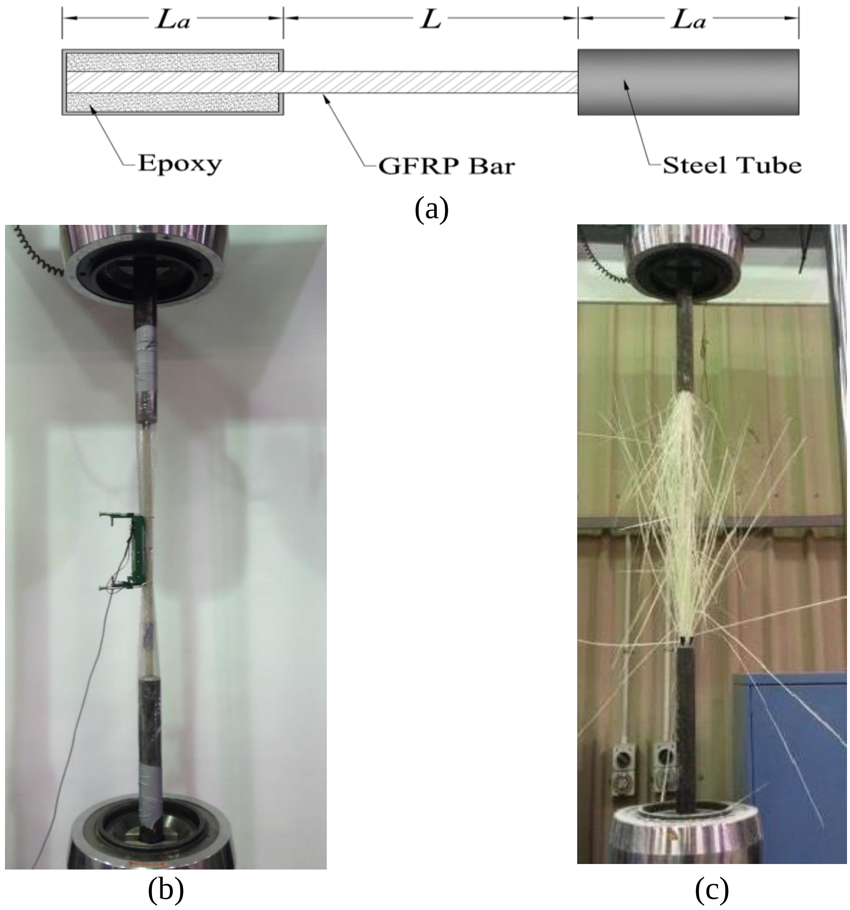

Figure 6.11. Tensile testing of GFRP bars (a) Dimensions of test specimens; (b) Experimental set-up; and (c) Typical failure mode

Table 6.5. Tensile properties of the GFRP Bars (averages and sample standard deviations) [(Hadi and Youssef 2016)]

Bar Size	Nominal diameter (mm)	Tensile strength, f_{fu} (MPa)[a]	Tensile rupture strain, ε_{fu} (%)[a]	Tensile modulus of elasticity, E_{ft} (GPa)[a,b]
#3	9.5	1855 ± 60	2.39 ± 0.12	77.6 ± 1.1
#4	12.7	1641 ± 73	2.41 ± 0.10	67.9 ± 1.3

[a] The material properties calculated are based on the bars standard cross-sectional area determined by the nominal diameter.
[b] Calculated as the slope of the elastic linear region of the stress-strain relationship.

It should be noted that the No. 3, 9.5 mm diameter stirrups made by bending GFRP bars have their own production lot number and thus they were not from the same batch as the No. 3, 9.5 mm diameter straight bars that were tested in tension. According to Ehsani et al. (1995) the minimum ratio of radius of bend to the stirrup diameter is three. However, in this study the radius of bend was only 12.7 mm and the ratio of radius of bend to stirrup diameter was 1.34 due to manufacturing errors. In addition, according to Pultrall (2012) the tensile strength of the GFRP stirrups straight portions is lower than the tensile strength of the corresponding straight bars with the same diameter. However, for the purpose of this study it is assumed that the properties of the tested 9.5 mm diameter straight bars are equal to that of the straight portions of the 9.5 mm diameter stirrups. Furthermore, Nanni et al. (1998) reported that the tensile strengths in the bend portion of FRP bars are 40% to 50% lower compared to that of a straight bar due to stress concentrations or fibre bending. Lastly, due to the small dimensions of the GFRP stirrups, the manufacturing process was by hand which resulted in the regions at the bend radius being relatively square in cross section rather than circular which may have posed a further region of stress concentration.

6.4.4 Pultruded GFRP Structural Sections

GFRP pultruded I-sections and C-sections were used in the specimens of Group I and C, respectively and they were supplied by GRP (Glass Reinforced Products) Australia (GRP 2008) who purchased the sections from China. These GFRP sections are orthotropic materials with the properties varying in each direction. The fibres are laid mainly in the longitudinal direction, which makes these sections stronger in the longitudinal direction as compared with the transverse direction. The I - section had a nominal height of 152 mm, nominal flange width of 152 mm and nominal thickness of 9.5 mm. The C-sections had a nominal height of 152 mm, nominal flange width of 42 mm and a nominal thickness of 9.5 mm. The test method and results of the material testing for the C-sections in compression, tension and shear were discussed in Chapter 5. Therefore, in this chapter only the material properties of the I-section are discussed.

Considering the dimensions of the sections supplied by the manufacturer are nominal, the real values must be established. The external dimensions and wall thicknesses of the I-section were measured with a digital caliper. The average dimensions and standard deviation of six I-sections measured are shown in Table 6.6. As can be seen, some variations between the nominal and measured dimensions were seen for the I-sections. However, these variations are not significant (i.e. the measured dimensions were not less than 95% of the nominal). Furthermore, no significant variations were observed within individual sections, with the coefficients of variations for all the measurements below 1%. It is important to note that the average thickness of the flanges were slightly higher than the average thickness of the webs.

Table 6.6. Cross-section geometry of the GFRP pultruded I-sections

Measurement		I-section
Web thickness, t_{web}(mm)	Nominal	9.50
	Measured	9.25 ± 0.01
Flange thickness, t_{flange} (mm)	Nominal	9.50
	Measured	9.38 ± 0.03
Depth, d_s (mm)	Nominal	152.40
	Measured	151.75 ± 0.12
Width, b_f (mm)	Nominal	152.40
	Measured	152.53 ± 0.05
Cross section area, A (mm^2)	Measured	4092

6.4.4.1 Tensile Properties

The longitudinal tensile properties of the GFRP pultruded sections were determined based on the test method ISO 527-4 (ISO 1997). Five coupon samples from the web of the I-section (IW1-IW5) and five coupons from the flange of the I-section (IF1-IF5) were extracted and tested. The test method, apparatus and dimensions of the coupons were the same as that used for the C-sections as explained in Chapter 5. Furthermore, the dimensions of the coupons and positioning of the strain gauges are shown in Figure 5.7 of Chapter 5.

The sections were too narrow in the transverse direction to enable the extraction of standard coupons with dimensions as specified by the test standards. Therefore, the transverse tensile properties of the pultruded structural sections could not be determined. Three of the coupons from the web of the I-section (IW1-IW3) and two of the coupons from the flange of the I-section (IF2-IF3) were bonded with two back-to-back strain gauges with a gauge length of 12.7 mm positioned at the mid-length in the longitudinal direction. The rest of the coupons were instrumented with one strain gauge at the mid-length. The strain gauges were of type CEA-06-500UW-120. The results of the tensile testing of the coupons in the longitudinal direction are shown in Table 6.7.

The average tensile strength of the web and flanges of the I-section were 386 and 430 MPa, respectively. Also the average modulus of elasticity in tension of the web was 20.79 GPa, while the same value for the flange was 26.02 GPa. Therefore, the average tensile strength as well as the average modulus of elasticity in tension of the flange of the I-section was higher than that of the web of the same I-section.

The results of the tensile testing of the C-sections are shown in Table 5.3 of Chapter 5. Originally, based on the supplier, it was assumed that the GFRP I-section and C-sections were from the same batch. However, from material testing it can be seen that the two shapes of GFRP sections varied in tensile properties as shown in Table 5.3 of Chapter 5 and Table 6.7.

Further examination and investigation of other manufacturer's specifications, testing and fabrication procedures showed that the material properties of different shapes of sections from the same manufacturer vary due to the placement of the rovings through the section and other manufacturing issues. Therefore, material properties vary with the shape of the section regardless if they were of the same material.

Table 6.7. Results of the I-section coupons tested in tension

Coupon Location	Coupon Name	Tensile Strength $\sigma_{tu,L}$ (MPa)	Modulus of Elasticity in Tension $E_{t,L}$ (GPa)	Tensile Rupture Strain $\varepsilon_{tu,L}$ (%)
Coupons from the web of the I-section	IW1	379	20.14	1.88
	IW2	410	20.53	2.00
	IW3	399	20.08	2.00
	IW4	376	21.50	1.83
	IW5	368	21.41	1.72
	Average ± S.D	**386 ± 17.41**	**20.73 ± 0.68**	**1.89 ± 0.12**
	COV (%)	**4.51**	**3.29**	**6.33**
Coupons from the flange of the I-section	IF1	384	25.37	1.51
	IF2	459	24.11	1.93
	IF3	432	29.10	1.48
	IF4	-	27.45	-
	IF5	446	24.08	1.85
	Average ± S.D	**430 ± 32.66**	**26.02 ± 2.20**	**1.70 ± 0.23**
	COV (%)	**7.59**	**8.46**	**13.52**

Notes: S.D is the standard deviation and COV represents the coefficient of variation. Missing values represent strain gauge malfunction and no result could be obtained.

6.4.4.2 Compression Testing

As mentioned in the literature in Chapters 4 and 5, the compression testing of pultruded composites has been widely investigated. The compressive properties of pultruded materials have been reported to be very difficult to measure, most notably when using the end loading method. Hodgkinson (2000) reported that the compression testing of pultruded samples is difficult due to the high longitudinal strength and low transverse strength of the material (Hodgkinson 2000). This difficulty is also due to the strong tendency of the material toward premature failure due to geometric instability, local end crushing, or local end brooming. Furthermore, the property measured may not be the actual compressive strength but represent the composite bearing strength and the direct end loading of the samples is not possible to determine the compressive strength (Barbero et al. 1999).

The compression properties of the C-sections were determined by both direct end loading coupons and also by using a simple fixture to confine the ends of the coupons and prevent the premature failures associated with end crushing, as explained in Chapter 5. However, due to the materials and resources available, the compression properties of the I-sections were determined only by direct end-loading.

A total of seventeen coupon samples from the web of the GFRP I-section and seventeen coupons from the flange of the I-section with nominal dimensions of $9.5 \times 12.7 \times 37.6$ mm were extracted in the longitudinal direction using a wet saw machine from the sections. The same testing procedure and apparatus as used for the C-section coupons were used for the I-section coupons. A total of seven samples each from the web and flange of the I-section were instrumented with one strain gauge at mid-length to measure the modulus of elasticity in compression. The test method includes coupon dimensions for strength and modulus of elasticity measurements. For the purposes of the I-sections the dimensions required for modulus of elasticity measurements was utilized with 37.6 mm long coupons tested.

The longitudinal compressive strengths (in MPa) for the coupons from the web in ascending order are 157, 176, 179, 185, 185, 185, 188, 190, 195, 197, 212, 229, 244, 249 and 250. The longitudinal compressive strengths (in MPa) for the coupons from the flange in ascending order are 160, 188, 191, 192, 194, 199, 200, 202, 224, 247, 248, 254, 255, 256, 259 and 273. The moduli in compression for the web (units in MPa) in ascending order are: 18.2, 19.7, 21.3, 21.3, 22.1, 22.7 and 25.6. The moduli in compression for the flange (units in MPa) in ascending order are: 18.7, 20.0, 22.1, 23.0, 24.2, 24.5 and 24.6. Therefore, the average modulus of elasticity in compression and standard deviation for the web was 21.6 and 2.3 MPa, respectively. The average modulus of elasticity in compression and standard deviation for the flange was 22.4 and 2.3 MPa, respectively. Therefore, using both the testing from the web and flange, the total global average of the compressive strength and modulus of elasticity in compression for the I-section were 212 MPa and 22.0 MPa, respectively.

The majority of the coupons failed prematurely due to end crushing or end brooming. Therefore, the average compressive strength of the coupons could not be calculated based on all these data points because the majority of these coupons failed prematurely. Therefore, the comparison of the compression properties for the I-section and C-section could not be investigated.

However, as mentioned above, the material properties of different shapes of sections from the same manufacturer vary due to the placement of the rovings through the section and other manufacturing issues. Therefore, although both shapes of GFRP pultruded sections are from the same manufacturer it is assumed that the material properties are not identical herein. Having said this, for all the loading cases, the Group I and Group C specimens behaved in a similar manner both based on the stress and strain relationships as well as the failure mechanisms, which will be explained in Chapter 7. Therefore, although the material properties of both the sections were not similar, a comparison of the general structural behaviour of both these two groups of specimens could be established.

6.4.5 CFRP sheets

The ends of each specimen were wrapped with CFRP to ensure failure occurs in the instrumented regions of the columns as explained above in Section 6.3.4. In addition, some of the beams may have been required to be wrapped with CFRP sheets in the shear zone to ensure failure occurred by flexure rather than shear. Since the CFRP sheets are only preventing certain failure modes and do not add to the structural capacity of the members, testing of this material was not required for the purposes of this study.

6.5 Instrumentation and Specimen Testing

All of the specimens were tested with the Denison 5000 kN compression testing machine until failure. The column specimens were capped with high strength plaster at the top and bottom ends to ensure the bearing surfaces were parallel and the load was distributed evenly during testing. The typical compression testing setup of the column specimen is shown in Figure 6.12. The eccentric load was applied to the column specimen by an eccentric loading system manufactured at the University of Wollongong, as illustrated by Hadi and Widiarsa (2012) and shown in Figure 6.12.

The loading system comprised a set of high strength steel loading heads which were attached to both ends of the columns. The loading heads consisted of two parts: a 50 mm thick square plate, called the adaptor plate and a 25 mm thick bottom plate that had a ball joint, known as the bottom plate. The eccentric load was applied to the column by the interaction of the adaptor plate and bottom plate. The load generated by the testing machine was transferred to the adaptor plate by the bottom plate through the ball joint. The ball joint was offset from the centre of the column by the amount of eccentricity required (25 or 50 mm). For columns tested under concentric loading, only the adaptor plate was used to apply the load. The line of application of eccentric load for the column specimens is shown in Figure 6.1 and Figure 6.2.

External instrumentation was used to obtain the displacement data of the column specimens. To measure the axial displacement of the column specimens, two linear variable differential transformers (LVDTs) were directly connected to the testing machine at opposite ends. In addition to this, for the eccentrically loaded columns a laser triangulation was positioned horizontally at mid-height of the columns on the tension side in order to measure the lateral deflections (δ) as shown in Figure 6.12(a). The LVDTs, laser triangulation and strain gauges were connected to a data logger to record readings on a control computer at a user controlled time interval. Depending on the amount of data, the time interval for recording of the data varied from 2 to 5 seconds.

The data read from the instrumentations and strain gauges were recorded at the same time as the load data were recorded by the testing machine. Prior to the start of testing, calibration was carried out to ensure the specimens were placed at the centre of the testing machine and the instrumentations were positioned and operating adequately. The concentrically loaded specimens were initially preloaded to approximately 10 – 20 kN and then tested under displacement control with a loading rate of 0.3 mm/min until failure. On the other hand, the eccentrically loaded specimens were initially loaded to 100 kN (approximately 10% of the anticipated ultimate capacity) under force control with a loading rate of 2.5 kN/s and then unloaded to a load of 20 kN to ensure adequate contact between the loading plates. The test was then resumed using displacement control with a loading rate of 0.3 mm/min until failure of the specimens.

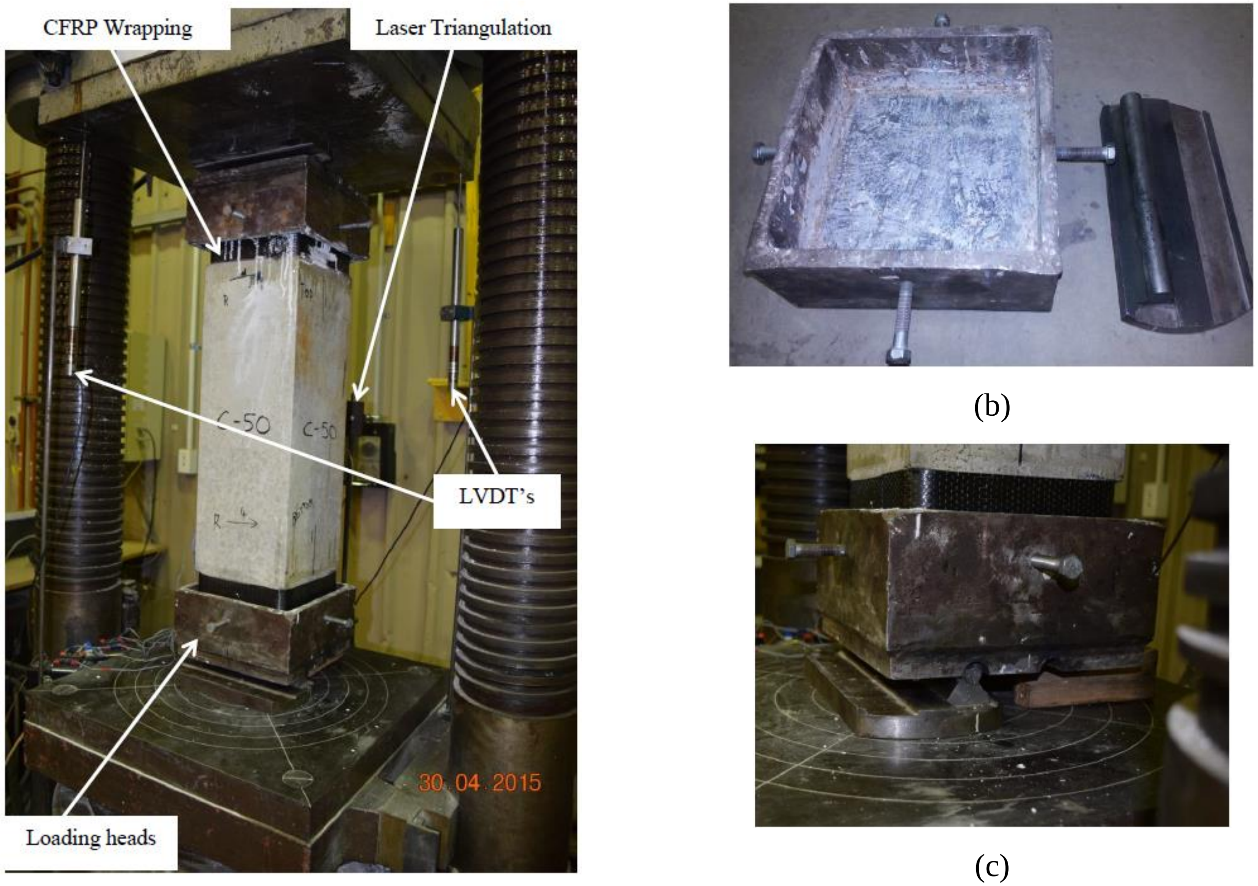

(a)

(b)

(c)

Figure 6.12. Eccentric loading setup: (a) Loading system; (b) Eccentric loading heads; and (c) Interaction of eccentric loading heads (Hadi and Youssef 2016)

As highlighted above, five of the specimens were tested as beams under flexural loading in order to determine the flexural capacity. The beam specimens were subjected to pure bending by a four-point bending system manufactured at the University of Wollongong, as described by Hadi and Widiarsa (2012). The typical flexural testing setup of the beams is shown in Figure 6.13. The bottom rig was placed diagonally on the bottom plate of the testing machine with the beam specimen then placed on top of the bottom rig. The top rig was then placed on the top of the beam.

The beams were loaded with a pin support at one end and a roller support at the other. In addition, one contact area on the top rig was provided with a roller. To measure the mid-span deflection of the beam, a laser triangulation was placed vertically underneath the bottom rig through which the laser is shot through a slot in the bottom rig.

The test for the beams initially started with force control at a loading rate of 2.5 kN/s up to a load of 25 kN (approximately 10% of the anticipated ultimate capacity). This level of preload ensured the proper interaction of the steel rigs and specimen at the start of testing. The test was then continued using displacement control under a loading rate of 0.3 mm/min until failure of the specimens.

During testing there were issues with the premature failure mechanism of the beams due to bearing failure. The next chapter detailing the experimental results will describe this problem and solutions in detail. For each of the column and beam specimens, the test was terminated either once the load dropped down to approximately 35% of the first maximum peak load or due to the failure of the GFRP reinforcements.

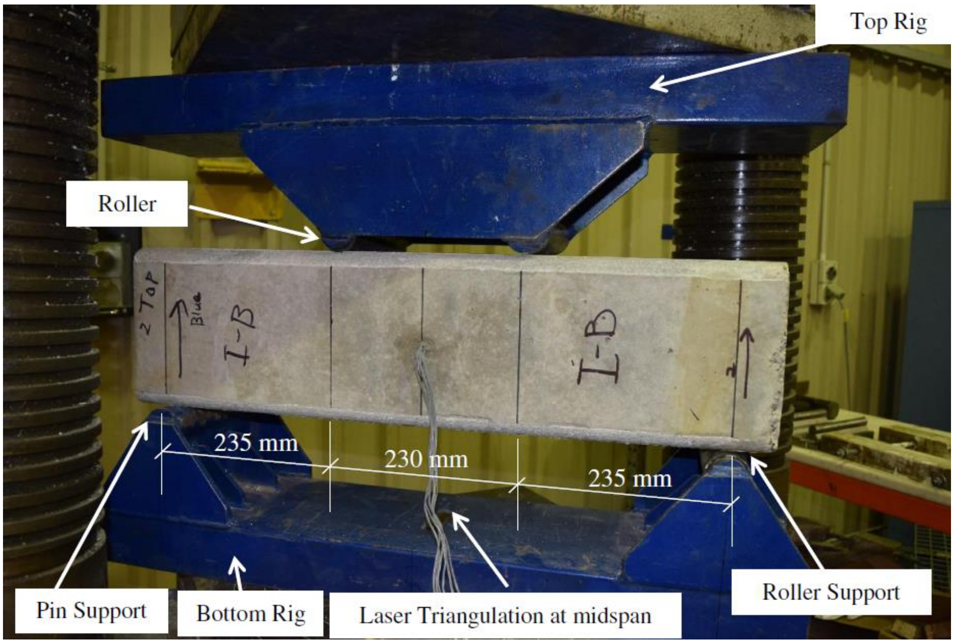

Figure 6.13. Typical flexural testing setup (Hadi and Youssef 2016)

6.6 Summary

This chapter explained the specimen design methodology, specimen preparation, instrumentation and testing procedure for the experimental program of this study. Preliminary testing of the materials used in this study was also described and the material properties summarised. A total of seventeen square specimens subdivided into four different groups were designed and tested. The first group was reinforced with conventional steel bars and stirrups whereas the second group was reinforced with GFRP bars and stirrups. The third and fourth groups were embedded with GFRP structural sections of I-sections and C-sections, respectively. Each group consisted of three columns that were tested in compression under different eccentricities and one beam tested under flexural loading. The aim of the study was to investigate the influence of eccentricity, type of internal reinforcement and presence of embedded GFRP structural sections on specimen load carrying capacity and structural behaviour.

The next chapter presents analyses of the results of the experimental tested specimens outlined in this chapter. The strength, ductility and failure modes of the experimentally tested specimens are discussed.

7 EXPERIMENTAL RESULTS

7.1 Introduction

As explained in Chapter 6, a total of seventeen square specimens subdivided into four different groups were designed and tested. The specimens of the first group were reinforced with conventional steel bars and stirrups whereas the specimens of the second group were reinforced with GFRP bars and GFRP stirrups. The specimens of the third and fourth groups were embedded with GFRP structural sections of I-sections and C-sections, respectively. Each group consisted of three column specimens tested under different eccentricities and one beam specimen tested under flexural loading. All the specimens were tested in the Denison 500 tonne compression testing machine. External and internal instrumentation were used on the specimens to obtain the relationships of the applied axial load and the corresponding axial and lateral displacements. Based on these relationships, the strength, ductility and failure modes of each group of specimens under different types of loading were analysed. This chapter explains the results of the experimental program.

7.2 Behaviour of Column Specimens

To analyse the structural behaviour of the column specimens, the relationship of the applied axial load and the corresponding axial and lateral displacements were plotted. Based on these relationships, the strength and ductility of each group of specimens under different types of eccentric loading were analysed.

Ductility can be defined as the ability of a structural material to deform plastically without fracturing. Ductility is commonly measured by the ratio of the ultimate displacement (δ_u) divided by the yield displacement (δ_y), which can be written as follows:

$$\lambda = \frac{\delta_u}{\delta_y} \tag{7.1}$$

The yield displacement is assumed to be the axial displacement at the yield load or at the limit of the elastic behaviour, as defined by Pessiki and Pieroni (1997). Various authors have used different percentages of the peak load to calculate the corresponding ultimate displacement. Pessiki and Pieroni (1997) calculated the ultimate displacement as the axial displacement at an axial load equal to 85% of the peak load in the descending part of the axial load – displacement curve. Other research studies calculated the ultimate displacement at 80% of the peak load (Sheikh and Legeron 2014).

In this study two methods were used to calculate the ductility of the columns. For the first method the ductility (λ) was calculated based on the ratio of the ultimate displacement (δ_u) divided by the yield displacement (δ_y), as shown in Equation 7.1. In terms of notation herein, P_{max} is the first maximum load achieved just after the initial linear region and P_{peak} is the peak load after concrete cover spalling and is obtained for columns experiencing a strength increase after concrete spalling ($P_{peak} > P_{max}$). For the steel-reinforced columns, no increase in strength occurred after concrete spalling and the ultimate displacement was taken at 80% of P_{max}, as shown in Figure 7.1. However, for the GFRP-reinforced and GFRP-encased columns, the ultimate displacements were taken at either the first fracture load of the GFRP reinforcement ($P_{fracture}$), at the peak load (P_{peak}), or at 80% of P_{peak}, whichever gave the smallest axial displacement. For GFRP-reinforced columns experiencing an increase in strength after concrete spalling it was safer to define the ultimate displacement at this peak load rather than at 80% of peak load considering the unpredictable and sudden brittle failure of the internal GFRP reinforcement after peak load. This is further discussed in the sections below.

For the second method, the ductility was calculated based on the ratio of the area under the axial load-displacement curve up to the ultimate displacement (A_2), divided by the area under the curve up to the yield displacement (A_1), which is written as follows:

$$\lambda = \frac{A_2}{A_1} \tag{7.2}$$

The same definitions of the ultimate and yield deflections were used for the two methods.

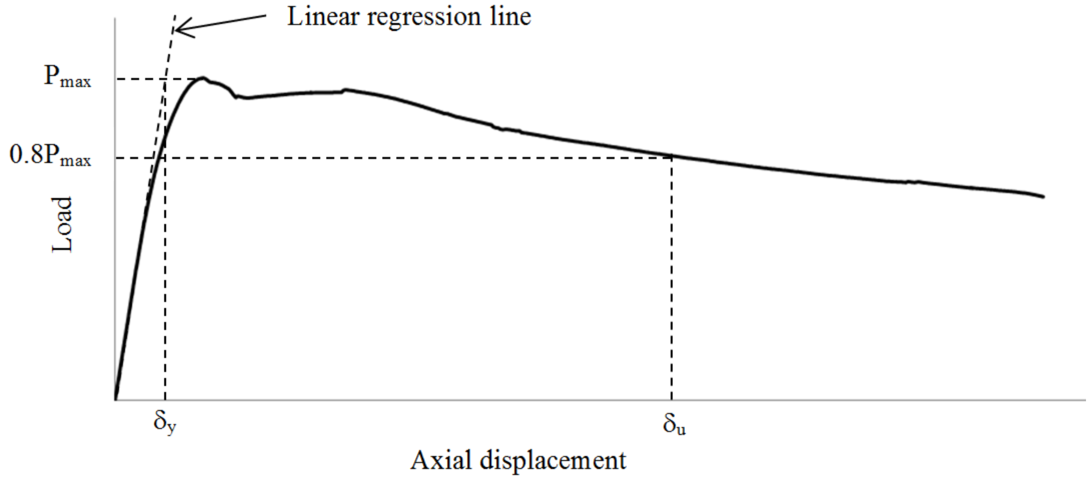

Figure 7.1. Determining the ductility of the steel reinforced concentrically loaded specimen

7.2.1 Behaviour of Column Specimens under Concentric Loading

The first specimen from each group was tested under concentric loading. The experimental results of the concentrically loaded column specimens are summarized in Table 7.1 with the axial load displacement curves shown in Figure 7.2. Initially, all the specimens experienced similar behaviour, with the ascending region of the load-displacement curve being almost linear up to the beginning of concrete spalling. As mentioned in Chapter 6, the column edges were rounded at the top and bottom at a width of 100 mm to allow for the wrapping of CFRP sheets. The connection between this corner radius and the sharp edge of the specimen created a point of stress concentration. This resulted in cracks first appearing at the top of the specimen at this weak transition zone. As the test continued the cracks started to propagate to all sides of the specimen and eventually along its instrumented region. After the maximum load (P_{max}) was achieved, the load dropped as a result of the sudden spalling of the concrete cover.

Table 7.1. Experiment results of column specimens tested under concentric loading (Hadi and Youssef 2016)

Test Specimen	Max. Load P_{max} (kN)	Axial Displ. at P_{max} (mm)	Yield Load P_{yield} (kN)	Axial Displ. at P_{yield} δ_y (mm)	Fracture Load $P_{fracture}$ (kN)	Ultimate Displ. δ_u (mm)	Ductility Method 1[d]	Ductility Method 2[d]
RS-0	1350	2.87	1122	1.68	-	15.24[a]	9.07	16.80
RF-0	1285	2.59	1089	1.58	1126	7.72[b]	4.89	8.37
I-0	1425	3.13	1173	1.86	1258	4.65[b]	2.50	3.98
C-0	1385	3.24	1199	2.27	-[c]	7.33[c]	3.23	5.19

[a] The displacement at the 80% of P_{max}

[b] The displacement at the fracture of the GFRP reinforcement

[c] Data was lost and the fracture load of the GFRP C-section could not be obtained. Therefore the ultimate displacement was based on 80% of P_{max}, although failure did occur before this point but could not be accurately determined.

[d] Refer to Section 7.2 for definitions of the methods

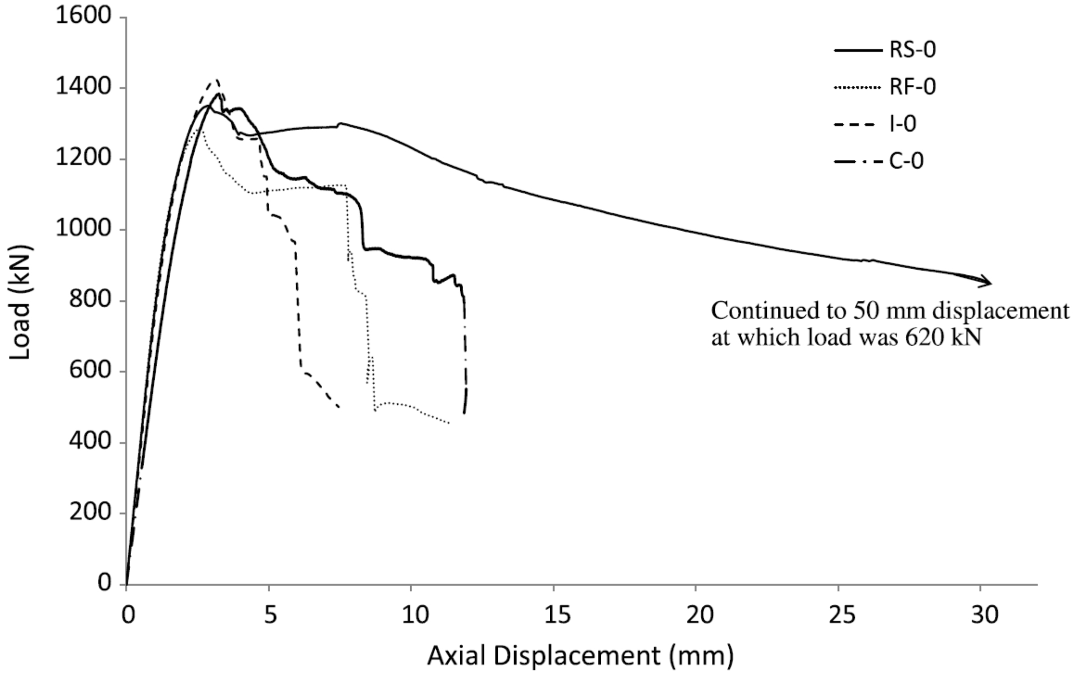

Figure 7.2. Axial load-deflection curves of the concentrically loaded column specimens, e=0mm (Hadi and Youssef 2016)

A decrease in maximum load of 4.8% relative to Specimen RS-0 was achieved for Specimen RF-0. Specimen I-0 achieved the highest maximum load of all the concentrically loaded specimens with an increase of maximum load of 5.6% and 10.9% relative to Specimens RS-0 and RF-0, respectively. Similarly, an increase of maximum load of 2.6% and 7.8% relative to Specimens RS-0 and RF-0 was achieved for Specimen C-0, respectively. After the maximum load was achieved spalling of the concrete cover occurred which resulted in a decrease in the cross-sectional area resisting the load with a corresponding drop in the load-carrying capacity of the specimens. After this drop the load then stabilized for Specimens RS-0 and RF-0. This meant that the passive confinement provided by the stirrups was activated to prevent the lateral expansion of the concrete core and the specimen was able to sustain the load up until failure.

The cracking appearance and failure modes of the concentrically loaded specimens after failure are shown in Figures 7.3 and 7.4. The axial-displacement curve of Specimen RS-0 shows the behaviour up until an axial displacement of 30 mm. This was the point at which the data limit of the data logger was exhausted. At this point, the specimen was still able to carry approximately 63% of the maximum load. The test was continued to an axial displacement of 50 mm, as obtained from the machine readings rather than the average readings of the LVDTs. At this displacement the specimen was still able to carry approximately 46% of the maximum load, with the load gradually decreasing.

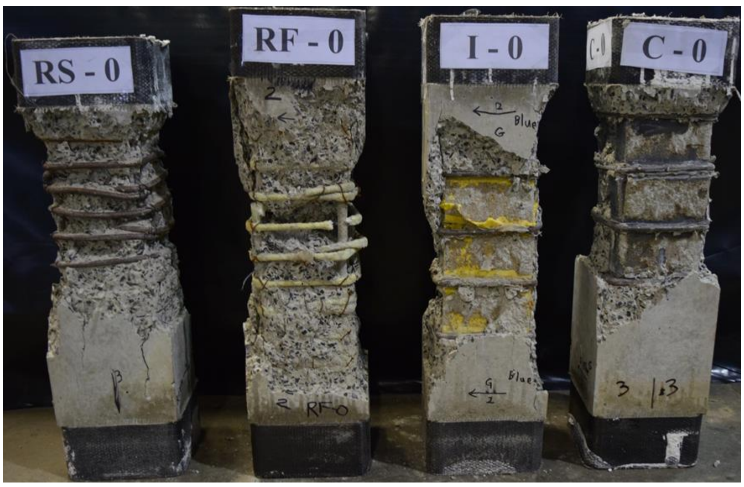

Figure 7.3. Overview of concentrically loaded column specimens after failure (Hadi and Youssef 2016)

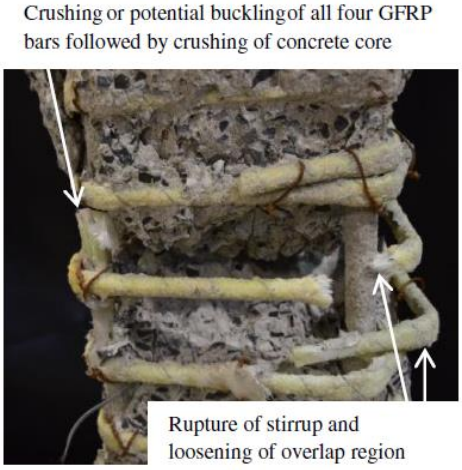

(a) (b)

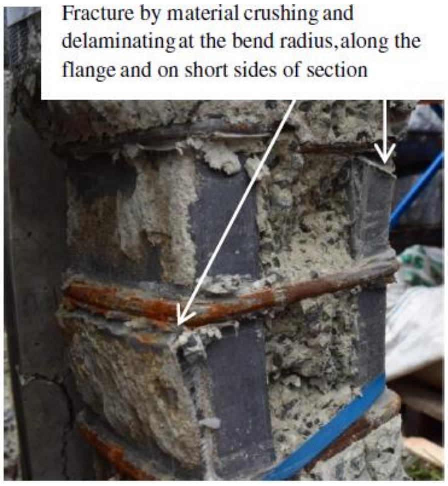

(c) (d)

Figure 7.4. Close-up view of the failure modes of concentrically tested columns (a) Specimen RS-0; (b) Specimen RF-0; (c) Specimens I-0; and (d) Specimen C-0 (Hadi and Youssef 2016)

After an axial displacement of 50 mm was reached for Specimen RS-0, the test was terminated and it was observed that after the concrete spalled off, all four longitudinal bars had substantially buckled and some of the ties were deformed and distorted as a result of the concrete core dilating, as shown in Figure 7.4(a). Specimen RS-0 experienced the most ductile behaviour of the four specimens. As a result of the stress concentrations at the rounded corners as mentioned above, the buckling of the bars was predominately at the top third of the specimen.

Unlike Specimen RS-0, Specimen RF-0 failed in a brittle manner as the result of the explosive failure of the internal reinforcement at a load of 1,125.7 kN and an axial ultimate displacement of 7.72 mm (δ_u). After this failure point the load dropped down drastically. It was unclear whether the first failure was due to the rupture of a stirrup or due to the crushing or buckling and explosive fracture of a longitudinal bar. The rupture of the tie occurred at the bend portion at the connection with a longitudinal bar at mid-height of the specimen. This was anticipated as the bend radius of the ties was 12.7 mm, which was well below the recommended radius based on the required ratio of the bend radius and tie diameter, as reported in Section 3.3.4 of Chapter 3.

Furthermore, it was seen that one tie experienced slippage (at the splice locations) of the overlap regions resulting in a potentially inadequate confinement to the concrete core. The GFRP ties were spliced by steel ties at the overlap regions. The exact timing of the rupture and slippage of the tie could not be established. The test was continued until all four longitudinal bars had failed in compression by complete crushing, with each drop in the load-displacement curve representing the explosive fracture of each bar. At the end of testing there was considerable crushing of the concrete core. As a result during the removal of the steel loading caps by force, the specimen separated into two regions with the four bars split into two, although Figure 7.4(b) shows the two regions placed on top of each other for completeness.

The GFRP-encased specimens showed little ductile behaviour after the maximum load was reached as compared to the other two specimens. Not long after the maximum load was achieved for Specimen I-0, a small cracking noise was heard on one of the flanges of the I-section at a load of 1,257 kN and corresponding axial ultimate displacement of 4.65 mm (δ_u). This load was assumed to be the first failure load of the specimen. At this point, the load dropped with a few more cracking noises being heard as the concrete cover started to completely spall off.

Eventually, as the test progressed a larger cracking noise occurred on the opposite flange at a load of 965 kN and axial displacement of 8 mm with a large drop in load occurring. This point is assumed to be the second fracture load. Therefore, on observation it is clearly seen that the two flanges of the I-section at mid-height failed in compression due to the material crushing and delamination of the fibres at the different loads. The crushing occurred along the flange with the combination of axial load and pressure from the concrete core resulting in the crushed area delaminating outwards as shown in Figure 7.4(c).

Similarly, Specimen C-0 experienced a brittle failure manner as a result of the progressive crushing of both the GFRP C-sections at different locations after the first maximum load. Just before the first fracture of the GFRP sections, a small cracking noise could be heard, followed by a loud noise. Two other explosions occurred, which resulted in the load suddenly dropping each time due to the subsequent damage of the material. Crushing and splitting of the C-sections occurred on the flange, at the bend radius and on all four short sides as shown in Figure 7.4(d).

Again due to the pressure from the concrete core, the crushed areas were pushed outwards. Having noted this, data were lost for Specimen C-0 and the exact fracture load and ultimate displacement at this load could not be accurately obtained. Therefore, for the ductility calculations the ultimate displacement was based on 80% of the maximum load as done for the steel-reinforced specimen.

Upon observation of the GFRP-encased specimens after testing, the stirrups at the welded locations were still intact and there were no signs of strength reductions at the overlap region. In fact, no failure of the stirrups was evident and the GFRP sections failed first. Based on this, the welded steel stirrups in the encased specimens served their purpose and did not affect the behaviour of the encased specimens as failure of the GFRP sections occurred first.

7.2.2 Behaviour of Column Specimens under 25 mm Eccentric Loading

A specimen from each group was subjected to 25 mm of eccentric loading. The experimental results of the 25 mm eccentricity loaded column specimens are summarized in Table 7.2 with the axial and lateral load-displacement curves shown in Figure 7.5. Initially, Specimens RS-25, I-25, and C-25 experienced similar behaviour before reaching the maximum load. However, the slope of the load displacement curve of Specimen RF-25 was lower than that of the other specimens, as shown in Figure 7.5. This could be due to errors in aligning the specimen resulting in load not being applied exactly at 25 mm eccentricity. The first maximum load (P_{max}) of Specimens RS-25, I-25, and C-25 were approximately equal. However, a decrease in the first maximum load of 19.3% relative to Specimen RS-25 was achieved for Specimen RF-25.

The cracking appearance of the specimens at failure in the tension and compression zones is shown in Figure 7.6. Similar to the concentrically loaded specimens, stress concentrations on the top of the specimens at the transition between the rounded corners and square edges produced stress concentrations resulting in cracks first appearing in those locations. As testing progressed, the cracks propagated to all four sides of the specimen and to the instrumented region. The application of the eccentric load resulted in the bending of the specimens with one side of the specimen under compression and the other under tension. After the maximum load the concrete in compression started to spall, with horizontal tension cracks originating on the tension side of the specimens. As the load increased the concrete in compression completely spalled off, tension cracks increased and all the specimens failed in compression.

Table 7.2. Results of column specimens tested under 25 mm eccentric loading (Hadi and Youssef 2016)

Test Specimen	First Max. Load P_{max} (kN)	Axial Displ. at P_{max} (mm)	Lateral Displ. at P_{max} (mm)	Yield Load P_{yield} (kN)	Axial Displ. at P_{yield} δ_y (mm)	Second Peak Load, P_{peak} (kN)	Fracture Load $P_{fracture}$ (kN)	Ultimate Displ. δ_u (mm)	Ductility Method 1[d]	Ductility Method 2[d]
RS-25	995	2.72	2.11	904	2.13	-	-	8.04[a]	3.77	5.96
RF-25	803	3.00	2.27	701	2.20	823	353	8.21[b]	3.62	6.10
I-25	1008	2.51	2.05	905	2.00	1024	1024	4.97[c]	2.49	3.96
C-25	985	2.86	2.96	866	2.03	-	948	5.68[c]	2.80	4.65

[a] The displacement at the 80% of P_{max}

[b] The displacement at P_{peak}

[c] The displacement at the first fracture of the GFRP reinforcement

[d] Refer to Section 7.2 for definitions of the methods

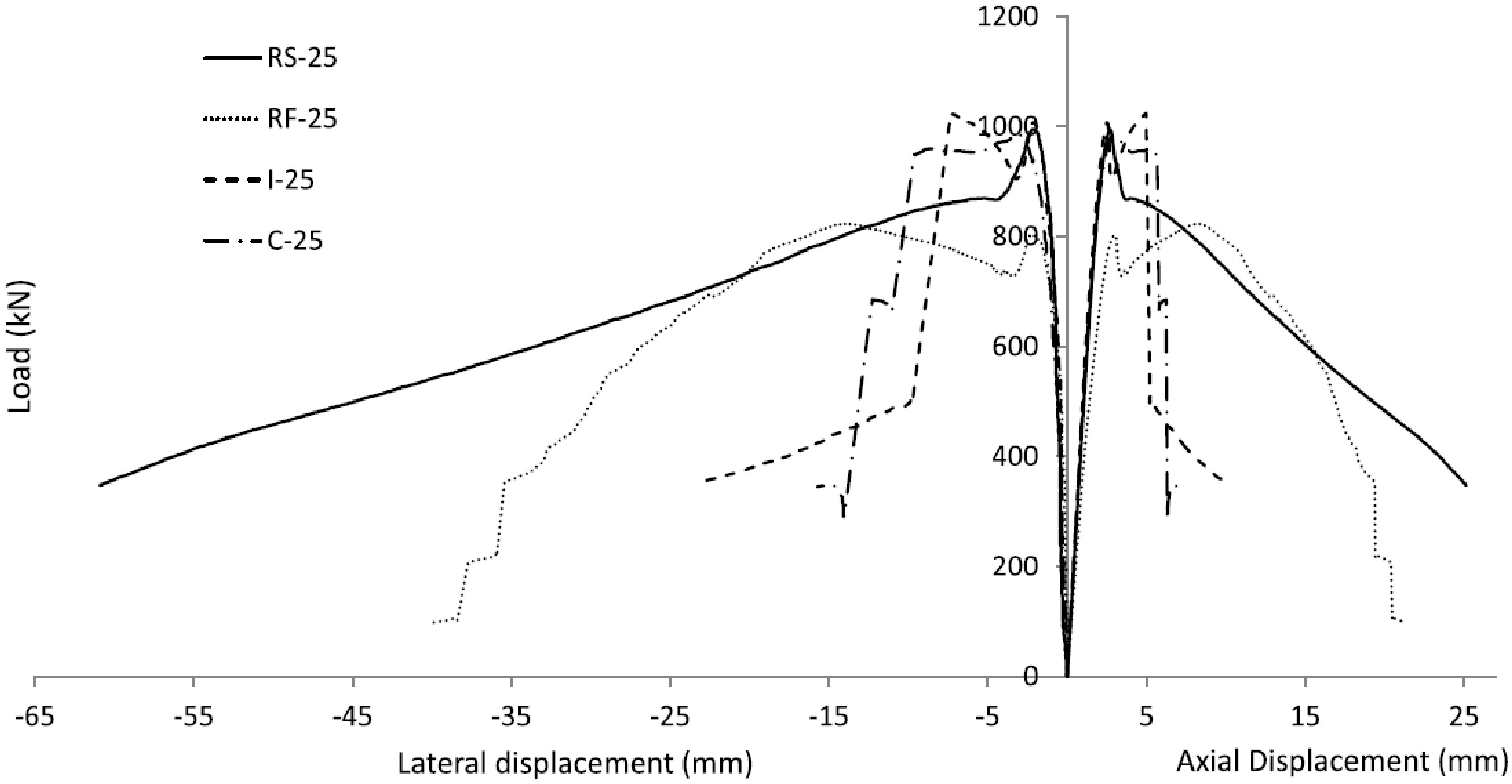

Figure 7.5. Axial and lateral load-deflection curves of the 25 mm eccentrically loaded column specimens, *e*=25mm (Hadi and Youssef 2016)

(a)

(b)

Figure 7.6. Failure modes of the 25 mm eccentrically loaded column specimens (a) Tension side, and (b) Compression side (Hadi and Youssef 2016)

After the maximum load was achieved, the specimens lost a percentage of their maximum capacity due to the sudden spalling of the concrete cover in the compression zone. Specimen RS-25 lost approximately 13% of its maximum value, whereas Specimen RF-25 lost about 9% of the maximum load. After this drop in the capacity the load-carrying capacity of Specimen RS-25 gradually decreased until the eventual termination of the test occurred when the load reached 35% of the maximum load. Specimen RS-25 displaced both axially and laterally the most out of all the specimens, with no sudden failure in the steel occurring providing a good ductile behaviour. On termination of the test it was realized that the two longitudinal steel bars on the compression side had substantially buckled as shown in Figure 7.6(b) depicting the failure of the specimens in the compression side. Furthermore, the tension cracks at mid-height of the specimen had grown substantially as shown in Figure 7.6(a).

On the other hand, Specimen RF-25 was able to sustain an increase in load after the sudden concrete spalling and eventually a second peak load (P_{peak}) of 823 kN was achieved at an axial ultimate displacement of 8.21 mm (δ_u). After this point, the load decreased at a high rate until the eventual brittle and explosive failure of the internal reinforcement in compression at a load of 353 kN and axial displacement of 19.4 mm. On observation, after this failure, both a longitudinal bar had fractured and a tie at the bend portion had ruptured on the compression region at the top third of the specimen. It was unclear whether the bar or tie failed first and whether the fracture of the bar was due to crushing or buckling (Figure 7.7).

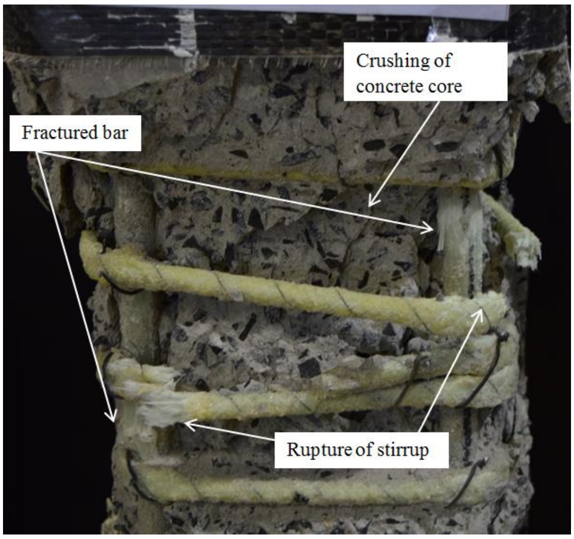

Figure 7.7. Failure mode of Column RF-25 (Hadi and Youssef 2016)

Quickly following the failure of the bar and tie, another tie at the bend portion and the other longitudinal bar failed in a similar manner on the compression side with another drop in the load occurring. Unlike Specimen RS-25, the failure region of Specimen RF-25 was at the top of the specimen, which is not in the instrumented region as shown in Figure 7.7. In addition, the large tension cracks also developed at the top of the specimen rather than at mid-height, with concrete spalling also occurring in tension as seen in Figure 7.6(a). The reason for this, as mentioned above, may be due to the stress concentrations at the top of the specimen due to the transition of the rounded and sharp edges. Furthermore, another reason is the fracture of the compression bars resulted in these bars not being able to carry any more load resulting in the top of the specimen bowing towards the compression region. The longitudinal bars in tension did not fail. After termination of the test it was evident that the crushing of concrete core occurred at the top of the specimen. Considering the unpredictable failure of the GFRP reinforcement after the peak load, the ultimate displacement for the ductility definition was taken as the axial displacement at peak load rather than at a higher displacement corresponding to 80% of the peak load.

Although the peak load of Specimen RF-25 (803 kN) was substantially lower than that of Specimen RS-25 (995 kN), the ductility of both specimens was calculated to be approximately similar based on the ductility definition in Section 7.2 with the steel reinforced column obtaining a slightly higher ductility. Having said this, the eventual failure of Specimen RF-25 was brittle and explosive with the load dropping substantially after the peak load unlike that of Specimen RS-25 which did not fail abruptly but continued to displace and sustain the load until the termination of the test.

Specimens I-25 and C-25 did not displace laterally or axially as much as Specimens RS-25 and RF-25. After the maximum load, the load of Specimen I-25 slightly dropped and then increased up until a second peak load of 1,024 kN at which sudden failure occurred (P_{peak} equals P_{fracture}). The failure was marked by the crushing and delamination of the compression flange of the I-section at mid-height. The failure mode of the I-sections was similar to that of the concentrically loaded specimen but only occurred in the compression flange. The concrete had not completely spalled at this point but just after the fracture load the concrete in compression was broken apart explosively at mid-height. Similarly, Specimen C-25 failed due to the crushing and rupture of the C-sections in the compression region. However, after the maximum load was achieved, the load did not decrease suddenly as experienced by the other specimens but instead the load stabilized until a load of 948 kN at which the failure of the C-sections occurred in compression due to material crushing and delaminating. After the fracture point there was a sudden drop in the load with a second drop occurring not long after due to the failure of another section of the C-section.

The ultimate displacement of the GFRP-encased specimens was taken at the fracture load. After the failure load of the GFRP-encased specimens was achieved, testing continued until the load reached 35% of the first maximum load. After observation, it was realized that the tension cracking patterns of the GFRP encased specimens was different to the reference specimens as shown in Figure 7.6(a). These vertical cracks seem to originate at the edges of the sections which could potentially mean inadequate confinement to the concrete core which results in the concrete cover spalling similar to that of concentrically loaded columns. In addition to tensile cracks, it is observed that the concrete cover in the tensile region spalled off, which was marked by the vertical cracks. Similar to the concentrically loaded specimens, the GFRP-encased specimens showed little ductile behaviour after the maximum load was reached as compared to the other two specimens. Specimen C-25 experienced a slightly higher ductility than that of Specimen I-25, which may be as a result of the confinement provided by the box arrangement of the internal C-sections.

7.2.3 Behaviour of Column Specimens under 50 mm Eccentric Loading

A specimen from each group was subjected to 50 mm of eccentric loading. The experimental results of the 50 mm eccentrically loaded specimens are summarized in Table 7.3 with the axial and lateral load-displacement curves shown in Figure 7.8. Similar to the 25 mm eccentrically loaded specimens, the specimens experienced similar behaviour before reaching the maximum load. The maximum load for Specimen RS-50 was obtained to be 747 kN and experienced good ductility. A decrease of first maximum load of 17.7% relative to Specimen RS-50 was achieved for Specimen RF-50. Unlike the other loading cases, Specimen C-50 obtained a lower maximum load as compared to Specimen RS-50. However, Specimen I-50 experienced a slight increase in maximum load with reference to Specimen RS-0 but experienced low ductility with failure occurring slightly after the maximum load. In addition, Specimen RF-50 experienced a second peak load, with the load-carrying capacity increasing after the sudden spalling of the concrete cover. After this point the load substantially decreased until the eventual failure of the GFRP bars in compression at a load of 374 kN and axial displacement of 13.61 mm. After this failure point the specimen could not carry any more load.

Table 7.3. Results of column specimens tested under 50 mm eccentric loading (Hadi and Youssef 2016)

Test Specimen	First Max. Load P_{max} (kN)	Axial Displ. at P_{max} (mm)	Lateral Displ. at P_{max} (mm)	Yield Load P_{yield} (kN)	Axial Displ. at P_{yield} δ_y (mm)	Second Peak Load, P_{peak} (kN)	Fracture Load $P_{fracture}$ (kN)	Ultimate Displ. δ_u (mm)	Ductility Method 1[d]	Ductility Method 2[d]
RS-50	747	2.65	2.66	672	2.02	-	-	7.55[a]	3.74	5.94
RF-50	615	2.33	2.46	558	1.77	626	374	9.44[b]	5.33	9.44
I-50	765	2.88	3.18	688	2.19	769	769	5.04[c]	2.30	3.56
C-50	679	3.04	3.69	607	2.08	695	695	6.84[c]	3.29	5.67

[a] The displacement at the 80% of P_{max}

[b] The displacement at P_{peak}

[c] The displacement at the first fracture of the GFRP reinforcement

[d] Refer to Section 7.2 for definitions of the methods

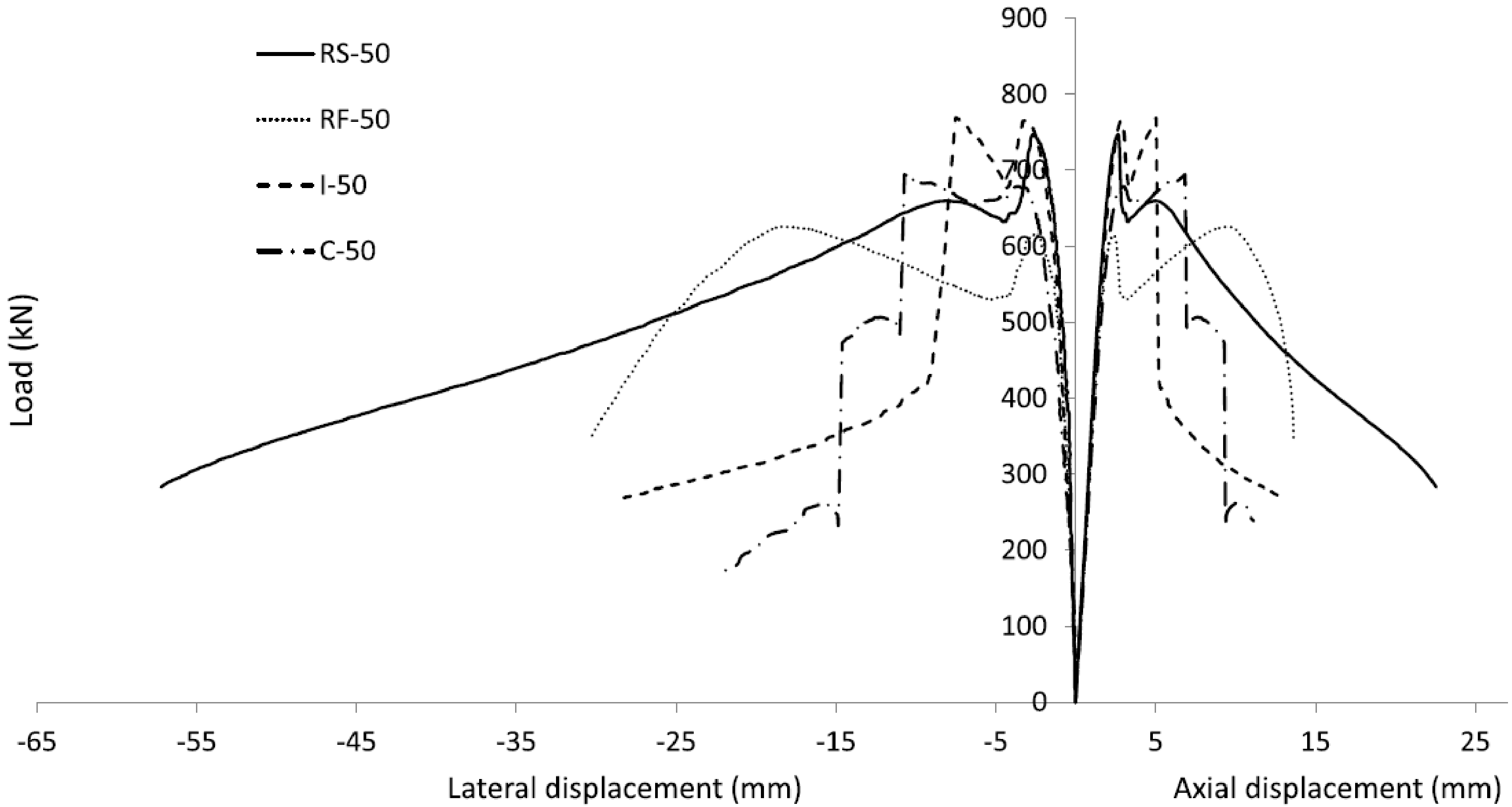

Figure 7.8. Axial and lateral load-deflection curves of the 50 mm eccentrically loaded column specimens, *e*=50mm (Hadi and Youssef 2016)

In terms of ductility and based on the definitions in Section 7.2, Specimen RF-50 showed a slight improvement in ductility as compared to Specimen RS-50. Furthermore, although the ductility values of the GFRP-encased specimens show a reasonable value for ductility, failure was sudden and brittle as opposed to that of Specimen RS-50. Similar to the 25 mm eccentric loading condition, Specimens I-50 and C-50 did not displace laterally or axially as much as the reference specimens.

The failure of the specimens was also observed to be in compression, similar to the failure mechanisms of the 25 mm eccentricity loaded specimens. During or after concrete spalling in the compression side, the steel reinforcement on the compression side buckled and the two GFRP longitudinal bars crushed and explosively fractured, while the reinforcement in tension did not fail. Again due to stress concentrations at the transition of the sharp and round edges, the failure of Specimen RF-50 was at the top of the specimen with the two longitudinal bars completely crushing and separating with no notable rupture in the stirrups (Figure 7.9).

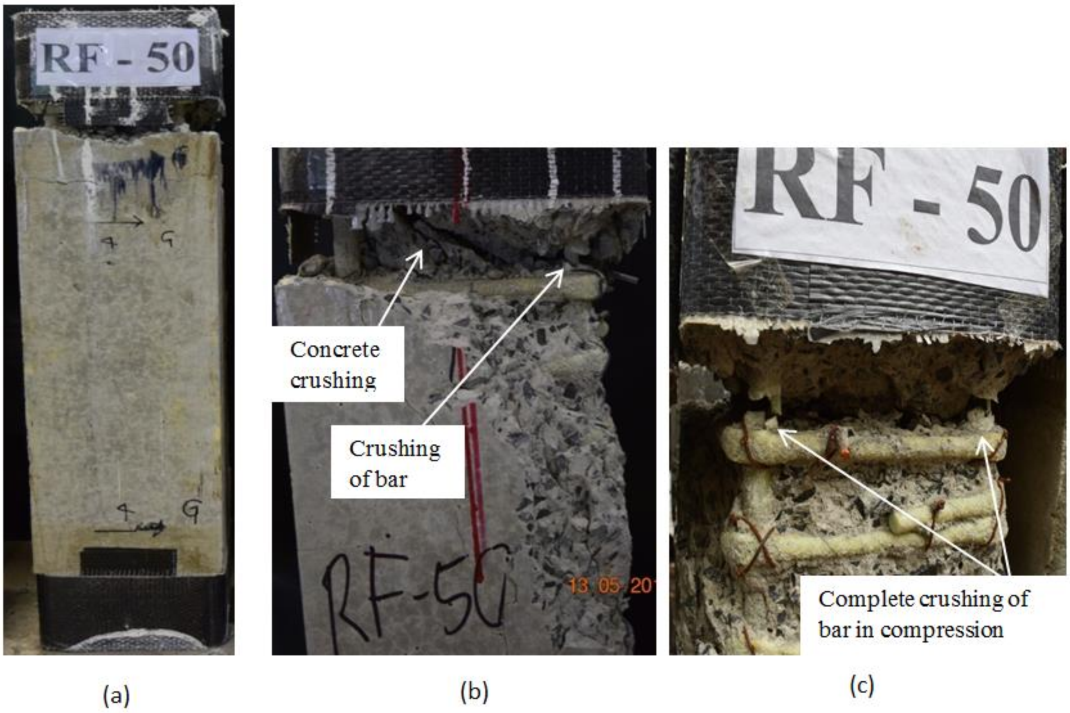

Figure 7.9. Failure mode Column RF-50 (a) Tension side; (b) Side-view; and (c) Crushing of compression bars (Hadi and Youssef 2016)

The tension cracks were larger on the top of the specimen [Figure 7.9(a)] with severe crushing of concrete occurring on the top of the specimen at the fracture location of the bars throughout the cross section in both compression and tension, as shown in Figures 7.9(b and c). The CFRP tension-strengthening strips were also de-bonded from the concrete [Figure 7.9(a)].

Sudden failure of the I-section occurred for Specimen I-50 at a second peak load of 769 kN after the maximum load was achieved. The failure mode of the I-sections was similar to that of the 25 mm eccentrically loaded specimen, which was marked by the crushing and delamination of the compression flange at mid-height. Similarly, Specimen C-25 failed due to the crushing and rupture of the C-sections in the compression region. Although the failure load for Specimen C-25 of 695 kN was lower than that for Specimen I- 50 of 769 kN, the ductility of the C-section–encased specimen (3.29) was greater than that of the I-section–encased specimen (2.30), which proves the benefits of the confinement mechanism of the C-sections.

Furthermore, the cracking appearance on the tension side of the specimens at the end of testing was similar to that of the 25 mm eccentrically loaded specimen with concrete cover appearing to be spalled on the GFRP-encased specimens. The GFRP sections in the tension side did not appear to fail during testing.

Based on the material testing of the pultruded sections explained in Chapter 5 and 6, it was evident that the two shapes of GFRP sections (I and C-sections) varied in tensile properties and possibly compressive properties even though they were claimed to be from the same batch by the manufacturer. Furthermore, the compressive properties were hard to establish considering the premature failure mechanism of the coupons by end crushing. However, for all the loading cases, the Group I and Group C specimens behaved in a similar manner both based on the stress and strain relationships as well as the failure mechanisms. Therefore, although the material properties of both the sections were not similar, a comparison of the general structural behaviour of both these two groups of specimens could be established.

7.2.4 Strain Data for the Column Specimens

The detailed description of positioning of the strain gauges of the internal reinforcement for all the groups of specimens was discussed in Chapter 6. Strain gauges were bonded on the internal longitudinal reinforcements and imbedded sections. The location of the attached strain gauges is shown in Figures 6.1 and 6.2 of Chapter 6. For each concentrically loaded specimen, two strain gauges were bonded to the longitudinal reinforcement and imbedded sections at mid-height. Similarly, for the eccentrically loaded specimens, two strain gauges were bonded on to the longitudinal bars, with one strain gauge on the compression side and one on the tension side. For the imbedded GFRP I-sections, the strain gauges were bonded in the middle of the two outside flanges at the mid-height. Only one GFRP C-section per specimen was instrumented with strain gauges which were located on the two flanges at mid-height, as shown in Figure 6.2 of Chapter 6.

At the maximum load the average axial strain in the steel longitudinal bars for Specimen RS-0 was obtained to be 0.379%. At this point the steel had reached its yield point, considering the yield strain of the longitudinal steel bars was determined to be 0.324% from tensile testing. Therefore, the longitudinal steel bars contributed to approximately 21.7% of the ultimate column capacity by using the yield strain in the calculation considering that at $P_{\max}$ the steel bars were at yield. The corresponding average axial strain for the longitudinal GFRP bars in Specimen RF-0 at the maximum load was obtained to be 0.354%, which is lower than 14.7% of the ultimate tensile rupture strain (2.41%). The GFRP longitudinal bars contributed to approximately 9.5% of the ultimate column capacity by taking into account the bars cross-sectional area determined by using a diameter of 12.7 mm rather than by the diameter obtained from immersion testing. Furthermore, the contribution of the GFRP bars to the overall column capacity for the GFRP reinforced specimen was calculated by assuming that the GFRP bars modulus of elasticity in compression is equal to the modulus of elasticity in tension as reported by Deitz et al. (2003). It was determined that at the first maximum load the average axial strain in the bars and GFRP sections for Specimens RS-0, RF-0, I-0 and C-0 ranged between 0.35% and 0.40%.

In addition, at this maximum load the measured average strains in the steel (Specimen RS-0) and GFRP stirrups (Specimen RF-0) were 0.097% and 0.138%, respectively, which is approximately 26.2% and 2.8% of the yield strain of steel stirrups (0.37%) and ultimate tensile strain of the GFRP stirrups (2.39%), respectively. Therefore, at the maximum load, the confinement of the steel and GFRP stirrups had not yet been activated. After the maximum load was achieved, the column Specimens RS-0 and RF-0 lost a percentage of their maximum capacity due to the sudden spalling of the concrete cover. After this drop in the capacity the load then stabilized for both the column specimens. This meant that the passive confinement provided by the ties was activated to prevent the lateral expansion of the concrete core and the column specimens was able to sustain the load up until failure.

Similar to the concentrically loaded specimens, the strain for all four groups of eccentrically loaded specimens in the instrumented compression reinforcement and sections ranged between 0.35% and 0.40% at the first maximum load. Most notably, at the maximum load the compressive strain of the steel longitudinal bars for Specimen RS-25 and RS-50 was 0.374% and 0.368%, respectively. Therefore, at the first maximum load the steel bars in compression had reached the yield strain of 0.324%. Unfortunately, the strain reading of the GFRP bars in compression for Specimen RF-25 was lost, while Specimen RF-50 obtained a reading of 0.355% compressive strain at the first maximum load, which is 14.7% of the ultimate tensile strain.

On the other hand, the strain in the reinforcement located in the tensile zone of the eccentrically loaded specimens varied. At maximum load, the steel bar in the tension zone was still under slight compression for Specimen RS-25, while the instrumented reinforcement and sections for Specimens RF-25, I-25 and C-25 were under slight tension with values ranging from 0.01% to 0.06%. However, the tensile reinforcement and sections for the specimens loaded under 50 mm eccentric load were exposed to higher tensile strains at maximum load with values ranging from 0.08% to 0.19%. As mentioned above, for the eccentrically loaded specimens only one strain gauge was placed on the tension and compression longitudinal bars and sections and no average could be obtained for each.

7.2.5 Influence of Eccentricity

The influence of eccentricity on the structural behaviour of the column specimens is described by examining the reduction in the capacity of the columns with increasing eccentricity (Figure 7.10) and from the axial load and displacement curves for each group of specimens, as plotted in Figure 7.11. In Figure 7.10 each point on the curve represents the first maximum axial load (P_{max}) obtained for each eccentricity loading. It can be seen that the steel reinforced and GFRP encased columns all had similar performances. Having said this, the first maximum load for the GFRP encased specimens were higher than that of the steel reinforced specimens for concentrically loading condition, but were relatively similar for the loading of 25 mm eccentricity. However, the first maximum load for the GFRP reinforced column specimens was lower than the other group of specimens for all loading conditions. It can also be clearly seen from Figure 7.10 and 7.11 that for all the groups of specimens, there was a reduction in the axial load carrying capacity with an increase in load eccentricity.

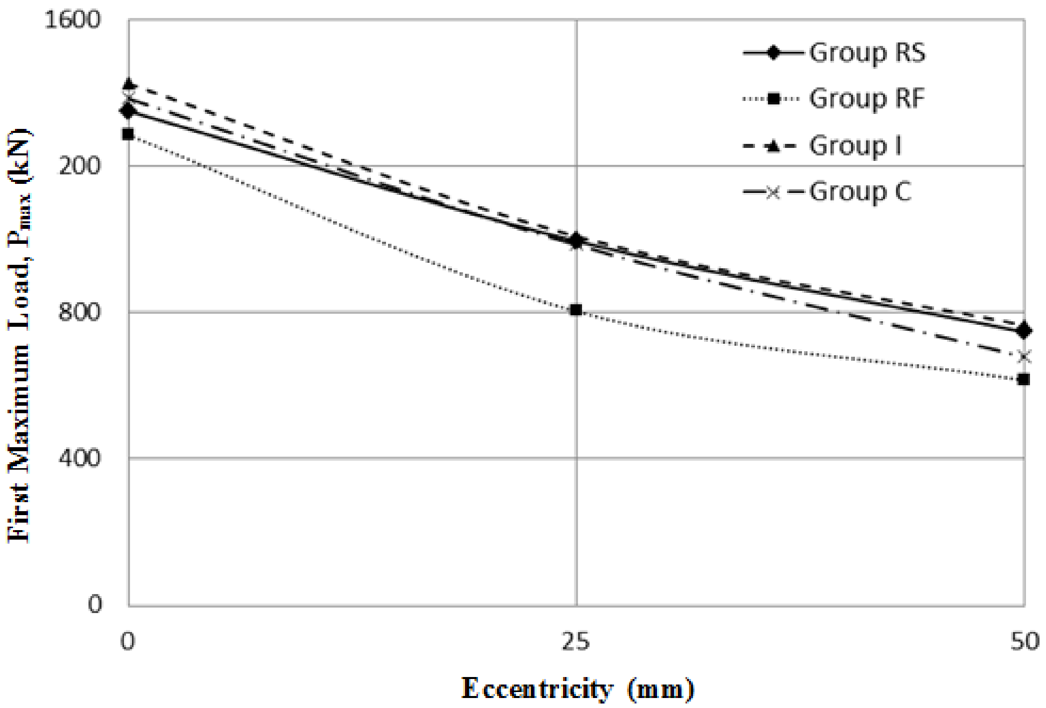

Figure 7.10. Influence of eccentricity for column specimens

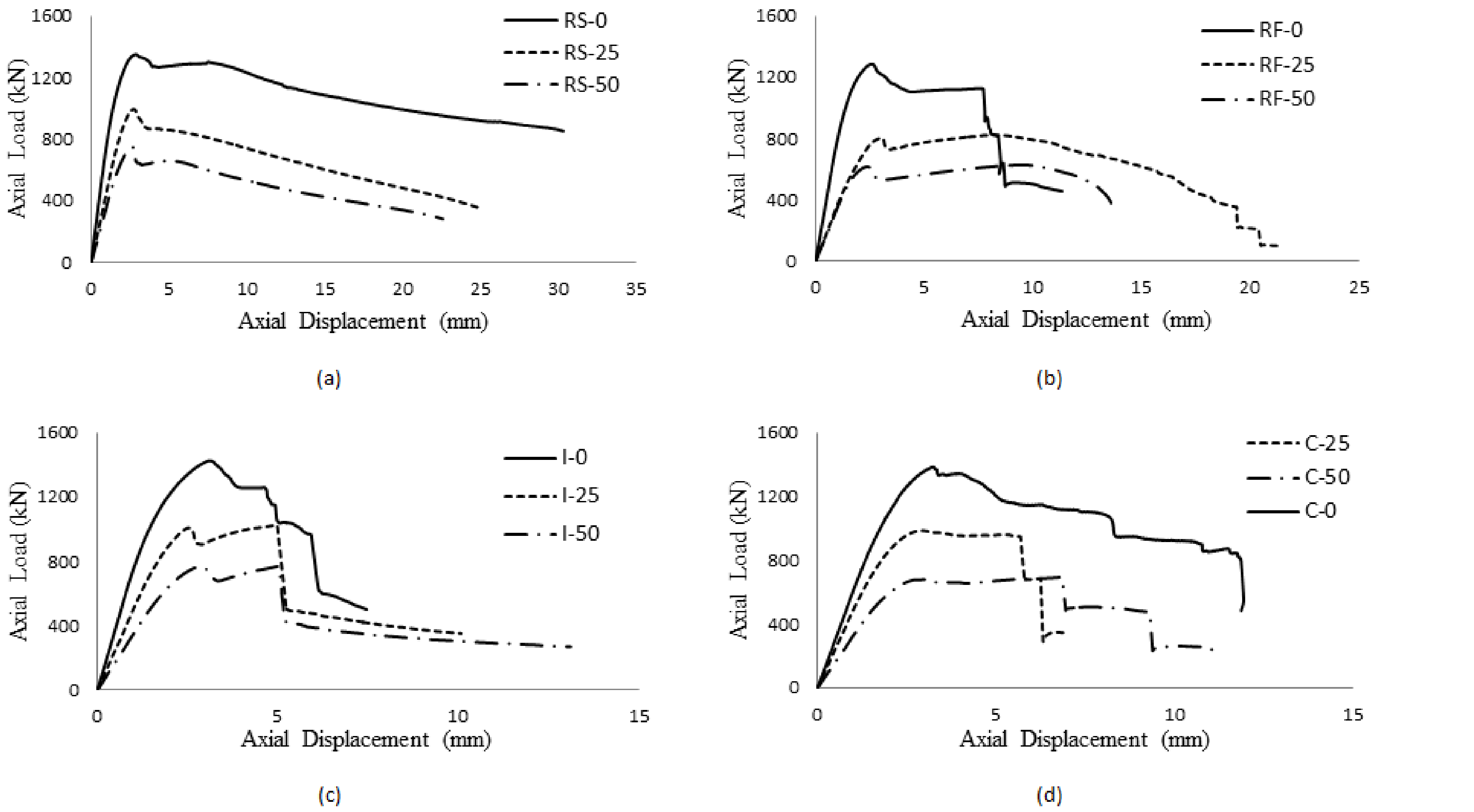

Figure 7.11. Axial load-displacement relationships of column specimens with varying load eccentricities (a) Group RS; (b) Group RF; (c) Group I; and (d) Group D (Youssef and Hadi 2017)

7.3 Behaviour of Beam Specimens

The last specimen from each group was tested as a beam under four-point bending. The experimental results of the beam specimens are summarized in Table 7.4 with the load versus mid-span deflection curves shown in Figure 7.12. The first specimen tested was Specimen RS-B. Because of a malfunction in the data logger, the mid-span deflections obtained from the laser triangulation were lost. Therefore, the mid-span deflection for Specimen RS-B was recorded from the readings of the testing machine, with a maximum load of 232 kN achieved at a mid-span deflection of 8.1 mm.

After the maximum load was reached for Specimen RS-B, the load was maintained until sudden failure occurred in the tension region of the beam specimen, at a mid-span defection of 20.1 mm. The failure was a typical flexural failure with large tension cracks evident at the mid-span of the specimen with considerable crushing of the concrete in the compression zone occurring, as shown in Figure 7.13.

Table 7.4. Results of beam specimens tested under four-point bending (Hadi and Youssef 2016)

Test Specimen	Maximum Load, P_{max} (kN)	Mid-span deflection at P_{max} (mm)
RS-B	232.0	8.10
RF-B[a]	340.3	12.13
I-B[b]	215.7	13.47
C-B	370.0	12.78

[a] The shear zones were wrapped with two layers of CFRP in the hoop direction

[b] Failed prematurely by bearing

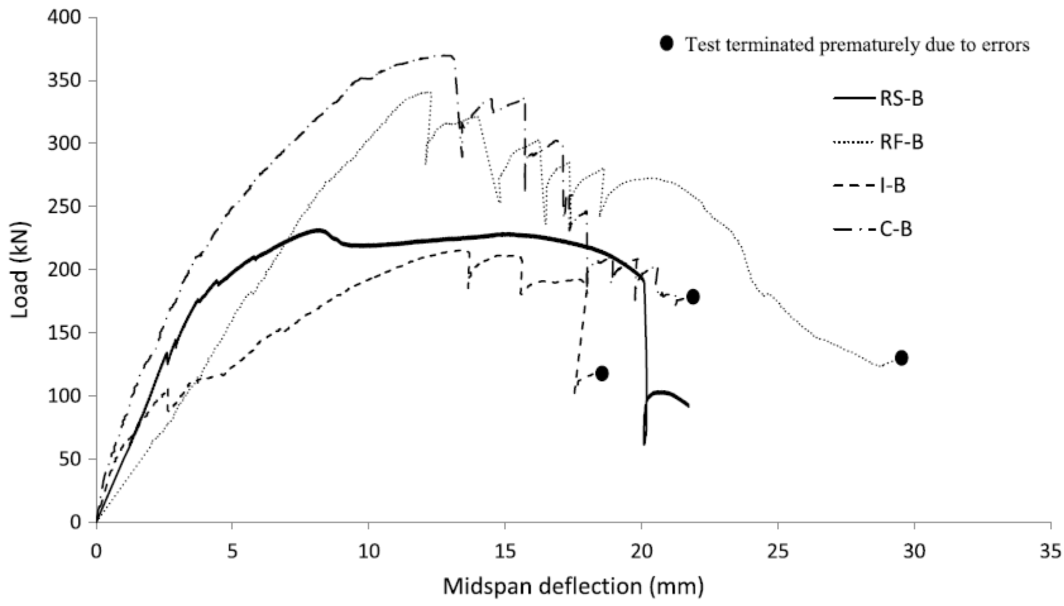

Figure 7.12. Load-mid-span deflection curves of the beam specimens (Hadi and Youssef 2016)

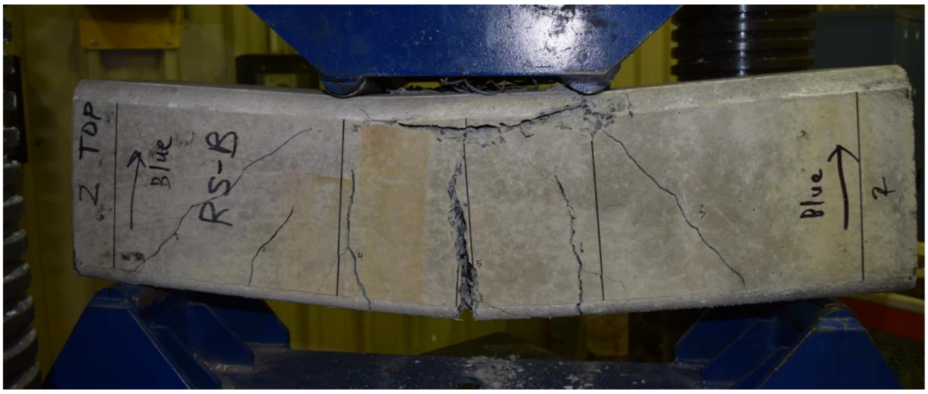

Figure 7.13. Beam Specimen RS-B after testing

The second beam specimen tested was Specimen I-B. At the early stages of loading, bearing failure occurred at the two ends of the specimen with concrete crushing at the two supports, as shown in Figure 7.14 after testing was terminated. This can be seen from the slight drop and then increase in load on the load versus mid-span deflection curve. As a result of this initial bearing failure mode, a lower than expected maximum load of 215.7 kN was obtained at a mid-span deflection of 13.47 mm. The test was terminated prematurely due to human errors in setting up the safety precautions of the test.

Figure 7.14. Bearing failure of Specimen I-B (Hadi and Youssef 2016)

The third specimen tested was Specimen C-B. To ensure no bearing failure occurred, a 50 mm wide by 8 mm thick rectangular steel plate was placed as a bearing plate on the two supports which ran along the width of the beam, as shown in Figure 7.15. In addition, as added precaution the two ends of the specimen, at 100 mm length, were wrapped with two layers of CFRP wrap (Figure 7.15). Specimen C-B achieved the highest maximum load of all the specimens, with a load of 370 kN obtained at a mid-span deflection of 12.78 mm.

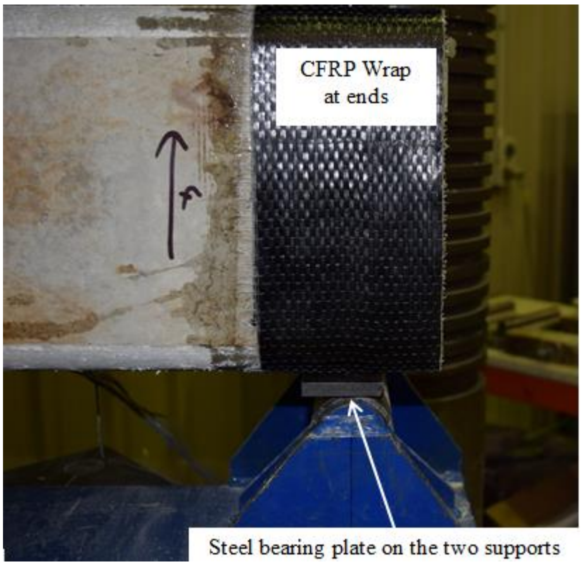

Figure 7.15. Measures to prevent bearing failure of beam specimens (Hadi and Youssef 2016)

Therefore, Specimen C-B achieved an increase of 59.5% in maximum load as compared to Specimen RS-B. At the maximum load there was a drop in the load-deflection curve. After this point, small cracking noises were heard and subsequent drops in the curve occurred due to possible failure of the C-sections at different areas, as shown in Figure 7.12. The failure of the Specimen C-B is shown in Figure 7.16, with a typical shear failure mechanism evident.

Figure 7.16. Beam Specimen C-B after testing

The last beam specimen tested was Specimen RF-B. Two beams reinforced with GFRP bars were prepared, with one acting as spare. The first beam tested failed in shear (Figure 7.17) and errors in testing occurred with unreliable results. As a result, the results of this specimen are unreliable and will not be mentioned. To increase the shear capacity the second beam specimen reinforced with GFRP bars was wrapped with two layers of CFRP at the shear zones at the outer thirds of the specimen with the specimen unwrapped between the two point loads, as shown in Figure 7.18.

Figure 7.17. Shear failure of beam Specimen RF-B without shear strengthening

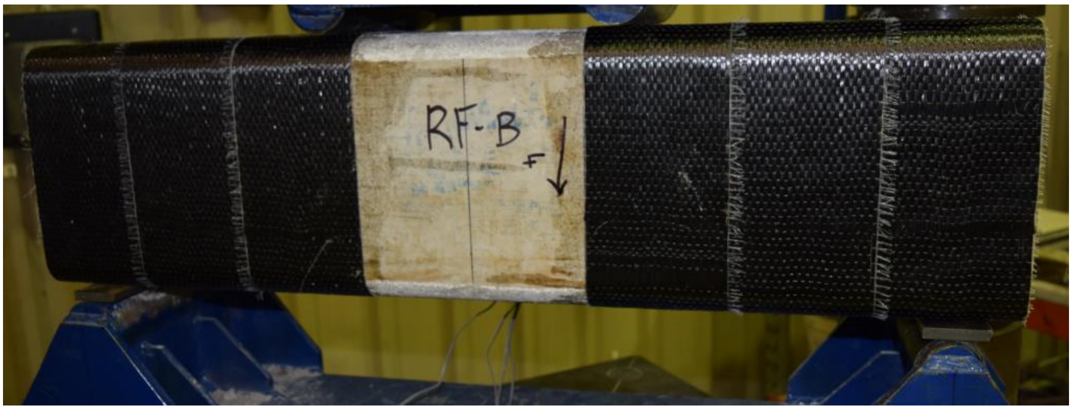

Figure 7.18. Strengthening of beam Specimen RF-B in the shear zone

The load mid-span deflection response was almost linear up until a maximum load of 340.3 kN at a mid-span deflection of 12.13 mm. It should be noted that the results of the beam Specimen RF-B plotted in Figure 7.12 and shown in Table 7.4 is for the beam specimen strengthened in the shear zones. Again steel-bearing plates were provided at the supports. At the maximum load the first rupture of the CFRP sheets resulted in a sudden decrease in load. The specimen then still resisted the load under increasing deflection until the second peak load was achieved. Another rupture of the CFRP sheet resulted in a drop of the load. After several ruptures, the bearing plate had shifted as a result of the roller on the supports, as shown in Figure 7.19. The slippage of the bearing plates resulted in the plate being wedged under the specimen and explains the behaviour after mid-span deflections of 20 mm where no eventual failure occurred in the internal reinforcement of the specimen and the load plateaued out with the test terminated not long after, as shown in Figure 7.12. The addition of the bearing plates would have resulted in slippage at the connection with the pin and roller supports, which would have had an impact on the mid-span deflections and load carried. For the purposes of this study these slippages were ignored.

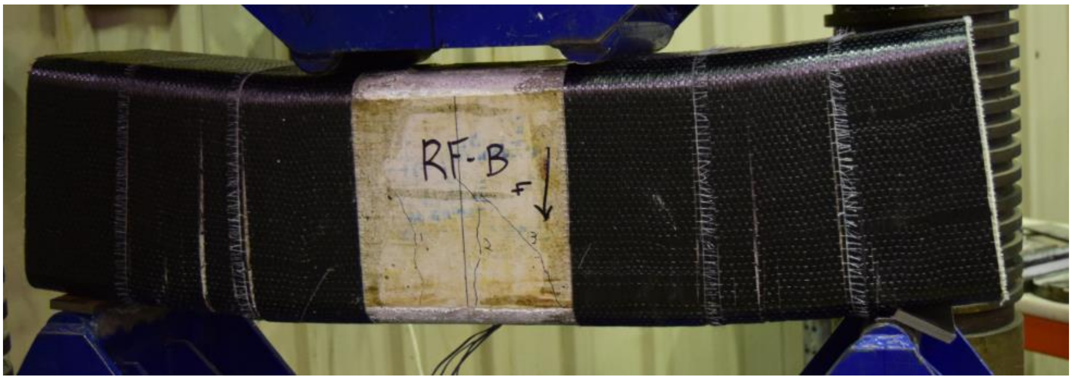

Figure 7.19. Beam Specimen RF-B strengthened in the shear zone after testing

By observation, the failure of the steel-reinforced specimen was a typical flexural failure. However, the GFRP-reinforced and GFRP-encased specimens appear to have failed in shear rather than in flexure even though the GFRP-reinforced specimen (RF-B) was wrapped with two layers of CFRP in the shear zone. It is unclear whether the steel-reinforced specimen would have experienced an increase in load-carrying capacity if the steel bearing pads and ends of the specimen were wrapped with CFRP, which was done for the other beam specimens.

The initial stiffness of all the beams was different as shown in Figure 7.12. Possible reasons for these differences are that some beams were provided with a bearing pad (Group C and RF) while others were not. Other reasons may be the wrapping of the Group RF specimen resulted in a change in the load-mid-span behaviour with respect to the other specimens or the small ratio of the shear span to depth ratio of the specimens resulted in inconsistency in testing. Therefore, the ductility of the beam specimens were not determined and analysed.

7.4 Summary

This chapter presents the experimental results of the study on the axial and flexural behaviour of square concrete members reinforced with GFRP bars and embedded with pultruded GFRP structural sections under different loading conditions. The strength, failure modes, failure locations, ductility and strain data of each group of specimens are explained. The experimental results have shown that the steel-reinforced specimens have a higher load carrying capacity than specimens reinforced with GFRP bars for all loading conditions. In addition, for concentrically loaded specimens, steel-reinforced specimens have a better ductile performance than specimens reinforced with GFRP bars. In terms of eccentric loading, specimens reinforced with GFRP bars experienced similar ductility as compared to the corresponding steel-reinforced specimens. However, the eventual failure mode of specimens reinforced with GFRP bars was sudden and brittle in nature. Furthermore, specimens encased with GFRP structural sections have a higher load-carrying capacity but considerably lower ductility than the steel-reinforced and GFRP bar–reinforced specimens.

Based on the results of the beam specimens the use of encased GFRP structural sections can provide a significant improvement in the load-carrying capacity when comparing conventional beams reinforced with steel and GFRP bars. There is potential in encasing structural GFRP sections in concrete beams, although further research elaboration is necessary to investigate this considering some of the errors and premature failure mechanisms experienced in the experimental program of the beam specimens.

In the next chapter an analytical model is presented to predict the axial load-bending moment interaction diagrams of the experimentally tested specimens. The analytical predicted load and bending moment capacities are compared to the experimentally determined values for all the four groups of specimens.

8 AXIAL LOAD-BENDING MOMENT DIAGRAMS OF GFRP REINFORCED COLUMNS AND GFRP ENCASED SQUARE COLUMNS

8.1 Introduction

In reality, columns are not subjected to perfect concentric loading but are influenced by a combination of axial compression loads and bending moments (Hadi 2006). Even for columns nominally carrying only axial compression load, bending moments always exist. These bending moments are introduced by unintentional load-eccentricities and by out-of-straightness of the constructed column (Warner et al. 2007). Consequently, the behaviour and performance of the experimentally tested GFRP-reinforced and GFRP-encased concrete columns subjected to eccentric loading were discussed in Chapter 7.

In this chapter, an analytical model is presented to predict the axial load-bending moment interaction diagrams of the experimentally tested specimens. Firstly, the stress-strain relationships of the constituent materials used in this study are described, and then followed by a detailed explanation of the two methods used to determine the analytical axial load-bending moment capacities of the experimentally tested specimens. The two methods are the conventional rectangular stress block method and the small strips method. The predictions of the theoretical load and bending moment capacities are then compared with the experimental results. Finally, a parametric study was conducted to study the effects of the concrete compressive strength and longitudinal GFRP reinforcement ratio on the structural performance of GFRP reinforced square concrete columns.

8.2 Theoretical Considerations of Material Properties

This section describes the stress-strain relationship of the constituent materials used in this study. These materials include the concrete, steel reinforcement and GFRP reinforcement. The relationships and the experimental material properties are used to theoretically calculate the prediction of the bending moment and corresponding load carrying capacities of the eccentrically loaded concrete specimens.

8.2.1 Concrete

The stress-strain model proposed by Yang et al. (2014) was used to develop the compressive stress of the unconfined concrete in terms of the strains as follows:

$$f_{concrete} = \left[\frac{(\beta_1 + 1)\left(\frac{\varepsilon_c}{\varepsilon_{co}}\right)}{\left(\frac{\varepsilon_c}{\varepsilon_{co}}\right)^{\beta_1+1} + \beta_1} \right] f_{co} \quad (8.1)$$

where $f_{concrete}$ is the compressive stress corresponding to the compressive strain ε_c; f_{co} is the unconfined concrete strength which is equal to 85% of the compressive cylinder strength of concrete at the first day of testing (f_c); ε_{co} is the strain corresponding to f_{co}; and β_1 is a parameter that determines the slopes of the ascending and descending branches as illustrated below. It should be noted that a factor of 85% of the compressive cylinder strength of concrete is used in this study in order to take into account the size effect of the large concrete specimens as compared to the small cylinders used to develop the stress-strain model. A factor of 90% has also been investigated in the analysis as shown below in the later sections.

The parameter $\beta_1$controls the slope of the ascending and descending branch of the stress-strain relationship, with Equation 8.2 is used for the ascending branch and Equation 8.3 is used for the descending branch.

$$\beta_1 = 0.2exp(0.73\xi) \quad \text{for } \varepsilon_c \leq \varepsilon_0 \quad (8.2)$$

$$\beta_1 = 0.41exp(0.77\xi) \quad \text{for } \varepsilon_c > \varepsilon_0 \quad (8.3)$$

$$\xi = \left(\frac{f_{co}}{f_0}\right)^{0.67} \left(\frac{w_0}{w_c}\right)^{1.17} \quad (8.4)$$

where f_o is a reference value for the concrete compressive strength equal to 10 MPa; w_o is a reference value for the concrete density equal to 2300 kg/m^3; and w_c is the concrete density assumed to be 2400 kg / m^3 for normal-weight concrete.

The modulus of elasticity (E_c) is calculated using Equation 8.5 as proposed in AS3600–2009 (AS 2009) for concrete strengths less than 40 MPa. The unconfined concrete strain (ε_{co}) corresponding to f_{co} is calculated using Equation 8.6 as proposed by Yang et al. (2014).

$$E_c = \left(0.043\sqrt{f_{co}}\right)(w_c)^{1.5} \tag{8.5}$$

$$\varepsilon_{co} = 0.0016exp\left[240\left(\frac{f_{co}}{E_c}\right)\right] \tag{8.6}$$

As noted in Section 6.4.1 of Chapter 6, the average compressive strength of concrete at 28 days, the first day and last day of testing the specimens was 29.3 MPa, 31 MPa and 35.3 MPa, respectively. Therefore, herein the strength of each specimen in the analytical model was calculated using the concrete compressive strength at the first day of testing of 31 MPa.

8.2.2 Steel Longitudinal Bars

The stress-strain relationship of the experimentally tested N12 bars is shown in Figure 8.1(a). For simplicity, in the analytical study the stress-strain relationship of the longitudinal steel reinforcing bars is idealised to exhibit a bilinear elasto-plastic behaviour for both tension and compression as shown in Figure 8.1(b). In the linear elastic region, the tensile strain in the steel does not reach the yield stress and the stress of the steel reinforcement is determined as follows:

$$f_s = \varepsilon_s E_s \tag{8.7}$$

where f_s is the tensile stress and E_s is the modulus of elasticity of the steel reinforcements.

On the other hand, in the post yield stage, the steel reinforcement reaches yield such that the stress is equal to the yield tensile stress (f_{sy}), as follows:

$$f_s = f_{sy} \tag{8.8}$$

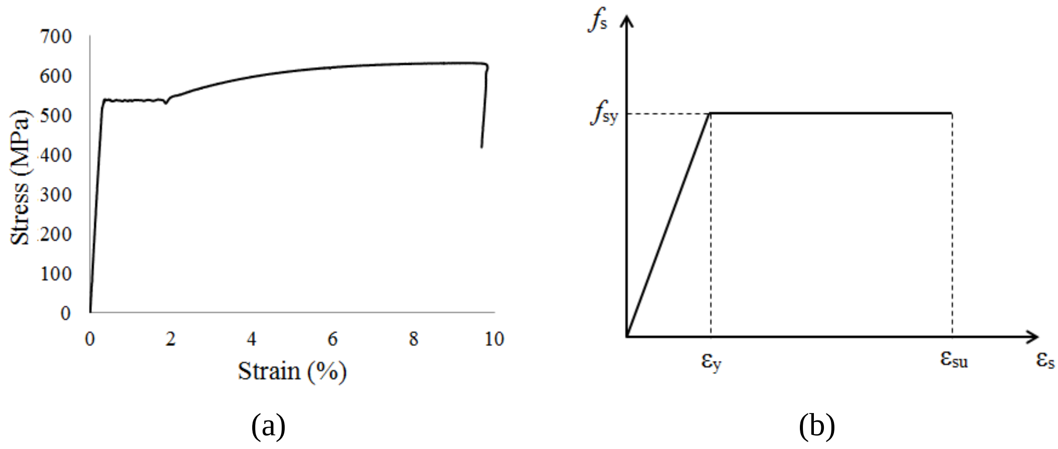

Figure 8.1. Stress-Strain Relationships of N12 longitudinal steel bar: (a) Experimental; and (b) Idealised (Youssef and Hadi 2017)

8.2.3 GFRP Longitudinal Bars

The GFRP reinforcing bars behave in a linear brittle manner up to failure when loaded in tension. In this study, the actual stress-strain response of the GFRP bars obtained by tensile testing illustrates the idealised linear elastic behaviour, as shown in Figure 8.2.

When loaded in compression, the behaviour of FRP bars is influenced by different modes of failure including transverse tensile failure, fibre micro buckling, or shear failure ACI 440.1R-15 (ACI 2015). Therefore, there is no standard axial compression test method for FRP composites. However, the behaviour of FRP bars in compression needs to be established to allow for the design of FRP RC columns. It has been reported that the compressive strengths of FRP bars are relatively low compared to the tensile strengths.

In early studies, the compressive strengths of GFRP bars were reported to be 55% of the tensile strengths, while the compressive modulus of elasticity were 80% of the tensile modulus of elasticity (Mallick 1988; Wu 1990; and Ehsani 1993). Chaallal and

Benmokrane (1993) showed that the compressive strength of GFRP rods were 77% of the tensile strength. Kobayashi and Fujisaki (1995) found that the compressive strengths of the GFRP bars were 30 to 40% of their tensile strengths. Deitz et al. (2003) reported that the ultimate compressive strength is approximately equal to 50% of the ultimate tensile strength, whereas there was no difference in the modulus of elasticity in compression compared to that in tension.

These studies indicate the test data of compression testing of GFRP bars are widely scattered and subjected to significant variations, unlike the tensile properties. Taking this into account, the compressive properties used in the analytical study are explained in the sections below.

Considering the linear brittle behaviour of GFRP bars, the tensile stress in each bar can be calculated using Hooke's Law, as follows:

$$f_{ft} = \varepsilon_{ft} E_{ft} \tag{8.9}$$

where f_{ft} is the tensile stress and E_{ft} is the tensile modulus of elasticity of GFRP longitudinal reinforcements.

Similarly, the compressive stress in each bar can be calculated using Hooke's Law, as follows:

$$f_{fc} = \varepsilon_{fc} E_{fc} \tag{8.10}$$

where E_{fc} is the compressive modulus of elasticity of GFRP longitudinal reinforcements.

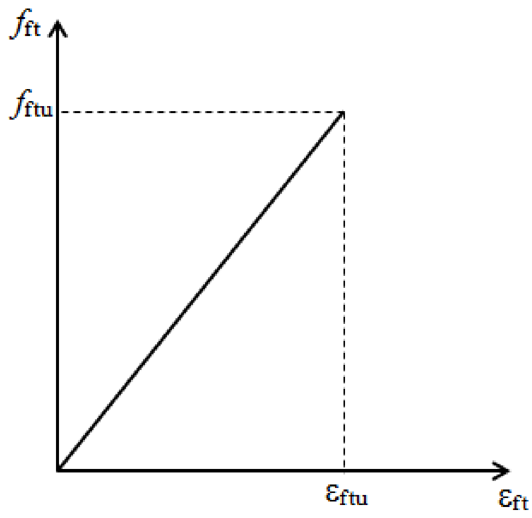

Figure 8.2. Experimental and Idealised Stress-Strain Relationship of longitudinal GFRP bar (Youssef and Hadi 2017)

8.2.4 GFRP Pultruded Sections

GFRP pultruded sections are orthotropic materials with the fibres laid mainly in the longitudinal direction. Therefore, these sections are stronger in the longitudinal direction as compared with the transverse direction. The sections are usually too narrow in the transverse direction to enable the extraction of standard coupons for tensile testing with dimensions as specified by the test standards.

Therefore, the transverse tensile properties of the pultruded structural sections could not be determined. Furthermore, considering the loads on columns are in the longitudinal direction, only the longitudinal properties will be used in the analytical study.

Similar to GFRP bars the GFRP pultruded sections are linear elastic materials in both tension and compression. Therefore, the tensile and compressive stresses can be calculated from Hooke's Law similar to that of Equations 8.9 and 8.10, respectively.

8.3 Summary of Experimental Results

A detailed discussion of the strength, failure modes, failure locations and ductility of each group of specimens under different types of eccentric loading were analysed and addressed in Chapter 7. The following outlines the general behaviour and results of the tested column and beam specimens. The summary of the specimen testing results is shown in Table 8.1.

For the eccentrically loaded column specimens (25 mm and 50 mm), the bending moment capacities (M_{exp}) corresponding to the first maximum axial load (P_{max}) was calculated by Equation 8.11. It should be noted that P_{max} corresponds to the first maximum load before the total onset of concrete spalling after the initial linear region of the axial load – displacement curves. When calculating the bending moments, both the application of the load at an eccentricity (e) and secondary moments arising from the lateral deflection of the column at P_{max} (δ) were taken into account.

For the beam specimens loaded under four-point bending, the bending moment capacity was calculated by Equation 8.12. This equation was obtained from simple statics as the bending moment value between the two point loads as equalling half the maximum applied load on the beam specimens multiplied by the shear span length (a = 235 mm in this study).

$$M_{exp} = P_{max}(e + \delta) \tag{8.11}$$

$$M_{exp} = \frac{P_{max}}{2} a \tag{8.12}$$

Table 8.1. Experimental maximum load and bending moment capacity of specimens (Youssef and Hadi 2017)

Test Specimen	1st Maximum Load, P_{max} (kN)	Axial displacement at P_{max}, Δ (mm)	Lateral deflection at P_{max}, δ (mm)	Bending Moment, M_{exp} $[P_{max}(e+\delta)]$ (kN.m)
RS-0	1350	2.87	0	0
RS-25	995	2.72	2.11	27.0
RS-50	747	2.65	2.66	39.3
RS-B	232	-	8.08[c]	27.3[d]
RF-0	1285	2.59	0	0
RF-25	803	3.00	2.21	21.9
RF-50	615	2.33	2.46	32.3
RF-B	340[a]	-	12.13[c]	40.0[d]
I-0	1425	3.13	0	0
I-25	1008	2.51	2.05	27.3
I-50	765	2.88	3.18	40.7
I-B	216[b]	-	13.47[c]	25.3[d]
C-0	1385	3.24	0	0
C-25	985	2.86	2.96	27.5
C-50	679	3.04	3.69	36.4
C-B	370	-	12.78[c]	43.4[d]

[a] The shear zones of only this specimen were wrapped with two layers of CFRP sheets; [b] Failed prematurely by bearing. Data point could not be used on the *P-M* interaction diagram; [c] Midspan deflection of the beam specimens; [d] Calculated using Equation 8.12.

8.4 Load Capacity of Concentrically Loaded Column Specimens

8.4.1 Steel Reinforced Specimens (Group RS)

When a column is subjected to a concentric load (e = 0), the column shortens uniformly with increasing load. The longitudinal strains in the steel reinforcement and concrete are equal at all stages of loading (ACI 318-14 2014). ACI 318-14 (ACI 2014) uses the following equation to represent the axial load capacity of conventional steel RC columns under concentric loading:

$$P_o = 0.85 f_c (A_g - A_{st}) + f_{sy} A_{st} \tag{8.13}$$

where f_c is the concrete compressive strength; A_g is the gross sectional area of concrete; A_{st} is the total area of longitudinal reinforcement; and f_{sy} is the yield strength of the longitudinal reinforcement.

For Specimen RS-0, the predicted axial load capacity using Equation 8.13 and the concrete strength at the first day of testing (f_c = 31 MPa) is 1394 kN. Therefore, the ratio of the experimental axial capacity to the predicted value is 0.968. Some possible reasons for the theoretical capacity being slightly higher than the experimental value may be due to misalignment in the reinforcement or due to the variation in concrete strength.

8.4.2 GFRP Reinforced Specimens (Group RF)

The current American guide, ACI 440.1R-15 (ACI 2015) states the contribution of FRP bars should be neglected when used as reinforcement in columns. Similarly, the Canadian standard, CSA-S806 2012-R2017 (CSA 2012-R2017) allows the use of FRP bars as longitudinal reinforcement in axially loaded columns only, but ignores the compressive contribution of the FRP bars when calculating the ultimate axial capacity, as shown in Equation 8.14.

$$P_o = \alpha_1 f_c (A_g - A_f) \tag{8.14}$$

where $\alpha_1 = 0.85 - 0.0015 f_c \geq 0.67$; and A_f is the total cross-sectional area of the longitudinal GFRP bars.

Based on the literature, other equations have been developed to predict the nominal axial capacity of the GFRP RC specimen. Tobbi et al. (2012) showed that ignoring the compressive contribution of the GFRP bars in Equation 8.14 underestimates the maximum axial capacity. Therefore, the compressive contribution of the GFRP bars to the overall column capacity was taken into account. This was done by considering the GFRP bars compressive contribution to be 35% of the tensile strength as suggested by Kobayashi and Fujisaki (1995), as shown in Equation 8.15.

$$P_o = 0.85 f_c (A_g - A_f) + 0.35 f_{fu} A_f \tag{8.15}$$

where f_{fu} is the ultimate tensile strength of the longitudinal GFRP bars

Tobbi et al. (2014) proposed the most recent equation to calculate the nominal axial capacity, which also takes into account the compressive contribution of the GFRP longitudinal bars. In this equation, the compressive contribution of the GFRP longitudinal bars is calculated based on the elastic theory and from the material properties as shown in Equation 8.16.

$$P_o = 0.85 f_c (A_g - A_f) + \varepsilon_o E_f A_f \tag{8.16}$$

where ε_o is the concrete strain at peak stress which is equal to 0.003 as defined by ACI 318-14 (ACI 2014); and E_f is the modulus of elasticity of the GFRP longitudinal reinforcement.

The ratios of the experimental axial capacity for the concentrically loaded column specimen reinforced with GFRP bars (Specimen RF-0) as compared to the theoretical values obtained from Equations 8.14, 8.15 and 8.16 are shown in Table 8.2. It should be noted that the cross-sectional area used in the calculations was determined on the GFRP bar's standard diameter of 12.7 mm rather than by a value obtained from Immersion testing. As per ASTM D7205-2010, the standard cross-sectional area is the conventionally accepted area of a steel bar with the same number designation as a FRP bar being tested and the nominal cross-sectional area is determined by Immersion testing. Furthermore, the concrete strength at the first day of testing was used in the formulas. Furthermore, it was assumed that the compressive modulus of elasticity was equal to the tension modulus of elasticity as reported by Deitz et al. (2003).

It can be seen that ignoring the contribution of the GFRP bars in Equation 8.14 results in an underestimation of the maximum capacity of 18.3%. Furthermore, the ratio of the experimental maximum load to the predicted value using Equation 8.15 is below one with a value of 0.892. This value indicates that this equation over estimates the nominal axial capacity of Specimen RF-0. On the other hand, Equation 8.16 provides an under estimation of the maximum capacity of 2.6%. Therefore, Equation 8.16 provided the most accurate estimate of the maximum capacity and was used in this study for the GFRP reinforced and GFRP encased specimens.

Table 8.2. Experimental and theoretical axial capacity of Specimen RF-0 (Youssef and Hadi 2017)

Experimental Max. Axial Load P_{max} (kN)	Theoretical, P_o (kN)			$\frac{P_{max}}{P_o}$		
	Equation 8.14	Equation 8.15	Equation 8.16	Equation 8.14	Equation 8.15	Equation 8.16
1285	1086	1440	1252	1.183	0.892	1.026

8.4.3 GFRP Encased Specimens (Group I and C)

In this study, the same formula proposed by Tobbi et al. (2014) was used to predict the axial capacity of the GFRP encased specimens with the assumption that the strain in the GFRP sections is approximately equal to the concrete ultimate strain, as shown in Equation 8.16. The compressive modulus of elasticity was used in the calculations. It should be noted that the compression properties of the C-sections were determined by both direct end loading coupons and also by using a simple fixture to confine the ends of the coupons and prevent the premature failures associated with end crushing, as explained in Chapter 5. Only the webs of the C-sections were tested. However, due to the materials and resources available, the compression properties of the web and flanges of the I-sections were determined only by direct end-loading, as explained in Chapter 6.

Therefore, for the I-section, the compressive modulus of elasticity was taken as the total average values from the web and flanges of the I-section of 22.0 MPa (global value in Section 6.4.4.2 of Chapter 6). For the C-sections, the compression modulus of elasticity determined by using the confined coupons tested (24.7 MPa, global value in Table 5.2 of Chapter 5) was adopted in calculating the axial capacity for Group C specimens. Furthermore, the actual measured dimensions of the cross-sections were slightly smaller than the nominal dimensions provided by the manufacturer. Therefore, the measured dimensions were used to determine the cross-sectional areas (Table 5.1 of Chapter 5 for C-sections and Table 6.6 of Chapter 6 for I-sections).

The ratios of the experimental axial capacity for the concentrically loaded specimen reinforced with GFRP sections (Specimens I-0 and C-0) as compared to the theoretical values obtained from Equation 8.16 are shown in Table 8.3. It can be seen that there is a reasonable and accurate agreement between the experimental and calculated load capacity for these column specimens, especially for Specimen C-0.

Table 8.3. Experimental and theoretical axial capacity of Specimen I-0 and C-0 (Youssef and Hadi 2017)

Specimen	Experimental Max. Axial Load P_{max} (kN)	Theoretical P_o (kN) Equation 8.16	$\frac{P_{max}}{P_o}$
I-0	1425	1324	1.076
C-0	1385	1349	1.027

8.5 Theoretical P-M Interaction Diagrams

An analytical axial load-bending moment (P-M) interaction diagram was plotted to represent the axial load (P) and corresponding bending moment (M) of each of the specimens. A number of assumptions consistent with those applicable to steel reinforced cross sections were used in the analysis to develop the theoretical *P-M* interaction diagrams of GFRP reinforced and GFRP encased concrete cross-sections.

These assumptions are as follows:

- The distribution of strain is assumed to be linear along the height of the section or in other words plane sections remain plane after deformation.
- Strain compatibility exists between the constituent materials, i.e. concrete, steel and GFRP reinforcement and sections, such that a perfect bond is assumed amongst these materials
- In tension, concrete is weak and therefore its tensile strength is ignored
- The steel reinforcing bars behave as an elastic-perfectly plastic material in both tension and compression as shown in Figure 8.1.
- The GFRP reinforcing bars and GFRP pultruded sections behave as a linear brittle material with orthotropic properties, as shown in Figure 8.2.
- For the GFRP pultruded sections, only the flanges in compression and flanges in tension is assumed to contribute to the compressive and tensile resistance, respectively. In other words, the compressive and tensile resistance of the web of both the I-sections and C-sections is neglected. Furthermore, only the longitudinal tensile and compressive properties were used in the analysis with the transverse properties ignored.
- The confinement effect of the lateral steel and GFRP stirrups is ignored.
- The stress-strain model of Yang et al. (2014) for unconfined concrete in compression is adopted as defined in Section 8.2.1.
- Considering the column specimens are considered as short specimens, the effect of slenderness was not taken into account when determining the theoretical *P-M* interaction relationships.

For calculation of the axial load capacities and bending moment capacities under eccentric loads and pure bending, two methods were analysed. The first method is the conventional rectangular stress block method to construct the interaction diagrams of steel RC columns following the Australian Standard AS3600–2009 (AS 2009). The second method is the small strips concrete method as described by Yazici and Hadi

(2009). What varies in the two methods is the approach to determining the concrete response in compression.

In the rectangular stress block method, the concrete compressive stresses are assumed to be uniform along the cross section along a depth of γd_n as shown in Figure 8.3, with the compressive force in the concrete determined by Equation 8.17 for specimens of Groups RS and RF. The rectangular stress block method was not implemented for specimens of Group I and C.

$$C_{c1} = \alpha_2 f_c b \gamma d_n \tag{8.17}$$

where, C_{c1} is the compressive force in the concrete; f_c is the concrete compressive strength on the first day of testing (31 MPa); d_n is the neutral axis depth from the top of the section; $\alpha_2 = 1.0 - 0.003 f_c$ within the limits $0.67 \leq \alpha_2 \leq 0.85$; and $\gamma = 1.05 - 0.007 f_c$ within the limits $0.67 \leq \gamma \leq 0.85$.

On the other hand, in the small strips method the concrete cross section is assumed to consist of small finite parallel strips with a thickness (*t*) of 1 mm and a width equal to the cross section width (*b*) of 210 mm, as shown in Figure 8.4. The number of strips (*n*) is equal to the depth of the cross section of 210 mm divided by the thickness of each strip. Therefore, the cross section was divided into 210 small strips. Based on the assumption that strain distribution is linear along the height of the section after bending, the strain in the centre of each strip ($\varepsilon_{c,n}$) can be calculated, by assuming the extreme concrete compressive fibre has reached the ultimate compressive strain of 0.003 as shown in Equation 8.18.

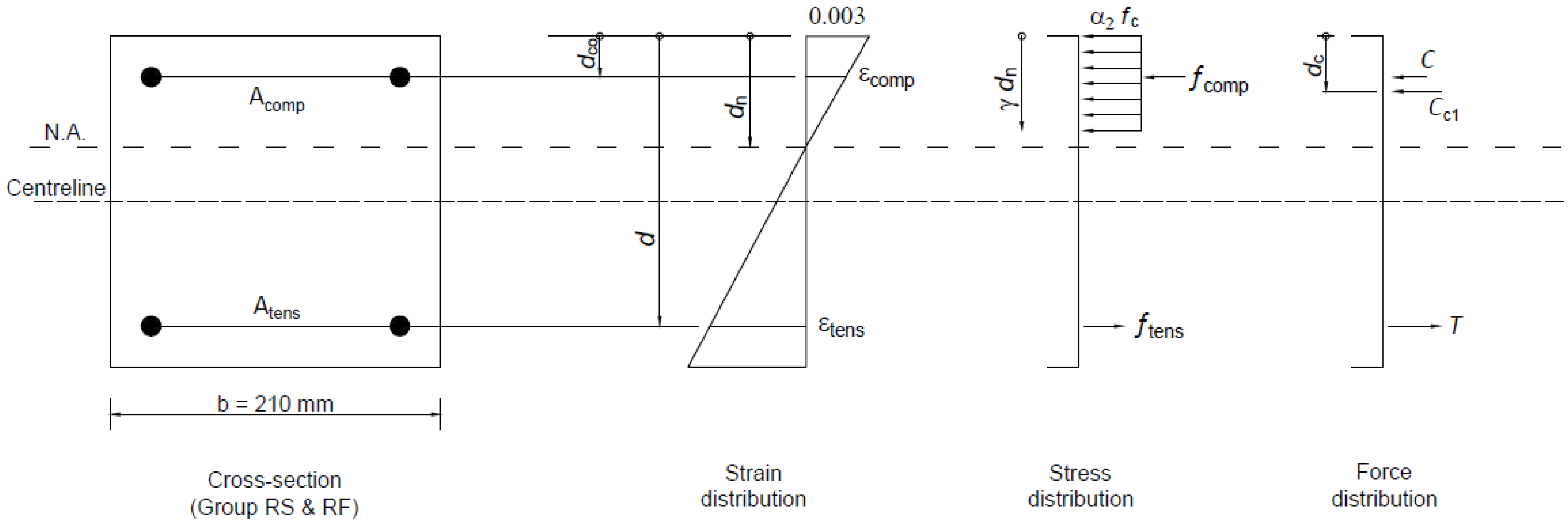

Figure 8.3. Rectangular stress block method and force distribution of reinforcement for Group RS and RF specimens (Youssef and Hadi 2017)

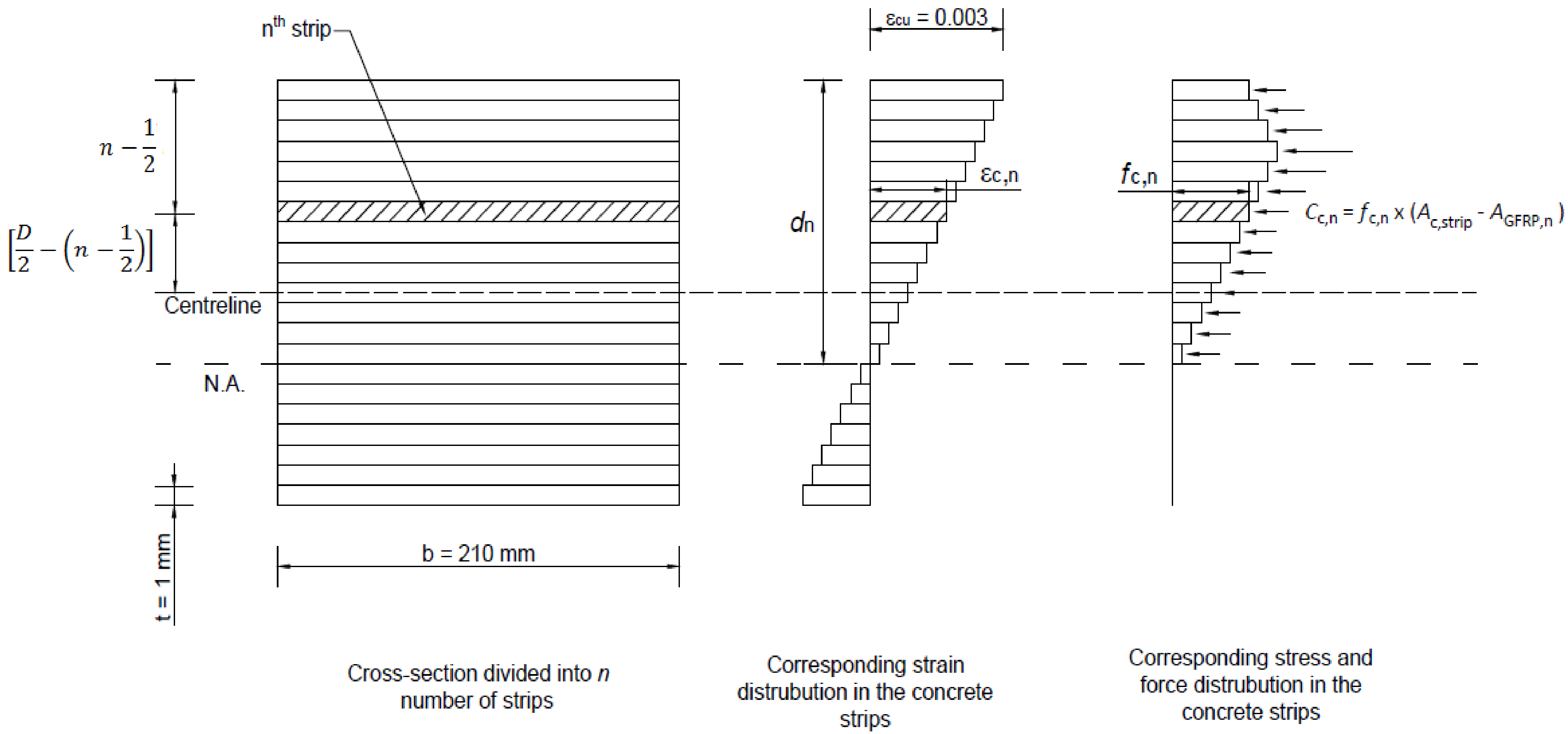

Figure 8.4. Small strips method to determine the concrete compressive response (Youssef and Hadi 2017)

After calculating the strain in each concrete strip, the corresponding stress value ($f_{c,n}$) on the centre of each strip is calculated according to the stress-strain model for unconfined concrete explained above in Equation 8.1. With the basic assumption that the tensile strength of concrete is ignored in the calculations, the stresses corresponding to tensile strains (i.e. $\varepsilon_{c,n} < 0$) are assumed to be zero. After determining the stresses, the force reaction in the centre of each concrete strip ($C_{c,n}$) is calculated from Equation 8.19 for specimens of Groups RS and RF and from Equation 8.20 for specimens of Groups I and C. The differences in these two formulas are explained below. The moment created by the force on each strip is calculated as the force in each strip multiplied by the distance to the centreline of the section as shown in Equation 8.21. Therefore, the overall response of the concrete section is calculated as the summation of the forces acting on the strips, as shown in Equation 8.22. In addition, the overall moment response of the concrete section is calculated as the summation of the moments with respect to the centreline of the section.

$$\varepsilon_{c,n} = 0.003 \times \frac{d_n - (n - \frac{1}{2})}{d_n} \tag{8.18}$$

$$C_{c,n}(Specimens\ RS\ \&\ RF) = f_{c,n} \times A_{c,strip} \tag{8.19}$$

$$C_{c,n}(Specimens\ I\ \&\ C) = f_{c,n} \times (A_{c,strip} - A_{GFRP,n}) \tag{8.20}$$

$$M_{c,n} = C_{c,n}\left[\frac{D}{2} - \left(n - \frac{1}{2}\right)\right] \tag{8.21}$$

$$C_{c,2} = \sum_{n=1}^{210} C_{c,n} \tag{8.22}$$

where, n = 1, 2, 3,….., 210th strip starting from the top of the section; $f_{c,n}$ is the concrete stress in the n^{th} strip, determined by Equation 8.1; $A_{c,strip}$ is the gross concrete cross sectional area for each strip ($b \times t$); and $A_{GFRP,n}$ is the area of the GFRP sections in the n^{th} strip.

In both these methods the same approach is taken to find the stresses and forces in the tensile and compressive reinforcement. First the strains in the tensile and compressive reinforcement or flanges of the GFRP sections are calculated using similar triangles with the assumptions of linear strain distribution and the strain in the extreme concrete compressive fibre has reached the ultimate compressive strain of 0.003. The tensile strains are considered negative while the compressive strains are positive. The stress in each layer of reinforcement or flanges of the sections is then calculated by applying the stress-strain relationships for the constitutive materials. The forces in the reinforcement are calculated as the stresses multiplied by the area.

However, it is important to note that the compressive response of the concrete using Equation 8.17 and Equation 8.19 for Specimens RS and RF does not take into account the existence of the compression reinforcement (top layer of bars) occupied in the concrete compression zone. Therefore, to take into account the compression reinforcement in the calculations, the force in the compression reinforcement is calculated using Equations 8.23 and 8.24 such that if the top layer of bars is within the concrete compression zone, it is necessary to subtract $0.85f_c$ multiplied by the cross-sectional area of the bars in the top layer from the total force contribution of those bars. Both Equation 8.23 and Equation 8.24 are for the rectangular stress block method. The same equations exist for the small strips method but the concrete compression zone occupies a height of d_n instead of γd_n. Furthermore, for the bottom layer of reinforcement these equations were not applied and the force in that layer was simply calculated as the stress in that layer multiplied by the area even if that layer of bars occupied the concrete compression zone.

On the other hand, a slightly different approach was taken for specimens of Groups I and C to take into account the existence of the GFRP sections ($A_{GFRP,c}$) occupied in the concrete compression zone for the small strips method. This was done by subtracting the area of the GFRP sections, including flanges and also the webs, located in each concrete strip in the compression zone as shown in Equation 8.20.

The forces for either the top or bottom flanges for Group I and C specimens were simply calculated as the area of the flanges (shaded regions in Figure 8.5) multiplied by the stresses in the flanges with positive force denoting compression and negative force implying tension. As mentioned above, the force contribution of the webs were ignored. It is important to note that the rectangular stress block was not used for specimens of Groups I and C as it was quite complex to take into account the areas of the GFRP sections located in the concrete compression block and the corresponding lever arms and hence only the small strips method was utilised for these specimens considering each concrete layer is analysed separately instead of one whole block.

If $\gamma d_n < d_{co}$: $$C = f_{comp} A_{comp} \tag{8.23}$$

If $\gamma d_n > d_{co}$: $$C = f_{comp} A_{comp} - 0.85 f_c A_{comp} \tag{8.24}$$

where, d_{co} is the distance from the top of the section to the centre of the top layer of reinforcement; and f_c is the concrete compressive cylinder strength at the first day of testing.

Therefore, using the two methods the axial load carrying capacity is equal to the summation of forces acting on the reinforcement, forces acting on the flanges of the GFRP encased sections and the forces acting on the concrete compressive section. Similarly, the moment carrying capacity is equal to sum of the moments with respect to the centreline of the section under a given eccentricity. The applied eccentricity is equal to the bending moment capacity divided by the axial load capacity.

The theoretical load-moment interaction diagrams for each method were drawn based on twelve data points. The first point represents the axial load capacity of the specimens under concentric loading with no applied eccentricity. The axial capacity for all the groups of specimens loaded concentrically were as explained in Section 8.4. The rest of the points represent the axial load and bending moment capacity specimens loaded with a combined axial load and bending moment with the second point expressing the data point of the 25 mm eccentric loaded specimen. The rest of the data points are obtained with gradually increasing the eccentricity up until the pure bending condition. The process is as follows:

Using the goal seek function in MS Excel, the applied eccentricity is set to the required value by changing only the neutral axis depth value (d_n). The eccentricity is calculated as the moment capacity divided by the load capacity. The goal seek function determines the corresponding strains, stresses and force components acting in the reinforcement and concrete strips or blocks and subsequently determines the respective axial and bending moment capacities to obtain the set chosen value of eccentricity, by only changing the neutral axis depth input. This process is repeated by varying the eccentricity value to obtain the data points on the load-moment interaction diagram up until the pure bending condition. As mentioned above, the compressive strength at the first day of testing was used to develop the theoretical *P-M* interaction diagrams. Simply using the 28 day cylinder compressive strength of concrete would underestimate the theoretical *P-M* interaction diagrams.

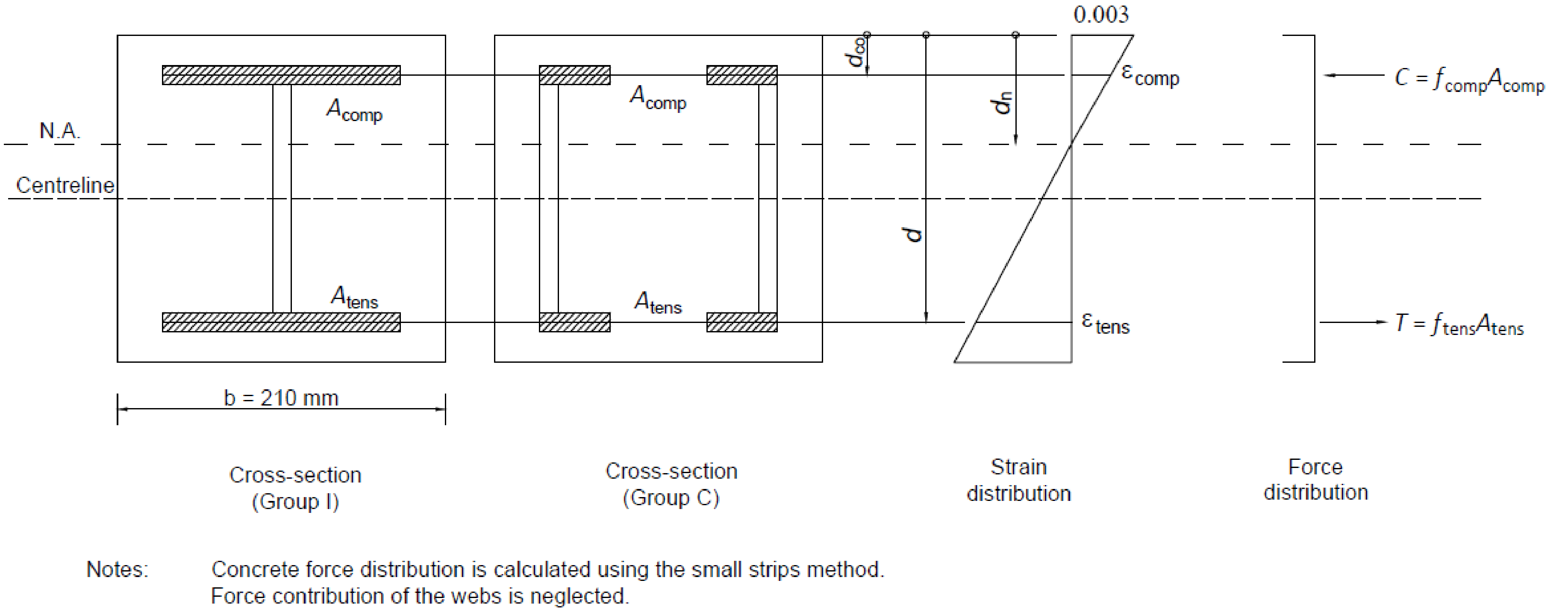

Figure 8.5. Force distribution of specimens of Group I and C (Youssef and Hadi 2017)

8.6 Analytical versus Experimental Results

Plotting an experimental *P-M* diagram based on four points of loading would not accurately predict the load and bending moment capacities especially when all the loading points are not identified, most notably the balanced points. Therefore, the first maximum load (P_{max}) and corresponding bending moment capacities (M_{exp}) of the experimentally tested specimens, as shown in Table 8.1, were plotted as points on the theoretical *P-M* interaction diagrams.

Although the eccentrically loaded GFRP reinforced and GFRP encased specimens were able to sustain a slight increase in load after P_{max} (as explained in Chapter 7), the eventual failure after this second peak load (P_{peak}) was brittle and explosive with no warning signs with failure occurring at or not long after this load, as shown in Figure 8.6 (as explained in Section 7.2.2 of Chapter 7). As a result, the analytical axial load-bending moment diagrams were drawn for the GFRP reinforced and encased specimens corresponding to the first maximum load (P_{max}) before the activation of the confinement effect of the stirrups and thus just before the onset of concrete spalling. Therefore, the confinement effect of the lateral steel and GFRP stirrups is ignored and an unconfined concrete model was adopted in the analysis.

The theoretical *P-M* interaction diagrams and the experimental results for all the groups of specimens are shown and analysed below. For comparison purposes, the theoretical load and bending moment capacities for the 25 mm and 50 mm eccentrically loaded specimens were plotted as circular data points on the *P-M* diagram, in order to compare the same values obtained experimentally which were denoted by the square data points. It should be noted that the results of the GFRP reinforced and GFRP encased beam specimens were not presented and plotted against the theoretical *P-M* diagrams as the failure of these beam specimens were in shear or bearing rather than in flexure and there were inconsistencies in the testing of these specimens as discussed in Section 7.3 of Chapter 7. In addition, the experimental results of the GFRP reinforced beam specimen could not be compared to the theoretical models. Further research elaboration is necessary to investigate the beams by taking into account ACI 440.1R–15 (ACI 2015) provides guidelines for the flexural design of FRP reinforced beams designed to be controlled by either concrete crushing or FRP rupture.

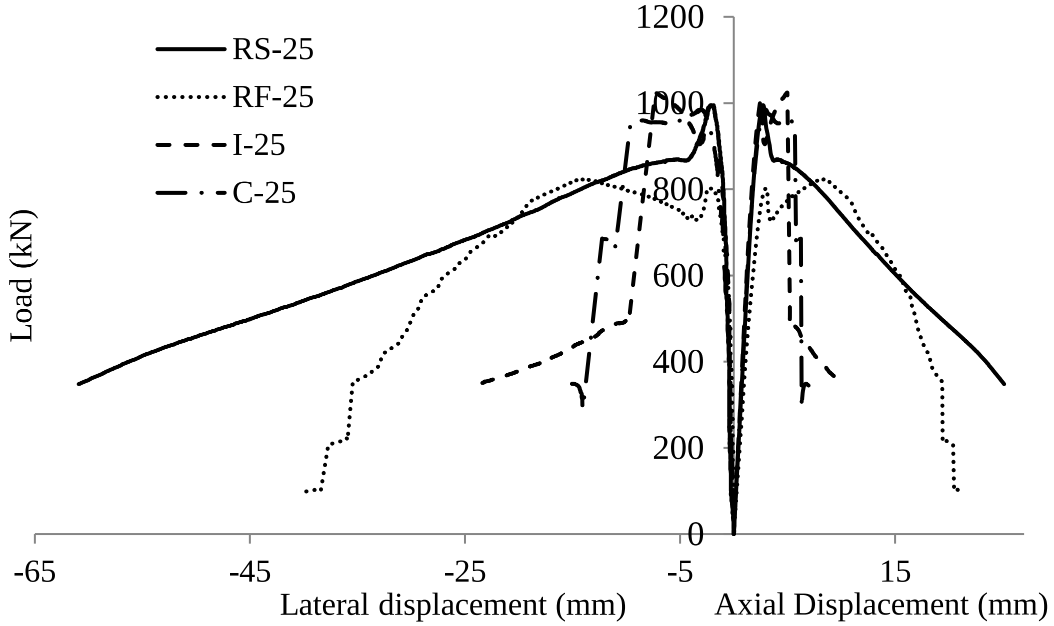

Figure 8.6. Axial and lateral load-deflection curves of the 25 mm eccentrically loaded column specimens, *e*=25mm (Youssef and Hadi 2017)

8.6.1 Steel Reinforced Specimens (Group RS)

The experimental load and moment capacities of the steel reinforced specimens (Group RS) for all loading types were close to the theoretical *P-M* diagrams for both methods, as shown in Figure 8.7. All the experimental data points except for the pure compression point lied above the *P-M* diagram using the small strips method. However, for the rectangular stress block *P-M* diagram, the data point of the 25 mm eccentric loaded specimen was slightly under the *P-M* interaction diagram, with the theoretical load capacity being 3.9% greater than the experimental load capacity. Some possible reasons for the theoretical load capacity of this data point being slightly higher than the experimental value may be due to either misalignment in the reinforcement, or variation in concrete strength, or specimen alignment errors. Therefore, the *P-M* diagram developed from the small strips method provided a more conservative estimate of the load and bending moment capacities as compared to the rectangular stress block. In general, both the developed theoretical models yielded results that are comparable to the experimental results for Group RS specimens.

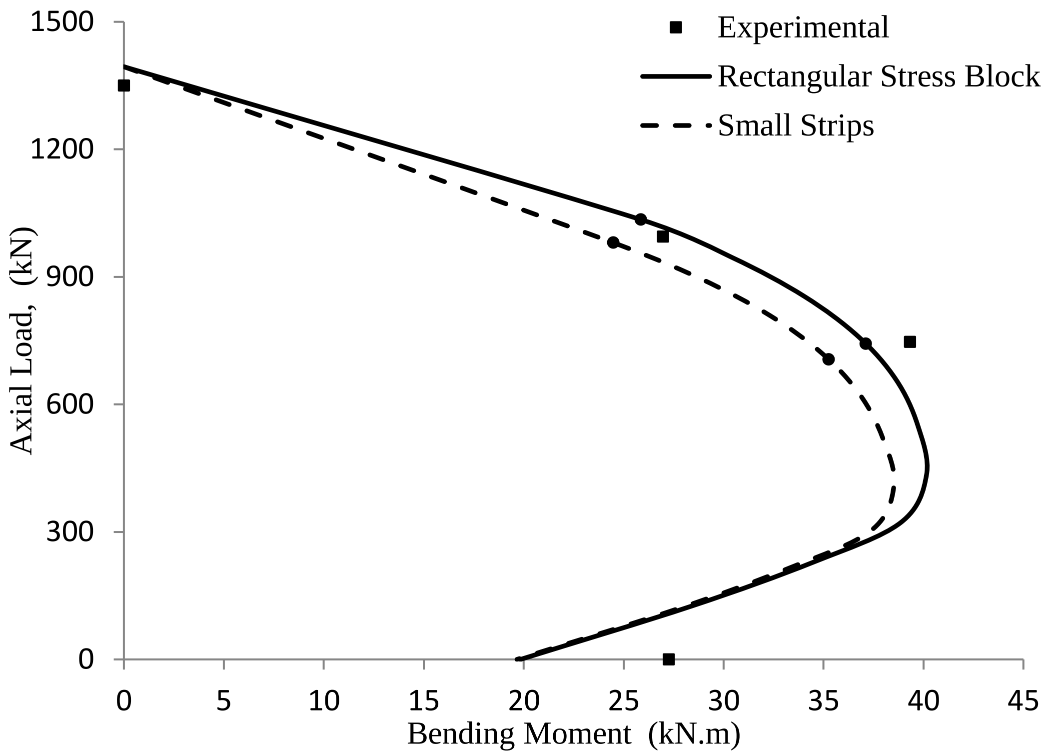

Figure 8.7. Comparison of theoretical *P-M* diagrams and experimental results for Group RS specimens (Youssef and Hadi 2017)

8.6.2 GFRP Reinforced Specimens (Group RF)

For the GFRP reinforced specimens (Group RF), the effect of the compressive contribution of the GFRP bars when determining the *P-M* interaction diagram was investigated. A total of two theoretical diagrams were drawn with the first including the compressive contribution of the GFRP bars by assuming the modulus of elasticity in compression is equal to the modulus of elasticity in tension (i.e. $E_{fc} = E_{ft}$), as shown in Figure 8.8(a), whereas the second theoretical diagram ignored the compressive contribution of the bars (i.e. $E_{fc} = 0$), as shown in Figure 8.8(b).

When taking into account the compressive contribution of the GFRP bars the experimental result of the concentrically loaded and 50 mm eccentrically loaded specimens (RF-0 and RF-50) yielded values above the theoretical *P-M* diagram using the small strips method with comparable results, as shown in Figure 8.8(a). However, the data point of the 25 mm eccentrically loaded specimen fell below the theoretical *P-M* diagram developed by the small strips method. Errors in testing may be the reason for the low experimental results. This can be seen in the load versus axial deformation curves for the four groups of specimens loaded in 25 mm eccentricity, as shown in Figure 8.6. The initial slope of the load-displacement curve of Specimen RF-25 was lower than that of the other specimens. This could be due to errors in aligning the specimen resulting in load not being applied exactly at 25 mm eccentricity (as explained in Chapter 7). Furthermore, the failure location of the internal reinforcement of this specimen was located at the top of the specimen rather than at mid-height (as explained in Chapter 7). On the other hand, the experimental results of the eccentrically loaded specimens yielded values below the theoretical *P-M* diagram using the conventional rectangular stress block method. Therefore, when taking into account the compressive contribution of the GFRP bars, the small strips method provided a more accurate approximation of the experimental loads and bending moment capacities for Group RF specimens for the different types of loading as compared to the conventional rectangular stress block method.

When ignoring the compressive contribution of the GFRP bars, the axial load capacity in pure compression is decreased as the second part of Equation 8.16 is reduced to 0 ($E_{fc} = 0$) providing a conservative approach for the concentric loading condition. It should be noted that similar to Specimen RF-25, Specimen RF-50 also failed at the top of the specimen rather than in the instrumented region as discussed in Chapter 7. Having said this, the 50 mm eccentrically loaded column shows good agreement with the interaction diagram for this case with the experimental data point above the theoretical diagram for the two methods. However, the 25 mm eccentrically loaded column falls below the rectangular stress block method diagram but shows relatively good agreement with the small strips method, although the experimental load capacity value is 3.4% lower than that obtained theoretically using the small strips method. As mentioned above errors in testing of this column did occur.

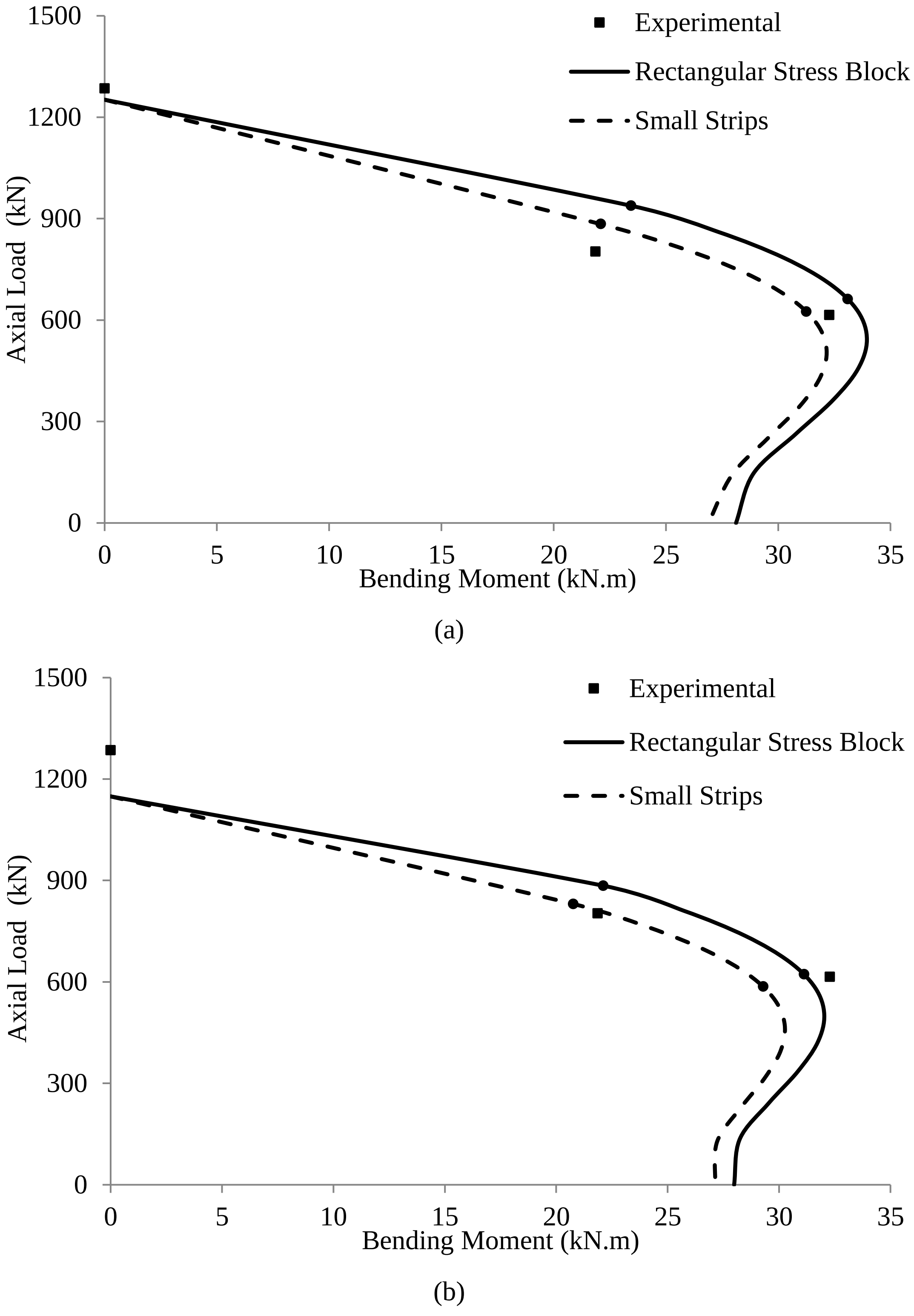

Figure 8.8. Comparison of theoretical *P*-*M* diagrams and experimental results for Group RS specimens: (a) Compressive contribution of GFRP bars included (E_{fc} = E_{ft}); and (b) Compressive contribution of GFRP bars ignored (E_{fc} = 0) (Youssef and Hadi 2017)

In general, considering that the compressive properties of FRP bars has not been extensively understood, especially when embedded in concrete, it is safer to say that ignoring the compressive contribution of the GFRP bars and drawing the theoretical *P-M* diagram based on the small strips method is the most accurate and safe alternative for the design of such columns at this stage. Having said this, for the small strips method further consideration of the maximum stress limited to the concretes stress-strain curve to allow for differences between the cylinder strength and in-place column specimen strengths, which may vary between $0.85f_c$ to $0.9f_c$, as well as each specimen's strength at the respective day of testing should be taken into account when drawing the *P-M* diagrams as explained below with the conclusions slightly varying.

Considering that the theoretical *P-M* diagrams were drawn based on the concrete compressive strength at the first day of testing and knowing that the strength of concrete is ever increasing, a discussion of the effects of this is necessary. The concentric specimens were tested first, followed by the 25 mm eccentrically loaded specimens then the 50 mm loaded specimens and lastly the beam specimens. The concrete strength of each specimen tested on each day could be determined based on a linear trend of the known concrete compressive strength determined at each day tested. The increase in concrete strength for each specimen tested on a different day will shift the theoretical *P-M* diagrams upwards, since the load and bending moment capacity will increase. Therefore, the relationship between the experimental data points as a comparison to these revised theoretical *P-M* diagrams should be taken into account.

In summary with the slight increase in concrete strength for each specimen, it was realised that although the revised *P-M* diagrams would be shifted slightly upwards for both methods, with the experimental data point of RF-50 now slightly below the *P-M* diagram for the small strips method (when $E_{fc} = E_{ft}$) and rectangular stress block method (when $E_{fc} = 0$), the same outcomes and conclusions stated above for Groups RS and RF specimens were acceptable. Therefore, the small strips method for predicting the *P-M* interaction relationship was a more safe and accurate approach as compared to the rectangular stress block method. Furthermore, ignoring the compressive contribution of the GFRP bars is also the best method for those specimens.

Furthermore, it should be noted that the Australian standard AS3600–2009 (AS 2009) mentions that if a stress-strain relationship is used for concrete, the maximum stress of the concrete shall be modified to $0.9f_c$. In the standard the parameter f_c denotes the characteristic compressive cylinder strength of concrete at 28 days (f_c'), but in this study f_c was represented as the concrete strength at the first day of testing, as mentioned above. In this study the maximum stress was limited to $0.85f_c$ as explained in Section 8.2.1 to take into account size and shape effects between the cylinders and column specimens. If the maximum stress is modified to $0.9f_c$ the *P-M* diagram for the specimens of Group RS and RF developed using the small strips method will shift upwards to just slightly under the diagram developed using the rectangular stress block method, as shown in Figure 8.9. Similar *P-M* interaction diagrams were also obtained for the Group RS specimens with the diagram developed by the small strips method using a maximum stress of $0.9f_c$ approximately equal but just slightly under the diagram using the rectangular stress block method.

However, in terms of the Group RF specimens, the experimental data points are more matched or appropriate at this stage with the level of knowledge on GFRP reinforced columns to the values obtained by the small strips method using a maximum stress of $0.85f_c$ rather than those obtained by the rectangular stress block method, as explained above and shown in Figure 8.8 and Figure 8.9. Most notably, when utilising the small strips method with a maximum stress of $0.9f_c$ and assuming $E_c = 0$ (Figure 8.9), the data point of Specimen RF-50 is above the *P-M* diagram when using the concrete strength at the first day of testing but when using the concrete strength at the day of testing the specimen (as explained above), the experimental load capacity is just slightly lower than that of the theoretical value whereas the theoretical moment capacity is similar to the experimental value. Therefore, for the GFRP reinforced specimens it is recommended to limit the maximum concrete stress to $0.85f_c$ and neglect the compressive contribution of the bars as a conservative approach for design. Having said this, further experimental verification of the theoretical P-M diagrams is required for the GFRP reinforced specimens.

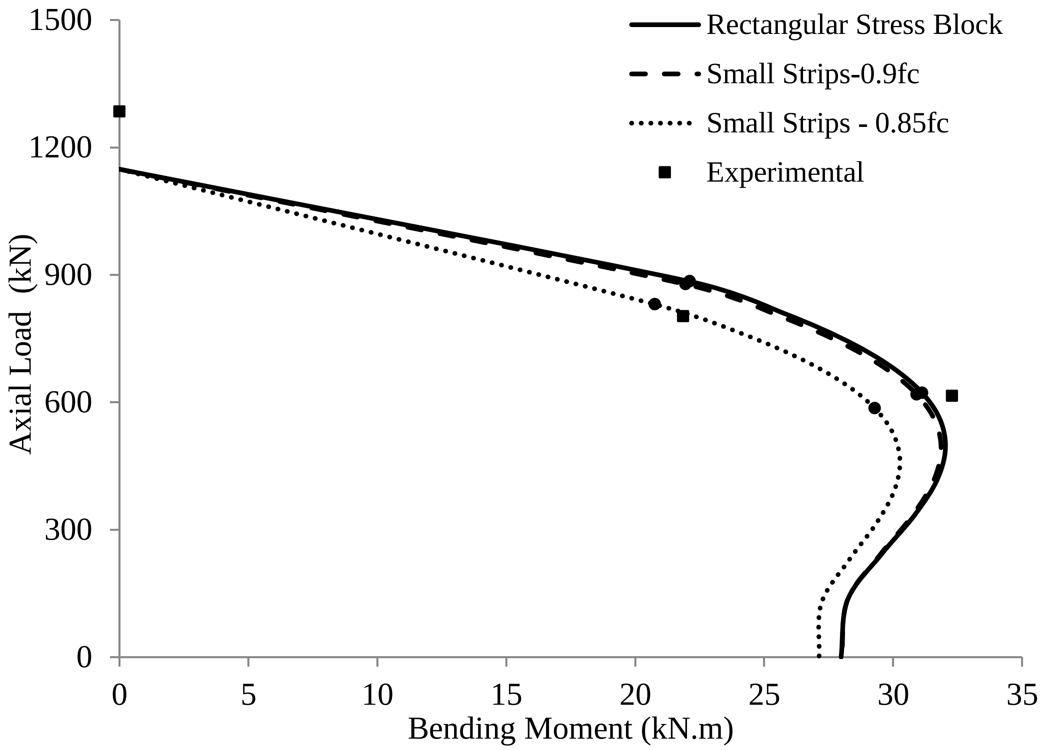

Figure 8.9. Theoretical *P-M* diagrams of Group RF specimens when varying the maximum stress of concrete from $0.85f_c$ to $0.9f_c$ and assuming $E_{fc} = 0$ (Youssef and Hadi 2017)

In addition, the experimental results of the GFRP reinforced beam specimen could not be compared to the theoretical models. Further research elaboration is necessary to investigate the beams by taking into account ACI 440.1R–15 (ACI 2015) provides guidelines for the flexural design of FRP reinforced beams designed to be controlled by either concrete crushing or FRP rupture. The data point of the theoretical *P-M* interaction diagram proposed in this study for the pure bending condition will need to be compared with the value obtained from the guidelines for the flexural design of flexural members in ACI 440.1R–15 (ACI 2015).

8.6.3 GFRP Encased Specimens (Group I and C)

For both the GFRP I-section and C-section encased specimens, the developed theoretical models using the small strips method utilising a maximum stress of $0.85f_c$

and $0.9f_c$ yielded results that were conservative as compared to the experimental results, as shown in Figures 8.10 and 8.11. This may be due to the assumption of using only the flanges of the sections for the determination of the forces. If the contributions of the webs of these sections are taken into account, the theoretical load and moment interaction diagram will shift upwards. Having said this, considering the limited studies and the orthotropic nature of the GFRP pultruded material as well as the high dispersion in compressive properties it is safer to have a higher factor of safety for the members encased with such materials.

Further research is required to fully develop and understand the *P-M* interaction diagrams of these specimens. It is interesting to note that although Specimen C-B showed signs of a typical shear failure and was not plotted in Figure 8.11, the experimental bending moment capacity of this specimen was well above the theoretical prediction. In fact, the experimental bending moment of 43.4 kN.m was approximately 43% higher than that obtained by the theoretical approach using the small strips method adopting $0.9f_c$ for the concrete stress.

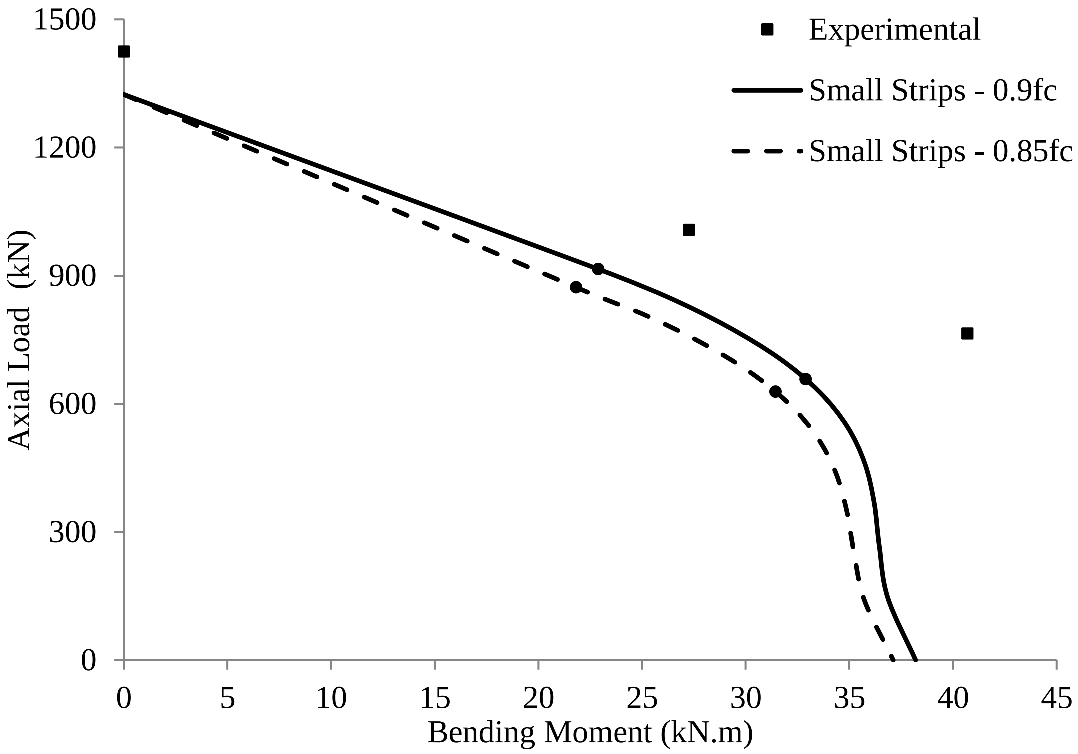

Figure 8.10. Comparison of theoretical *P-M* diagrams and experimental results for Group I specimens (Youssef and Hadi 2017)

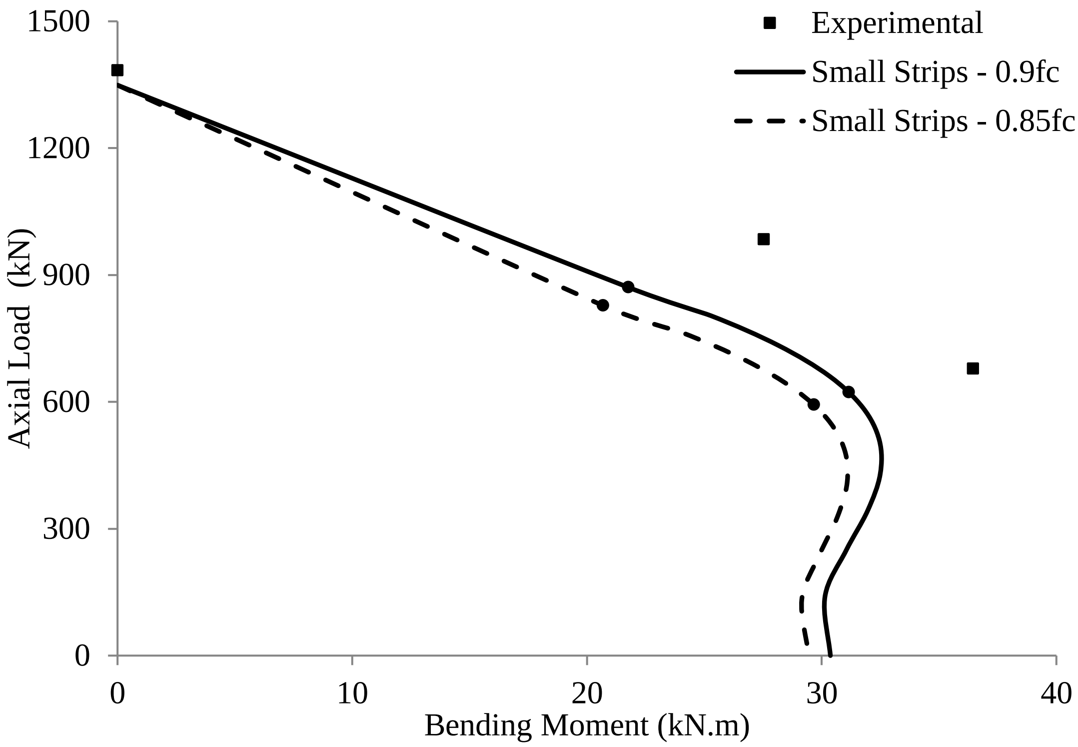

Figure 8.11. Comparison of theoretical *P-M* diagrams and experimental results for Group C specimens (Youssef and Hadi 2017)

8.6.4 Readings of Strain Gauges

As explained in Section 6.3.3 of Chapter 6, strain gauges were bonded on the internal longitudinal reinforcements and imbedded sections. For each concentrically loaded specimen, two strain gauges were bonded to the longitudinal reinforcement and imbedded sections at mid-height. Similarly, for the eccentrically loaded specimens, two strain gauges were bonded on to the longitudinal bars, with one strain gauge on the compression side and one on the tension side. For the imbedded GFRP I-sections, the strain gauges were bonded in the middle of the two outside flanges at the mid-height. Only one GFRP C-section per specimen was instrumented with strain gauges which were located on the two flanges at mid-height.

The strains in tension and compression in the GFRP bars and GFRP sections for all the points along the interaction diagram were checked in terms of the ultimate strains even when the compressive contribution of the GFRP bars were neglected. No failure in these bars or flanges of the sections occurred when the strain in concrete reached its ultimate value of 0.003. The compressive ultimate strain of the GFRP bars was calculated by assuming the compressive modulus of elasticity was equal to the tension modulus of elasticity and the compressive strength was equal to 50% of the tensile strength as reported by Deitz et al. (2003).

It should be noted that as mentioned in the material testing of the GFRP sections in Section 5.2.1 of Chapter 5, potential premature failure may have occurred for these sections when tested in compression due to local end crushing, local end brooming, or geometric instabilities. This premature failure will result in a lower rupture strain and compressive strength obtained but will not affect the compressive modulus of elasticity, which is determined as the initial slope of the stress and strain curves. In drawing the *P-M* interaction diagram, the theoretical strain in compression was checked against the rupture strain obtained from the compression testing and it was found that at the first peak load no failure of the flanges of the sections occurred. Further investigation into the compressive properties of these materials is required before they can be properly used in design and construction.

As an extension, the strain data obtained from the steel and GFRP reinforcement in compression and tension were used to determine the experimental neutral axis for the specimens loaded in 25 and 50 mm eccentricity, which led to calculating the load and bending moment capacities. This was done by assuming a linear strain distribution and by calculating the concrete response using the small strips method. Furthermore, only Specimens RS and RF were investigated since the assumption of neglecting the contribution of the webs of the GFRP encased specimens would not provide a good comparison with the experimental values. The details of the strain gauge readings for all groups of specimens are discussed in Chapter 7.

Table 8.4 shows the comparison of the capacities by three methods; obtained experimentally, by the small strips method utilising a maximum concrete stress of $0.85f_c$ and assuming concrete has reached ultimate strain of 0.003 as explained above and by using the strain gauge data. Unfortunately, the strain readings of the GFRP bar in compression for Specimen RF-25 were lost and therefore it was assumed to be equal to the value obtained for Specimen RS-25 of 0.374%.

It can be seen that good correlation in the capacities obtained by the three methods was obtained for Specimens RS-50 and RF-50 when assuming the compressive modulus of elasticity is equal to zero. However, when assuming the compressive and tensile moduli are equal for Specimen RF-50, the moment capacity obtained by the strain gauge data is 4% higher than that obtained experimentally.

On the other hand, there was not a good correlation in the capacities for Specimens RS-25 and RF-25, with the moment capacities calculated using the strain gauge data much higher than those obtained experimentally, while the load capacities also varied considerably, as shown in Table 8.4. This was also the case for Specimens I-25 and C-25. This would question the accuracy of the strain gauge data for the tensile reinforcement in the 25 mm eccentrically loaded specimens which may be prone to sensitivity issues with the bars subjected to small values of compressive and tensile strains close to the maximum load.

Furthermore, as mentioned above only one strain gauge was placed on the tension and compression longitudinal bars and sections and no average could be obtained for each value. Also un-warranted premature stressing of the bars from the pouring of concrete and curing could cause some issues. It should be noted similar conclusions were drawn when the rectangular stress block method was utilized in conjunction with the strain gauge data to obtain the capacities when compared with the theoretical values obtained by the same method along with the experimental values.

Table 8.4. Comparison of load and bending moment capacities for eccentrically loaded specimens reinforced with bars (Youssef and Hadi 2017)

Specimen	Experimental		Theory – Small strips method[a]		Theory – Strain gauge data[b]		
	P (kN)	M (kN.m)	P (kN)	M (kN.m)	P (kN)	M (kN.m)	e (mm)
RS-25	995	27.0	980	24.5	887	31.1	35.1
RS-50	747	39.3	705	35.3	717	37.8	52.7
RF-25 ($E_{fc} = E_{ft}$)	803	21.9	884	22.1	713	31.9	44.7
RF-50 ($E_{fc} = E_{ft}$)	615	32.3	625	31.3	624	33.6	53.9
RF-25 ($E_{fc} = 0$)	803	21.9	831	20.8	656	27.9	42.6
RF-50 ($E_{fc} = 0$)	615	32.3	586	29.3	570	30.0	52.6

[a] Calculated by assuming concrete has reached ultimate compressive strain of 0.003 (refer to Section 4.3)

[b] Calculated from the experimental strain gauge data and calculating the concrete response using the small strips method

8.7 Parametric Study

The analytical model was used to study the effects of two main parameters on the structural performance of GFRP reinforced square concrete columns in terms of the interaction diagrams. The parameters studied are: (a) concrete compressive strength (f_c), and (b) longitudinal GFRP reinforcement ratio. Only the small strips method utilising a maximum stress of $0.85f_c$ was implemented to draw the *P*-*M* interaction diagrams in this parametric study and the compressive contribution of the GFRP bars was neglected.

The cross-section dimensions and the material properties of the columns studied were the same as that used in the experimental testing. The columns were square in cross-section with a side width of 210 mm. In addition, while the effect of each parameter was investigated, all other parameters were kept constant. Therefore, default values of each parameter were set when that parameter was not being used in the study. The following default values were set for each parameter: the compressive strength of concrete at the first day of testing (f_c) was 31 MPa; the longitudinal GFRP reinforcement ratio was 1.15%; and the ratio of the compressive modulus of elasticity to the tensile modulus of elasticity was 0 ($E_{fc} = 0$). Essentially these values were the same as those of the experimentally tested specimens.

8.7.1 Influence of Concrete Strength, f_c

Depending on the quality control that is implemented, variations in concrete strengths most likely occur. Therefore, it is important to study the effects of varying the concrete compressive strength on the structural behaviour of GFRP RC columns. A total of four concrete cylinder strengths were studied as follows: 31 MPa, 40 Mpa, 50 MPa and 60 MPa. The *P*-*M* strength interaction diagram for all the different cases is shown in Figure 8.12. It should be noted that the formula for the modulus of elasticity of concrete also varies for strengths over 40 MPa.

As expected, as the concrete strength increases, so does the load and bending moment capacities. The strains in the tension and compression bars for all the points along the interaction diagram were checked in terms of the ultimate strains for each case and no failure in these bars occurred for all concrete strengths when the strain in concrete reached its ultimate value. In fact, as the concrete strength increased, the strains in the tensile bars at the ultimate bending condition (*P* = 0 kN) increased, but remained below the ultimate value. It was seen that a tensile strain of 1.4% was obtained at the ultimate bending condition when the concrete strength at the first day of testing was 60 MPa which is lower than the ultimate value of 2.41%.

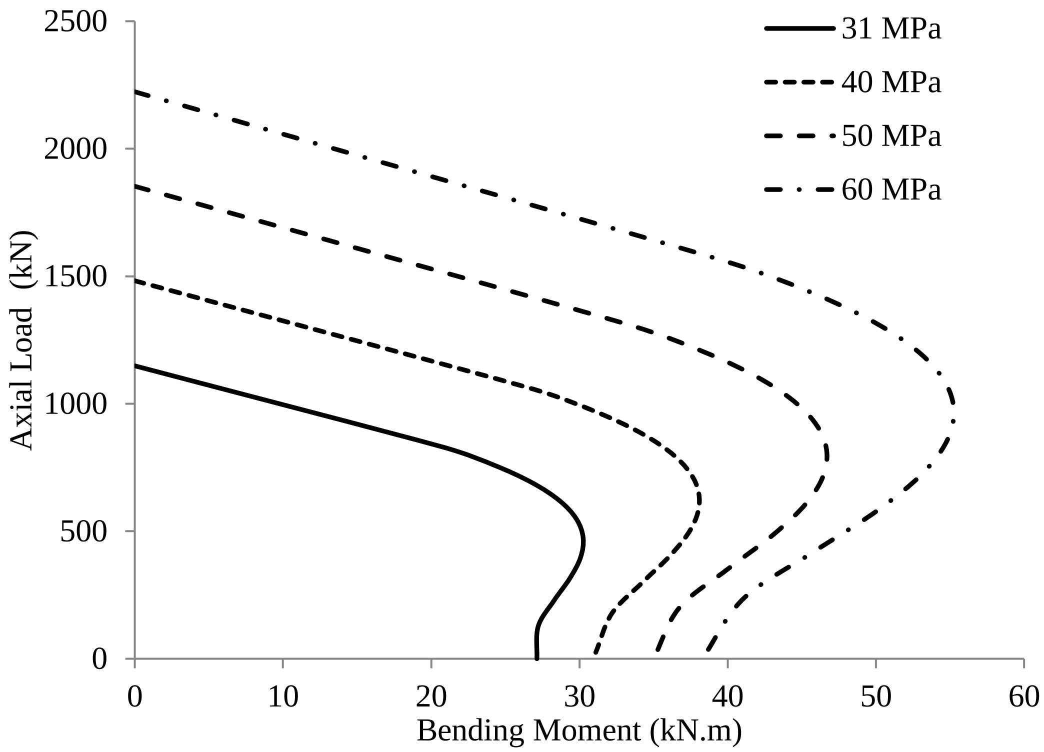

Figure 8.12. Influence of concrete strength on *P-M* interaction diagrams for Specimens of Group RF (Youssef and Hadi 2017)

8.7.2 Influence of Longitudinal GFRP Reinforcement Ratio

A total of four longitudinal GFRP reinforcement ratios were studied as follows: 1.15%, 3%, 5% and 7%. The *P-M* strength interaction diagram for the different reinforcement ratios when neglecting the compressive contribution of the GFRP bars ($E_{fc} = 0$) is shown in Figure 8.13(a). It can be seen that as the reinforcement ratio increases, the axial load capacities for pure compression decreases slightly because the modulus of elasticity in compression is reduced to zero and the second part of

Equation 8.16 becomes also zero. Furthermore, as the reinforcement ratios increases, the bending moment capacity at lower levels of load capacity increases.

It is interesting to see the behaviour of the P-M interaction diagram when taking into account the compressive contribution of the GFRP bars ($E_{fc} = E_{ft}$) as shown in Figure 8.13(b). Most notably, to calculate the axial capacity for pure compression the second part of Equation 8.16 is taken into account unlike that when $E_{fc} = 0$. As a result, for this case as the reinforcement ratio increases so does the axial capacity for pure compression.

On the other hand similar to Figure 8.13(a), as the reinforcement ratio increases the bending moment capacity at lower levels of load capacity increases. Therefore, as reported by Choo et al. (2006a) the *P*-*M* interaction diagrams of GFRP reinforced columns do not experience any balanced points, unlike that of steel reinforced columns.

Furthermore, for all the cases no failure occurred for the GFRP bars in tension or compression when the concrete reached the ultimate strain. In fact, as the reinforcement ratio increased, the strains in the tensile bars at the ultimate bending condition (P = 0 kN) decreased.

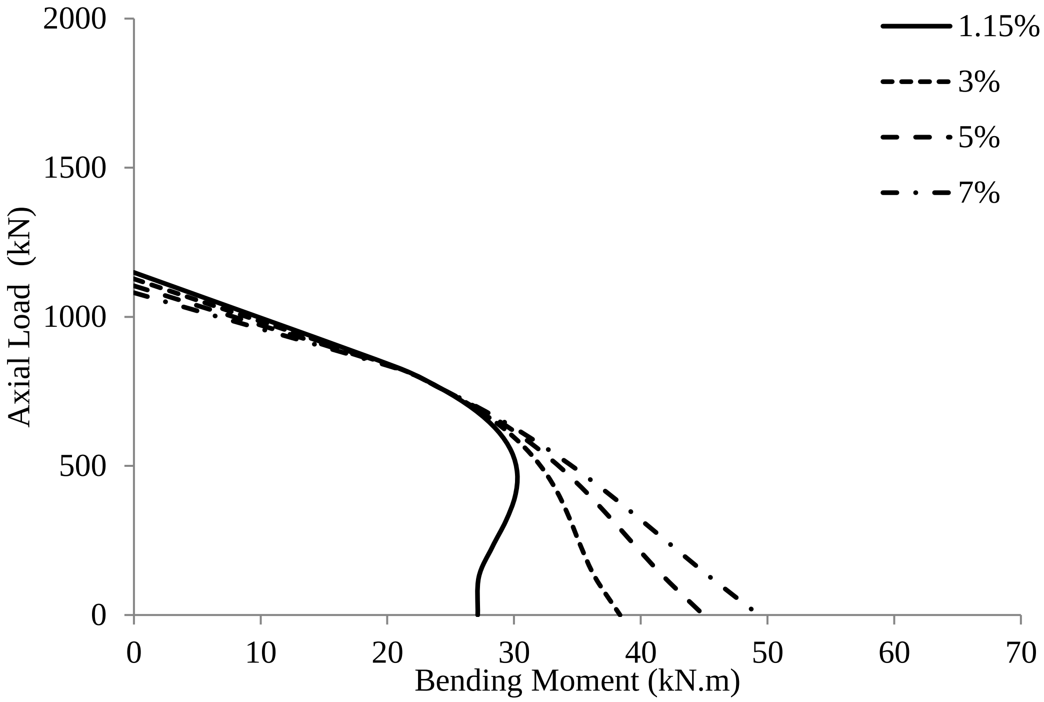

(a)

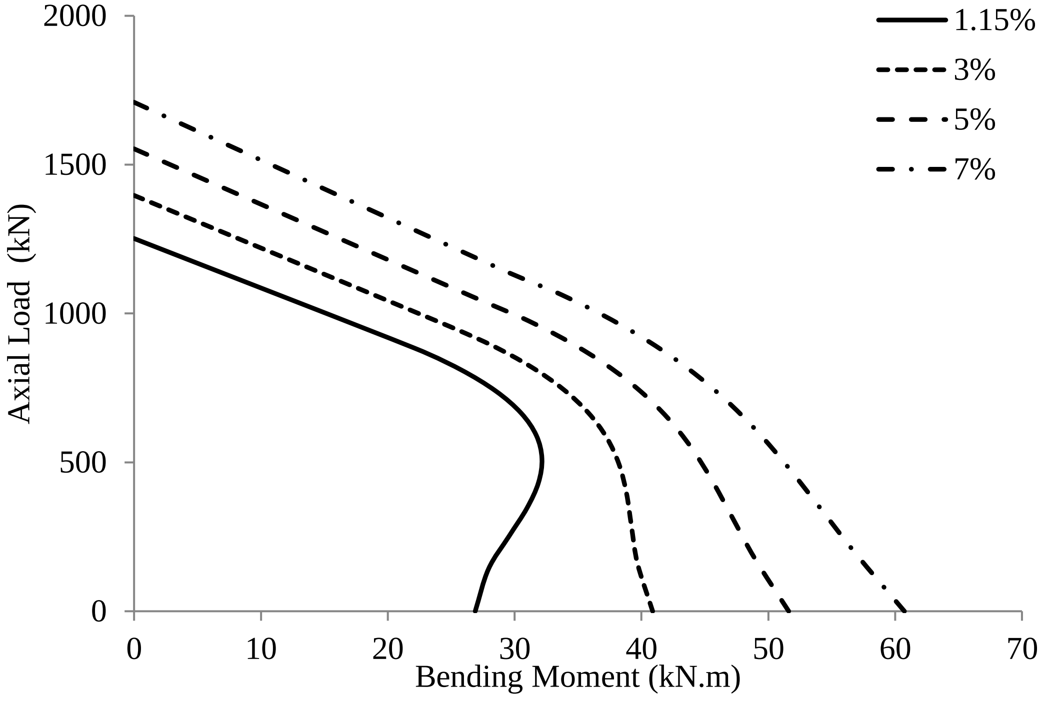

(b)

Figure 8.13. Influence of longitudinal GFRP reinforcement ratio on *P-M* interaction diagrams: (a) Compressive contribution of GFRP bars ignored (E_{fc} = 0); and (b) Compressive contribution of GFRP bars included ($E_{fc} = E_{ft}$) [Youssef and Hadi 2017]

8.8 Summary

This chapter described two analytical methods to determine the axial load and bending moment interaction diagrams of the experimentally tested specimens with a comparison of the analytical and experimental results discussed. In general, based on the experimental results and the analytical analysis of this study it can be concluded that concrete columns reinforced with GFRP bars and encased with pultruded GFRP sections can be potentially analysed using the same procedure used for conventional steel RC columns. It was found that ignoring the compressive contribution of the GFRP bars and using the small strips method for GFRP reinforced specimens is the most accurate and safe alternative for the design of such specimens, considering that the compressive properties of FRP bars has not been extensively understood. Based on the parametric study of GFRP reinforced specimens, the load and bending moment capacities increase with the increase in concrete strength and the interaction diagrams of GFRP reinforced columns do not experience balanced points unlike that of steel reinforced columns.

The next chapter summarises the conclusions that can be drawn based on the experimental and analytical studies carried out in this study. In addition, recommendations are proposed for further studies relating to GFRP-reinforced and GFRP-encased concrete column specimens.

9 CONCLUSIONS AND RECCOMENDATIONS

9.1 Introduction

The main objective of this study was to investigate the axial and flexural behaviour of square concrete members reinforced with glass fibre-reinforced polymer (GFRP) bars and embedded with pultruded GFRP structural sections under different loading conditions. The main parameters investigated were the influence of the type of internal reinforcement (steel bars, GFRP bars and pultruded GFRP structural I-sections and C-sections) and magnitude of load eccentricity on the flexural and compressive behaviour of square concrete members. To fulfil the objectives of this study, seventeen RC specimens were tested, of which twelve were tested as columns under compressive loading and five were tested as beams under flexural loading. The concrete specimens were square in cross section with a side dimension of 210 mm and a height of 800 mm.

Based on the experimental results, the strength, failure modes, failure locations and ductility of each group of specimens under different types of loading were analysed. Furthermore, an analytical model was presented to predict the axial load-bending moment interaction diagrams of the experimentally tested specimens which followed similar assumptions as those used for conventional steel reinforced members. Also, a parametric study was conducted to study the effects of concrete compressive strength and longitudinal GFRP reinforcement ratio on the structural performance of GFRP reinforced square concrete columns.

Another study was carried out to further understand the compression behaviour of pultruded GFRP channels used in the GFRP encased concrete columns. First, the mechanical compressive properties of the GFRP channels were obtained by two methods. The first method involved testing coupons extracted from the channels, while in the second method full-size specimens having free lengths of 100 mm and 200 mm were subjected to axial compression. The behaviour and failure modes of the coupons and full-size specimens were investigated. Furthermore, a numerical model was developed using the finite element analysis program ABAQUS to simulate the compressive behaviour of the full-size specimens. A failure criterion was investigated to determine the location of failure initiation.

This chapter presents the conclusions of these studies and recommendation for future research related to these studies.

9.2 Conclusions

Based on the experimental and analytical investigation carried out on the study of GFRP reinforced and GFRP encased concrete members subjected to different loading conditions as discussed in Chapters 6, 7 and 8, the following conclusions can be drawn:

1. The column specimens reinforced with steel bars achieved a higher load carrying capacity as compared to the column specimens reinforced with GFRP bars for all loading conditions. The load-carrying capacity of the column specimen reinforced with GFRP bars loaded concentrically (RF-0) was 4.8% lower than its steel counterpart (RS-0). On the other hand, the load-carrying capacity of the column specimens reinforced with GFRP bars and loaded eccentrically (RF-25 and RF-50) were on average 18.5% lower than their steel counterparts (RS-25 and RS-50). Therefore, a higher drop in load-carrying capacity was experienced for the eccentrically loaded GFRP-reinforced column specimens with respect to the equivalent steel-reinforced column specimens.

2. For concentrically loaded columns, the steel-reinforced column specimen achieved a better ductile performance compared to the GFRP-reinforced column specimen. For eccentric loading conditions, GFRP-reinforced column specimens achieved similar ductility as compared to the steel-reinforced specimens, based on the ductility definition in this study. However, the eventual failure mechanism of the GFRP-reinforced column specimens was brittle and sudden in nature, whereas the steel-reinforced column specimens did not fail abruptly but continued to displace until the termination of the test.

3. The GFRP-reinforced column specimens subjected to eccentric loading were able to sustain an increase in load after the sudden concrete spalling and eventually a second peak load was achieved. This was not the case with the steel reinforced column specimens subjected to eccentric loading.

4. For the concentrically loaded specimens, the longitudinal steel bars contributed to approximately 21.7% of the ultimate column capacity (RS-0) and the GFRP longitudinal bars contributed to approximately 9.5% of the ultimate column capacity (RF-0) by taking into account an assumption that the GFRP bars modulus of elasticity in compression is equal to the modulus of elasticity in tension as reported by Deitz et al. (2003).

5. The GFRP-encased column specimens achieved a higher load carrying capacity but lower ductility as compared to both the steel-reinforced and GFRP-reinforced specimens for all loading conditions. The C-section encased column specimens experienced better ductility as compared to that of the I-section encased column specimens, which is attributed to the confinement effect of the C-sections box arrangement. However, the I-section encased column specimens achieved a slightly higher load-carrying capacity as compared to the C-section encased column specimens.

6. Based on the results of the beam specimens the use of encased GFRP structural sections can provide a significant improvement in the load-carrying capacity when comparing conventional beams reinforced with steel and GFRP bars. There is potential in encasing structural GFRP sections in concrete beams, although further research elaboration is necessary to investigate this considering some of the errors and premature failure mechanisms experienced in the experimental program of the beam specimens.

7. Based on the analytical analysis of this study it can be concluded that concrete columns reinforced with GFRP bars and encased with pultruded GFRP sections can be potentially analysed using the same procedure used for conventional steel RC columns.

8. The small strips method adopted in this study for predicting the *P-M* interaction relationship provided more accurate results as compared to the rectangular stress block method for the GFRP-reinforced specimens. In terms of the GFRP encased specimens, the small strips method provided satisfactory and conservative estimates of the maximum load and bending moment capacities.

9. Considering that the compressive properties of FRP bars has not been extensively understood, especially when embedded in concrete, it is safer to say that ignoring the compressive contribution of the GFRP bars and drawing the theoretical *P-M* diagram based on the small strips method is the most accurate and safe alternative for the design of such columns at this stage.

10. The most accurate estimate of the maximum axial capacity for the GFRP reinforced specimen under concentric loading was achieved when taking into account the compressive contribution of the GFRP bars based on the elastic theory and assuming the strain in the bars is equal to the concretes ultimate compressive strain.

11. Based on the parametric study, the load and bending moment capacities increase with the increase in concrete strength. Furthermore, the interaction diagrams of GFRP reinforced columns do not experience balanced points unlike that of steel reinforced columns.

12. This study is believed to give an understanding on the behaviour of GFRP reinforced and GFRP encased concrete columns subjected to various loading conditions.

Based on the experimental and numerical investigation carried out on the study of the compression behaviour of pultruded GFRP channels as discussed in Chapter 5, the following conclusions can be drawn:

1. The coupons tested by direct end loading experienced high variations in the compressive properties and the compressive strength could not be obtained

accurately due to premature failures associated with end crushing and geometric instabilities. Therefore, the ends of the coupons were confined to avoid stress concentrations and to prevent end crushing. Confining the ends of the coupons resulted in less variation in the compressive strengths and an acceptable failure mode.

2. The compressive properties of pultruded sections may be influenced by the bad workmanship in producing these materials such as non-uniform placement of the fibres or inaccurate curing and heating conditions. All these issues including the intrinsic nature of the test set-up prove that it is very difficult to obtain the compressive properties of pultruded materials.

3. The transverse compressive strength and modulus of elasticity were substantially lower than that of the longitudinal compressive strength and modulus of elasticity.

4. The Hashin failure criterion was used to predict the failure stresses and strains in the numerical model, which provided conservative estimates of the failure stresses and strains as compared to the values obtained experimentally. It was found that using the strain value at failure obtained experimentally to calculate the numerical failure stress resulted in closer predictions.

5. Using the failure index visualisation of the Hashin criterion showed that the location of failure initiation was similar for both Group 100 and Group 200 specimens. This predicted failure location was similar to the experimental failure location of Group 100 specimens. However, this predicted location did not quite correlate with the failure location determined experimentally for Group 200 specimens. In general, the results showed that the numerical analysis reasonably simulated the actual compressive behaviour of the pultruded GFRP channels with conservative estimates of the ultimate values obtained.

9.3 Recommendations for future studies

Based on the experimental results, analytical and numerical investigation carried out in this study, the following recommendations for future studies are suggested:

1. The experimental results of the GFRP reinforced and GFRP encased beam specimens could not be compared to the theoretical models. Furthermore, these beam specimens failed by shear rather than by the preferred flexural mode. Therefore, further research elaboration is necessary to investigate the behaviour of these types of beams along with the development of accurate *P-M* diagrams for GFRP encased specimens that take into account the contribution of the whole GFRP section. Most notably, for the GFRP reinforced beams, the data point of the theoretical *P-M* interaction diagram proposed in this study for the pure bending condition will need to be compared with the value obtained from the guidelines for the flexural design of flexural members in ACI 440.1R–15 (ACI 2015).

2. The experimental results of the GFRP reinforced beam specimen could not be compared to the theoretical models. Further research elaboration is necessary to investigate the beams by taking into account ACI 440.1R–15 (ACI 2015) provides guidelines for the flexural design of FRP reinforced beams designed to be controlled by either concrete crushing or FRP rupture. The data point of the theoretical *P-M* interaction diagram proposed in this study for the pure bending condition will need to be compared with the value obtained from the guidelines for the flexural design of flexural members in ACI 440.1R–15 (ACI 2015).

3. Further experimental verification of the theoretical *P-M* diagrams is required for the GFRP reinforced and GFRP encased specimens considering the following: the limited number of specimens in this study; the value of the maximum stress on the stress-strain diagram for concrete varies between $0.85f_c$ to $0.90f_c$; and the compressive strength of each specimen varies according to the day of testing.

4. Similar studies on GFRP RC columns with different concrete strengths, reinforcement ratios and different cross-sections tested under varying loading

conditions can be investigated further in order to develop general design guidelines for such columns.

5. Similar studies on GFRP encased concrete columns with different concrete strengths, cross-sections (rectangular and circular) and shapes of embedded structural sections can be investigated further in order to fully understand the behaviour of such members. Furthermore, testing GFRP encased concrete columns reinforced with transverse GFRP stirrups instead of steel stirrups is also recommended.

6. The slenderness effect of GFRP reinforced and GFRP encased concrete columns is recommended to be studied in the future.

7. In terms of the GFRP pultruded channel sections, a high dispersion in the compressive properties of these types of materials will require better testing procedures to prevent premature failures, better quality control at the manufacturing level, and further investigation into the compressive properties of these materials before they can be properly used in design and construction.

REFERENCES

ABAQUS (2013). "ABAQUS 6.12-1 Documentation." Dassault, Systemes. Dassault Systémes: Providence, RI

ACI. (2008). "Guide for the design and construction of externally bonded FRP systems for strengthening concrete structures."American Concrete Institute, *ACI 440.2R-08,* Farmingtion Hills, PA.

ACI. (2011). "Building Code Requirements for Structural Concrete."American Concrete Institute, *ACI 318-11,* Farmington Hills, MI, USA.

ACI. (2012). "Guide Test Methods for Fiber-Reinforced Polymers (FRPs) for Reinforcing or Strengthening Concrete Structures." American Concrete Institute, *ACI 440.3R-12,* Farmington Hills, MI, USA.

ACI. (2014). "Building code requirements for structural concrete."American Concrete Institute, *ACI 318-14,* Farmington Hills, MI, USA.

ACI. (2015). "Guide for the Design and Construction of Structural Concrete Reinforced with Fiber-Reinforced Polymer (FRP) Bars."American Concrete Institute, *ACI 440.1R-15,* Farmington Hills, MI, USA.

Adam, M. A., Said, M., Mahmoud, A. A., and Shanour, A. S. (2015). "Analytical and experimental flexural behavior of concrete beams reinforced with glass fiber reinforced polymers bars." *Construction and Building Materials*, 84, 354-366.

Adams, D. F., and Welsh, J. S. (1997). "The Wyoming combined loading compression (CLC) test method." *Journal of Composites, Technology and Research*, 19(3), 123-133.

Afifi, M. Z., Mohamed, H. M., and Benmokrane, B. (2014). "Axial capacity of circular concrete columns reinforced with GFRP bars and spirals." *Journal of Composites for Construction*, 18(1), 04013017.

Alsayed, S., Al-Salloum, Y., Almusallam, T., and Amjad, M. (1999). "Concrete columns reinforced by glass fiber reinforced polymer rods." *Special Publication*, 188, 103-112.

Aravinthan, T., and Manalo, A. (2012). "Field applications and case studies of FRP in civil infrastructure: the Australian experience." *Proceedings of the 6th International Conference on FRP Composites in Civil Engineering (CICE 2012),* 13-15 Jun 2012, Rome, Italy.

AS. (1976). "Methods for the Calibration and Grading of Extensometers."Standards Australia, *AS 1545-1976*, Homebush, NSW, Australia.

AS. (2000-R2014). "Methods of testing concrete - Determination of indirect tensile strength of concrete cylinders ('Brasil' or splitting test)."Standards Australia, *AS 1012.10-2000 (R2014)* Reconfirmed in 2014, Sydney, Australia.

AS. (2000-R2014). "Methods of testing concrete - Determination of the modulus of rupture."Standards Australia, *AS 1012.11-2000(R2014)*, Reconfirmed in 2014, Sydney, Australia.

AS. (2007). "Metallic materials – Tensile testing at ambient temperatures."Standards Australia, *AS 1391-2007*, Sydney, Australia.

AS. (2009). "Concrete Structures."Standards Australia, *AS3600-2009*, Sydney, Australia.

AS. (2014a). "Methods of testing concrete - Method for making and curing concrete - Compression and indirect tensile test specimens."Standards Australia, *AS 1012.8.1-2014*, Sydney, Australia.

AS. (2014b). "Methods of testing concrete - Method for making and curing concrete - Flexure test specimens."Standards Australia, *AS 1012.8.2-2014*, Sydney Australia.

AS. (2014c). "Methods of testing concrete - Compressive strength tests - Concrete, mortar and grout specimens."Standards Australia, *AS 1012.9-2014*, Sydney, Australia.

ASCE. (2010). "Pre-Standard for Load & Resistance Factor Design (LRFD) of Pultruded Fibre Reinforced Polymer (FRP) Structures (Final)."American Society of Civil Engineers (ASCE), Submitted to American Composites Manufacturers Association (ACMA), *ASCE 2010*, Virginia, USA.

Ascione, L., Razaqpur, A. G., and Spadea, S. (2014). "Effectiveness of FRP stirrups in concrete beams subject to shear." *Proceedings of the 7th International Conference on FRP Composites in Civil Engineering*, 20 - 22 August, 2014, Vancouver, Canada.

ASTM. (2008). "Standard test method for tensile properties of polymer matrix composite materials."American Society for Testing and Materials, *ASTM D3039*, West Conshohocken, PA.

ASTM. (2010). "Standard test method for tensile properties of fiber reinforced polymer matrix composites used for strengthening of civil structures."American Society for Testing and Materials, *ASTM D7565-10,* West Conshohocken, PA.

ASTM. (2011). "Standard test method for tensile properties of fiber reinforced polymer matrix composite bars,."American Society for Testing and Materials, *ASTM D7205-11,* West Conshohocken, PA, USA.

ASTM. (2014a). "Standard practise for verification of testing frame and specimen alignment under tensile and compressive axial force application."American Society for Testing and Materials, *ASTM E1012,* West Conshohocken, PA.

ASTM. (2014b). "Standard Test Method for Tensile Properties of Plastics."American Society for Testing and Materials, *ASTM D638-14,* West Conshohocken, PA, USA.

ASTM. (2015). "Standard test method for compressive properties of rigid plastics, American Society for Testing and Materials."American Society for Testing and Materials, *ASTM D695-15,* West Conshohocken, PA, USA.

ASTM. (2016a). "Standard Test Method for Compressive Properties of Polymer Matrix Composite Materials with Unsupported Gage Section by Shear Loading."American Society for Testing and Materials, *ASTM D3410 - 16,* West Conshohocken, PA, USA.

ASTM. (2016b). "Standard Test Method for Compressive Properties of Polymer Matrix Composite Materials Using a Combined Loading Compression (CLC) Test Fixture."American Society for Testing and Materials *ASTM D6641-16e1,* West Conshohocken, PA, USA.

Bank, L. C. (2006). *Composites for construction: structural design with FRP materials*, John Wiley & Sons.

Bank, L. C., Oliva, M. G., Han-Ug, B., Barker, J. W., and Seung-Woon, Y. (2007). "Pultruded FRP plank as formwork and reinforcement for concrete members." *Advances in Structural Engineering*, 10(5), 525-535.

Barbero, E., Cosso, F., Roman, R., and Weadon, T. (2013). "Determination of material parameters for Abaqus progressive damage analysis of E-glass epoxy laminates." *Composites Part B: Engineering*, 46, 211-220.

Barbero, E., and Tomblin, J. (1994). "A phenomenological design equation for FRP columns with interaction between local and global buckling." *Thin-Walled Structures*, 18(2), 117-131.

Barbero, E. J. (2000). "Prediction of buckling-mode interaction in composite columns." *Mechanics of composite materials and structures*, 7(3), 269-284.

Barbero, E. J., Makkapati, S., and Tomblin, J. S. (1999). "Experimental determination of the compressive strength of pultruded structural shapes." *Composites Science and Technology*, 59, 2047-2054.

Benmokrane, B., Chaallal, O., and Masmoudi, R. (1996). "Flexural response of concrete beams reinforced with FRP reinforcing bars." *ACI structural journal*, 93(1), 46-55.

Bestech. (2014). "TML Pam E-101S - TML Precise & Flexible Strain Gauges." http://www.bestech.com.au/.

Boyle, H. C., and Karbhari, V. M. (1994). "Investigation of bond behavior between glass fiber composite reinforcements and concrete." *Polymer-Plastics Technology and Engineering*, 33(6), 733-753.

Cardoso, D., Harries, K., and Batista, E. (2014a). "Compressive Local Buckling of Pultruded GFRP I-Sections: Development and Numerical/Experimental Evaluation of an Explicit Equation." *Journal of Composites for Construction*, 0(0), 04014042.

Cardoso, D. C. T., Harries, K. A., and Batista, E. d. M. (2014b). "Compressive strength equation for GFRP square tube columns." *Composites Part B: Engineering*, 59(0), 1-11.

Carlsson, L., Adams, D. F., and Pipes, R. B. (2002). *Experimental Characterization of Advanced Composite Materials*, CRC Press, Boca Raton, Florida, USA.

Chaallal, O., and Benmokrane, B. (1993). "Physical and mechanical performance of an innovative glass-fiber-reinforced plastic rod for concrete and grouted anchorages." *Canadian Journal of Civil Engineering*, 20(2), 254-268.

Chaallal, O., Shahawy, M., and Hassan, M. (2003). "Performance of axially loaded short rectangular columns strengthened with carbon fiber-reinforced polymer wrapping." *Journal of Composites for Construction*, 7(3), 200-208.

Chen, J., Li, S., and Bisby, L. (2013). "Factors affecting the ultimate condition of FRP-wrapped concrete columns." *Journal of Composites for Construction*, 17(1), 67-78.

Chen, J. F., Ai, J., and Stratford, T. (2010). "Effect of geometric discontinuities on strains in FRP-wrapped columns." *Journal of Composites for Construction*, 14(2), 136-145.

Cheng, L., and Karbhari, V. M. (2006). "New bridge systems using FRP composites and concrete: a state-of-the-art review." *Progress in Structural Engineering and Materials*, 8(4), 143-154.

Choo, C. C., Harik, I. E., and Gesund, H. (2006a). "Strength of rectangular concrete columns reinforced with fiber-reinforced polymer bars." *ACI structural journal*, 103(3), 452.

Choo, C. C., Harik, I. E., and Gesund, H. (2006b). "Minimum reinforcement ratio for fiber-reinforced polymer reinforced concrete rectangular columns." *ACI structural journal*, 103(3), 460.

Clarke, J., L. (1996). *Structural design of polymer composites: EUROCOMP design code and handbook,* CRC Press, London, England.

CNR-DT203. (2006). "Guide for the Design and Construction of Concrete Structures Reinforced With Fiber-Reinforced Polymer Bars."National Research Council, *CNR-DT 203/206*, Rome Italy.

CNR-DT205. (2007). "Guide for the Design and Construction of Structures made of FRP Pultruded Elements ",National Research Council of Italy, *CNR-DT 205 (2007)*, Rome, Italy.

Colomb, F., Tobbi, H., Ferrier, E., and Hamelin, P. (2008). "Seismic retrofit of reinforced concrete short columns by CFRP materials." *Composite Structures*, 82(4), 475-487.

Correia, J. R., Branco, F. A., and Ferreira, J. (2009). "GFRP–concrete hybrid cross-sections for floors of buildings." *Engineering Structures*, 31(6), 1331-1343.

Correia, J. R., Branco, F. A., and Ferreira, J. G. (2007). "Flexural behaviour of GFRP–concrete hybrid beams with interconnection slip." *Composite Structures*, 77(1), 66-78.

Correia, J. R., Branco, F. A., Ferreira, J. G., Bai, Y., and Keller, T. (2010). "Fire protection systems for building floors made of pultruded GFRP profiles: Part

1: Experimental investigations." *Composites Part B: Engineering*, 41(8), 617-629.

Correia, J. R., Branco, F. A., Silva, N. M. F., Camotim, D., and Silvestre, N. (2011). "First-order, buckling and post-buckling behaviour of GFRP pultruded beams. Part 1: Experimental study." *Computers & Structures*, 89(21–22), 2052-2064.

Correia, M., Nunes, F., Correia, J., and Silvestre, N. (2013). "Buckling Behavior and Failure of Hybrid Fiber-Reinforced Polymer Pultruded Short Columns." *Journal of Composites for Construction*, 17(4), 463-475.

Correia, M., Nunes, F., Correia, J., and Silvestre, N. (2013). "Buckling behavior and failure of hybrid fiber-reinforced polymer pultruded short columns." *J. Compos. Constr.*, 463.

Creative-Pultrusions (2017). "The Pultex® Pultrusion Design Manual of Standard and Custom Fiber Reinforced Polymer Structural Profiles - Volume 5: Revision 4." *Creative Pultrusions, Inc.*, Alum Bank, PA, USA, www.creativepultrusions.com.

CSA. (2006-R2012). "Canadian Highway Bridge Design Code."Canadian Standards Association, *CSA-S6: 06(R2012),* Reaffirmed in 2012.

CSA. (2012-R2017). "Design and Construction of Building Structures with Fiber-Reinforced Polymers."Canadian Standards Association*, CSA S806-12(R2017),* Reaffirmed in 2017, Toronto, Canada.

De Luca, A., Matta, F., and Nanni, A. (2010). "Behavior of Full-Scale Glass Fiber-Reinforced Polymer Reinforced Concrete Columns under Axial Load." *ACI structural journal*, 107(5), 589-596.

De Luca, A., and Nanni, A. (2010). "Single-parameter methodology for the prediction of the stress-strain behavior of FRP-confined RC square columns." *Journal of Composites for Construction*, 15(3), 384-392.

Deitz, D. H., Harik, I. E., and Gesund, H. (2003). "Physical properties of glass fiber reinforced polymer rebars in compression." *Journal of Composites for Construction*, 7(4), 363-366.

Deskovic, N., Triantafillou, T. C., and Meier, U. (1995). "Innovative design of FRP combined with concrete: short-term behavior." *Journal of Structural Engineering*, 121(7), 1069-1078.

Dieter, D., Dietsche, J., Bank, L., Oliva, M., and Russell, J. (2002). "Concrete bridge decks constructed with fiber-reinforced polymer stay-in-place forms and grid reinforcing." *Transportation Research Record: Journal of the Transportation Research Board*(1814), 219-226.

Dong, Q., and Gu, X. (2012). "Laboratory test and numerical simulation of bond performance between basalt fiber reinforced polymer rebar and concrete." *Journal of Testing and Evaluation*, 40(7), 1-8.

Ehsani, M. (1993). "Glass-fiber reinforcing bars." *Alternative Materials for the Reinforcement and Prestressing of Concrete*, JL Clarke, Blackie Academic & Professional, London, England, 35-54.

Ehsani, M., Saadatmanesh, H., and Tao, S. (1995). "Bond of hooked glass fiber reinforced plastic (GFRP) reinforcing bars to concrete." *ACI materials journal*, 92(4), 391-400.

El-Hacha, R., and Chen, D. (2012). "Behaviour of hybrid FRP–UHPC beams subjected to static flexural loading." *Composites Part B: Engineering*, 43(2), 582-593.

El-Nemr, A., Ahmed, E. A., and Benmokrane, B. (2013). "Flexural behavior and serviceability of normal-and high-strength concrete beams reinforced with glass fiber-reinforced polymer bars." *ACI structural journal*, 110(6), 1077.

Etman, E. E.-S. (2011). "Innovative Hybrid Reinforcement for Flexural Members." *Journal of Composites for Construction*, 15(1), 2-8.

Fam, A., and Rizkalla, S. (2002). "Flexural Behavior of Concrete-Filled Fiber-Reinforced Polymer Circular Tubes." *Journal of Composites for Construction*, 6(2), 123-132.

Faza, S., and GangaRao, H. (1993). "Glass FRP reinforcing bars for concrete." *Fiber reinforced (FRP) reinforcement for concrete structures: properties and applications. In: Developments in civil engineering*, 42, 167-188.

fib. (2001). "Externally bonded FRP reinforcement for RC structures."Féderation Internationale Du Béton, *Bulletin*, Vol. 14, pp. 138.

fib. (2007). "FRP Reinforcment in RC Structures."Féderation Internationale Du Béton, *Bulletin No. 40,* Lausane, Switzerland.

Gand, A. K., Chan, T.-M., and Mottram, J. T. (2013). "Civil and structural engineering applications, recent trends, research and developments on pultruded fiber reinforced polymer closed sections: a review." *Frontiers of Structural and Civil Engineering*, 7(3), 227-244.

Gedney, C., Pascual, C., Kolkailah, F., and Wilson, B. (1987). "Comparison of ASTM standard compression test methods of graphite/epoxy composite specimens." *Advanced materials technology'87*, 1015-1024.

Gosling, P., and Saribiyik, M. (2003). "Nonstandard Tensile Coupon for Fiber-Reinforced Plastics." *Journal of Materials in Civil Engineering*, 15(2), 108-117.

GRP. (2008). "Load test of pultruded sections - Report data."*Glass Reinforced Products*, Lytton, QLD, Australia, [www.grpaustralia.com.au], accessed Aug. 8, 2014.

Gu, X., Dai, Y., and Jiang, J. (2015). "Test and Evaluation for Bonding Property Between GFRP and Concrete." *Journal of Testing and Evaluation*, 44(2), 878-884.

Guades, E., Aravinthan, T., and Islam, M. M. (2014). "Characterisation of the mechanical properties of pultruded fibre-reinforced polymer tube." *Materials & Design*, 63, 305-315.

Häberle, J., and Matthews, F. (1994). "An improved technique for compression testing of unidirectional fibre-reinforced plastics; development and results." *Composites*, 25(5), 358-371.

Hadi, M. N. S. (2006). "Behaviour of FRP wrapped normal strength concrete columns under eccentric loading." *Composite Structures*, 72(4), 503-511.

Hadi, M. N. S., Karim, H., and Sheikh, M. N. (2016). "Experimental investigations on circular concrete columns reinforced with GFRP bars and helices under different loading conditions." *Journal of Composites for Construction*, 20(4), 04016009.

Hadi, M. N. S., Pham, T. M., and Lei, X. (2012). "New Method of Strengthening Reinforced Concrete Square Columns by Circularizing and Wrapping with Fiber-Reinforced Polymer or Steel Straps." *Journal of Composites for Construction*, 17(2), 229-238.

Hadi, M. N. S., Pham, T. M., and Lei, X. (2013). "New method of strengthening reinforced concrete square columns by circularizing and wrapping with fiber-reinforced polymer or steel straps." *Journal of Composites for Construction*, 17(2), 229-238.

Hadi, M. N. S., and Widiarsa, I. (2012). "Axial and Flexural Performance of Square RC Columns Wrapped with CFRP under Eccentric Loading." *Journal of Composites for Construction*, 16(6), 640-649.

Hadi, M. N. S., and Youssef, J. (2016). "Experimental Investigation of GFRP-Reinforced and GFRP-Encased Square Concrete Specimens under Axial and Eccentric Load, and Four-Point Bending Test." *Journal of Composites for Construction*, 20(5), 04016020.

Hashin, Z. (1980). "Failure criteria for unidirectional fiber composites." *Journal of applied mechanics*, 47(2), 329-334.

Hawileh, R. A., Rasheed, H. A., Abdalla, J. A., and Al-Tamimi, A. K. (2014). "Behavior of reinforced concrete beams strengthened with externally bonded hybrid fiber reinforced polymer systems." *Materials & Design*, 53, 972-982.

Hodgkinson, J. M. (2000). *Mechanical testing of advanced fibre composites*, Woodhead Publishing, Cambridge, England.

Honickman, H. N. (2008). "Pultruded GFRP sections as stay-in-place structural open formwork for concrete slabs and girders." Master of Science (Engineering), Queen's University, Kingston, Ontario, Canada.

Idris, Y., and Ozbakkaloglu, T. (2014). "Flexural behavior of FRP-HSC-steel composite beams." *Thin-Walled Structures*, 80, 207-216.

ISIS. (2007). "Design Manual 3: Reinforcing Concrete Structures with Fibre Reinforced Polymers."ISIS Canada Research Network, The Canadian Network of Centres of Excellence on Intelligent Sensing for Innovative Structures, *ISIS 2007*, Winnipeg, Canada.

ISO. (1997). "Determination of tensile properties of plastics. Part 4: Test conditions for isotropic and orthotropic fiber-reinforced plastic composites."European Committee for Standardisation, *ISO 527-4-1997*, Brussels, Belgium.

Issa, M., Metwally, I., and Elzeiny, S. (2012). "Performance of eccentrically loaded GFRP reinforced concrete columns." *World Journal of Engineering*, 9(1), 71-78.

Jones, R. M. (1999). *Mechanics of Composite Materials*, Taylor and Francis, Philadelphia, USA.

JSCE. (1997). "Recommendation for Design and Construction of Concrete Structures Using Continous Fiber Reinforcing Materials."Japan Society of Civil Engineers, *Concrete Engineering Series No. 23*.

Karim, H., Sheikh, M. N., and Hadi, M. N. S. (2016). "Axial load-axial deformation behaviour of circular concrete columns reinforced with GFRP bars and helices." *Construction and Building Materials*, 112, 1147-1157.

Karimi, K., El-Dakhakhni, W., and Tait, M. (2011b). "Performance Enhancement of Steel Columns Using Concrete-Filled Composite Jackets." *Journal of Performance of Constructed Facilities*, 25(3), 189-201.

Karimi, K., El-Dakhakhni, W., and Tait, M. (2012a). "Behavior of Slender Steel-Concrete Composite Columns Wrapped with FRP Jackets." *Journal of Performance of Constructed Facilities*, 26(5), 590-599.

Karimi, K., Tait, M. J., and El-Dakhakhni, W. W. (2011a). "Testing and modeling of a novel FRP-encased steel–concrete composite column." *Composite Structures*, 93(5), 1463-1473.

Kassem, C., Farghaly, A. S., and Benmokrane, B. (2011). "Evaluation of flexural behavior and serviceability performance of concrete beams reinforced with FRP bars." *Journal of Composites for Construction*, 15(5), 682-695.

Kawaguchi, N. (1993). "Ultimate strength and deformation characteristics of concrete members reinforced with AFRP rods under combined axial tension or compression and bending." *Special Publication*, 138, 671-684.

Keller, T. (2001). "Recent all-composite and hybrid fibre-reinforced polymer bridges and buildings." *Progress in Structural Engineering and Materials*, 3(2), 132-140.

Kobayashi, K., and Fujisaki, T. (1995). "Compressive Behavior of FRP Reinforcement in Non-prestressed Concrete Members." *Proceedings of the Second International RILEM Symposium on Non-Metallic (FRP) Reinforcement for Concrete Structures (FRPRCS-2)*, pp. 267-274, Ghent, Belgium.

Kollár, L. P. (2002a). "Buckling of unidirectionally loaded composite plates with one free and one rotationally restrained unloaded edge." *Journal of Structural Engineering*, 128(9), 1202-1211.

Kollár, L. P. (2002b). "Discussion of "Local Buckling of Composite FRP Shapes by Discrete Plate Analysis" by Pizhong Qiao, Julio F. Davalos, and Jialai Wang." *Journal of Structural Engineering*, 128(8), 1091-1093.

Kollár, L. P. (2003). "Local buckling of fiber reinforced plastic composite structural members with open and closed cross sections." *Journal of Structural Engineering*, 129(11), 1503-1513.

Kwan, W. H., and Ramli, M. (2013). "Indicative performance of fiber reinforced polymer (FRP) encased beam in flexure." *Construction and Building Materials*, 48(0), 780-788.

Lackey, E., Spoo, K., Gill, C., and Vaughan, J. (2010). "Comparison of Composite Properties from Different Test Standards - A Case Study form the Development of a Load and Resistance Factor Design (LRFD) Standard for Pultruded Composites." *COMPOSITES 2010, American Composites Manufacturers Association*, February 9-11, 2010, Las Vegas, Nevada, USA.

Lackey, E., Vaughan, J., Gupta, S., Rawls, S., and Wimbrow, W. (2007). "Comparison of compression test methods for pultruded composites." *Composites and Polycon 2007, American Composites Manufacturers Association*, October 17-19, 2007, Tampa, FL, USA.

Lam, L., and Teng, J. (2003). "Design-oriented stress–strain model for FRP-confined concrete." *Construction and Building Materials*, 17(6), 471-489.

Lam, L., and Teng, J. (2004). "Ultimate condition of fiber reinforced polymer-confined concrete." *Journal of Composites for Construction*, 8(6), 539-548.

Lau, D., and Pam, H. J. (2010). "Experimental study of hybrid FRP reinforced concrete beams." *Engineering Structures*, 32(12), 3857-3865.

Leung, H. Y., and Balendran, R. V. (2003). "Flexural behaviour of concrete beams internally reinforced with GFRP rods and steel rebars." *Structural Survey*, 21(4), 146-157.

Li, X., Lv, H., and Zhou, S. (2012). "Flexural behavior of GFRP-reinforced concrete encased steel composite beams." *Construction and Building Materials*, 28(1), 255-262.

Lotfy, E. M. (2010). "Behavior of reinforced concrete short columns with Fiber Reinforced polymers bars." *International Journal of Civil and Structural Engineering*, 1(3), 545.

Lu, X., Jiang, J., Teng, J., and Ye, L. (2006). "Finite element simulation of debonding in FRP-to-concrete bonded joints." *Construction and Building Materials*, 20(6), 412-424.

Maaddawy, T. E. (2009). "Strengthening of eccentrically loaded reinforced concrete columns with fiber-reinforced polymer wrapping system: Experimental investigation and analytical modeling." *Journal of Composites for Construction*, 13(1), 13-24.

Majdi, Y., Hsu, C.-T. T., and Punurai, S. (2014). "Local bond–slip behavior between cold-formed metal and concrete." *Engineering Structures*, 69, 271-284.

Mallick, P., K. (1988). *Fiber reinforced composites, materials, manufacturing and design*, Marcell Dekker, p. 469, New York, US.

Mander, J. B., Priestley, M. J., and Park, R. (1988). "Theoretical stress-strain model for confined concrete." *Journal of Structural Engineering*, 114(8), 1804-1826.

Mirmiran, A. (1998). "Length effects on FRP-reinforced concrete columns." *Proceedings of the Second International Conference on Composites in Infrastructure,* 1.

Mirmiran, A., Shahawy, M., Samaan, M., Echary, H., Mastrapa, J., and Pico, O. (1998). "Effect of Column Parameters on FRP-Confined Concrete." *Journal of Composites for Construction*, 2(4), 175-185.

Mirmiran, A., Yuan, W.-q., and Chen, X. (2001). "Design for slenderness in concrete columns internally reinforced with fiber-reinforced polymer bars." *ACI structural journal*, 98(1), 116-125.

Mohamed, H. M., Afifi, M. Z., and Benmokrane, B. (2014). "Performance evaluation of concrete columns reinforced longitudinally with FRP bars and confined with FRP hoops and spirals under axial load." *Journal of Bridge Engineering*, 19(7), 04014020.

Mottram, J. T. (1994). "Compression strength of pultruded flat sheet material." *Journal of Materials in Civil Engineering*, 6(2), 185-200.

Muttashar, M., Manalo, A., Karunasena, W., and Lokuge, W. (2016). "Experimental investigation on the flexural behaviour of pultruded GFRP beams filled with different concrete strengths." *Proceedings of the Eighth International Conference on Fibre-Reinforced Polymer (FRP) Composites in Civil*

Engineering (CICE 2016), Official Conference of the International Institute for FRP in Construction (IIFC), 14-16 December 2016, Hong Kong, China.

Nanni, A. (1993b). "Flexural Behavior and Design of Reinforced Concrete Using FRP Rods." *Journal of Structural Engineering Structures*, 119(11), 3344-3359.

Nanni, A., and Bradford, N. M. (1995). "FRP jacketed concrete under uniaxial compression." *Construction and Building Materials*, 9(2), 115-124.

Nanni, A., Rizkalla, S., Bakis, C., E., Conrad, J., O., and Abdelrahman, A., A. (1998). "Characterization of GFRP Ribbed Rod Used for Reinforced Concrete Construction." *Proceedings of the International Composites Exhibition (ICE-98)*, pp. 16A/1-6, Nashville, Tenn., USA.

Nunes, F., Correia, M., Correia, J., Silvestre, N., and Moreira, A. (2013). "Experimental and numerical study on the structural behavior of eccentrically loaded GFRP columns." *Thin-Walled Structures*, 72, 175-187.

Nunes, F., Silvestre, N., and Correia, J. R. (2016). "Structural behaviour of hybrid FRP pultruded columns. Part 2: Numerical study." *Composite Structures*, 139, 304-319.

Ozbakkaloglu, T. (2013b). "Concrete-Filled FRP Tubes: Manufacture and Testing of New Forms Designed for Improved Performance." *Journal of Composites for Construction*, 17(2), 280-291.

Ozbakkaloglu, T. (2013c). "Axial Compressive Behavior of Square and Rectangular High-Strength Concrete-Filled FRP Tubes." *Journal of Composites for Construction*, 17(1), 151-161.

Ozbakkaloglu, T., Lim, J. C., and Vincent, T. (2013a). "FRP-confined concrete in circular sections: Review and assessment of stress–strain models." *Engineering Structures*, 49(0), 1068-1088.

Pantelides, C. P., Gibbons, M. E., and Reaveley, L. D. (2013). "Axial load behavior of concrete columns confined with GFRP spirals." *Journal of Composites for Construction*, 17(3), 305-313.

Pessiki, S., and Pieroni, A. (1997). "Axial load behavior of large-scale spirally-reinforced high-strength concrete columns." *ACI structural journal*, 94(3), 304-314.

Pham, T., Hadi, M., and Youssef, J. (2017). "Effects of Fabrication Technique on Tensile Properties of Fiber Reinforced Polymer."

Pham, T. M., Doan, L. V., and Hadi, M. N. S. (2013). "Strengthening square reinforced concrete columns by circularisation and FRP confinement." *Construction and Building Materials*, 49, 490-499.

Pham, T. M., and Hadi, M. N. S. (2013). "Strain estimation of CFRP-confined concrete columns using energy approach." *Journal of Composites for Construction*, 17(6), 04013001.

Pham, T. M., and Hadi, M. N. S. (2014a). "Confinement model for FRP confined normal-and high-strength concrete circular columns." *Construction and Building Materials*, 69, 83-90.

Pham, T. M., and Hadi, M. N. S. (2014b). "Predicting Stress and Strain of FRP-Confined Square/Rectangular Columns Using Artificial Neural Networks." *Journal of Composites for Construction*, 18(6), 04014019-04014011–04014019-04014019.

Pham, T. M., and Hadi, M. N. S. (2014c). "Stress prediction model for FRP confined rectangular concrete columns with rounded corners." *Journal of Composites for Construction*, 18(1), 04013019.

Pham, T. M., Hadi, M. N. S., and Tran, T. M. (2015a). "Maximum usable strain of FRP-confined concrete." *Construction and Building Materials*, 83, 119-127.

Pham, T. M., Hadi, M. N. S., and Youssef, J. (2015b). "Optimized FRP wrapping schemes for circular concrete columns under axial compression." *Journal of Composites for Construction*, 19(6), 04015015.

Pham, T. M., and Hao, H. (2016). "Impact behavior of FRP-strengthened RC beams without stirrups." *Journal of Composites for Construction*, 20(4), 04016011.

Pultrall (2012). "V-ROD Specification HM." Thetford Mines, Canada.

Qiao, P., Davalos, J. F., and Wang, J. (2001). "Local buckling of composite FRP shapes by discrete plate analysis." *Journal of Structural Engineering*, 127(3), 245-255.

Saadatmanesh, H., and Ehsani, M. (1991). "RC Beams Strengthened with GFRP Plates. I: Experimental Study." *Journal of Structural Engineering*, 117(11), 3417-3433.

SACMA. (1994). "SACMA Recommended Test Method for Compressive Properties of Oriented Fiber-Resin Composites."Suppliers of Advanced Composite Materials Association, *SACMA SRM-1R-94*.

Saha, M., Prabhakaran, R., and Waters, W. A. (2000). "Compressive Properties of Pultruded Composites." *Mechanics of Composite Materials*, 36(6), 469-474.

Sheikh, M. N., and Legeron, F. (2014). "Performance based seismic assessment of bridges designed according to Canadian Highway Bridge Design Code." *Canadian Journal of Civil Engineering*, 41(9), 777-787.

Sheikh, S. A., and Uzumeri, S. M. (1980). "Strength and ductility of tied concrete columns." *Journal of the structural division*, 106(ASCE 15388 Proceeding).

Smith, S. T., Kim, S. J., and Zhang, H. (2010). "Behavior and effectiveness of FRP wrap in the confinement of large concrete cylinders." *Journal of Composites for Construction*, 14(5), 573-582.

Sonti, S. S., and Barbero, E. J. (1996). "Material Characterization of Pultruded Laminates and Shapes." *Journal of Reinforced Plastics and Composites*, 15(7), 701-717.

Tamužs, V., Tepfers, R., Zīle, E., and Valdmanis, V. (2008). "Mechanical behaviour of FRP-confined concrete columns under axial compressive loading." *Proceedings of the 5th international engineering and construction conference. American Society of Civil Engineering, International Committee, Los Angeles Section*, 223-241.

Teng, J., G., Yu, T., and Wong, Y., L. (2004). "Behaviour of hybrid FRP-concrete-steel double-skin tubular columns." *Proceedings of the 2nd International conference on FRP composites in civil engineering-CICE2014,* Adelaide, Australia, pp 811–818.

Teng, J., Jiang, T., Lam, L., and Luo, Y. (2009). "Refinement of a design-oriented stress–strain model for FRP-confined concrete." *Journal of Composites for Construction*, 13(4), 269-278.

Teng, J. G., Yu, T., Wong, Y. L., and Dong, S. L. (2007). "Hybrid FRP–concrete–steel tubular columns: Concept and behavior." *Construction and Building Materials*, 21(4), 846-854.

Theriault, M., and Benmokrane, B. (1998). "Effects of FRP reinforcement ratio and concrete strength on flexural behavior of concrete beams." *Journal of Composites for Construction*, 2(1), 7-16.

Tobbi, H., Farghaly, A. S., and Benmokrane, B. (2012). "Concrete Columns Reinforced Longitudinally and Transversally with Glass Fiber-Reinforced Polymer Bars." *ACI structural journal*, 109(4), 551-558.

Tobbi, H., Farghaly, A. S., and Benmokrane, B. (2014). "Behavior of Concentrically Loaded Fiber-Reinforced Polymer Reinforced Concrete Columns with Varying Reinforcement Types and Ratios." *ACI structural journal*, 111(2), 375-385.

Tomblin, J., and Barbero, E. (1994). "Local buckling experiments on FRP columns." *Thin-Walled Structures*, 18(2), 97-116.

Tomblin, J., Ng, Y., Bowman, K., Hooper, E., Smyth, T., and Showers, D. (2001). "‘Material Qualification Methodology for Epoxy-Based Prepreg Composite Material Systems." *United States Department of Transportation, Federal Aviation Administration Report DOT/FAA/AR-00/47, Washington, DC*.

Toufigh, V., Ouria, A., Desai, C. S., Javid, N., Toufigh, V., and Saadatmanesh, H. (2015). "Interface behavior between carbon-fiber polymer and sand." *Journal of Testing and Evaluation*, 44(1), 385-390.

Toutanji, H. A. (1999). "Stress-strain characteristics of concrete columns externally confined with advanced fiber composite sheets." *ACI materials journal*, 96(3), 397-404.

TR. (2012). "Design guidance for strengthening concrete structures usingfibre composite materials."TR, *TR 55,* Concrete Society, Camberley, England.

Tsai, S. W., and Wu, E. M. (1971). "A general theory of strength for anisotropic materials." *Journal of Composite Materials*, 5(1), 58-80.

Turgay, T., Polat, Z., Koksal, H., Doran, B., and Karakoç, C. (2010). "Compressive behavior of large-scale square reinforced concrete columns confined with carbon fiber reinforced polymer jackets." *Materials & Design*, 31(1), 357-364.

Turvey, G., and Zhang, Y. (2006). "A computational and experimental analysis of the buckling, postbuckling and initial failure of pultruded GRP columns." *Computers & Structures*, 84(22), 1527-1537.

Van Erp, G., Cattell, C., and Ayers, S. (2006). "The Australian approach to composites in civil engineering." *Reinforced Plastics*(International Buyers' Guide 2006), 16-20, 22-24.

Vilanova, I., Baena, M., Torres, L., and Barris, C. (2015). "Experimental study of bond-slip of GFRP bars in concrete under sustained loads." *Composites Part B: Engineering*, 74, 42-52.

Wagners. (2014). *Wagners Composite Fibre Technologies (CFT)*, Toowoomba, QLD, Australia, [http://www.wagner.com.au/], accessed Aug. 8, 2014.

Wang, H., and Belarbi, A. (2005). "Flexural behaviour of fibre reinforced-concrete beams reinforced with FRP rebars." *ACI-SP-230: 7th International Symposium on Fiber-Reinforced (FRP) Polymer Reinforcement for Concrete Structures*, pp. 895-914, Farmington Hills (MI), USA: ACI.

Wang, Q., Zhao, D., and Guan, P. (2004). "Experimental study on the strength and ductility of steel tubular columns filled with steel-reinforced concrete." *Engineering Structures*, 26(7), 907-915.

Wang, W., Sheikh, M. N., and Hadi, M. N. S. (2016). "Experimental study on FRP tube reinforced concrete columns under different loading conditions." *Journal of Composites for Construction*, 20(5), 04016034.

Warner, R. F., Foster, S. J., and Kilpatrick, A. E. (2007). *Reinforced concrete basics: analysis and design of reinforced concrete structures*, Pearson, Sydney, Australia.

Welsh, J., and Adams, D. (1997). "Current status of compression test methods for composite materials." *SAMPE journal*, 33(1), 35-43.

Welsh, J. S., and Adams, D. F. (1997). "An experimental investigation of the mini-sandwich laminate as used to obtain unidirectional composite compression strengths." *Journal of Composite Materials*, 31(3), 293-314.

West-System (2015). "Epoxy resins and hardeners—Physical properties." <http://www.westsystem.com/ss/typical-physical-properties>. (January 31, 2015).

Wong, Y. L., Yu, T., Teng, J. G., and Dong, S. L. (2008). "Behavior of FRP-confined concrete in annular section columns." *Composites Part B: Engineering*, 39(3), 451-466.

Wu, W.-P. (1990). "Thermomechanical properties of fiber reinforced plastic(FRP) bars." *Dissertation Abstracts International(USA)*, 52(8), 292.

Wu, Y.-F., and Jiang, J.-F. (2013). "Effective strain of FRP for confined circular concrete columns." *Composite Structures*, 95, 479-491.

Wu, Y.-F., Liu, T., and Oehlers, D. J. (2006). "Fundamental principles that govern retrofitting of reinforced concrete columns by steel and FRP jacketing." *Advances in Structural Engineering*, 9(4), 507-533.

Wu, Y.-F., and Zhou, Y.-W. (2010). "Unified strength model based on Hoek-Brown failure criterion for circular and square concrete columns confined by FRP." *Journal of Composites for Construction*, 14(2), 175-184.

Xue, W., Hu, X., and Fang, Z. "Experimental studies of GFRP reinforced concrete columns under static eccentric loading." *Proc., The 7th International Conference on FRP Composites in Civil Engineering*.

Yang, K.-H., Mun, J.-H., Cho, M.-S., and Kang, T. H. (2014). "Stress-strain model for various unconfined concretes in compression." *ACI structural journal*, 111(4), 819.

Yazici, V., and Hadi, M. N. S. (2009). "Axial load-bending moment diagrams of carbon FRP wrapped hollow core reinforced concrete columns." *Journal of Composites for Construction*, 13(4), 262-268.

Ye, L., Feng, P., Zhang, K., Lin, L., Hong, W., Yue, Q., Zhang, N., and Yang, T. (2003). "FRP in civil engineering in China: research and applications." *Fibre-Reinforced Polymer Reinforcement for Concrete Structures: (In 2 Volumes)*, World Scientific, 1401-1412.

Youssef, J., and Hadi, M. N. S. (2017). "Axial load-bending moment diagrams of GFRP reinforced columns and GFRP encased square columns." *Construction and Building Materials*, 135, 550-564.

Yu, T., Wong, Y., L., and Teng, J., G. (2010). "Behavior of Hybrid FRP-Concrete-Steel Double-Skin Tubular Columns Subjected to Eccentric Compression." *Advances in Structural Engineering*, 13 (5), 961-974.

Yu, T., Wong, Y. L., Teng, J. G., Dong, S. L., and Lam, E. S. S. (2006). "Flexural Behavior of Hybrid FRP-Concrete-Steel Double-Skin Tubular Members." *Journal of Composites for Construction*, 10(5), 443-452.

Yuan, J. S., and Hadi, M. N. S. (2016). "Experimental Study on Bond Behavior Between Concrete and GFRP Pultruded I-section using Push-out Test." *Proceedings of the Eighth International Conference on Fibre-Reinforced Polymer (FRP) Composites in Civil Engineering (CICE 2016)*, Official

Conference of the International Institute for FRP in Construction (IIFC), 14-16 December 2016, Hong Kong, China.

Zadeh, H., and Nanni, A. (2013). "Design of RC Columns Using Glass FRP Reinforcement." *Journal of Composites for Construction*, 17(3), 294-304.